technische universität
dortmund

HYPERFINE CHARACTERISATION AND ENHANCED OPTICAL TO SPIN STORAGE IN RARE EARTH ION DOPED CRYSTALS

MARKO LOVRIĆ

A thesis submitted for the degree of
Doctor rerum naturalium

Experimentelle Physik III

Fachbereich Physik

Technische Universität Dortmund

November 17, 2011

CONTENTS

AFC Atomic Frequency Comb

AOM Acousto-Optic Modulator

AWG Arbitrary Waveform Generator

BP Brewster-Plate or Band Pass

BS Beam Splitter

CNC Computerised Numerical Control machine

CP Carr-Purcell (sequence)

CPMG Carr-Purcell-Meiboom-Gill (sequence)

CRIB Controlled Reversible Inhomogeneous Broadening

CW Continous Wave

DAC Digital to Analog Converter

DC Direct Current

DD Dynamical Decoupling

DDS Direct Digital Synthesis

DSO Digital Storage Oscilloscope

EIT Electromagnetically Induced Transparency

EOM Electro-Optic Modulator

FID Free Induction Decay

FWHM Full Width Half Maximum

GEM Gradient Echo Memory

HP High Pass

KDD Knill (pulse) Dynamical Decoupling

LAS Laboratory Axis System

LCMCP Laboratoire de Chimie de la Matière Condensée de Paris (Condensed Matter Chemistry) - UMR 7574 CNRS - France

LP Low Pass

LSQ Least Squares

MC Master Clock

NMR Nuclear Magnetic Resonance

OTSS Optical To Spin Storage

PAS Principal Axis System

PBS   Polarising Beam Splitter

PID   Proportional-Integral-Derivative (amplifier)

PD   Photo Detector

PDD   Periodic Dynamical Decoupling

PDH   Pound-Drever-Hall (technique)

PrLaWO $Pr^{3+}:La_2(WO_4)_3$, trivalent praseodymium in lanthanum tungstate

PrYAP $Pr^{3+}:YAlO_3$, trivalent praseodymium in yttrium alluminum perovskite

PrYSO $Pr^{3+}:Y_2SiO_5$, trivalent praseodymium in yttrium orthosilicate

PZT   Piezoelectric Actuator

RE   Rare Earth

REIC   Rare Earth Ion Crystal

RF   Radio Frequency

RHS   Raman Heterodyne Scattering

RMS   Root Mean Square

ROSE   Revival Of Silenced Echo

SNR   Signal to Noise Ratio

SSB   Single SideBand

STD   STandard Derivation

TPPE   Two Pulse Photon Echo

UDD   Uhrig Dynamical Decoupling

VCO   Voltage Controlled Oscillator

WG   Word Generator

ZEFOZ   Zero First Order Zeeman (condition)

INTRODUCTION

In this work the characteristics of rare earth ion doped crystals are investigated by use of combined magneto-optical techniques. Precise Hamiltonian parameters are determined and used to study and improve processes, which are important for the storage of quantum information carried by optical photons into a solid material.

The narrow optical transitions of rare earth ions doped into dielectric crystals have fascinated researchers since the very early days of high resolution spectroscopy [153]. Their optical line widths can be as narrow as 50 Hz [146], which is about eight orders of magnitude smaller than typical electronic transitions in solids [37, 99, 146]. Typical rare earth ions in crystals have inhomogeneous optical line widths of about 10 GHz, which consist of very narrow $\approx$ 1 kHz frequency-shifted homogeneous optical lines, represented by single absorbing ions in the same spatial area [100]. Therefore, the medium can absorb at various optical frequencies at the same time. The narrow optical line width of the single frequency channels incorporates long coherence lifetimes. Together, high frequency bandwidth and long optical lifetime, allow storage of optical input data with very high bandwidths and storage times [84]. The storage times can even be extended, since the optical transitions are connected to long lived nuclear spin states [119]. In rare earth ion systems high bandwidth, multi-mode optical inputs can be transferred by fast coherent optical control pulses into long lived nuclear spin population gratings of the electronic ground state [84, 10, 90]. These properties offer an enormous potential for high density and high time-bandwidth product optical storage, but also can be used for state of the art real-time broadband spectral analysis [115] and high time-bandwidth signal processing [64].

With the upcoming of quantum information science [120], rare earth ions were soon identified as promising candidates for implementations [98, 73]. The optical transitions allow application of control-operations at timescales of $\gtrsim$ 100 ns and already offer decoherence times of the order of 1 ms. Mapping the quantum information by fast optical pulses into coherences between nuclear spin levels can utilise the nuclear lifetimes. Using well established radio frequency pulse based nuclear magnetic resonance decoupling techniques, the nuclear spin coherence lifetimes may become as long as tens of seconds [43]. This holds the potential to apply many control operations, before the information in the "qubits" are lost due to decoherence. On the track of quantum computing with rare earth ions milestones, including arbitrary single qubit rotations [132] and two-qubit conditional phase gates [94], have been demonstrated. In parallel the research has grown in the direction of quantum memories based on rare earth ions.

Beside the storage of the pulse energies quantum memories also require to accurately store the relative phases of the input photons, while keeping the "quantum" nature of the input state [148]. For example, a gain of the medium by stimulated emission violates the no-cloning theorem and would degrade the memory fidelity [133]. An "original" quantum memory has important applications, i.e. it represents a de-

terministic single photon source and is a key component for quantum repeaters [148]. Through the use of quantum repeaters [25] the maximum distance for secure quantum cryptographic communication in optical fibre networks could be extended. The underling quantum key distribution is already commercially available, but due to the lack of quantum repeaters and memories, is currently limited to distances of below $\approx 100 - 250$ km.[†]

[†]*See e.g.*
www.idquantique.com,
www.magiqtech.com.

In the last couple of years a few original quantum memory schemes have been proposed [117, 69, 4, 32] and experimental prototypes have been demonstrated. A lot of attention was focused on the quantum fidelity [30, 138], the multimode capability [151, 22] and the storage and retrieval efficiency [66] of the optical absorption process. The storage in the nuclear spin degrees of freedom and the later retrieval into an optical output have been demonstrated in principle [5]. Nevertheless, none of the more recent photon echo based quantum memory schemes have used the full potential of long nuclear spin storage by refocusing the nuclear spin dephasing with radio frequency pulses.

This may be attributed to a very early demonstration of coherence lifetimes of more than 30 s [46] and "stopped light" for impressive storage times greater than 1 s [95] in the nuclear spin states of the rare earth compound $Pr^{3+}: Y_2SiO_5$. The stopped light demonstration was carried out using electromagnetically induced transparency [63], which only allows storage of low bandwidth light pulses compared to the photon echo based techniques [134, 32]. $Pr^{3+} : Y_2SiO_5$ is known to be a "low-noise" sample with very long natural coherence lifetimes [38]. Up to now it represents the only compound for which the so-called zero first order Zeeman technique, which is essential for the observed long coherence lifetimes, was demonstrated [44].

One of the main points of the work presented in this thesis is the first test of the applicability of the zero first order Zeeman technique in an other sample, the "high-noise" sample: $Pr^{3+}: La_2(WO_4)_3$. Limiting the active research to low-noise samples sometimes comes at other costs. For instance in the high-noise compound $Pr^{3+}: La_2(WO_4)_3$ the inhomogeneous line broadening is much lower compared to $Pr^{3+}: Y_2SiO_5$ with the same level of Pr doping [54]. A high doping level incorporates high optical absorption density, which is required by all photon echo based quantum memory schemes in order to reach high memory efficiencies [148] and thus makes $Pr^{3+}: La_2(WO_4)_3$ an interesting new compound. Promising results for the zero first order Zeeman experiments in $Pr^{3+}: La_2(WO_4)_3$ demonstrate the potential of this compound. Motivated by this, an experimental investigation of the enhancement of the optical to nuclear spin storage times by radio frequency pulsed decoupling techniques, within the framework of high bandwidth photon echo storage schemes is also presented in this study.

All these experiments require a high level of control and accuracy, i.e. for the radio frequency pulses, the optical control fields and the static magnetic fields used for the zero first order Zeeman technique. Detailed knowledge of the rare earth ion Hamiltonian parameters is a prerequisite to apply the controls in exactly the right way. In this work a precise hyperfine Hamiltonian characterisation for three rare earth compounds is presented. The technique uses Raman heterodyne spectra collected for > 200 static magnetic fields for each sample. For $Pr^{3+}: La_2(WO_4)_3$ this represents the first full hyperfine characterisation. A previous characterisation of $Pr^{3+} : Y_2SiO_5$ [93] is refined to higher

precision and the new characterisation further resolves a controversy in the literature [122] for this very widely-used compound. For Pr^{3+}: $YAlO_3$ the characterisation results in Hamiltonian parameters of higher accuracy than previously published. This is especially the case for the excited state, since Pr^{3+}: $YAlO_3$ is analysed the first time with a more general Hamiltonian model, abandoning an approximation used in the literature.

1.1 OUTLINE

Part I introduces a variety of techniques that are required for the control of the optical transition and at the same time the nuclear spin transitions under the aspects discussed above. The relevant spectroscopic properties of trivalent rare earth ions and the connection between the nuclear spin and the electronic degrees of freedom, forming the hyperfine Hamiltonian, are discussed in chapter 2. In chapter 3 a short description of the basic experimental methods is presented.

Part II of the thesis describes the experimental apparatus. Chapter 4 explains the optical setup, with an emphasis on the improvements achieved for the laser phase stability and the recently set up calibration system for accurate arbitrary optical pulse generation. Both systems are a crucial prerequisite for optical to nuclear spin storage experiments. The radio frequency control for the various nuclear spin transition frequencies involved, and the signal demodulation for optically detected Raman heterodyne nuclear magnetic resonance experiments are described in chapter 5. Chapter 6 presents the magnet systems, which have been used and developed during this thesis as well as the cryogenic system for cooling the samples to liquid helium temperature.

Part III is dedicated to the experiments investigating rare earth ionic crystals. The characterisation of all three compounds are presented in chapter 7. This includes a description of the scheme collecting about 200 Raman heterodyne spectra in precisely controlled magnetic fields. Furthermore the procedure for fitting the theoretical Hamiltonian parameters to the spectra, which is based on simulated annealing for robust convergence to the global minimum solution, is presented in detail.

Chapter 8 presents the first successful experimental demonstration of the zero first order Zeeman technique by an independent research group and in an other compound, using Pr^{3+}: $La_2(WO_4)_3$. The coherence times and mechanism for the ground state of Pr^{3+} :$La_2(WO_4)_3$ are discussed for different magnetic fields as well as for single and multiple radio frequency pulse rephasing and decoupling techniques. The same decoupling techniques are further applied to photon echo based optical to nuclear spin storage schemes, which makes this the first study of their performance in a high bandwidth quantum memory test bed.

Part I

GENERAL BACKGROUND

2

All experiments within this work use the electronic and nuclear transitions of the rare earth ion praseodymium.

^{141}Pr, which has a nuclear spin of $I = 5/2$, has the atomic number $Z = 59$ and therefore belongs to the lanthanides ($Z = 57 - 71$). This class of elements has completely filled 5s and 5p orbitals, whereas the 4f shell is filled with increasing atomic number. A characteristic is that the radial extent of the filled 5s and 5p electrons is larger than that of the 4f electrons (see figure 1). This shields the 4f electrons from the environment and leads to very narrow optical line widths for inner 4f-4f transitions [47], which are excited by the optical fields in this work.
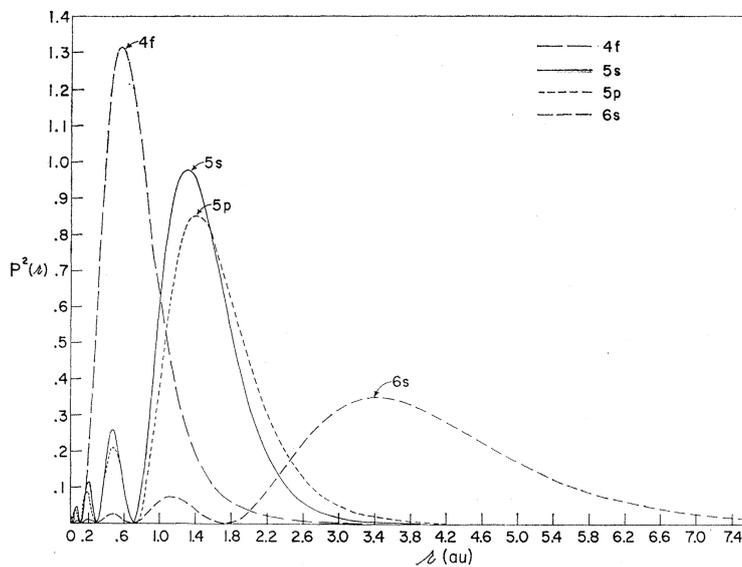
Figure 1: Typical radial charge density plot for the 4f, 5s, 5p and 6s electrons of rare earth ions (here Gd+). The figure was taken from Ref. [47].

In its compounds praseodymium appears as triple ionised Pr^{3+}, which has a $[Xe]4f^2$ electron configuration. In the used samples praseodymium substitutes the atomic positions of other triply ionised lanthanoids in the matrix of optically transparent single crystal compounds. In particular this crystal host materials are $YAlO_3$, Y_2SiO_5 and $La_2(WO_4)_3$, with yttrium and lanthanum being substituted by praseodymium. The crystals are grown out of a melt of the host crystal compounds, to which a small amount of praseodymium is added. Typical doping levels are 0.1% at. of praseodymium. In the following the rare earth ionic crystal (REIC) compounds Pr^{3+}: $YAlO_3$, Pr^{3+}: Y_2SiO_5 and Pr^{3+}: $La_2(WO_4)_3$ will be named by the short-forms PrYAP, PrYSO and PrLaWO respectively. The wavelength of the optical Pr^{3+} inner $4f^2$ transition changes by less than 1% between these compounds, which is attributed to the shielding of the 4f electrons. The low doping levels lead to very low Pr ion-ion couplings and the trapping in the crystal matrix removes Doppler broadening, which together lead to very nar-

row optical lines. The crystals are of high optical quality, mechanically and chemically stable, which simplifies their handling.

The host material subjects the Pr^{3+} ions to its local crystal field. Ions in different substitution sites of the crystal unit cell often are exposed to different local crystal fields, which may give rise to different signals of these Pr-sites. The effect of the crystal field on the electronic level structure is discussed in the following section.

2.1 HAMILTONIAN

Within this work a simple approximation for the rare earth Hamiltonian [11] is sufficient:

$$\mathcal{H}_0 = [\mathcal{H}_{FI} + \mathcal{H}_{CF}] + [\mathcal{H}_{HF} + \mathcal{H}_Q + \mathcal{H}_Z + \mathcal{H}_z] . \qquad (2.1)$$

The first two terms describe the free ion, including the spin-orbit coupling, and the crystal field Hamiltonian. Although the explicit form of $\mathcal{H}_{FI}$ and $\mathcal{H}_{CF}$ is not important for this work, they represent the dominant part of $\mathcal{H}_0$. They determine the optical transition wavelength and the form of the remaining terms of the Hamiltonian.

Russell-Saunders symbol: $^{2S+1}L_J$

Using Hund's rules for the free ion of praseodymium, which has a $[Xe]4f^2$ electron configuration, results in a $^3H_4$ ground state [72]. All 4f states of the free ion are (2J+1)-fold degenerate in their magnetic quantum number m_J.

Interaction of the ion with the charges of a lattice - the crystal field - may lift this degeneracy partially [13]. Rare earth ions with an even number of 4f-electrons, like Pr^{3+}, show singlet levels when they are doped into crystals of less than axial symmetry, thus the degeneracy is lifted completely. Figure 2 a) and b) show a schematic energy level diagram for this situation.

This work focuses on transitions between the lowest energy levels of the corresponding J-manifolds. Due to the lack of intra-J-level spontaneous phonon emission channels, these transitions exhibit long lifetimes [100] and are referred to as "zero phonon lines". The lifetimes are also relatively long, since the transitions between 4f-states are forbidden due to the parity selection rules of the electric dipole radiation. The crystal field causes weak admixture of states with different parity to the 4f-wave functions, which causes the transitions to become at least weakly allowed and explains the relatively low oscillator strengths in these compounds [153].

The remaining terms of equation 2.1 represent the hyperfine interaction $\mathcal{H}_{HF}$, the quadrupolar interaction $\mathcal{H}_Q$, the electron $\mathcal{H}_Z$ and the nuclear Zeeman interaction $\mathcal{H}_z$. Together, they will be referred to as the spin or hyperfine Hamiltonian. The individual parts are expressed in terms of effective Hamiltonians, which are specific for an electronic state (e.g. $^{2S+1}L_J$ or $^{2S'+1}L'_{J'}$ in figure 2) and are determined by the eigenfunctions of $\mathcal{H}_{FI} + \mathcal{H}_{CF}$, as they dominate the total energy structure. For the case of electronic singlets the electronic angular momentum is quenched [152] to first order and its expectation value vanishes as the J-degeneracy is lifted completely [142]. The hyperfine interaction $\mathcal{H}_{HF}$ and the electronic Zeeman interaction $\mathcal{H}_Z$ depend on the electronic angular momentum operator J [100], therefore can only contribute in
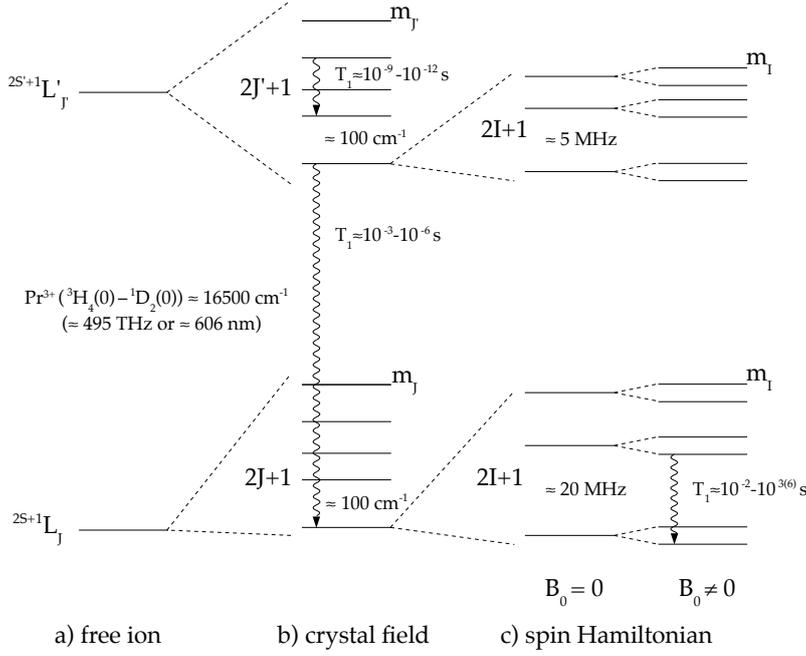
Figure 2: Schematic energy level diagram for an REI with an even number of 4f-electrons. It shows the kind of degeneracy for different degrees of approximation a), b) and c), further details are given in the text. The numbers represent typical values for lifetimes T_1 and energy level splittings for trivalent rare earths [100]. The quoted optical zero phonon line transition wavelength is typical for the Pr compounds studied in Part iii of this thesis.
(Conversions: y cm$^{-1} \hat{=}$ y 29.98 GHz $\hat{=}$ y^{-1} 10^7 nm.)

second order perturbation theory. Their effective Hamiltonians can be represented by [147]:

$$\mathcal{H}_Z^{\text{eff}} + \mathcal{H}_{\text{HF}}^{\text{eff}} = -g_J^2 \mu_B^2 \vec{B} \cdot \hat{\Lambda} \cdot \vec{B} - 2A_J g_J \mu_B \vec{B} \cdot \hat{\Lambda} \cdot \vec{I} + A_J^2 \vec{I} \cdot \hat{\Lambda} \cdot \vec{I}, \quad (2.2)$$

where g_J is the Landé g-value, μ_B the Bohr magneton, $\vec{B}$ the external magnetic field vector and $\vec{I} = (I_{x'}, I_{y'}, I_{z'})$ the vector of the nuclear spin operators. A_J is the hyperfine constant of the J-multiplet state, the tensor $\hat{\Lambda}$ follows from second order perturbation theory and can be written as:

$$\Lambda_{\alpha'\beta'} = \sum_{n=1}^{2J+1} \frac{\langle 0| J_{\alpha'} |n\rangle \langle n| J_{\beta'} |0\rangle}{E_n - E_0}. \quad (2.3)$$

Here α' and β' denote the axes (x', y', z') and E_n the energy of the nth crystal field level $|n\rangle$, whereas $|0\rangle$ is the J-multiplet level to which the effective Hamiltonian of equation 2.2 applies, e.g. the $^3H_4(0)$ or $^1D_2(0)$ level. The purely nuclear Zeeman and quadrupolar interaction Hamiltonians can be expressed by [147]:

$$\mathcal{H}_z = -g_I \mu_N \vec{B} \cdot \vec{I} \quad (2.4)$$

and

$$\mathcal{H}_Q = P\left[I_{z''}^2 - \frac{1}{3}I(I+1) + \frac{1}{3}\eta\left(I_{x''}^2 - I_{y''}^2\right)\right],\tag{2.5}$$

here g_I is the nuclear g-factor, μ_N the nuclear magneton. P is the quadrupole coupling constant and $\eta = (V_{x''x''} - V_{y''y''})/V_{z''z''}$ describes the asymmetry of the electric field gradient, given in its principal axis system (PAS) tensor components $V_{\alpha''\alpha''}$, underling the quadrupolar interaction with nuclear spins of $I > 1/2$.

The quenching of the electronic angular momentum causes the contributions to the Hamiltonian arising from the electron spin (Eq. 2.2) and due to nuclear spin (Eq. 2.4-2.5) to become comparable. Using

$$D_{pQ} = A_J^2\left[\frac{1}{2}\left(\Lambda_{x'x'} + \Lambda_{y'y'}\right) - \Lambda_{z'z'}\right]\tag{2.6}$$

and

$$E_{pQ} = A_J^2\frac{1}{2}\left(\Lambda_{y'y'} - \Lambda_{x'x'}\right)\tag{2.7}$$

the last term of equation 2.2, representing the second order hyperfine interaction, can be written in the same form as $\mathcal{H}_Q$ (Eq. 2.5), i.e. $\mathcal{H}_{pQ}$. In the literature [11] this is referred to as pseudo-quadrupole interaction. Since $\mathcal{H}_Q$ and $\mathcal{H}_{pQ}$ are of the same functional form, they usually can not be distinguished in experiments, and thus are combined in one effective quadrupole Hamiltonian, using

$$D = P + D_{pQ}, \quad E = \frac{1}{3}P\eta + E_{pQ}.\tag{2.8}$$

The resulting Hamiltonian, $\mathcal{H}_{eQ} = \mathcal{H}_Q + \mathcal{H}_{pQ}$, can be diagonalised in a third PAS with the axes (x''', y''', z'''). The effective quadrupolar Hamiltonian lifts the nuclear spin I-degeneracy of the energy levels typically by some MHz as shown in figure 2 c), leaving them twofold degenerate in the magnetic nuclear spin quantum number m_I. With the abbreviation

$$g_{\alpha'} = g_I\mu_N + 2g_J\mu_B A_J\Lambda_{\alpha'\alpha'}, \quad \alpha'=x',y' \text{ or } z'\tag{2.9}$$

the second term of Eq. 2.2 can be combined with the isotropic nuclear Zeeman interaction, which leads to an enhanced nuclear Zeeman Hamiltonian [20, 3]. Thus the effective spin Hamiltonian can be written in the form:

$$\begin{aligned}\mathcal{H}_S &= -g_J^2 A_J^2\vec{B}\cdot\hat{\Lambda}\cdot\vec{B} - \sum_{\alpha'} g_{\alpha'}B_{\alpha'}I_{\alpha'}\\&+ \left[D\left(I_{z'''}^2 - \frac{1}{3}I(I+1)\right) + E\left(I_{x'''}^2 - I_{y'''}^2\right)\right].\end{aligned}\tag{2.10}$$

The quadratic Zeeman effect, the first term of Eq. 2.10, only leads to an uniform shift of all spin levels. This effect can be neglected for the typically applied external magnetic fields. The enhanced nuclear Zeeman Hamiltonian, given by the second term, leads to non-degenerate levels for non-zero magnetic fields $\vec{B}$. It is also responsible for an energy structure which is not only a function of the absolute value, but also

of the direction of $\vec{B}$. This property will be utilised in chapter 7 to determine the spin Hamiltonian parameters form measured spectra.

2.2 SPECIFIC PROPERTIES

Magnetic and Optical Transitions

The hyperfine energy levels, which are determined by the effective spin Hamiltonian (Eq. 2.10), will by convention be labelled with $m_I = \pm 1/2$, $\pm 3/2$ and $\pm 5/2$ in the following. Nevertheless for non-zero B field and non-axial symmetries ($E \neq 0$) the six non-degenerated hyperfine levels are not represented by pure eigenstates of I_z, but given by linear combinations of I_z eigenstates. The admixture of different I_z eigenstates allows violation of the $\Delta m_I = \pm 1$ selection rule and all transitions between the hyperfine levels $m_I = \pm 1/2$, $\pm 3/2$ and $\pm 5/2$ can be observed.

The admixture of different I_z eigenstates in the ground and excited state hyperfine levels has also implications for the relative optical transition strengths. Assuming that the electronic ($|\phi\rangle$) and the nuclear wave functions ($|m\rangle$) are separable for the ground (g) and excited state (e), the optical transition matrix elements (μ_{eg}) can be written as [111]:

$$\mu_{eg} = \langle\psi_g|\mu|\psi_e\rangle = \langle\phi_g|\mu|\phi_e\rangle\langle m_g|m_e\rangle = \mu_{opt}\langle m_g|m_e\rangle.$$

μ represents the transition dipole moment operator.

The optical part μ_{opt} is equal for all transitions. The nuclear wave function overlap $\langle m_g|m_e\rangle$ differs for all transitions and therefore determines the relative optical transition strengths $|\langle m_g|m_e\rangle|^2$. This can be used to verify spin Hamiltonian parameters by comparison of calculated $|\langle m_g|m_e\rangle|^2$ values to optically measured relative transition strengths (Sec. 7.4.1-7.4.3).

Homogeneous and Inhomogeneous Line Widths

The homogeneous line width is the line width of a single ion. The optical homogeneous line width Γ_h is ultimately limited by the radiative lifetime of the excited state T_1^{opt}. The homogeneous line width can be calculated from the coherence time T_2^{opt}, $\Gamma_h = 1/\pi T_2^{opt}$. With increasing temperature T_2^{opt} decreases rapidly due to phonon interaction processes, which typically limits the temperature for coherent experiments to below 10 K [100]. For PrYAP, PrYSO and PrLaWO, the excited state lifetimes are in the range of $T_1^{opt} \approx 50 - 200$ μs and the coherence times are about $T_2^{opt} \approx 20 - 150$ μs (see Sec. 7.4.1-7.4.3).

Intrinsic crystal defects and strain cause small local variations of the crystal field, which cause individual ions to have different optical transition frequencies [99]. The effect typically increases with the doping level, since the dopants have different ionic radii (or charge) [100]. Typical inhomogeneous optical line widths are of the order of 10 GHz, which is also the case for the used samples.

Due to the hyperfine interaction (see Λ in, e.g. Eq. 2.2) the effects causing an inhomogeneous broadening in the nuclear spin transition of the ground and exited state are the same and the inhomogeneous width is typically in the range of $20 - 200$ kHz (see Sec. 7.4.4). The nuclear coherence times are in the range of $T_2^{HF} \approx 200 - 500$ μs and the lifetimes are $T_1^{HF} \approx 1 - 100$ s (see Sec. 7.4.1-7.4.3).

BASIC EXPERIMENTS

This chapter contains a qualitative description of the main types of experiments, which are used in the subsequent chapters. Relevant terms are introduced.

3.1 HOLE BURNING

Optical hole burning used within this work is due to population redistribution in the hyperfine levels of the ground state [100]. Since the splittings of the hyperfine levels in the ground state are of the order of 10 MHz, at a temperature of 2 K all ground state levels are populated with the same probability. A pump laser which is resonant with the transition between one ground state level and an excited state hyperfine level, will transfer the population of the ground state level to the excited state. From there, after a time limited by the excited state lifetime, the population may decay into any of the (in zero field) three ground state levels. If the population redistribution within the ground state is slower than the pump rate of the laser, the resonant ground state level will be de-populated effectively after a few optical cycles. Probing the absorption of this transition results in weak absorption compared to the thermal equilibrium situation due to the reduced population. This is referred to as a spectral hole and the situation is illustrated in the energy level scheme (Ia) of figure 3. In contrast, the absorption of a probe laser, which connects the same excited state level with a different ground state level, will result in a higher absorption due to the additional population in this ground state level. Accordingly, this is referred to as an anti hole (see Fig.3 (Ic)). Since there are three excited state levels, a probe laser can become resonant with any of the transitions between the excited state levels and the de-populated ground state level. In the pump/probe situation illustrated in Fig.3 (Ib) this creates a "side hole" at the frequency of the next higher excited state hyperfine level.

The inhomogeneous optical transition line width of the rare earth compounds, investigated in this work, are in the range of a few GHz. A weak laser pulse, which probes the inhomogeneous optical transition in a range of a few tens of MHz, has an almost uniform absorption over the whole frequency scan range. Since the homogeneous line width is in the range of $2-10$ kHz, this absorption is be due to the excitation of many individual ions, which have slightly different optical transition frequencies. As the electronic ground and the excited states each have three levels, multiple different combinations of one ground and one exited state level are resonant at the same time, too. In a hole burning experiment the pump and probe beams can be resonant with different ion classes, whose optical transition frequencies differ by either a ground or excited state hyperfine transition frequency. In figure 3 this is illustrated for three ion classes "I", "II" and "III" and their contributions to the main hole (a) and a specific side (b) and anti hole (c).

At zero field the ground and excited state have three hyperfine levels and therefore a total of nine different ion classes exists (see Fig. 49a). A
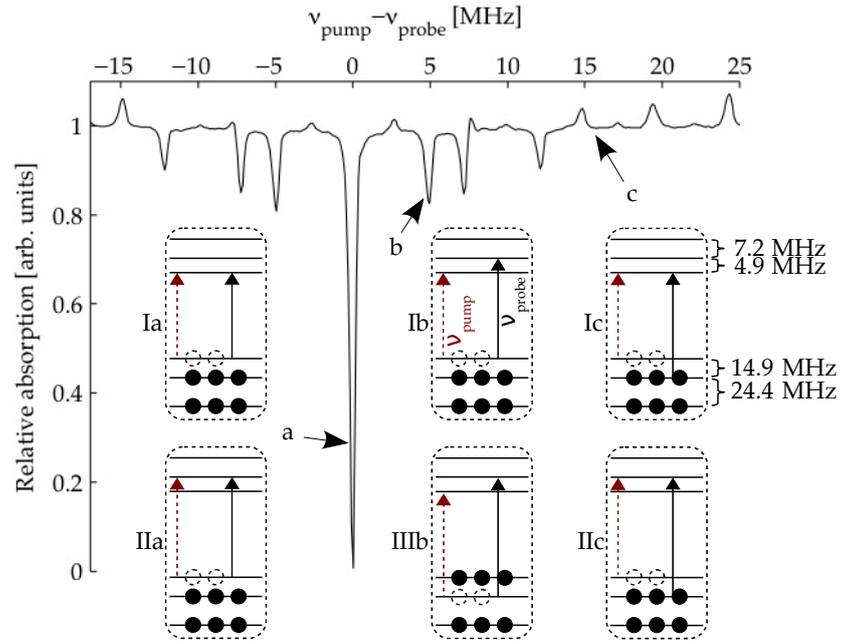
Figure 3: Hole burning spectrum for PrLaWO at zero field. The inserts (Ia-Ic, IIa, IIc and IIIb) show hyperfine energy levels of the ground and excited state for zero magnetic field. Within the inserts, schematic examples of pump (ν_{pump}) and probe (ν_{probe}) beam frequency combinations are shown, which explain the frequency position of the main hole "a" (Ia, IIa), the side hole "b" (Ib, IIIb) and the anti hole "c" (Ic, IIc) in the hole burning spectrum. By usage of the population decay from the excited state, the pump beam transfers all population from the connected ground state level (dashed circles) to the other non-pumped ground state levels (solid circles). In (Ia-Ic) and (IIa, IIc) respectively the pump beam excites the same optical transition. (Ia-Ic), (IIa, IIc) and (IIIb) distinguish three of a total of nine ion classes at zero field (see also Fig. 49a).

total of 81 possible lines in the hole burning spectra results, but since some frequency differences for the ion classes are equal, at maximum 49 are visible in the spectra. As discussed, due to the hole burning mechanism, the line positions directly yield the hyperfine splittings. Due to the symmetry of the hole burning spectra with respect to the frequency, the energetic order of the levels is not accessible. Combined magneto-optic techniques [16] or selective hole burning techniques, burning at multiple frequencies in one experiment [122], can break the symmetry and yield the level order, which determines the sign of the effective quadrupole coupling constant D (see Eq. 2.10). The mentioned selective hole burning techniques are used in Sec. 8.3.2 to select one specific class of ions only and create a pure population state for one specific ground state hyperfine transition (see Fig. 49b). Since different optical transitions contribute to each hole burning line, the spectrum contains also information about the relative oscillator strengths. Comparison of experimental spectra to theoretical hole burning spectra, which can be calculated using rate equations, can yield relative oscillator strengths [82].

The resolution of hole burning spectra is often limited by the laser stability. Laser frequency instability makes the holes wider, since the burn laser pumps at different frequencies during its interaction time.
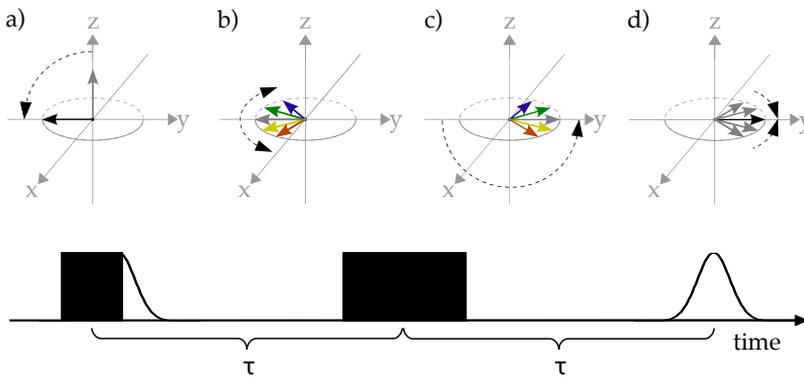
Figure 4: Two pulse Hahn echo schematic. On the top a representation of the rotating frame system [42] is shown and the bottom shows the pulse sequence applied to the two level system. a) starting from a population state along $+z$, a pulse at time $t = 0$, with a $\pi/2$-flip angle and rotating around the x-axis, creates a coherence with a $-y$-phase in the rotating frame. The pulse excites an inhomogeneous ensemble of width Δ in the frequency domain. For a duration of about $1/\Delta$ a FID is visible after the pulse (see bottom trace). During this time, the single ensemble members dephase due to their different transition frequencies. b) Some individual frequencies are higher (red) than the rotating frame frequency, others are lower (blue). For times $t \gtrsim 1/\Delta$ this leads to destructive interference of all signal contributions. c) A π-pulse, at $t = \tau$ and along the x-axis, inverts the y-components and the phase differences start to decrease. Complete rephasing is accomplished at $t = 2\tau$ and leads to the formation of a macroscopic dipole-moment, which involves the emittance of an echo.

The laser jitter further is present while the laser probes the hole burning spectrum. This often dominates the line width in comparison to other contributions like the optical homogeneous line width, power broadening or the inhomogeneous broadening of the hyperfine levels [99].

3.2   PHOTON AND SPIN ECHO

Echos can be used to measure the coherence life time in inhomogenous ensembles [59]. The process is illustrated in figure 4.

In a first step a pulse with $\theta = \pi/2$[†] area creates coherent superposition states. The lifetime of this superpositions is given by the coherence lifetime T_2 of the system. Directly after the excitation (Fig. 4 a)) the created coherences, which can be represented as transverse vectors on the Bloch sphere, have the same phase. In the case of an optical excitation, these coherences are associated with a macroscopic optical polarisation [1, 100]. The polarisation oscillates with the frequency of the transitions and thereby emits an electromagnetic field. This will be referred to as free induction decay (FID) in analogy to the signal of a oscillating macroscopic magnetic-dipole moment from nuclear spins.

Since an inhomogeneous ensemble was excited, the total signal is the sum over all single ensemble member contributions. The inhomogeneous frequency width of the ensemble is given by Δ. The individual members (i) of the ensemble all have slightly different transition frequencies $\nu_0^{(i)}$. Each ensemble member allocates a specific phase over

[†]$\theta = \int \mu_{12} E(t) dt$, *with μ_{12} the transition matrix element of the involved two level system and E the field strength of the pulse.*

time (see Fig. 4 b). After $t \gtrsim 1/\Delta$ the individual phases $2\pi\nu_0^{(i)}t$ are effectively distributed uniformly in the xy-plane. Summation leads to a destructive interference of the single contributions in the xy-plane. Typically the decay constant of the pure dephasing is smaller than the (homogeneous) coherence time $1/\Delta < T_2$. The inhomogeneous dephasing therefore dominates the signal decay and prohibits to infer T_2 directly from the FID.

A second pulse with a π-flip angle, applied at a time $\tau \lesssim T_2$ after the first pulse, inverts the y-components (see Fig. 4 c)). Therefore the phase differences between the components, which increase during $t = 0 \rightarrow \tau$, decrease in the same way during $t = \tau \rightarrow 2\tau$. This leads to a rephasing of all coherences and accordingly to a reestablished macroscopic polarisation at $t = 2\tau$, which leads to emittance of a photon echo. T_2 can be inferred from the decrease of the echo height as a function of the pulse separation τ.

For the investigated rare earth compounds and applied laser powers the inhomogeneous optical broadening is much larger than the typical optical pulse bandwidths. The width of the inhomogeneous distribution Δ is therefore typically predetermined by the optical pulse bandwidth used for the generation of the photon echos. This may be altered by the preparation of narrow absorption lines in a previously prepared transparency window within the inhomogeneous optical line (see Fig. 50).

The laser stability is not a limiting factor for measurements of the optical coherence times, as long as it is stable during the single optical pulse durations. A laser phase change in between the pulses only changes the rotation axis orientation in the xy-plane. The echo stills occur at $t = 2\tau$, but it has a different phase. This does not affect the intensity of the echo and therefore results in the same T_2 when τ is varied. Nevertheless this effect prohibits the accumulation of photon echos detected with heterodyne detection [100].

The inhomogeneous distribution width Δ in the case of spin echos, e.g. excited between the ground state hyperfine levels (Ch. 8), is typically determined by the inhomogeneous broadening of the hyperfine levels. The RF pulse bandwidths are usually comparable to or larger than the inhomogeneous broadening. Therefore the temporal shape of the spin echo usually is dominated by the inhomogenous hyperfine line broadening.

If the pulse bandwidth is large enough to excite multiple hyperfine levels at the same time, quantum-beat-like interference as a function of τ may become visible in the echo signal [100]. This applies for both, the optical and the RF bandwidths and sometimes make it difficult to extract T_2 from the recorded data (see Fig. 52).

3.3   RAMAN HETERODYNE SCATTERING

Raman heterodyne scattering (RHS) [114, 162] is a magneto-optical technique. As in the case of nuclear magnetic resonance (NMR), radio frequency magnetic fields applied by a coil are used to excite nuclear spin coherences. Unlike conventional NMR techniques, which use the magnetic induction in the same coil also for detection, the response of the system is detected optically. Figure 5 shows a schematic of the RHS signal generation. To generate a RHS signal at minimum three transitions are required. In Fig. 5 these are given between two ground
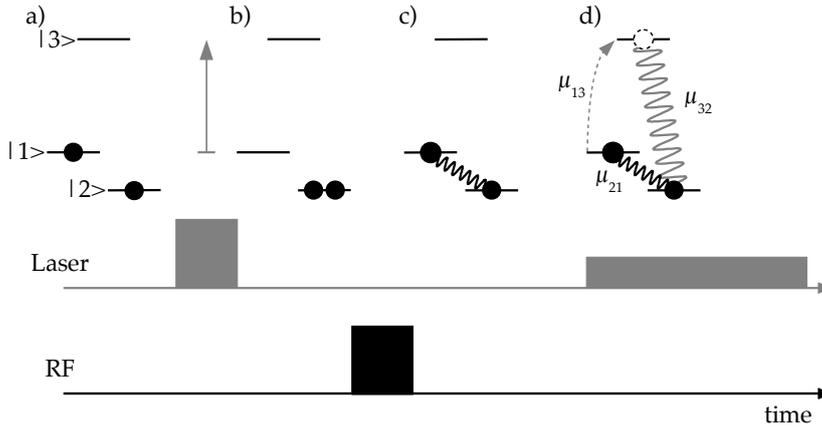
Figure 5: Schematic for the generation of the Raman heterodyne scattering signal. Starting from a thermal equilibrium population distribution (a), a laser depletes the ground state level $|1\rangle$ (b). In c) a resonant RF pulse generates a coherence in the $|1\rangle \leftrightarrow |2\rangle$ ground state transition. As final step (d) a weak resonant laser field is applied to the optical transition $|1\rangle \leftrightarrow |3\rangle$. The laser scatters the ground state coherence in the optical transition $|3\rangle \leftrightarrow |2\rangle$ and at the same time serves as a heterodyne field. μ_{21}, μ_{13} and μ_{32} denote the transition matrix elements involved in the RHS signal generation.

state hyperfine levels ($|1\rangle$ and $|2\rangle$) and one excited state hyperfine level ($|3\rangle$). As discussed in Sec. 3.1 optical excitation can create a non-thermal population distribution in the ground state. Conventional NMR works with thermal population differences, which are of the order of 10^{-5} between the nuclear spin levels. In rare earth systems, hole burning can almost completely depopulate one level, which is one major source for an enhanced sensitivity of the RHS technique compared to conventional NMR. In the schematic of Fig. 5 b) a previously applied laser pulse or hole burning scheme has depleted ground state level $|1\rangle$ and has transferred its population to state $|2\rangle$. In a second step a resonant radio frequency field creates a coherence between the ground state nuclear spin levels $|1\rangle \leftrightarrow |2\rangle$ (Fig. 5 c)). Finally a weak laser field, resonant with one optical transition, e.g. $|1\rangle \leftrightarrow |3\rangle$, scatters the ground state coherence in the other optical transition, in the given example $|2\rangle \leftrightarrow |3\rangle$ (Fig. 5 d)). Since the optical coherence in $|2\rangle \leftrightarrow |3\rangle$ represents an oscillating polarisation, it is the source of an electromagnetic field. This "Raman field", is superimposed with the same laser light which is also used for the scattering process. This results in an optical heterodyne beat, which beats with the frequency of the involved ground state transition. In the case of weak applied fields, the pump effect of the laser field can be neglected and the beat signal is dominated by the hyperfine coherence evolution. Whereas the figure suggests a pulsed excitation scheme the technique works equivalently using continuos excitation fields. A second order perturbation theory of the RHS process [162] yields

$$I_s \propto |E_L|^2 \, |H_{RF}| \left(\rho_{22}^0 - \rho_{11}^0 \right) \mu_{21} \mu_{13} \mu_{32}$$

for the steady state solution of the Raman heterodyne scattering beat signal I_s. The term $\left(\rho_{22}^0 - \rho_{11}^0 \right)$ represents the population difference

between the hyperfine levels in the first step and μ_{21}, μ_{13} and μ_{32} are the transition matrix elements involved in the RHS signal generation (see Fig. 5 d)). E_L represents the (weak) scattering laser field strength and H_{RF} the (weak) RF field strength.

The heterodyne detection brings a twofold enhancement for the detection sensitivity. First of all, the heterodyne laser field power $|E_L|^2$ and not the weak Raman field signal ($\propto |E_L H_{RF}|^2$) is detected. Furthermore the modulation with the hyperfine transition frequency shifts the signal away from low frequency noise components. Compared to conventional NMR, shot noise limited detection of optical photons yields a further increase of sensitivity. Typical RHS signals within this thesis originate from only about 10^8 spins, which may be compared to the $\approx 10^{18}$ spins required for conventional NMR experiments. Although the scheme shown in Fig. 5 detects the ground state nuclear spin coherences, the method works equivalently with excited state coherences. In this case, by creating a hyperfine coherence between two excited state hyperfine levels and scattering it into an optical transition connecting to a ground state level, optically detected NMR of excited states becomes possible.

The method is to first order insensitive to laser frequency jitter, since the laser interacts at the same time with both involved optical transitions. Thus the RHS technique can yield the hyperfine transition frequencies with a higher precision than, e.g. optical hole burning.

I_s is linear in the transition matrix element μ_{21} of the nuclear spin coherence. This allows to measure the effect of the RF field on the coherence directly using the RHS signal and further enables for phase sensitive quadrature detection of the coherence like in NMR. Unlike many other optical techniques the RHS signal is linearly dependent on all involved transition matrix elements. The triple product $\mu_{21}\mu_{13}\mu_{32}$ can lead to interference effects. One effect is the destructive interference of RHS signals from two different rare earth ion sites (see Sec. 7.4.1-7.4.3) in the host crystal [110]. The RHS signals of the two sites have the same frequencies and magnitudes, but opposing signs due to μ_{32} and μ_{13}. A necessary requirement for this is that the principal axes of the nuclear quadrupole tensors (Eq. 2.10) in the ground and excited state are incongruent [110]. The signals from a single site can also interfere due to an effect called Zeeman interference [111]. For zero magnetic field site and Zeeman interference cause the RHS signal to vanish [111] or, under typical laboratory conditions, to be vanishingly small. Furthermore the signals from different RHS "scattering-pathways", which are due to different ion classes (see Sec. 3.1), can interfere destructively [19].

As indicated above RHS experiments can be performed with continuous RF and laser fields (CW RHS) or with pulsed fields (pulsed RHS). In the pulsed scheme a single RF pulse excites multiple hyperfine coherences at a time. All coherences contribute to the RHS heterodyne beat signal and Fourier transformation of the transient yields the transition frequencies. In the CW RHS scheme the beat signal is recorded, while the RF frequency is varied over a range of hyperfine transition frequencies. A coherence is excited when the CW RF frequency is resonant with a hyperfine transition. This gives rise to a beat signal with the resonant RF frequency. For phase sensitive detection the signal is demodulated with the RF frequency, this applies for both CW and pulsed RHS (see Sec. 5.1). For the pulsed technique the accessible frequency width of the spectra is determined by the pulse excitation bandwidth, which is typically below 2 MHz. Broader spectra can be recorded with the

CW technique. For the different hyperfine transitions and samples, pulsed and CW spectra often yield different signal to noise ratios. For the experiments shown in the following chapters each time the most appropriate technique for the specific situation was chosen.

At non-zero static magnetic field each of the three ground and excited state hyperfine levels splits into two non-degenerate Zeeman levels (see Fig. 2 c)). Typically only one hyperfine manifold, e.g. $|\pm 1/2\rangle \leftrightarrow |\pm 3/2\rangle$, is addressed in a single pulsed or CW RHS experiment.

As an example, figure 6 shows the transitions excited in the RHS experiments with non-zero field for the $|\pm 1/2\rangle \leftrightarrow |\pm 3/2\rangle$ manifold. For small fields the inner transitions, $|+3/2\rangle \leftrightarrow |-3/2\rangle$ and $|+1/2\rangle \leftrightarrow |-1/2\rangle$, are smaller than the zero field splitting of the manifold $|\pm 1/2\rangle \leftrightarrow |\pm 3/2\rangle$. Therefore these inner transitions usually are not in the scan range of the CW RF or the excitation bandwidth of the RF pulse. In the most general case, the sites of the investigated samples are inequivalent with re-

Figure 6: Different $|\pm 1/2\rangle \leftrightarrow |\pm 3/2\rangle$ hyperfine manifold level splittings of the sites 1 and 2 in a non-zero field (Ba).

spect to their Zeeman splittings at non-zero magnetic field. Each nuclear site has different transition frequencies for the same connected hyperfine levels, which is indicated by the different colour arrows in Fig. 6. Therefore at maximum eight transition frequencies are visible in the RHS spectra of a single hyperfine manifold.

Part II

EXPERIMENTAL APPARATUS

OPTICAL EXCITATION

The wavelength of the $^3H_4$-$^1D_2$ transition in praseodymium based REIC is in the range of about 600 to 610 nm. Since high power diode lasers were not available for a long time for this wavelength range, the experimental setup consists of a solid-state pump laser and a dye laser. Figure 7 shows a schematic of this setup.

A Nd:YVO$_4$ laser (Coherent Verdi-V8) pumps the continuos wave (CW) dye laser at optical powers of about 7 W. Using Rhodamine 6G dissolved in ethylene glycol as dye, the Coherent 899-21 dye-jet laser offers a spectral range from about 570 to 630 nm. With optimum cavity tuning and dye absorption the system yields optical powers of up to 1.25 W (602 nm). Furthermore the 899-21 offers a 30 GHz scan range in high resolution single frequency mode.

An inherent problem of dye lasers are fast fluctuations of the dye-jet. Since the jet is an optical element of the laser cavity, any variation of its effective optical length directly affects the laser wavelength. The active stabilisation system of the manufacturer monitors and compensates such fluctuations, but the level of stability is insufficient for many high resolution experiments with REIC. Therefore a fraction of the laser output is guided to additional stabilisation systems, which provide sufficient active suppression of laser wavelength and intensity fluctuations.

For time resolved experiments the continuos laser radiation can be cut into pulses with durations of about 10 ns at minimum. On the same time scales the setup can also modify the laser frequency in the range of the ground and excited state hyperfine splittings, which for example, allows fast chirped hole burning experiments.

A more detailed discussion of the optical pulse generation and laser stabilisation setups, with a focus on the achieved improvements, is given in the following sections.
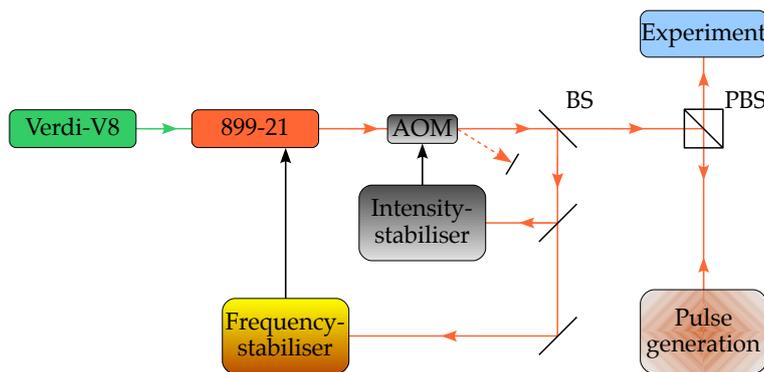

Figure 7: Schematic of the optical setup. (P)BS denotes a (polarising) beam splitter and AOM the acousto-optic modulator, which is part of the intensity stabilisation.

4.1   LASER STABILISATION SYSTEM

The general laser stability is improved by minimisation of fluctuations in the laser environment. This includes stabilisation of the room and dye temperature, limitation of humidity (hygroscopic dye), reduction of dust (flow box) and passive acoustic damping (air buffered optical breadboard). Residual variations, which affect the laser efficiency on a daily basis or on short time scales, are reduced by active feedback.

4.1.1   *Intensity Stabilisation*

In its original version, the Coherent 899-21 laser system shows low intensity variation, when using the internal frequency scan controls. The insertion of the intra-cavity EOM (electro-optic modulator), which is required for the homebuilt frequency stabilisation (see Sec. 4.1.2), reduces the stability with respect to such scans and leads to intensity variations of up to 15 %. Furthermore, there is no active stabilisation for fast random intensity fluctuations.

Internal manual no. 150.

The homebuilt intensity stabilisation measures the current laser intensity using a high bandwidth photodiode. The difference between the photodiode voltage and an adjustable set-point voltage is applied to a PID (proportional–integral–derivative) amplifier, which generates a control voltage for the RF amplifier supplying the intensity stabilisation AOM (acousto-optic modulator, see Fig. 7). A part of the incoming laser power, proportional to the AOM driving power, is diffracted into an other direction. Adjusting the set-point voltage to a level below the largest laser fluctuation induced photodiode voltage drop, will ideally remove any intensity fluctuation from the non-diffracted beam. Besides removing noise, the stabilisation is also used to get a constant intensity for all the following parts of the setup, independent of the actual total 899-21 laser power, which may change from day to day.

The real performance is limited mainly due to the bandwidth of the PID circuit and the diffraction efficiency of the AOM. In combination, these characteristics also limit the useable dynamical range for the stabilised laser intensity. Adjusting a too low or too high set-point leads to uncontrolled oscillations of the regulating circuit. In addition to a limited dynamical range of about 30 % of the input intensity, the original setup tended to induce periodic intensity oscillations with about 20 % of the set-point amplitude and periods of a few minutes.

Through optimisation of the individual P, I and D gains and bandwidths the dynamical range could be increased to about 80 %, with a generally lower tendency of uncontrolled oscillations. The overall bandwidth could be increased by about 50 %($\approx$ 10 kHz). The periodic low frequency intensity oscillations have not been observed anymore afterwards.

4.1.2   *Frequency Stabilisation*

In its passive operation mode, a birefringent filter and two etalons, limit the 899-21 laser line width to approximately 10 MHz. The active compensation system included with the Coherent 899-21 laser further stabilises with respect to a small, thermally stabilised optical cavity. A part of the laser light is coupled into the low finesse Fabry-Pérot cavity and the change of its transmission is used as a reference for laser
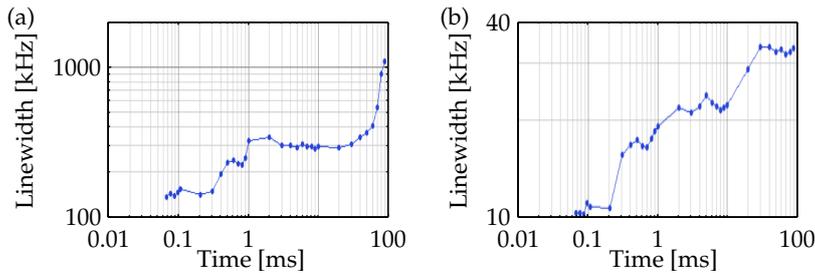
Figure 8: Stabilised laser line width, using the commercial Coherent (a) and homebuilt (b) stabilisation. The Allen deviation data was acquired with kind support of the Sirah Laser- und Plasmatechnik GmbH, using their EagleEye optical spectrum analyser.

wavelength drifts and fast random frequency fluctuations (jitter). The 899-21 control unit generates an error signal using this information and drives two active tuning elements in the laser to compensate the error by changing the effective laser cavity length. Slow ($\lesssim$ 100 Hz), and big range ($\lesssim$ 30 GHz) changes are covered by a tiltable transparent plate within the cavity light path. Faster fluctuations are corrected using a mirror, which is mounted on a piezoelectric actuator allowing for cavity length adjustment in the range of acoustic frequencies ($\lesssim$ 1kHz). Figure 8(a) shows the typical line widths achieved for this stabilisation system.

On typical timescales for hole burning in REIC, the commercial Coherent stabilisation yields a laser line width of 0.3 to 1.3 MHz. The homogenous optical line width of, e.g., PrYSO is about 2 kHz, therefore a higher grade of stabilisation is required for high resolution hole burning, but also for experiments with high demands on coherent control.

Principle Function

The homebuilt stabilisation is based on the Pound-Drever-Hall (PDH) technique [36]. Figure 9 shows a schematic of the 899-21 ring laser cavity and the homebuilt frequency stabilisation.

Before the diagnosis laser beam is coupled into a high finesse Fabry-Pérot reference cavity, its frequency is modulated using a local oscillator of 8 MHz and an EOM. The PDH scheme uses the reflection from the entrance of the reference cavity to generate an error signal. Using a Faraday isolator the reflected light is guided to a fast photodiode. When the laser is in resonance with one of the narrow cavity modes (500 kHz), the signal of the photodiode contains modulation sidebands at the frequency of the local oscillator. Phase sensitive demodulation of the cavity-reflection signal, with the original local oscillator RF, generates the error signal, which is proportional to the current laser frequency offset from the cavity mode. Within the window defined by the modulation sidebands, the error signal yields information about the direction the effective laser cavity length has to be adjusted to compensate for the error.

The controller electronics, consisting of different PID based amplifiers, distribute the error signal to the different intra laser cavity tuning elements. In this step the signal bandwidths (see Fig. 9) and amplifications are adapted for the different elements. Besides the already included tilting Brewster-plate (BP) and the piezoelectric mounted mirror (PZT) an additional EOM (Gesänger PM25) was built into the optical path of
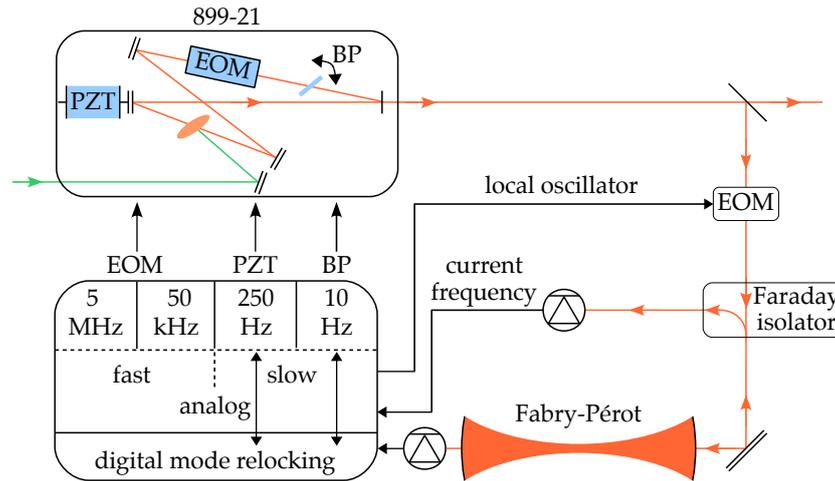
Figure 9: Schematic of the homebuilt laser frequency stabilisation and the Coherent 899-21 ring laser cavity. The blue elements denote the intra laser cavity tuning elements: a Brewster-angle tilt-plate (BP), a mirror mounted on a piezoelectric actuator (PZT) and the intra-cavity EOM. The lower part of the figure indicates the error signal generation with respect to a high finesse external Fabry-Pérot cavity and the values in the box denote the driving control bandwidths (-3 dB) for the intra cavity tuning elements.

the 899-21 ring laser cavity. It is configured as a phase-modulator, to change only the effective cavity length and is driven by the signal of two fast regulation circuits. This increases the bandwidth for corrections from ≈ 1 kHz to ≈ 5 MHz.

As indicated above, the laser fluctuations may only be corrected as long as the laser frequency resides close to a resonator mode, or more precisely, within the window defined by the modulation sidebands. To relock the laser to the same mode, after it was steered out of the modulation sideband window by some event, the error signal is extended by a digital information. This extended error signal uses the signals of the light, which is reflected and transmitted through the cavity, and contains information about the direction in which the laser frequency deviated with respect to the last lock of the laser to a resonator mode. The digital error signal is applied to the slow, but high frequency range, PZT and BP tuning elements, until the laser frequency matches the resonator mode again.

Final Performance

Most of the electronics included were originally developed at the Australian National University by Dr. Matt Sellars. In Dortmund, the system was set up and run by two predecessors of the author. Since the system was not operable at the beginning of the author's work and several defects occurred after reestablishment, the system was rebuilt, in particular most of the phase sensitive demodulation electronics were replaced. By shortening the electronic closed loop controller path length and replacing some of the PID integrated circuits by faster low noise amplifiers, the effective control bandwidth of the fast analog part could be tripled. General reduction of noise in the error signal and re-adaptation of all analog control bandwidths to each other, led to a generally bet-

The detailed changes can be found in the chair's internal manual no. 151-152.
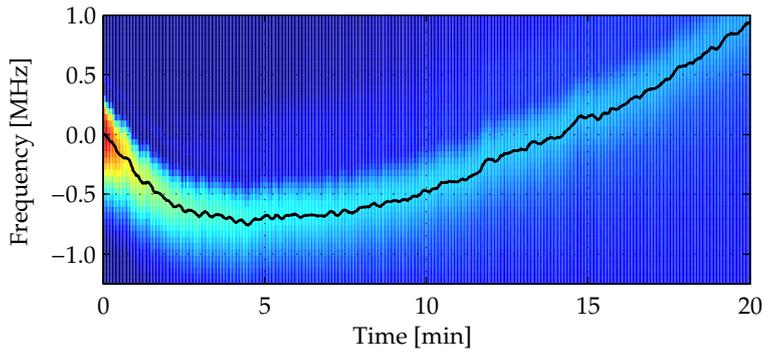
Figure 10: Laser frequency drift (black line) over 20 minutes. The central hole position of a PrYSO hole burning spectrum (colour coded intensity plot) was used as a reference.

ter performance compared to the previously documented benchmarks. The shielding of the reference cavity with respect to external impacts was improved, too. This included a long term active temperature stabilisation of the Invar-reference cavity to $32 \pm 0.01\,^\circ$C and improved acoustical shielding against vibrations transmitted through the optical table into the vacuum box, which contains the reference cavity. Under typical conditions, the improved stability allows for continuos laser locking to one cavity mode over several hours, without prohibiting (careful) work on the optical table. The fast and robust locking now allows tracking of the reference cavity mode, while scanning the Fabry-Pérot mirror distance by the incorporated piezoelectric mirror. This enables for ultra-high resolution scans of up to 500 MHz width and minimum scan durations of about 50 ms.

The line width of the stabilised laser (see Fig. 8(b)) is well below 20 kHz for the typical timescales of the coherent experiments shown in chapter 8. Nevertheless, the Allen deviation in Fig. 8 was measured with an optical spectrum analyser (Sirah EagleEye) whose resolution limit is about 20 kHz. Furthermore, the EagleEye reference cavity was not placed in a vacuum, nor was it thermally stabilised to prevent cavity drifts. This motivated for independent measurements of the short term laser jitter and the long term drifts.

Low laser frequency drift rates are of special importance for spectral tailoring experiments (see, e.g. Sec. 8.3.2). In these experiments, specific ground state populations are prepared, based on the precise relative frequencies of short laser pulses, which are applied over periods of typically about 100 ms. To probe the laser drift of the current system on these time scales, the long spectral hole lifetimes of about 100 s in PrYSO have been utilised. In a first step, using a 2 ms long laser pulse, a spectral hole was burned into the inhomogenous optical line. Then the hole burning spectrum was repetitively read out every second. The faint readout probe was chirped by 32 MHz within 100 µs and otherwise switched off. This enabled monitoring of the hole position over about 20 minutes. Since the hole was only burned once at the beginning, any change of the hole position with respect to the current probe laser frequency is due to laser drift. Figure 10 shows a typical hole decay (colour coded) and the associated laser drift (black line) during this time. The highest absolute drift rate could be observed at the beginning of the measurement and was about 5 kHz/s. The
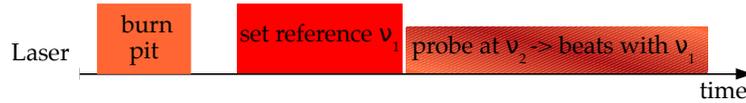
Figure 11: Coherence beat experiment pulse sequence. Using chirped pulses a transparent window (pit) is prepared in the inhomogeneously broadened optical line. The optical reference coherence is excited with a laser pulse of frequency ν_1, outside the pit. The probe field has a frequency of $\nu_2 = \nu_1 + 13$ MHz and is in the centre of the transparent pit.

mean absolute drift, averaged from periods of 1 second duration, is (0.4 ± 1.9) kHz/s. Comparing spectra with 10 s separation yielded a mean of (2.5 ± 3.6) kHz/s and for 60 s (26 ± 7) kHz was found. These rates compete very well with those of laser systems stabilised to a persistent hole, e.g. ≈ 1 kHz/s averaged over 1 second in Ref. [74].

The short term laser phase stability is important for pulsed coherent experiments like photon echos. To measure the laser stability for these time scales, a coherent beat note experiment was used. Figure 11 shows the schematic pulse sequence. As a first step a transparent window was prepared in the inhomogeneous optical line of PrYSO. Then a narrow band pulse with frequency ν_1 excited an absorbing part of the line, setting up an optical FID. Ideally the ions will keep radiating for a time limited by the optical coherence time, here up to $T_2^{opt} = 150$ μs, and the inverse bandwidth of the pulse. During this time the ions are no longer being excited, and thus their FID represents a fingerprint of the laser phase during the excitation pulse. Finally, a weak heterodyne probe laser pulse with a frequency of ν_2 was applied, which interferes with the optical field irradiated by the macroscopic optical polarisation of the FID. The frequency of the probe laser was set to the centre of the prepared transparent window to avoid any excitation of the medium. The beat note between the two fields, with a frequency of $\nu_2 - \nu_1$, was recorded using a fast photodiode. Typical transients are shown in figure 12(a).

The beat notes, recored using the home built stabilisation, were typically visible for durations of 50 to 120 μs. After Fourier transformation the longest beat notes yield spectral line widths of about 13 kHz (FWHM) (see Fig. 12(b)). Figure 12(c) shows the laser phase deviation as a function of time. The green and blue curves show the instantaneous phase of the previously shown beat notes, with respect to the RF signal generating the laser pulse frequency difference $\nu_2 - \nu_1$. Since the beat notes varied from shot to shot, a series of $n = 400$ single beat notes were recorded. The data was divided into i short bins along its time axis as long as the signal to noise ratio was larger than 5. The magenta line in Fig. 12(c) shows the absolute value of the mean bin phase of all beat notes j, $\phi_{m,i} = |\frac{1}{n} \sum_j \phi_{i,j} - \phi_{0,j}|$, relative to the first time bin. Its low variation and mean value close to zero indicates that the laser frequency did not show a significant drift over the beat note
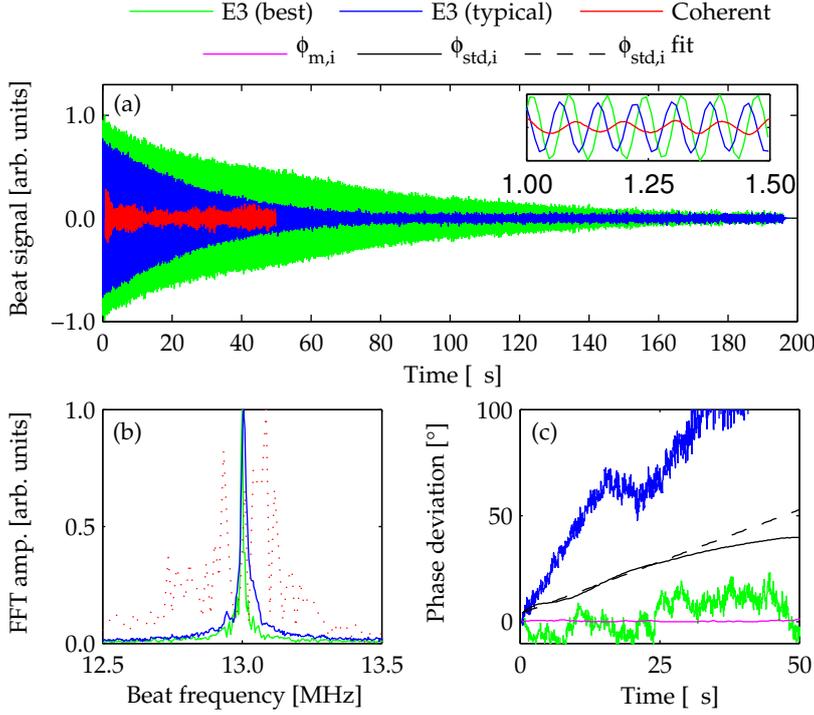
Figure 12: Short term laser stability characterisation, using a PrYSO coherence beat note. (a) compares the best observed beat note using the home built stabilisation (green), to a typical other single shot (blue) and a beat note acquired with the commercial Coherent stabilisation (red). The inset shows a magnification. In (b) the corresponding spectra are plotted (commercial system now red dots). (c) shows the phase deviation over time. Besides the instantaneous phase of the of the two ultra high resolution beat notes (green and blue), statistical data from 400 processed beat notes is presented. The absolute of the mean phase (magenta, $\phi_{m,i}$ see text) is shown. Further, the standard deviation of the phase relative to the first time bin (solid black line, $\phi_{std,i}$ see text), together with a corresponding linear fit of the first 20 µs (dashed line), is shown.

time. Following the analysis presented in reference [131], the standard deviation of the phase relative to the first time bin is calculated:

$$\phi_{std,i} = \sqrt{\frac{1}{n-1} \sum_j (\phi_{i,j} - \overline{\phi}_i)^2}.$$

$\phi_{std,i}$ (solid black line in Fig. 12(c)) represents the evolution of the laser phase error with time. A linear fit (dashed line) for bin times below 20 µs yields a phase error evolution of $\phi_{std}(t) \approx 4° + \frac{1°}{\mu s} \cdot t$. Using the relation $f = \frac{\partial \phi}{\partial t}$ the authors of Ref. [131, 74] calculated a characteristic laser frequency error of $f_{std,i}(10\mu s) \approx 1.1$ kHz for their laser, which is stabilised to a spectral hole in PrYSO. The analogous value for the laser system used here, following from the data shown in Fig. 12(c)), is $f_{std,i}(10\mu s) \approx 1.3$ kHz.

4.2   OPTICAL PULSE GENERATION

The experimental techniques introduced in chapter 3 require the continuos output of the laser to be modified in several ways. The selection of different ions in the inhomogenous optical line requires control of the laser frequency. Time resolved experiments require the continuos output of the laser to be cut into pulses with precise timings. Furthermore the pulse power, as well as all previously mentioned parameters, needs to be adjusted in a wide range and on miscellaneous time scales. Acousto-optic modulators (AOM) enable control of all three parameters, i.e. power, frequency and pulse duration, with sufficient accuracy and dynamic range. Figure 13 shows a schematic of the optical beam lines, including some of the controls for pulse forming and calibration.

The heart of each beam line is an AOM, which consists of a transparent crystal (e.g. TeO_2) to which a piezo-electric transducer is attached. The transducer is driven by a RF and thereby induces acoustic sound waves in the crystal. A laser beam, which passes the crystal perpendicular to the sound wave direction, is diffracted at the induced periodic density modulation, since the latter acts as a grating. The laser is diffracted into n different orders at angles θ, which can be described by Bragg's law:

$$\sin(\theta) = \frac{n\lambda_L}{2\lambda_{RF}}, \; n = \pm 0, 1, 2, \dots,$$

with λ_{RF} representing the RF- and λ_L the light wavelength in the AOM crystal. Typically the face of the AOM crystal is aligned at the Bragg angle for a first order diffraction, relative to the input laser beam. This maximises the optical power in the first order of diffraction. Variation of the driving RF power affects the magnitude of the density modulation, and thus the amount of diffracted light. This is used to vary the optical power in (e.g.) the first order and in case of switching the RF to generate light pulses. The process can also be understood on the basis of a scattering of the light photons at the sound wave phonons. Besides changing the direction of the light as a function of the number n of scattered phonons, the light energy and thus the light frequency $\nu_{L,n}$ also changes in the same way:

$$\nu_{L,n} = \nu_L + n\nu_{RF}.$$

The laser beam is always supposed to interact with the same spatially fixed ions in the crystal, thus the frequency induced change of the diffraction angle has to be compensated. This is accomplished by a retro-reflection setup (see "Retro-reflection 1" in Fig. 13), where the laser light passes the AOM twice. Since the laser direction is opposite for the second pass, but the phonon direction does not change, the single pass diffraction angles cancel each other. The double passage further doubles the RF induced optical frequency shift. At the same time the available optical power is reduced, since the single passage zero-to-first order diffraction efficiency is only $0.7 \sim 0.8$. Due to double passage through a $\lambda/4$-wave plate, the linear polarisation of the first order diffraction light is rotated by a total of $90°$, which allows it to be separated from the incident light with a polarising beam splitter.
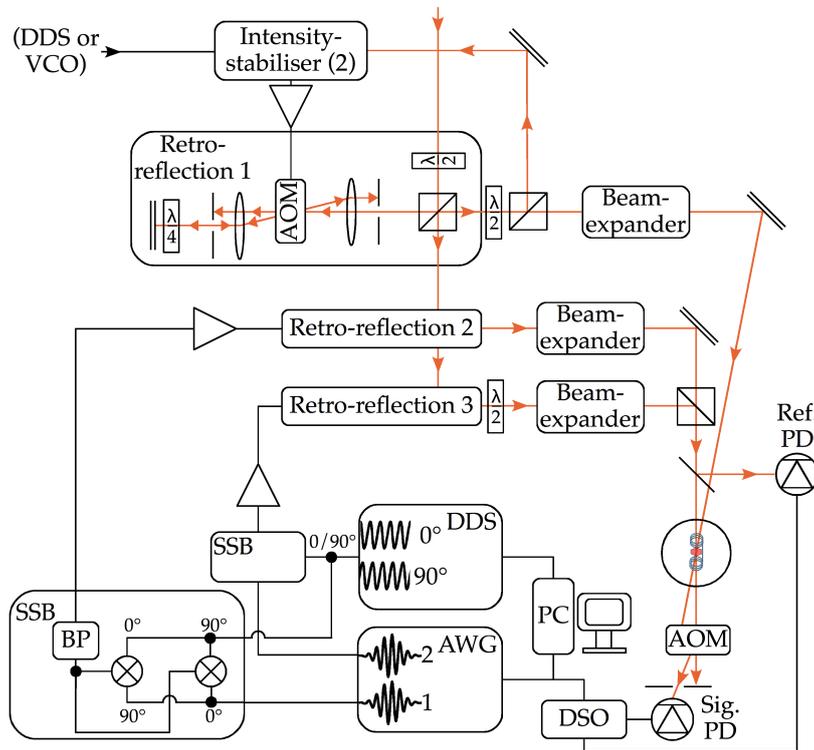
Figure 13: Schematic representation of the pulsed optical beam lines. Retro-reflection setup 1, which uses a DDS or a VCO as RF source, is used for low power and small rate frequency chirps. The frequency dependent AOM deflection efficiency is compensated by active feedback (Intensity-stabiliser 2). λ/2-wave plates, together with polarising beam splitters, are used to adjust the relative maximum power levels for the three retro-reflection pulsed beam lines. Each beam line has a beam expander, which is used for spatial mode cleaning and to adjust the minimum focal spot width, if the beams are focused into the sample by a lens (not shown). Beam 3 and 2 are guided collinearly to the sample, but at 90° relative (linear) polarisation. Beam 1 crosses beam 2 in the centre of the sample. The transmission of each beam can be detected by the signal photodiode (Sig. PD, Thorlabs APD110A). To avoid saturation or destruction of the detector, intense pulses may be gated by an AOM (NEC OD-8813A) in front of the Sig. PD. A 8% reflection beam splitter and a matched reference photodiode (Ref. PD), in front of the cryostat are used for pulse monitoring and AWG waveform pre-calibration (see Sec. 4.2.1). The RF for the retro-reflection setups 2 and 3 is generated by the sketched single sideband (SSB) up-conversion of the RF from a DDS and one AWG channel per beam line. The DDS directly generates the required 0/90°- quadrature RF signals, whereas the AWG signal is split up by quadrature power splitters. Power splitters are indicated by black dots at line crossings and RF frequency mixers are represented by circles with crosses. After combining the single sideband hybrid signals (see inside SSB), a further reduction of spurious sidebands is achieved by a bandpass filter (BP).

The diffracted intensity of the laser changes as a non-linear function with respect to the RF power and frequency. One reason is that the optimum alignment of the AOM, with respect to the input laser beam, can only be met for one specific frequency [87]. Other reasons are the limited bandwidth of the AOM piezo-electric transducer RF-impedance-matching circuits, or RF amplifier power non-linearity and saturation. A way to compensate such unwanted non-linear responses is by active feedback. Retro-reflection beam line 1 employs this method. It is connected to an intensity stabiliser (see Fig. 13), which is equivalent to that used for reduction of the general laser power fluctuations (see Sec. 4.1.1). This works well for slow changing intensities, e.g. due to slow frequency chirping, and in the optimum case may further reduce the noise of this beam. Nevertheless, the control response time is of the order of 10 μs, therefore this method is unsuitable for pulses with total durations of e.g. 1 μs, as used in Sec. 8.3.2. Furthermore, some experiments require specific pulse power shapes. For such high bandwidth and arbitrary shape pulse beam lines 2 and 3 (see Fig. 13) are used. To correct for AOM related distortion of the optical pulses a system using pre-corrected input RF-waveforms from an arbitrary waveform generator (AWG) RF-source was implemented.

4.2.1 *AOM Calibration System*

As discussed in the previous section the intensity of the light diffracted by an AOM depends on the RF frequency and power, but also on "environmental" parameters, like the optical alignment and for example the RF characteristics of incorporated amplifiers, mixers etc.. Most of the environmental impacts change only very slowly, e.g. on a daily base, and therefore may be considered as constant for the duration of most experiments. As long as this is fulfilled, it is sufficient to characterise the intensity of the diffracted light by a function of the RF power and frequency, which are used to control the optical pulse forming:

$$I_L = f(\nu_{RF}, P_{RF}). \tag{4.1}$$

For the beam lines 2 and 3 (see Fig. 13) arbitrary variations of ν_{RF} and P_{RF} can be generated by a two channel arbitrary waveform generator (AWG). The retro-reflection setup of beam line 3 (and 1) use a NEC OD-8813A AOM, which has a RF centre frequency of 140 MHz. For beam line 2 an AA model MT200-B100A0.5-VIS AOM is used, which has a centre frequency of 200 MHz. The maximum useable RF bandwidths for light diffraction are for both AOM types about half of their RF centre frequency. The AWG, a Tabor Electronics WW1072, has 14bit vertical resolution, 1 MS waveform memory and 100 MS/s sampling rate. The 100 MS/s sampling rate limits the useable output frequency to about $\nu_{AWG} = 45$ MHz. To supply the AOMs with their required RF centre frequencies (140 and 200 MHz), the AWG output frequency is up-converted by RF-mixing with the constant local oscillator frequency of a direct digital synthesis (DDS) RF source. To reduce mixing sidebands, e.g. the down-converted frequencies, single sideband (SSB) up-conversion mixers (see Fig. 13) have been built for each AWG channel. To avoid a frequency overlap of the SSB output with the DDS local oscillator, the AWG is only operated in the range of $\nu_{AWG} = 10 - 45$ MHz. Therefore, the effective range for frequency

changes at the output of the SSB mixers is about 35 MHz. Due to the (first order) double passage in the retro-reflection setups, a range of 70 MHz results for the laser light. All incorporated RF power have been adjusted to obtain an almost linear dependence of the SSB output as a function of the AWG power. Nevertheless, residual non-linear responses will be accounted for by the calibration, explained in the following.

The light used for the calibration is separated from the beam line by a beam splitter in front of the cryostat and subsequently detected by a 50 MHz bandwidth avalanche photodetector (Ref PD, see Fig. 13). The laser pulse intensity is characterised as a function of the frequency and output power of the AWG (Eq. 4.1). To achieve a high resolution in both variables the frequency is varied in 50 steps and the intensity is varied in 100 steps. The intensity variation is done in four separate measurements. For each step different (calibrated) neutral density filters are placed in front of the sensitive detector, starting with no filters for the first 25 low intensity steps. The different attenuations cover 4 orders of magnitude. By averaging, the resolution of the digitalisation is enhanced up to 11bits. In this way the dynamic range of the characterisation for intensity changes is approximately 6 orders of magnitude. Figure 14(a) shows the AWG waveform output power P_{AWG} (black), programmed for the intensity steps $75 - 100$, and the measured light intensity $I_L(\nu_{AWG}, P_{AWG})$ (red). For each step with constant P_{AWG}, the AWG frequency ν_{AWG} is varied in 50 steps. To allow for more convenient handling of the data, for each pair of ν_{AWG} and P_{AWG} a single pulse is generated, as shown in the blow-up Fig. 14(b). The complete mesh of characterised $I_L(\nu_{AWG}, P_{AWG})$ values is shown in Fig. 14(c).

By linear interpolation a continuous function $I_L = f(\nu_{AWG}, P_{AWG})$ is calculated. Its inverse with respect to the AWG power

$$P_{RF} = f^{-1}(\nu_{AWG}, I_L)$$

allows calculation of pre-calibrated AWG waveform powers P_{AWG} for any required optical pulse power I_L and optical frequency $\nu_{L,1} = \nu_L + 2\nu_{AWG}$.

Programmed and measured calibrated intensity shapes and absolute powers typically deviate by less than 2%. Due to the limited sampling rate of the AWG, the deviation becomes larger, especially for $\nu_{AWG} > 40$ MHz. For high duty cycles the pulse droop of the 3 W RF amplifiers can further increase the deviation slightly. In general the highest accuracy is achieved directly after the characterisation isv carried out. Changes of the laboratory temperature, e.g. due to the additional heat generated by the full setup equipment running, as well as changes of the optical alignment, e.g. due to some work on the optical table, may require re-characterisation and generation of calibrated waveforms more frequently than on a daily base.

An initial version of the calibration system was developed together with the bachelor student Timo Paschen [125].

The characterisation data processing and creation of calibrated waveforms for various pulse forms (chirps, complex hyperbolic secant pulses [130], etc.) was implemented in the MATLAB script TaborCalib.m.
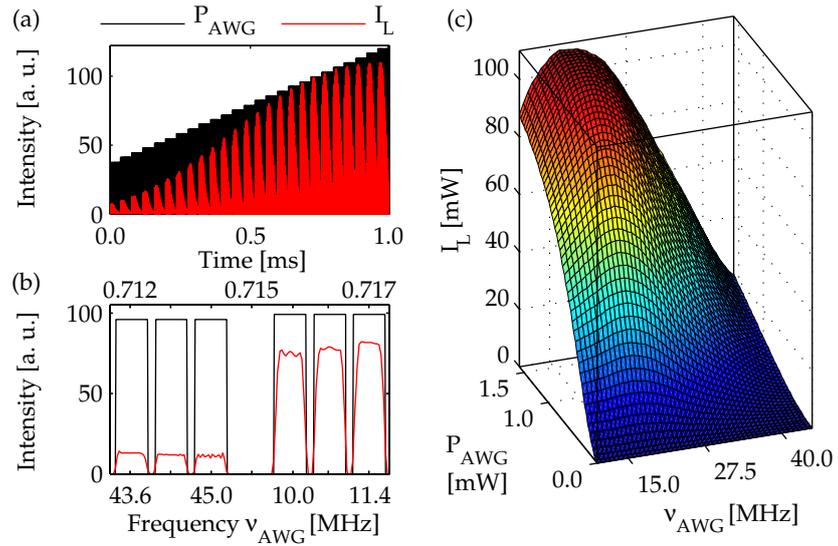
Figure 14: Typical calibration system input data. (a) shows the light intensity measured by the reference photodetector (red, I_L) for the 25 largest programmed AWG output power levels (black, P_{AWG}). The vertical scale is in mW for I_L. P_{AWG} was normalised in order to show the non-linear increase of the I_L intensity with linear increasing P_{AWG}. All single AWG intensity and frequency (ν_{AWG}) steps are programmed in form of pulses, within a single AWG waveform (in total four waveforms, each covering 25 different intensity steps, see text). For one constant P_{AWG}, 50 pulses with different, during one pulse constant, ν_{AWG}-values are applied. Part (b) show a blow-up of the data shown in (a). The scale on the top is in ms whereas the bottom scale shows the increase of the (constant) frequency for each pulse. (c) shows the full space of parameters covered in one AOM characterisation, with 100 points in the P_{AWG} and 50 points in the ν_{AWG} dimension, which in total takes about 10 minutes to record and process.

34

RADIO FREQUENCY SYSTEM

The nuclear spin hyperfine level splitting of the investigated samples ranges from $7 - 40$ MHz for the electronic ground states and from $0.9 - 12$ MHz for the excited states (see Sec. 7.4). The transitions between levels of one electronic state can either be driven indirectly by bi-chromatic laser pulses or by direct resonant excitation with resonant radio frequency (RF) fields. Unlike the bi-chromatic optical method, the direct excitation with RF typically excites all rare earth ions within the used samples, since the inhomogeneous broadening of the hyperfine levels is $\lesssim 200$ kHz (see 7.4.4) and moderate RF powers of about 100 W already achieve comparable Rabi frequencies if resonance circuits are used.

The RF system enables the excitation with continuos wave (CW) and pulsed RF, which is synchronised with the optical pulse generation (see Sec. 4.2). Furthermore it allows to demodulate optically detected transients, e.g. those of Raman heterodyne experiments.

5.1 RF EXCITATION AND DEMODULATION

The timing for all experiments is controlled by a digital word generator. Figure 15 shows a schematic of the RF system including its main components. The WG triggers the AWG waveforms, which generate the optical pulses (see Sec. 4.2) and controls fast high-isolation RF switches, which cut RF pulses out of the CW output of the direct digital synthesis (DDS) RF sources used to excite the nuclear spin transitions. Compared to the use of pre-programmed AWG waveforms the use of the CW DDS output has the advantage, that the relative phase between two cut-out RF pulses is always well defined. Using an AWG the experimentalist has to take care of the relative RF phases of the pulses by pre-programming correct waveforms, which single phases account for the frequency and timing of the pulses in the actual sequence. Especially for multi-pulse sequences, as used in Sec. 8.3, a DDS has clear advantages. Changes of the DDS and thus of the RF pulse frequency, phase and amplitude can be controlled by instruction patterns using the WG. The change of a single DDS parameter is limited only by the internal 300 MHz system clock and the analog output bandwidth of ≈ 120 MHz of the DDS as long as two subsequent changes are separated in time by more than the instruction word processing duration ($\gtrsim 120 - 300$ ns). Faster, quasi-continuos changes of the RF amplitude and phase can also be applied by the optional usage of one channel of the 100 MS/s AWG, which was originally used for the pulse generation in one optical beam-line (compare Fig. 15 and 13).

Different RF power amplifiers[†] increase the pulse powers to levels of ≈ 10 W for CW Raman heterodyne experiments and for pulsed experiments to ≈ 200 W. The pulses are applied to the sample using appropriately tuned RF resonance circuits, which will be described in Sec. 5.1.1.

Optical transients that contain relevant information modulated in the frequency of the photodetector signal are routed to the RF demodula-

[†] *ENI 3200L: 0.25 − 150MHz, 200W. ENI 5100L: 1.5 − 400MHz, 100W. Barthel RFPA: 0.1 − 50MHz, 300W.*
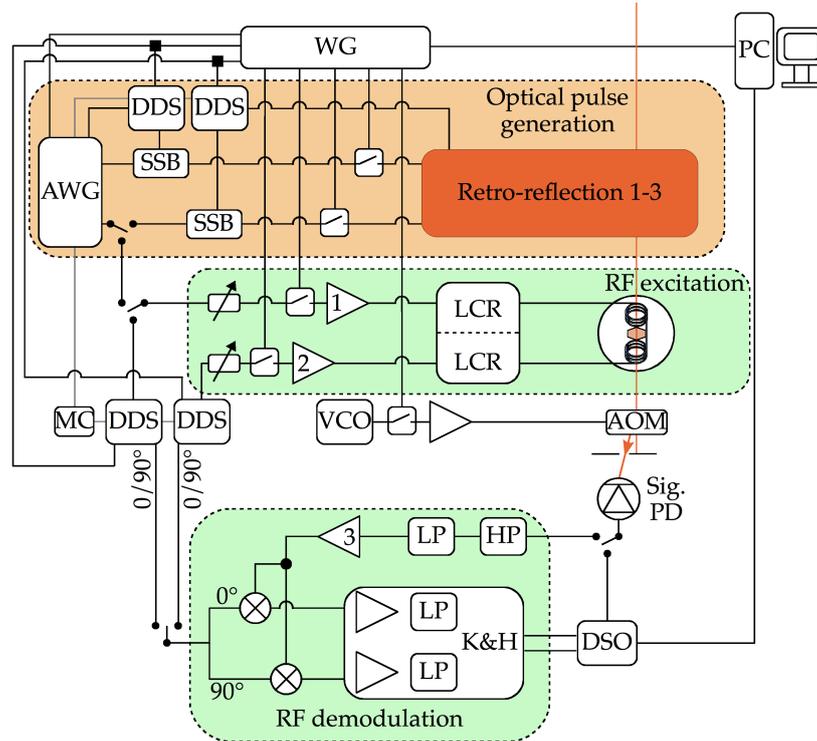
Figure 15: Schematic of the RF excitation and demodulation (green) system, including synchronisation to the optical pulse generation (orange, see Fig. 13). A 250 MHz digital word generator (WG, Interface Technology RS-690) controls all relative timings. It triggers the AWG and can reset the general phase of the DDSs. AWG and DDS frequencies are synchronised by a stabilised master clock (MC, grey connections). All excitation lines can be interrupted by fast switches, which are controlled by the WG and used to generate RF pulses from CW RF. The sources for the RF excitation and demodulation are given by DDS. Their frequency (fixed or linearly chirped) and amplitude can be set and changed by the WG on time scales of $\gtrsim 200$ ns. One WG output can control two DDSs using diplexers (black squares). One channel of the AWG, which is part of the optical pulse generation setup can optionally be used for arbitrary RF power shape and frequency pulses with 10 ns resolution. The pulse power levels are adjusted or limited by variable attenuators, which are in between the RF sources and the power amplifiers "1" and "2". The amplifiers can be connected directly (see text) or by using lumped elements resonance circuits (LCR, for details see Fig. 16) to the RF coils, which are mounted on two sides of the sample within the cryostat. The RF excitation and demodulation share the same DDSs as sources, but only one of the excitation channel DDSs is connected to the demodulator at a time. Optical transients are detected with a photo detector of high bandwidth (Sig. PD, 50 MHz Thorlabs APD110A, 125 MHz New Focus 1801 or 100 MHz balanced Femto HCA-S). The transient signal may be gated optically by an AOM or by a RF switch in the demodulator (not shown). A combination of tuneable high and low pass filters at the input of the demodulator (HP, LP) allows signal-adapted filtering to avoid saturation of the following (optional) preamplifier "3" (Miteq AU-1114), e.g. by strong DC or other signals outside the signal carrier bandwidth. The signal is split by a power splitter (black circle) and then demodulated in a quadrature scheme using the fixed 0/90° DDS outputs as local oscillators. The following amplification and filtering of the demodulated (DC-2 MHz) signal is accomplished by a programable filter (Krohn-Hite 3940). The transients are recorded by a digital oscilloscope (DSO, LeCroy WR 104Xi).

tion system (see Fig. 15). The DC intensity of the heterodyne signals in some situations can be very high compared to the amplitude of the relevant frequency modulation of the signal. For very small modulation signal pre-amplification with a low-noise amplifier is beneficial before the signal is actually demodulated. To avoid saturation of the pre-amplifier by large DC components or other unwanted frequency signals, a combination of adjustable high and low pass filters is used. The phase sensitive demodulation uses the $0/90°$ quadrature RF of the same DDS that is used for the excitation. The demodulated signal can be further amplified and low pass filtered by programmable filters before it is recorded for further processing by a digital oscilloscope.

All DDS and the AWG use a central oven-stabilised master clock oscillator as frequency reference. This reduces frequency drifts to the minimum, determined by the difference of the 300 MHz clock of the DDS and the 100 MHz clock of the AWG, which is sufficient for all performed experiments since the laser stability is lower (see Sec. 4.1.2). To enable the accumulation of heterodyne beats without RF demodulation the internal phase-wheel of the DDS can be reset with the WG before execution of each single shot.

5.1.1 *Resonance Circuits*

The RF pulses are applied to the sample by a solenoid coil of about 6 mm diameter. The sample is in the centre of the coil, which is split into two equal parts connected in series by a short piece of wire. Both coil ends are accessible from the outside of the cryostat. Figure 16 shows the different configurations in which the coil is connected to the RF amplifiers and resonance circuits.

For CW RHS experiments the power amplifier is directly connected to the sample coil. To reduce power reflection due to impedance mismatch a small ten-turn coil is used and grounded at its other side by a $R = 50\Omega$ resistance (Fig. 16 a)). The cables connecting the sample coil to the external terminals of the cryostat, represent a "stray capacitance" of (together) about 30 pF connected in parallel to the sample coil. This represents a low pass characteristic for the RF transmitted through the coil. The damping at ≈ 30 MHz is about -3 dB and therefore has to be considered for wide-scan or high frequency CW RHS experiments.

For pulsed experiments resonance circuits are used to increase the effective Rabi frequency of the RF pulses. Depending on the sample and the resonance frequency of the hyperfine transition, different circuits are used, in particular for PrLaWO and PrYSO these are simple single resonance circuits (Fig. 16 b) and c)). The sample coil and a capacitor (C_T), which is connected in series (a) or in parallel (b), form a resonance circuit. In conjunction, a second capacitor (C_M) is used for impedance matching to the 50Ω RF system. To allow a broader tuning range all capacitors have a variable capacity. Stray capacities and inductivities, due to the about 30 cm long cables inside the cryostat, cause series and parallel resonance circuits to have other resonance frequency ranges, although the same capacitors are used. One of both configurations is chosen for each experiment on the basis of the best achievable impedance matching. The impedance matching can be verified using bi-directional couplers. Readily achievable transmission to reflection voltage ratios are about $10 - 30$, typically limited by the harmonic output of the RF amplifiers.
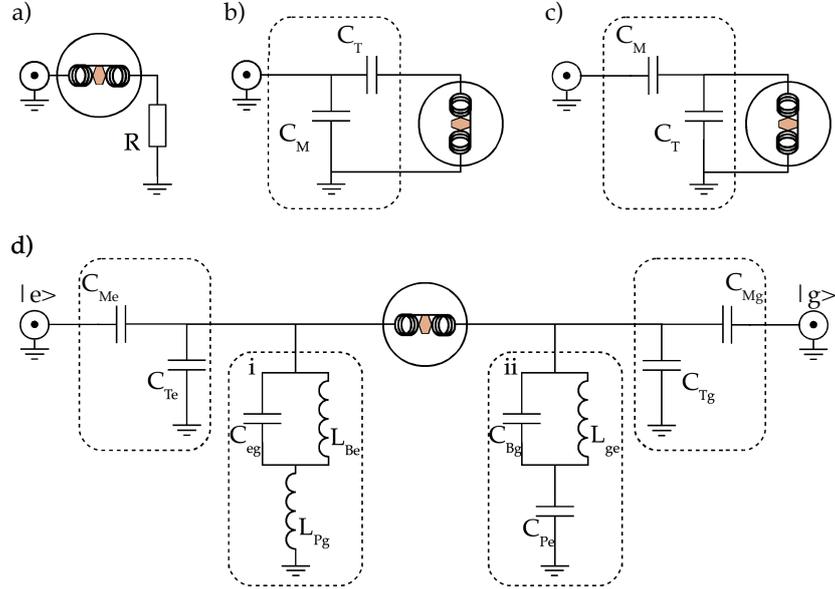
Figure 16: Different configurations for the RF coil and resonance circuits.. The configuration shown in a) is used for CW RHS experiments. The power amplifier is directly connected to a ten-turn coil. The other side of the coil is grounded using a R=50 Ω resistance out side of the cryostat. For single resonance experiments with PrLaWO and PrYSO the sample coil forms a resonance circuit with a variable capacitor (C_T), which is connected in series (b) or in parallel (c). For these samples also a ten-turn coil is used. The variable capacitors for resonance tuning (C_T) and for impedance matching (C_M) are connected to the coil end on the outside of the cryostat (indicated by the dashed boxes). Different capacitance values in the range of $10-150$ pF are used for these samples. d) shows the double-tuned single (sample) coil resonance circuit, which is used for the excitation of the PrYAP hyperfine transitions. The excitation of the excited state ($|e\rangle$) and the ground state ($|g\rangle$) is based on parallel resonance circuits (like in c)) and a 48-turn sample coil. The variable capacitors for the excited state resonance frequencies are tuneable in the range of $C_{M/Te} = 35 - 1500$ pF. For the ground state $C_{Te} = 1-7$ pF and $C_{Me} = 11-52$ pF are used. The amplifiers are isolated against each other by (tuneable) double frequency switches (i and ii). In ii the ground state frequency "blockade" capacitor range is $C_{Bg} = 35 - 1500$ pF, the excited state "pass" capacitor range is $C_{Pe} = 1.4 - 72.3$ nF. For i $C_{eg} = 44$ pF is a fixed value capacitor. All coils in i and ii are homemade multilayer coils with ferrite cores, L_{Be} and L_{Pg} are tuneable. The inductances have not been measured.

For PrYAP a doubly tuned resonance circuit is used (Fig. 16 d)). It allows to excite ground and excited state hyperfine transitions at the same time. The sample coil in this case is doubly tuned by two distinct parallel resonance circuits from each of its sides. A cross-talk between the two distinct resonance circuits is effectively suppressed by double frequency switches (see Fig. 16 d) i and ii boxes) on each side of the sample coil. Each double frequency switch consists of a series resonance circuit, which has low impedance in resonance, and a parallel resonance circuit, which has a high impedance in resonance. In double frequency switch "ii" (see Fig. 16 d)) the parallel resonance circuit given by C_{Bg} and L_{ge} has a very high effective impedance for ground state frequencies, which therefore pass to the sample coil. The series resonance circuit, which follows on the other side of the coil and is given by C_{eg} and L_{Pg} in double frequency switch "i", has a very low impedance for ground state frequencies and therefore effectively terminates this RF frequencies to the ground at this point. For the excited state frequencies the "pass" and "block" parts of the double frequency switches exchange accordingly. The distinct resonance circuits and the connected RF power amplifiers are in this way isolated by more than 50 dB. The single tuning ranges, for the particular capacitance values given in the caption of figure 16, are $\approx 0.8 - 1.4$ MHz for the excited state and $\approx 4 - 6$ MHz for the ground state. By using modular exchangeable sample coils and capacitors $C_{M/Te,g}$ other frequency-range combinations are achievable.

6

CRYOGENIC SETUP AND STATIC MAGNETIC FIELD

6.1 CRYOSTAT AND SAMPLE MOUNT

Raman heterodyne experiments can be performed in the temperature range between 2 K and 12 K for the samples investigated in this work. For photon echo and hole burning experiments the temperature is more critical and usually did not exceed 5 K. A continuos flow cryostat (Cryo Industries RC110) is used to reach these temperatures. A pressure of about 130 mbar transfers liquid helium from a storage dewar through the flow cryostat, which has a sample mount at its coolest point. To this "cold finger" adapted sample mounts for the crystals can be attached. The sample mounts are made out of oxygen-free copper. Two silicon diodes together with a temperature controller (Conductus LTC 10) are used to monitor the temperature directly at the cold finger and at the far end of the crystal sample mount. If not quoted differently, the temperatures are given for the sensor mounted directly at the cold finger. This may be lower than the real sample temperature due to non-perfect thermalisation.[†] The cold finger and the sample are placed in a vacuum, pumped within a four window optical dewar. The cold finger and the sample mount are surrounded by an aluminium (or brass) thermal radiation shield. If thermal radiation is shielded maximally, with leaving only two 3 mm holes for laser transmission, temperatures of 1.6 K are reached and the liquid helium consumption is about $0.7 - 1.5$ litres per hour.

[†]*See Fig. 55 for a sample temperature estimate based on optical coherence time measurements.*

Figure 17a shows the sample mount attached to the cold finger and the fixed PrLaWO crystal as an example. The samples are pressed by fitted brass clamps or swivelled delrin frames (see Fig. 17b) to the lapped sample mount surface. The crystals thereby are centred over a 3 mm hole in the centre of the mount, which allows laser transmission. For fluorescence measurements, the construction allows to observe the sample in a small solid angle from the side, too. To enlarge the thermally contacted areas all joints are coated by a thin layer of heat conducting silver paint or, which proved to be slightly better, Apiezon N vacuum grease. The RF coils are mounted centric around the laser axis and as close as possible to the sample using delrin frames (see Fig. 17 a and b). To reduce induction of eddy-currents in the copper, which would heat the sample and reduce the resonance circuit quality factor, the sample mounts have two perpendicularly cut slits.

6.2 MAGNET SYSTEMS

The characterisation of the hyperfine Hamiltonians requires precisely set magnetic field vectors, which have to be applied in various directions (see Sec. 7.1.2). Arbitrary magnetic field vectors are applied either by three orthogonal Helmholtz coil-pairs or a superconducting 3-axis vector magnet.

The room temperature Helmholtz coil-pairs are mounted centrically around the cryostat vacuum dewar with the sample in their centre

(see figure 17c). The coils have diameters ranging from $\approx 20 - 40$ cm, depending on the field direction. A highly stable linear current source (Servowatt, three channel DCP-390/30) applies currents of ≈ 15 A to the coils, which generates fields of $\approx 10 - 12$ mT at maximum in the centre of the coil-pairs. The individual coil fields are controlled by setting an analog control voltage for the current sources with 12bit precision (National Instruments NI USB-6009). The actual field vector magnitude and direction is monitored by three perpendicularly oriented Hall effect sensors (Chen Yang CYTHS119), whose output voltages are amplified and recorded with 14bit resolution (NI USB-6009). Together with the diploma student Philipp Glasenapp a computer controlled feedback loop for the coil current control and the field monitoring was developed, which is documented in detail in Ref. [51]. The field strengths for all three coil-pairs are calibrated with a precision of

$$\delta B_i = \sqrt{(\frac{B_i}{400})^2 + (0.06 \text{ mT})^2}\,,\ i = x,\ y \text{ or } z,$$

where the linear uncertainty ($1/400 \,\hat{=}\, 0.25\%$) and the absolute field uncertainty (0.06 mT) are dominated by the precision of the calibrated Hall detector (Project Elektronik FM-205 and AS-LTM sensor) used for all calibrations.[†] The feedback control system allows to reduce the effect of non-linearity and drift of the components. Furthermore small background magnetic fields, e.g. due to a residual magnetic hysteresis of the optical table, may be compensated by measuring them in a controlled way and setting a compensation field (see Sec. 7.4.1 and Ref. [51]).

The control system is currently adapted to be used at the same time also for the superconducting coils, shown in figure 17b. The coils are designed to be cooled under the critical temperature for super-conduction by the available cold finger. The construction is adapted to the particular needs of sample accessibility, mounting precision and fitting and the exchangeable RF coils. The spatial dimensions preset by the available cryostat were maxed out to achieve (simulated) fields of about 200 mT with 9 A per coil axis. The calculated field homogeneity is better than $\pm 0.3\%$ in a 5x5x5 mm volume in the coil-system centre. The coil-system was manufactured by GVL-Cryoengineering using the preset specifications. The single-block coil-frame is made of oxygen-free copper. The superconducting single filament NbTi/Cu-matrix coil wire has an outer dimension of 102 μm. Together with the bachelor student Philipp Wirth a first test and calibration was carried out recently [160]. Thermalisation below the critical temperature (9.2 K) and operation in the superconducting regime was achieved. With the current status the coils enable 222, 165 and 136 mT per direction, where the latter two values are below 200 mT due to quenching at currents below 9 A. The achieved fields can be monitored by a miniature 3-axis Hall sensor (Arepoc, custom product) mounted as close to the sample as possible (see Fig. 17b.), which measures the field in a volume of ≈ 250 μm^3. The motivation for this coil-system is to enable the hyperfine characterisation (Sec. 7.4) and zero first order Zeeman experiments (Sec. 8.2) with the same coils.

[†]*The field (voltage) noise level is below 0.01 mT and the error due to calibration sensor spatial-misalignment is < 0.1 %.*

(a)　(b)

(c)
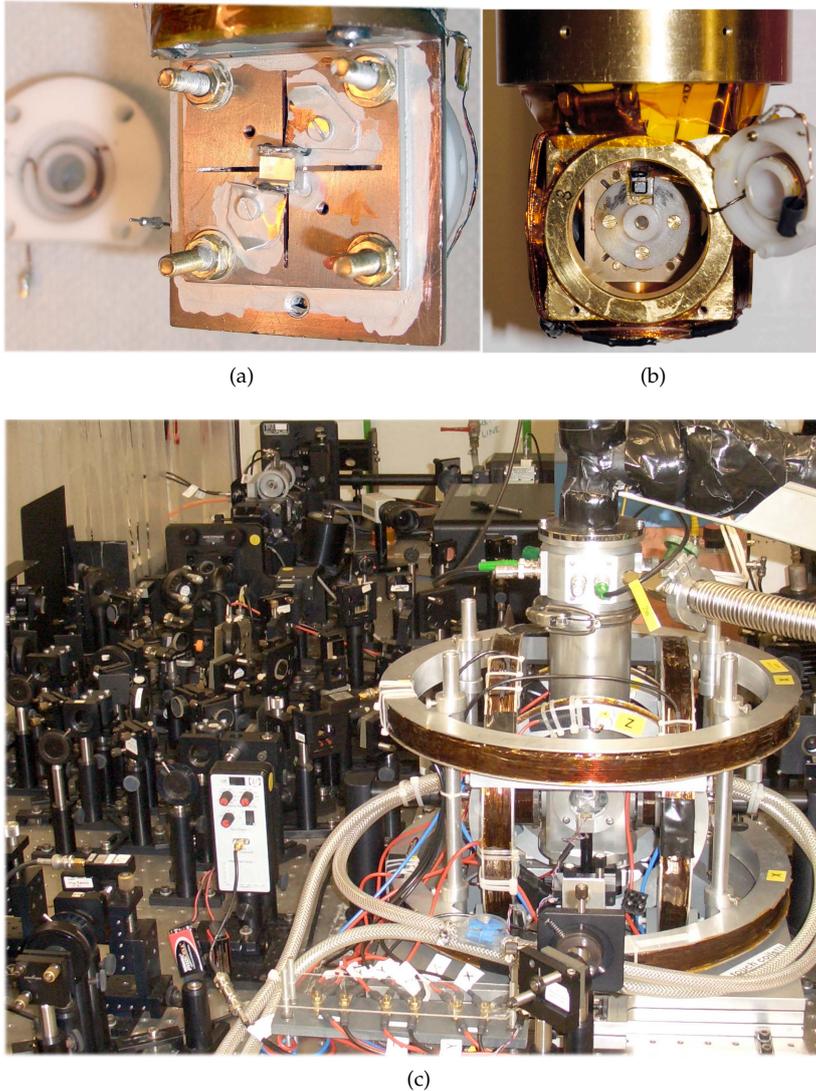
Figure 17: Magnet system and sample mount. In (a) the sample mount, which is mounted at the end of the cold finger (top of the figure), is show. The crystal (in the centre) is pressed and fixed onto the oxygen-free copper mount-plate by two brass clamps. The mount-plate itself is pressed to the sample mount by four screws. To avoid eddy-currents when RF pulses are applied perpendicular slits are cut into the mount-plate. To allow transmission of the laser a central hole of 3 mm is drilled in the mount-plate, which is not visible since the crystal covers it. On the left the front-RF coil and its mounting frame is visible. This part is centred and fixed using the four big screws. To increase thermal conduction silver paint is applied between all relevant surfaces. (b) shows the fully assembled 3-axis superconducting vector magnet, mounted at the cold finger. The swivelled delrin frame, which fixes the sample on the holder, and a part of the sample itself are visible. Thermal conduction is improved by use of Apiezon N grease between all contact surfaces. Above the central hole of the delrin frame, the miniature 3-axis Hall sensor is visible. The modular exchangeable RF coil on the right fits into the facing superconducting coil centre and can be fixed by two screws (in diagonal, only one screw is inserted here). The backside RF coil module is mounted in the same way. On the right side of the picture in (c) the three orthogonal room temperature Helmholtz coil pairs are visible. The cryostat dewar is in the centre of this arrangement. Close to the front window of the cryostat, a small cube on which three Hall sensors are mounted orthogonally is visible. In left backside, a part of the optical pulse generation setup and the $899-21$ laser cavity is visible.

Part III

RARE EARTH INVESTIGATIONS

SPIN HAMILTONIAN CHARACTERISATION

Detailed and precise knowledge of the Hamiltonian is a crucial prerequisite for the realisation of sophisticated experiments, like the attempts to implement a quantum memory.

Currently suggested schemes for quantum memories in RE systems use techniques like selective hole burning [122], coherent operations between specific levels [157] and special external magnetic field configurations, which result in so-called ZEFOZ (zero first order Zeeman) conditions for a specific transition and thereby enhance its coherence lifetime [44]. All those techniques heavily rely on the parameters determined by the spin Hamiltonian: the transition frequencies and relative oscillator strengths. Sometimes the optimisation of a single experimental step can be carried out by tweaking the single parameters in a trial and error procedure (e.g. for selective hole burning at zero magnetic field). In contrast, such a search for the specific ZEFOZ field vector is typically not feasible or possible to accomplish with reasonable experimental effort (see e.g. section 8.2). The same usually applies for the very precise parameters required by optimal control techniques [75]. Thus, the latter two techniques require prior knowledge of the spin Hamiltonian. The combination of such techniques also leads to a substantial increase of complexity, e.g. when the magnetic field used to enhance the coherence time leads to closely adjacent levels, which can not be resolved by the selective hole burning techniques. A completely characterised spin Hamiltonian allows identification and avoidance of such problems.

This chapter will introduce the experimental and numerical techniques used to characterise the spin Hamiltonian. Furthermore, the achieved results for three important Rare Earth systems will be presented.

7.1 INTRODUCTION OF THE METHOD

The method used to find the spin Hamiltonian parameters relies on the comparison of measured hyperfine spectra with calculated ones. Since the spin Hamiltonian determines the frequencies and the transition strengths, spectra measured with known external parameters can be used to fit the Hamiltonian parameters.

7.1.1 *Generation of the Spectra*

Hole burning experiments may often cover the whole spectral range of hyperfine transitions for a given optical transition. However, the resolution of the derived spectra is limited to the laser stability [100]. Furthermore, the spectra may become very difficult to interpret when a magnetic field lifts the hyperfine degeneracy, as the spectral line frequencies are determined by combinations of all hyperfine level splittings in the ground and excited state. The number of lines multiplies from a maximum of 49 lines at zero field, to 961 lines for non-zero fields, which causes overlaps and crossings. This makes the lines be-

come indistinguishable or trackable for relatively small magnetic fields. This is especially the case if the hyperfine splittings of the excited and the ground state are similar and the enhanced nuclear Zeeman effect becomes comparable to the effective quadrupolar interaction.

In pulsed or CW RHS (see Sec. 3.3) spectra the line positions are given by the level structure of one electronic state (ground or excited state), which reduces the number of lines to be interpreted in the spectra significantly. Furthermore, the resolution of RHS spectra is independent of the laser stability [162], which makes the line frequency become a very precise measure. In the ideal case the resolution is only limited by the (in-)homogeneous line width of the particular hyperfine transition. But RHS spectra also have some limitations. Even though it is possible to calculate the RHS spectra directly from the Hamiltonian, the resulting amplitudes typically do not match the experimental ones. In CW experiments the excitation dynamics are rather difficult to consider, and in general experimental details like RF amplifier non-linearity, the cable lengths, the tuning curves of the RF resonators and coil(s), etc., may change the local amplitude and the relative phase in the spectra as a function of all involved tuning parameters. One other point is that RHS spectra are insensitive to some symmetry related operations on the spin Hamiltonian (see Sec. 7.2.1), e.g. to the energetic order of the hyperfine levels, thus the sign of the Hamiltonian parameters can not be extracted from the spectra.

As a consequence of the above implications, within this work absolute value RHS spectra are used. Only the precise resonance line frequencies will be utilised to derive the spin Hamiltonian parameters. The absolute signs of the parameters will be considered as far as covered by the literature [55, 16, 78, 122].

7.1.2 *Variation of External Control Parameters*

For zero magnetic field $\vec{B} = 0$, the line positions are determined completely by the effective quadrupolar constants D and E (see Eq. 2.10 or Sec. 7.2). By measuring spectra with a finite magnetic field, whose magnitude and orientation within the laboratory reference frame are known, one can infer the magnetic parameters $g_{\alpha'}$ and the orientation of the tensor PA systems relative to the laboratory reference, or equivalently relative to each other. As the number of parameters which characterise the spin Hamiltonian completely is rather large (see Sec. 7.2), it is necessary to measure the spectra for many different magnetic fields to get unambiguous Hamiltonian parameters. Therefore, a scheme introduced by Longdell et al. [93] was implemented.

As a first step a series of RHS spectra for different $\vec{B}$-fields are collected for the electronic excited and the ground state. The field is generated by a precise and computer-controlled vector magnet (see. Sec. 6.2 and 6.2), allowing collection of $\gtrsim 100$ spectra for each series. In the second step, using appropriate numerical techniques (see. Sec. 7.3), all collected spectra are fitted simultaneously for one electronic state on its own.

The applied magnetic field vectors should cover a variety of spatial directions with sufficient resolution to allow a precise determination of the spin Hamiltonian tensors orientation with respect to the field's reference axis system, which in the following is the same as the laboratory axis system (LAS). Furthermore, the magnitude of the field should be

The relative orientation between LAS and the crystal lattice will be disscued in the results section 7.4.

large enough to get a sufficient absolute precision of the derived spin Hamiltonian (or tensor) eigenvalues, since the induced splittings are proportional to the magnitude, but the RHS line widths are assumed to be independent. To cover both aspects the field vectors trace a spiral, which itself lies on the surface of an ellipsoid. This is parameterised by:

$$\vec{B}(t) = \begin{pmatrix} B_x \sqrt{1-t^2} \cdot \cos(6\pi t) \\ B_y \sqrt{1-t^2} \cdot \sin(6\pi t) \\ B_z \cdot t \end{pmatrix}. \tag{7.1}$$

Herein

$$t = (N-1)\frac{2}{N_{tot}-1} - 1$$

is used to represent the discrete coordinate along the trajectory of the magnetic field vector trace, with $N = 1, 2, ..., N_{tot}$ being the index of the experiment and $B_{x,y,z}$ representing the maximum values of the applied field flux along the laboratory system coordinate axes. Figure 18 shows a typical trace of applied magnetic field vectors, using the maximum field strengths of the room temperature coils (see. Sec. 6.2) and Eq. 7.1 but starting at $\vec{B} = 0$ to include a zero-field reference spectrum.
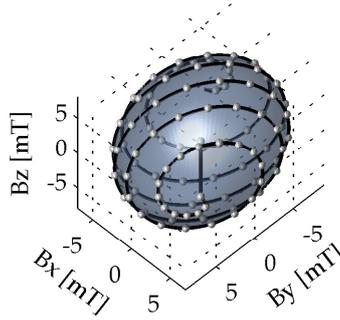

Figure 18: The magnetic field used for hyperfine characterisation. The black line indicates the trajectory of the field vector tip and the grey dots indicate the discrete applied fields for $N_{tot} = 101$ experiments.

7.2 SPIN HAMILTONIAN MODEL

All alignments relevant to the measurements, like coil axes, laser wave vector and crystal orientation with respect to each other, are done in the LAS (x, y, z). The most elegant way to write a Hamiltonian is to choose a diagonal representation, thus to write it in its own PAS. The relevant principal axis systems of the particular rare earth crystal typically do not coincide with the LAS. It is therefore convenient to use similarity transformations, considering the relative orientation of the principal axis systems to the LAS, in order to transform the diagonal representations of the Hamiltonians into the LAS.

Following section 2.1, the relevant principal axis systems are the PAS of the effective quadrupolar interaction (x''', y''', z''') and the PAS (x', y', z') of the $\hat{\Lambda}$ tensor (Eq. 2.3). (x', y', z') determines the PAS of the pseudo-quadrupolar and the quadratic and enhanced Zeeman interaction (see Eq. 2.2). Especially in related earlier work considering PrYAP [39, 161, 110, 111, 18, 79, 78] the approximation was made, that the PAS (x'', y'', z'') of the pure quadrupolar Hamiltonian (Eq. 2.5) coincides with the PAS (x', y', z') of the pseudo-quadrupole Hamiltonian, thus $(x''', y''', z''') \hat{=} (x', y', z')$. Considering both axis systems to be not coincident is more general and appropriate, since the Pr site symmetry of the other crystal systems studied in this chapter (C_1 [54, 71]) is lower

Section 7.4.2 gives more details on the symmetry of PrYAP.

than that of PrYAP (C_{1h} [39]). But even in the latter compound a better match of the data is achieved (see Sec. 7.4.2 on page 75).

By omitting the quadratic Zeeman effect, only the enhanced nuclear Zeeman effect and the effective quadrupolar interaction terms remain in the spin Hamiltonian (Eq. 2.10). Using the above model, the spin Hamiltonian can be represented in the LAS by:

$$\mathcal{H}_1 = \vec{B} \cdot \hat{M} \cdot \vec{I} + \vec{I} \cdot \hat{Q} \cdot \vec{I}, \tag{7.2}$$

$$\hat{M} = R_M \cdot \begin{bmatrix} g_{x'} & 0 & 0 \\ 0 & g_{y'} & 0 \\ 0 & 0 & g_{z'} \end{bmatrix} \cdot R_M^T, \tag{7.3}$$

$$\hat{Q} = R_Q \cdot \begin{bmatrix} E - \frac{1}{3}D & 0 & 0 \\ 0 & -E - \frac{1}{3}D & 0 \\ 0 & 0 & \frac{2}{3}D \end{bmatrix} \cdot R_Q^T. \tag{7.4}$$

The $R_i = R(\alpha_i, \beta_i, \gamma_i)$, with $i = M$ or Q, represent rotation matrices and Euler angles, transforming from the Zeeman ($\hat{M}$) and the quadrupole ($\hat{Q}$) PAS to the LAS. For these rotations the "zyz"-convention [53] with right-handed coordinate systems will be used. Accordingly, the rotation matrices are given by:

$$R(\alpha, \beta, \gamma) = C \cdot B \cdot A, \quad \text{with } \alpha \text{ and } \gamma \epsilon [-\pi, \pi], \ \beta \epsilon [0, \pi]$$

$$A = \begin{pmatrix} \cos\alpha & \sin\alpha & 0 \\ -\sin\alpha & \cos\alpha & 0 \\ 0 & 0 & 1 \end{pmatrix}, \quad B = \begin{pmatrix} \cos\beta & 0 & -\sin\beta \\ 0 & 1 & 0 \\ \sin\beta & 0 & \cos\beta \end{pmatrix},$$

$$C = \begin{pmatrix} \cos\gamma & \sin\gamma & 0 \\ -\sin\gamma & \cos\gamma & 0 \\ 0 & 0 & 1 \end{pmatrix}.$$

Since $\hat{M}$ and $\hat{Q}$ can not be diagonalised in the same PAS in general, the related Euler angles $(\alpha_i, \beta_i, \gamma_i)$ will differ for both.

To consider the crystal site symmetry (see e.g. Sec. 2, 3.3 and 7.4.1-7.4.3) with a minimum number of model parameters the spin Hamiltonian for the second Pr-site ions is defined utilising the underlying C_2 symmetry in the following way:

$$\mathcal{H}_2 = \vec{B} \cdot (R_{C_2} \cdot \hat{M} \cdot R_{C_2}^T) \cdot \vec{I} + \vec{I} \cdot (R_{C_2} \cdot \hat{Q} \cdot R_{C_2}^T) \cdot \vec{I}, \tag{7.5}$$

$$R_{C_2} = R_C^T \cdot R_\pi \cdot R_C,$$

$$R_C = R(\alpha_{C_2}, \beta_{C_2}, 0), \quad R_\pi = R(180°, 0, 0).$$

R_{C_2} represents a series of rotations, in which first the LAS tensors $\hat{Q}$ and $\hat{M}$ are transformed (R_C) into an axis system where the C_2 axis is along the z-coordinate. The rotation of 180° around this z-axis (R_π) is then applied. Finally, the tensor is transformed back into the LAS (R_C^T). In this way the angles α_{C_2} and β_{C_2} correspond to the spherical coordinates of the C_2 axis in the LAS.

While in one measurement only one electronic state is being measured, it is possible to extract the relative angles between the PAS of

the ground and excited state Hamiltonian, since all orientations are extracted with respect to the LAS. By mechanical alignment the latter is also fixed to the crystal axis system, with respect to which all tensors are intrinsically fixed. Nevertheless, the site assignment by the Hamiltonian parameters is arbitrary in the sense that, e.g., the physical ground state site described by $\mathcal{H}_1$ might be characterised by the $\mathcal{H}_2$ parametrisation in the excited state. This twofold ambiguity will be resolved by comparison to related studies sensitive to this issue (see results section 7.4 on page 62).

7.2.1 *Symmetries*

The Hamiltonian parameters will be extracted by fitting the frequencies resulting from the eigenvalues of the model spin Hamiltonian to that of the recorded RHS spectra. At this point it has to be realised that different Hamiltonians can lead to the same RHS spectra.

The most trivial symmetry operation that causes such ambiguity is sign inversion of the model Hamiltonian $\mathcal{H} \rightarrow -\mathcal{H}$. Typical minimum temperatures for the experiment are about $T = 2$ K and the splitting of the hyperfine levels of interest is approximately $\Delta E/h \approx 10$ MHz. In this regime the Boltzman factors $e^{-\Delta E/k_B T}$ are very close to one and no effect on the populations will be visible for the sign inversion of $\mathcal{H}$. The differences between its eigenvalues, that give the line frequencies in the RHS spectra, also do not change for $\mathcal{H} \rightarrow -\mathcal{H}$. Therefore the model parameters are insensitive, too.

At first, considering the $\hat{Q}$ tensor only, this inversion would correspond to simultaneous changes of the signs of D and E, as can be seen from Eq. 7.4. But also relative changes of the signs e.g. only $E \rightarrow -E$ can lead to the same spectra. This kind of inversion is equivalent to a exchange of the x and y-axis in the $\hat{Q}$ PAS (see Eq. 7.4 or 2.10). Using two different rotation matrices R_Q and R'_Q, both signs for E are compatible with the RHS spectra. In close analogy, permutations involving the z-axis lead to different values for D and E, *e.g.*:

$$\begin{pmatrix} 1 & 0 & 0 \\ 0 & 0 & 1 \\ 0 & 1 & 0 \end{pmatrix} \begin{bmatrix} E - \frac{1}{3}D \\ -E - \frac{1}{3}D \\ \frac{2}{3}D \end{bmatrix} = \begin{bmatrix} E - \frac{1}{3}D \\ \frac{2}{3}D \\ -E - \frac{1}{3}D \end{bmatrix} \stackrel{\wedge}{=} \begin{bmatrix} E' - \frac{1}{3}D' \\ -E' - \frac{1}{3}D' \\ \frac{2}{3}D' \end{bmatrix},$$

here the vector represents the diagonal of $\hat{Q}$. Solving the linear equation on the right leads to the new quadrupole constants $D' = D/2 + 3E/2$ and $E' = D/2 - E/2$. The 3! possible permutations of the axes (x, y, z) combined with the sign inversion lead to 12 equivalent solutions of the form

$$D' = \pm D \quad \text{and} \quad E' = \pm E \quad \text{or} \tag{7.6}$$

$$D' = \pm \left[\frac{D}{2} \pm \frac{3E}{2} \right] \quad \text{and} \quad E' = \pm \left[\pm \left(\frac{D}{2} \mp \frac{E}{2} \right) \right], \tag{7.7}$$

where in Eq. (7.7) the signs have to be evolved dependent on the bracket-rank/type, resulting in a total of three different |D| and |E| pairs. This and all other discussed ambiguities will be treated in section 7.2.2 by certain conventions.

For the $\hat{M}$ tensor the same implications concerning axes permutations and sign inversion apply. All transformations (expect from inversion) will require different R_M transformations to fit the RHS spectra.

Finally for the complete spin Hamiltonian, according to Longdell [92] the coordinate transformations P ($P^\dagger P = E$) which keep $\hat{Q}$ invariant ($P\hat{Q}P^\dagger = \hat{Q}$) have to be considered. These are:

$$ P = U_{QPAS} \begin{pmatrix} \pm 1 & 0 & 0 \\ 0 & \pm 1 & 0 \\ 0 & 0 & \pm 1 \end{pmatrix} U_{QPAS}^\dagger, $$

with the rotations U_{QPAS} being defined such that, the similarity transformation $U_{QPAS}^\dagger \hat{Q} U_{QPAS}$ transforms a given $\hat{Q}$ into its PAS (e.g., $U_{QPAS} = R_Q$). P therefore represents inversion, reflections at planes normal to the $\hat{Q}$ PAS axes, π-rotations around the $\hat{Q}$ principal axes and the identity. For the spin Hamiltonian this leads to:

$$
\begin{aligned}
\mathcal{H} &= \vec{B} \cdot \hat{M} \cdot \vec{I} + \vec{I} \cdot \hat{Q} \cdot \vec{I} \\
&= \vec{B} \cdot \hat{M} P P^\dagger \cdot \vec{I} + \vec{I} \cdot P P^\dagger \hat{Q} P P^\dagger \cdot \vec{I} \\
&= \vec{B} \cdot \hat{M} P \cdot (P^\dagger \vec{I}) + (P^\dagger \vec{I}) \cdot \hat{Q} \cdot (P^\dagger \vec{I}).
\end{aligned}
\tag{7.8}
$$

In the first and last line the eigenstates are given in an other representation resulting from the new angular momentum operators $\vec{I}' = (P^\dagger \vec{I})$, that now are given in terms of different axes.

Requiring $\hat{M}$ to be symmetric (Eq. 7.2 and 7.3) and using the same axes to represent $\hat{M}$ and $\hat{Q}$, it can be shown that inversion is the only possible operation for the term $\hat{M} \rightarrow \hat{M} P$ (see first term of Eq. 7.8) in order to fulfil Eq. 7.8. [92] For the most general case where the PAS of $\hat{Q}$ and $\hat{M}$ do not coincide, this means that the Hamiltonian is sensitive to the individual signs of $g_{x'}, g_{y'}$ and $g_{z'}$, but not to a simultaneous inversion of all the $g_{\alpha'}$.

7.2.2 *Conventions*

As discussed before, only $|g_{\alpha'}|$, $|D|$ and $|E|$ and the relative orientation of the connected PAS, up to the site assignment, can be deduced from the RHS spectra. The absolute signs have to be extracted using other methods. The relative signs between the $g_{\alpha'}$ values or between D and E can be changed by choosing different reference axis systems, or equivalently, different Euler matrices R_M and R_Q. $|D|$ and $|E|$ are connected to an additional ambiguity between three pairs of values.

Keeping all ambiguities unresolved, it is no obstacle to fit the RHS spectra appropriately, or to predict spectra for a given magnetic field. Nevertheless, comparing and discussing the fit results, different samples or fit trials becomes more difficult. Therefore the results for the Hamiltonian parameters presented in the next sections will obey following conventions:

The absolute signs of D and E can be extracted from the literature that covers (selective) hole burning [55, 122, 78], or two beam RHS [16] studies, and will be given in the sections (7.4.1-7.4.3) dealing with the samples.

The D and E ambiguity, arising from permutation of the coordinate axes (Eq. 7.6 and 7.7), will be resolved using the convention [2]

$$0 \leqslant \frac{3E}{D} = \eta \leqslant 1,$$

thereby fixing the sign of E and also forcing the z-principal value of $\hat{Q}$, $2/3D$, to be the one of the greatest magnitude.

Although the axis permutations are restricted in this way, the Euler rotations are not unambiguous in the sense that different Euler angles (α, β, γ) can give the same transformation matrices R. Typically, one set of Euler angles describing the $\hat{Q}$ tensor orientation in the LAS, resulting e.g. from multiple equivalent fit trials, serves as reference for the $\hat{M}$ tensor axis permutation and Euler angle set. Accounting for the fact that some sample systems are relatively close to axial symmetry ($|D| \gg |E|$), and therefore as described above the PAS of $\hat{Q}$ and $\hat{M}$ should be close to overlap, the permutation of the $g_{\alpha'}$ will be chosen such that the principal value of the biggest magnitude is aligned with the $\hat{M}$ PAS z-direction. Of the sets of Euler angles allowing for that, the set with the smallest deviation, which is defined as a vector norm $|(\alpha_Q, \beta_Q, \gamma_Q) - (\alpha_M, \beta_M, \gamma_M)|$, is chosen. The selection of the $\hat{M}$ principal value permutation and the Euler angle set is done post fitting using a script [51].

7.3 NUMERICAL FITTING

To treat the numerical problem of fitting the spin Hamiltonian, a package of *MATLAB* scripts was developed. These cover all necessary steps, beginning with importing the original *MacExp* data, which contains the RHS spectra, up to the analysis and visualisation of the final fit result properties. The following sections describe the subject matter relevant to reliably obtain the results presented in section 7.4.

7.3.1 *Spectral Line Identification*

The base data to fit either the parameters for the ground or excited state typically incorporates 200 spectra for each hyperfine transition manifold. Therefore, the frequency positions of about $200 \cdot 2 \cdot 8 = 3200$ lines have to be extracted from the RHS spectra for one electronic state. To improve speed, reduce false notes and offer more accuracy compared to a manual identification of the line peak maxima, a script-based fitting of all spectra was implemented.

As mentioned in Sec. 7.1.1 only the frequencies in the spectra are to be understood as precisely determined by the spin Hamiltonian. Several sources of noise and experimentally caused line shape distortions make it especially difficult to identify weak lines. Furthermore, adjacent lines can cause false identifications or frequency shifts, if e.g. a weak and a strong line overlap partially. The script therefore utilises features like the global noise level in the spectra or the mean RHS line widths to define thresholds and rejection-/acceptance discriminators.

As a first step, the script analyses all RHS spectra of a single hyperfine transition manifold (e.g. $|\pm 1/2\rangle \leftrightarrow |\pm 3/2\rangle$) and searches for spectra with well resolved single RHS lines and regions with undistorted noise. The corresponding data of all suitable spectra is averaged and thresholds for minimum signal levels ($S/N \gtrsim 1.5$) and acceptable line widths

(within $20 - 250\%$ of mean line width) are calculated based on empirical relationships. In a second step all spectra are processed again and each spectrum is analysed for peaks of sufficient S/N, then subdivided in regions with single or possibly multiple overlapping peaks. In the latter case the peaks are fitted to a corresponding number of Gaussian peaks simultaneously. Only fitted lines fulfilling the line width thresholds are kept. At maximum eight lines of those are kept, by discarding the ones with smaller amplitudes.

The drawn procedure typically captures 98% of all lines one would identify manually, but with more exact frequencies and further includes the fit parameters (amplitudes and frequencies of peaks and fits, widths from fits). To cover the remaining lines, each spectrum can be inspected manually together with the overlaid fit results. This especially helps in accounting for lines that can be traced through some of the spectra but at some point start to diminish due to a reducing overlap integral (see Sec. 2.2) or to sort out false lines that somehow managed to fulfil all thresholds before.

Besides the use of the precise RHS line frequencies to fit the Hamiltonian parameters, the fitted line widths and amplitudes are used to estimate the individual fit-errors and to analyse the properties of the inhomogeneous hyperfine line broadening (Sec. 7.4.4).

7.3.2   *Line Mapping*

As the spin Hamiltonian of Eq. 7.2 is a 6x6 matrix, and its RHS spectra are measured simultaneously with the one of the site 2 Hamiltonian Eq. 7.5, a maximum of 30 transition lines can be observed. Not all lines are visible or resolvable in each recored spectra. Some have a too small transition matrix element, overlap or might even interfere destructively (see Sec. 3.3). Others might be at frequencies not excited or detected (e.g. $|g, +1/2\rangle \longleftrightarrow |g, -1/2\rangle$). For the fitting at some point the experimentally observed lines have to be compared with those following from Eq. 7.2 and 7.5. Thus a mapping has to be established. It was found to be effective to map each experimental line with the closest theoretical line in frequency, if lines where this mapping is not unique are rejected for this fitting step. This simple scheme is intended to avoid ambiguous mappings, that could cause erroneous convergence of the fit. When the spin Hamiltonian parameters are not well determined, e.g. at the beginning of the fitting, it typically rejects 20 to 50% of the experimental lines. When the fitting becomes accurate, typically more than 99.5% of the experimental lines are mapped to unique theoretical lines.

7.3.3   *Simulated Annealing and the Fitting Algorithm*

The problem Hamiltonians (Eq. 7.2 and 7.5) require a total of 13 parameters to characterise one electronic state:

D, E, α_Q, β_Q, γ_Q, $g_{x'}$, $g_{y'}$, $g_{z'}$, α_M, β_M, γ_M, α_{C_2} and β_{C_2}.

Gradient based algorithms proved to be inefficient in fitting the RHS spectra line frequencies in this 13-dimensional space. They tended to lock to local minima in the large and complicated solution space. In the work of Longdell et al. [93] the simulated annealing algorithm [77] showed to be effective in finding a global minimum for this explicit problem.

Simulated annealing is based on the probabilistic Metropolis-Hastings algorithm [107, 65]†. The latter samples the probability distribution function of the system, e.g. determined by a Boltzmann distribution

$$p \propto e^{-\left(\frac{E}{k_B T}\right)},$$

by iterating many random variations of the model parameters. E is adapted to the problem, and here represents the deviation between theoretical and experimental spectra. The algorithm is intended to minimise the energy E of the system by choosing and modifying one of the model parameters (e.g. α_Q) at random for each iteration (k). If the system energy E_k becomes smaller compared to E_{k-1}, the modified set of parameters is accepted and the iteration goes on with those. In the case of $E_k > E_{k-1}$ the acceptance function

$$p_k = \exp\left(-\frac{E_k - E_{k-1}}{k_B T}\right) \tag{7.9}$$

defines the probability of accepting the modified parameter. The last step enables the Metropolis algorithm to leave local minima with a certain probability.

In simulated annealing this probability is modified during the optimisation process. As suggested by its name, the temperature T is gradually lowered while the iteration goes on. By this, the probability to accept worse trials is high at the beginning of the search and is successively lowered as the algorithm approaches the optimal model parameters. The annealing can reduce considerably the necessary number of total iterations to find a global optimisation minimum, compared to the pure Metropolis algorithm. The introduction of a variable temperature may also be seen as an adaptive "divide-and-conquer" approach [77]: At high temperatures coarse features of the problem (e.g. magnitude of the g_{α}'s) may be revealed first and fine details (e.g. exact orientation of the tensors) are probably developed later at lower temperatures.

Simulated annealing proves to be reliable by means of finding a global minimum, with respect to the Hamiltonian parameters for the different REIC (Sec. 7.4), starting from a random guess. Nevertheless, the time and the approximative number of iterations necessary are strongly dependent on the actual implementation. This includes the annealing schedule, the random parameter trial generation, the parameter space restrictions and the actual definition of the energy E or, in other terms, the objective function for the optimisation, which will therefore be defined in the corresponding paragraphs at the end of this section.

When the simulated annealing is finished an optimisation based on the pattern search [149] algorithm, which polls grids of adjacent (parameter-) points to seek for a better minimum, is performed. This helps to further reduce the number of necessary iterations in the annealing. On the other hand, as pattern search is also suitable to find global minima of complex problems [9], it represents a test of the quality of the suspected "global minimum" found by the annealing. If the simulated annealing worked satisfyingly, typically only very minor changes of the fit and of the parameters result from the pattern search iterations.

In this work the simulated annealing and pattern search implementations of *MATLAB* (*simulannealbnd* and *patternsearch*) have been used to supply a framework for the basic algorithmic steps. The actual im-

plementation of the relevant parts to consider the REIC system and the specific optimisation problem are described in the following paragraphs.

Objective Function

For the spin Hamiltonian characterisation the output of the objective function is selected to be the RMS (root mean square) deviation between the measured RHS line frequencies ν_i^{exp} and the frequencies calculated by using the model Hamiltonians (Eq. 7.2 and 7.5) ν_i^k for the input parameter set of the kth-iteration. To be effective for an unambiguous fitting, the objective function considers all available RHS lines of all measured spectra, respectively, all sampled $\vec{B}$-orientations:

$$f_k^{rms} = \sqrt{\sum_{N=1}^{N_{tot}} \frac{\sum_{i=1}^{Q_N} \left(\nu_{i,N}^{exp} - \nu_{i,N}^k \right)^2}{Q_N}}, \tag{7.10}$$

herein N is the index of the $\vec{B}$-orientation (see Sec. 7.1.2) used and Q_N is the number of RHS lines with unique mapping for the Nth spectrum (see Sec. 7.3.2). In the described optimisation algorithm f_k^{RMS} replaces the system energy E_k (e.g. in Eq. 7.9). Besides the calculation of the RMS deviation the implemented version of the objective function (*Hamdevi.m*) evokes the calculation of the actual Hamiltonian matrices (Eq. 7.2 and 7.5, *HamiltonOP.m*) and the theoretical frequencies ν_i^k (*HDdiffs.m*) at each call. The latter are derived by solving for the eigenvalues of the Hamiltonians and calculating all differences between those. The line mapping code is implemented in the objective function as well, since the mapping changes during iteration.

Besides the main features, given above, the objective function also can incorporate the RMS deviation of experimental and theoretical transition matrix elements (Sec. 2.2 and *HDdiffs.m*) by the use of the experimental line heights. As mentioned before (Sec. 7.1.1) the "true" RHS line heights are distorted, especially for CW RHS spectra, by effects of the experimental apparatus, which are difficult to compensate. Therefore the transition strengths have only been used in situations where the fitting did not converge sufficiently or to discriminate between two non-perfect fits of similar quality in early first trials.

Acceptance Function

As introduced before, the acceptance function decides if a trial parameter set is kept for the following optimisation iterations. A first discrimination is based on the comparison of the current trial (k) and the previous (accepted) trial $(k-1)$ RMS deviation. For $f_k^{RMS} < f_{k-1}^{RMS}$ the modified parameter is accepted $(p_k = 1)$. If $f_k^{RMS} > f_{k-1}^{RMS}$ then the acceptance probability (*MLacceptancesa.m*), analogous to Eq. 7.9,

$$p_k^{RMS} = \exp\left(\frac{-\left(f_k^{RMS} - f_{k-1}^{RMS} \right)}{k_{B_l} T_{k_l}} \right), \tag{7.11}$$

is calculated and compared to a random number $p_r \epsilon [0, 1]$. The last step implements the probabilistic feature of the Metropolis algorithm, as the new trial parameter is accepted only for $p_k^{RMS} > p_r$. In Eq. 7.11 the 13 Hamiltonian parameters are indexed by l. The temperatures

T_{k_l} are given in l^{th}-parameter units. The conversion factors k_{B_l} are constants and keep the exponent unit-free. Furthermore, they scale the denominator in p_k^{RMS}, such that the resulting acceptance probability is independent of the selected trial parameter (see the annealing schedule paragraph).

Annealing Function - Random Trial Parameter Generation

When the optimisation package (*FitRotplot.m*) is called, it is possible to specify if the required input parameter set or if a random trial, obeying the search bounds, shall be used as the starting point for the following iterative optimisation.

For each iteration k a new trial parameter set (*Annealingfun()*, see *FitRotplot.m*) is generated. To do so, first one of the 13 Hamiltonian parameters in the full set is chosen at random. This parameter is then varied at random by an amount proportional to the actual simulated annealing temperature. The last step may be repeated until the new parameter fulfils the predefined constrains for the search.

This constrains and parameter-bounds are typically chosen relatively diverse for the different Hamiltonian parameters. Usually the D and E values are known with good precision from hole burning experiments, whereas this is not the case for the effective gyromagnetic ratios and the tensor orientation angles of e.g. PrLaWO (Sec. 7.4.1). Thus, for the latter parameters it is advantageous to chose relatively unconstrained bounds, e.g $\pm100\%$ of the gyromagnetic ratio from a similar sample. To adapt the selection probability to this, the single trial parameter is chosen at random, but with a probability proportional to the relative size of the single parameter's search bounds with respect to the initial input parameter set value. A new trial for the selected parameter x_{k_l} is then generated by

$$x_{k_l} = x_{(k-1)_l} + T_{k_l} \left(2p_r - 1\right), \tag{7.12}$$

wherein $p_r \epsilon [0, 1]$ is a new random number. If x_{k_l} violates the parameter's constrain the process is repeated. D and E typically were constrained to $\pm10\%$ of the hole burning values, which are considered to be less accurate than values, which can be inferred from the RHS spectra. The g_α's were restricted to $\pm100\%$ of their initial input values and the angles $(\alpha, \beta, \gamma)_{Q/M/C_2}$ were allowed to vary over the whole definition range (see Sec. 7.2 and note $\gamma_{C_2} \overset{!}{=} 0$) .

Annealing Schedule

At a given stage of the iteration the simulated annealing temperature T_{k_l} controls the search radius and the acceptance probability for moves degrading the objective.

Initial temperatures T_{0_l} are defined relative to the initial input parameter set, using 2% for D, 5% for E , and 70% for the g_α's. For the angles 30° are used. This order of magnitude for the temperature allows the initial trial parameters to probe within the whole bounds using a few evaluations of Eq. 7.12. A change of an ideal parameter value by the given initial temperature results in an increase of the RMS deviation by typically 50 kHz to 500 kHz. For the studied samples this corresponds to 1 to10 inhomogeneous RHS line widths.

The conversion factors k_{B_l} (Eq. 7.11) are defined by setting the product $k_{B_l} T_{0_l} = \nu_\sigma^{RHS}$, where ν_σ^{RHS} is the mean width of all RHS lines in the spectra. The latter results in a balanced initial acceptance probability, which allows escape from local minima, but also avoids arbitrary scrambling of the parameters at medium stages of the annealing. The annealing schedule takes 80% of the maximum iterations (k_{max}) to reach the final temperature and then iterates keeping the temperature constant. The final temperatures are set by requiring $k_{B_l} T_{f_l} = 0.1 \cdot \nu_\sigma^{SNR}$, where the latter frequency is the expected statistical error in the line positions (see Eq. 7.21 in Sec. 7.3.4). This level is 1-2 orders below the typical best fit RMS deviations (Sec. 7.4), and thus is sufficiently low to sample the least significant changes of the parameters in the final stage of the optimisation. Explicitly the scheduler (*Tempfun()*, see *FitRotplot.m*) reduces the temperature using the following function:

$$T_{k_l} = (T_{0_l} - T_{f_l}) \cdot \left(1 - \frac{k}{k_{max}}\right)^{F_l} + T_{f_l} \quad , k \leqslant 0.8 \cdot k_{max} \quad (7.13)$$

$$T_{k_l} = T_{f_l} \quad , k > 0.8 \cdot k_{max}. \quad (7.14)$$

The implemented annealing scheduler includes an option to lower the temperature at three different rates ($F_{D,E}$, F_{g_α}, and $F_{(\alpha,\beta,\gamma)_{Q/M/C_2}}$ [51]), but it proved to be sufficient and, in the general case of an unknown global minimum, beneficial to reduce all parameter temperatures using $F_l = 2$ for the power law in Eq. 7.13. At times individual factors $F_l > 2$ caused the corresponding parameters to settle early at unfavourable values, even though the parameters with individual $F_l = 2$ were still changing. Nevertheless, individual F_l values might be beneficial if the initial input parameter set is already fitting the spectra well and only a minor refinement of single parameters is desired.

Additional Options

Besides the implementations described above the *FitRotplot*-package allows fitting of the spectra with different core options. Those incorporate modified spin Hamiltonian models e.g. where the two RE sites are not connected by a C_2 symmetry or e.g. the pure and pseudo-quadrupole hyperfine interaction PAS ($(x'', y'', z'') = (x', y', z')$) are forced to be aligned (see Sec. 7.4.2).

Furthermore, the objective function and acceptance function parameter $k_{B_l} T_{kl}$ can be selected to correspond to:

$$f_k^{lsq} = \sum_{N=1}^{N_{tot}} \sum_{i=1}^{Q_N} \left(\nu_{i,N}^{exp} - \nu_{i,N}^k\right)^2 , \quad (7.15)$$

$$\text{a) } k_{B_l} T_{0_l} = 2 \left(2 \cdot \nu_\sigma^{RHS}\right)^2 \text{ and b) } k_{B_l} T_{f_l} = 2 \left(\nu_\sigma^{SNR}\right)^2. \quad (7.16)$$

Both, the least squares based f_k^{LSQ} and the root mean squares based (Eq. 7.10, default) f_k^{RMS} objective function, have the same minima. Nevertheless, as f_k^{LSQ} scales quadratically with the single model/RHS lines deviation, its slope to the minima is much more steep than that of

the linearly dependent f_k^{RMS}. Furthermore, using Eq. 7.15 and 7.16 b), the acceptance probability (Eq. 7.9) becomes:

$$p_k^{LSQ} = \exp\left[\sum_{N=1}^{N_{tot}} \sum_{i=1}^{Q_N} -\frac{1}{2}\left(\frac{\nu_{i,N}^{exp} - \nu_{i,N}^k}{\nu_\sigma^{SNR}}\right)^2\right].$$ (7.17)

This is identical to the statistical expression for the probability for a series of data points $\nu_{i,N}^{exp}$, if the model given by $\nu_{i,N}^k$ is supposed to be "true" [127] (compare Eq. 7.19 in the next section). Concerning convergence and fit error estimation (see next section), the latter equations is an obvious choice and Longdell et al. [93] used these to fit the spin Hamiltonian of PrYSO for the first time. Serving as a reference, the implementation of Eq. 7.15-7.17 (including the parameter bounds and k_{B_l}) approximate that of Ref. [92].

Note: Longdell's [92] annealing schedlue differs from Eq. 7.13. This does not affect the following argument.

The least squares implementation in *FitRotplot.m* shows faster convergence than the RMS version, but at the same time, starting from a random trial, relatively often tends to remain locked in local minima, which can be attributed to the rapid scaling of Eq. 7.17 to very low acceptance probabilities during the first third of the complete number of iterations. The latter is the main reason to use the RMS deviation as objective by default for unknown spin Hamiltonians.

A typical local minimum lock-situation for PrLaWO yielded a 125% greater f_{best}^{LSQ}-based RMS deviation with respect to the f_{best}^{RMS}-based global minimum.

7.3.4 *Fit Error Estimation*

The probabilistic optimisation scheme can be interpreted using the Bayes theorem:

$$P(A|B) = P(A)\frac{P(B|A)}{P(B)},$$

herein e.g. $P(A|B)$ is the conditional probability of the event A given that B is true, whereas e.g. $P(A)$ is the unconditional (prior) probability for A. Identifying A with the "model" and B with measured "data" one can calculate the probability for the model. Obviously in most cases not "all" possible data and models can be measured or computed and the objective is to find the most "likely" model using the available data

$$P(\text{model}|\text{data}) \propto P(\text{data}|\text{model}),$$ (7.18)

setting the prior probabilities to be constants and supposing they are non-informative.

Assuming that the measurement error of the collected data points (ν_i) are independent, random and distributed normally, with the same standard deviation σ for all data points, around the ideal ("true") model ($\nu(x_{i,l})$) one gets [127]

$$P(\text{data}|\text{model}) \propto \prod_{i=1}^{N} \exp\left[-\frac{1}{2}\left(\frac{\nu_i - \nu(x_{i,l})}{\sigma}\right)^2\right],$$ (7.19)

which is identical to the product of the individual probabilities.

As indicated before, by comparison of Eq. 7.17 it is directly evident that $P(\text{data}|\text{model})$ is proportional to p_k^{LSQ}. Using Eq. 7.18 and remembering that σ and ν_σ^{SNR} are constants, this directly becomes

the justification to minimise f_k^{LSQ} (or, as showing the same global minimum, f_k^{RMS}) to find the "most feasible" model parameters.

Statistical (Fit) Error

Eq. 7.19 itself enables inference of the fit error of the "best" found parameters. Assuming the model (using the best-fit parameters $x_{i,l}^{best}$) is true, one can calculate the probability to accept a slightly deviated parameter $x_{i,,l}^{best} + \epsilon$, based on the finite width of the data point probability distributions. To approximate this, the simulated annealing part of the fitting procedure (Sec. 7.3) is repeated using a constant temperature T_{σ_l}. This temperature (see *ErrorTempBounds()* in *FitRotplot.m*) is selected such that adding it to a single best-fit parameter ($x_l^{best} + T_{\sigma_l}$) results in a rise of the objective function by the product $k_{\sigma_l} T_{\sigma_l}$- the denominator of the acceptance probability Eq. 7.11. By Following Eq. 7.19 strictly, this product has to be set to a level corresponding to the expected (random) error in the data points

$$k_{\sigma_l} T_{\sigma_l} = 2\nu_\sigma^2. \tag{7.20}$$

At this point the expected mean RHS line position error (ν_σ^{SNR}) is used to approximate ν_σ:

$$\nu_\sigma^{SNR} = \frac{1}{L} \sum_{i=1}^{L} \frac{\Delta\nu_i\,(1\sigma)}{SNR_i}, \tag{7.21}$$

here L is the total number of RHS lines identified (see Sec. 7.3.1), $\Delta\nu_i$ the 1σ-half width of a Gaussian fit to the ith's line and SNR_i is their individual signal to noise ratio (using the RMS-noise in a free region of the ith's line spectrum).

The results in Sec. 7.4 show that the mean (full width half max) line width of the RHS lines typically are 5 to 10 times bigger than the best fit RMS deviations. Thus, all the RHS lines can be explained very well by the fitted model. On the other hand it is also found that RMS $\left(f_{best}^{RMS/LSQ}\right)/\nu_\sigma^{SNR} \approx 20$, which implies that it is quite likely to find a single experimental line centre deviating by ν_σ^{SNR} from the calculated line position. Calculating the acceptance probability using the strict rule of Eq. 7.20 for an average deviation of ν_σ^{SNR} from the best fit gives $p_k = \exp(-1/2(1/1)^2)^N$. With $N \approx 10^3$, being the number of accepted lines by the mapping (Sec. 7.3.2), the probability becomes $p_k = 0 + \mathcal{O}\left(10^{-218}\right)$, which does not correspond to the observed number of such "outliners". An obvious reason for this is that the assumption of independent and normal distributed errors is false. More relevant reasons are that the lines are inhomogeneously broadened, leading to less defined line centres due to a distribution of the model parameters within the observed line widths (e.g. see Sec. 7.4.4) , or various systematic errors. The general impact of the latter will be discussed at the end of this section.

To estimate the error Longdell [92] scaled the error acceptance probability by choosing $k_{\sigma_l} T_{\sigma_l} = 2\left(f_{best}^{LSQ}\right)^2$. As a reference for comparisons the error estimation routine of *FitRotplot.m* does the same when f_k^{LSQ} (Eq. 7.15) is the objective for an error simulation. For the default implementation of the procedure, utilising the RMS deviation f_k^{RMS}, $k_{\sigma_l} T_{\sigma_l} = \nu_\sigma^{SNR}$ defines the acceptance level. Comparing the error ac-

ceptance probabilities for mean line position deviations of $0.1\nu_\sigma^{SNR}$, e.g. in PrLaWO, both give similar probabilities: $p_k^{LSQ} \approx 0.5$ and respectively $p_k^{RMS} \approx 0.9$. For line deviations of ν_σ^{SNR} the least squares version rejects all trials ($p_k^{LSQ} \approx 0$), whereas the RMS version has $p_k^{RMS} \approx 0.17$, which is already low but still supported by the observed line widths.

The parameter errors for the least squares and the RMS procedure are estimates, the first most probably under-estimating and the second over-estimating the effective sensitivity of the simulated annealing best fit parameters to noise in the line positions. Varying all the experimental line positions at random by the estimated noise ($\pm\nu_\sigma^{SNR}$) and then calculating the RMS deviation using the original best-fit parameter set, results after 1000 such trials, typically to a RMS deviation distribution with a standard deviation of ν_σ^{STD}, which typically approximates to $\nu_\sigma^{STD} \approx 0.03 \cdot \nu_\sigma^{SNR}$ and has its centre at $RMS(f_{best}) + 0.02 \cdot \nu_\sigma^{SNR}$. *FitRotplot.m* offers an option to calculate and set $k_{\sigma_l} T_{\sigma_l} = \nu_\sigma^{STD}$ for the error estimation procedure. As shown above this results in parameter errors reflecting the f_{best}^{RMS} parameter set sensitivity on random fluctuations of the line positions by $\pm\nu_\sigma^{SNR}$, expecting the latter to happen frequently.

Systematic Errors

The systematic errors are much more trivial to estimate and for the most Hamiltonian parameters these errors are larger than the statistical errors discussed above.

The most relevant systematic error is due to the calibration error of the static magnetic field. For the room temperature Helmholtz coils and fields smaller than 10 mT its relative error is below 0.65% (see Sec. 6.2). This error directly translates to the same fractional uncertainty for the gyromagnetic ratios $g_{\alpha'}$. The error for the orthogonality of the coils (static magnetic field) in both cases is estimated to be smaller than $1°$, as the super conducting and room temperature coil-frames were CNC-machined with high precision.

The surfaces of the crystals investigated are cut and polished perpendicular to the three principle axes of polarisation, (X, Y, Z), which typically are denoted by b, D1 and D2. The orientation of these axes with respect to the surfaces is usually determined by usage of a polarising microscope and is accurate to the order of $1°$. Thus, the orientation of the Pr-site symmetry axis C_2 with respect to the crystal surfaces is only known to about the same order. As tensor orientations in section 7.4 are given relative to the laboratory axis system (x, y, z), a misalignment of the crystal within the field coils does not contribute to the systematic error in the parameters. It translates to the angles α_{C_2} and β_{C_2} not being exactly those intended (e.g. $\alpha_{C_2} = \beta_{C_2} = 90°$) when mounting the crystal. Nevertheless, the uncertainty in the alignment of the crystal relative to the laboratory system (x, y, z) and that of the crystal surfaces to the principle axes of polarisation (X, Y, Z) can result in an error of up to $5°$ for the angles seen relative to the crystal axis system. Due to alignment of the laser by back-reflection, this error is smaller for the axis normal to this surface. In case one needs to calculate spectra with precise amplitudes for the axis of the RF coils, an alignment error of up to $5°$ can be expected.

Other sources of systematic error, e.g. drift of the RF frequency or the field calibration during the measurements, are better controlled and have much smaller impact on the data.

7.4   APPLICATION TO SPECIFIC COMPOUNDS AND RESULTS

All experiments in this work are carried out using the transitions of praseodymium, which resides as dopant in different crystal hosts. Due to its well characterised energy levels, strong transitions and their accessibility by rhodamine-6G dye lasers Pr^{3+} is one of the most studied rare earth ions [100, 99]. Although PrYAP (Pr^{3+}:YAlO$_3$) represents a testbed system for high resolution spectroscopy experiments (e.g. [101, 110, 111, 79, 80]) and the physical properties were studied in-depth in the past (e.g. [39, 40, 161, 15, 18, 81, 82]) its spin Hamiltonian was not fully characterised until now. PrYSO (Pr^{3+}:Y$_2$SiO$_5$) and PrLaWO (Pr^{3+}:La$_2$(WO$_4$)$_3$) represent systems in which proof of principle and experiments for methodical development in the context of quantum memories are preformed (e.g. [52, 66, 5]). PrYSO's spin Hamiltonian was fully characterised in the past [71, 38, 93], but there was some controversy in the results from the RHS based hyperfine characterisation and results from (amongst others) selective hole burning experiments [122, 123]. Section 7.4.3 will show a characterisation that proves to be consistent with the mentioned hole burning experiments.

The data for the characterisation of PrYAP and PrYSO were measured together with Philipp Glasenapp, who discussed them in his diploma thesis [51]. Section 7.4.2 and 7.4.3 will show an unique analysis including corrections, an updated error analysis (Sec. 7.3.4), conventions being in agreement with the terminology of the literature (Sec. 7.2.2) and further insights and results.

PrLaWO represents a novel compound of recent interest in REIC QIP [54, 55, 52]. As there was no published experimental data on the gyromagnetic part and the tensor orientations of the hyperfine Hamiltonian, this system is the main motivation for the deployment of the hyperfine characterisation within this work and the results will be presented in the next section.

Finally, section 7.4.4 will summarise the findings on the observed inhomogeneous (RHS) hyperfine line widths for all three compounds.

7.4.1   *PrLaWO*

Motivation

The efficiency of many quantum memory protocols and related techniques is a function of the available optical depth [148, 33, 4, 32]. The latter can be increased by doping the host material at higher levels with the desired REI. In many materials yttrium atoms are replaced by the doped REI, e.g. by praseodymium. Since the ionic radii for Y^{3+} and Pr^{3+} differ ($r_{Y3+} = 1.02$ Å, $r_{Pr3+} = 1.14$ Å [141]), raising the doping level increases the density of crystal defects and the crystal strain, which enlarges the inhomogeneous width of the Pr^{3+} transitions [100]. At the same time as the number of absorbers within the inhomogeneous line width is increased, the line width grows too, which limits the achievable optical depths [83].

With Pr^{3+}:$La_2(WO_4)_3$ a new quantum memory candidate material was proposed [54], wherein lanthanum is substituted by praseodymium instead. The close match of the Pr^{3+} and La^{3+} ($r_{LA^{3+}} = 1.18$ Å [141]) ionic radii results in an up to 15 times smaller inhomogeneous line width compared to PrYSO with the same doping level [71, 38, 54]. Besides this positive effect, the new compound incorporates a higher magnetic moment density, which is supposed to be detrimental for the coherence lifetimes [27] (see also Sec. 8.2). Whereas the tungstate host itself has low impact[†], lanthanum has a much higher magnetic moment (2.78 nm, ^{139}La 99.91% at. [128]) than yttrium (−0.14 nm, ^{89}Y 100% at. [128]), resulting in a 7.6 times higher magnetic moment density in LaWO compared to YSO [54].

Thus this material seems to be a compromise between a low inhomogeneous line width, allowing for high optical densities, and a high density of perturbing magnetic moments, being suspected to cause low coherence lifetime. Surprisingly, the coherence lifetimes for the ground state hyperfine transitions of PrYSO ($T_2^{HF} \approx 500$ µs [60]) and PrLaWO ($T_2^{HF} = 250 \pm 15$ µs [52]) are very similar and allow performance of quantum memory related experiments like EIT [52] in the latter, too.

To further exploit the potential of this material for QM related experiments, the full hyperfine characterisation was carried out within this work. This subsequently allowed to successfully apply special techniques to prolong the hyperfine coherence time by use of a precisely oriented external magnetic field vector, which will be presented in Sec. 8.2. Furthermore, these findings also motivated studies related to the question of how long an optical coherence can be stored within a ground state spin coherence in PrLaWO (see Sec. 8.3).

The results of Sec. 7.4.1 and 8.2 were recently published, see Ref. [97].

Crystal and Structure

$La_2(WO_4)_3$ forms a monoclinic crystal of space group C2/c. Its unit cell, shown in figure 19, contains four formula units of LaWO and measures a = 7.873(2) Å, b = 11.841(2) Å , c = 11.654 Å , with the angles of $\alpha = \gamma = 90°$ and $\beta = 109.25(3)°$ [48].

The eight lanthanum ions per unit cell occupy a single site of C_1 symmetry, which will also be occupied by the doping REI. This site can be subdivided into two groups of four REI positions connected by inversion, translation and C_2 symmetries. The C_2 axes are identical to the crystal b axis. If an external magnetic field is oriented along or perpendicular to the b axis the REI will give the same hyperfine line splittings, causing RHS interference effects [110, 111] (see Sec. 3.3). For general field orientation the splittings will be determined by Eq. 7.2 and 7.5. As defined in Sec. 7.2 the b axis orientation with respect to the laboratory frame is specified by the α_{C_2} and β_{C_2} angles of the characterisation.

The specific crystal used for the following experiments was grown, using the Czochralski method and the procedure of Ref. [91], by Philippe Goldner et al. at LCMCP. It contains 0.2% at. Pr^{3+} and measured 5x5x5 mm, its polished surfaces being orthogonal to the principle axes of polarisation (X, Y, Z) .

Note: For the experiments of Sec. 8.2 a (cutout) piece of this crystal was used.

Gathering of the RHS Data

The crystal was fixed by pressing it onto the sample holder by metallic clamps or a swivelled delrin frame. The Z axis was aligned parallel to
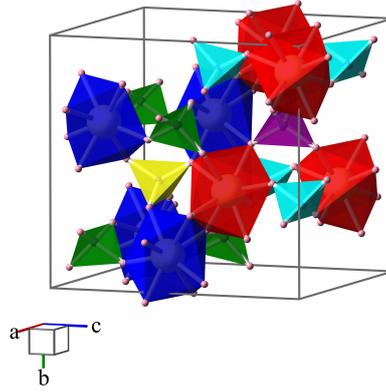
Figure 19: LaWO unit cell (grey bounding box). The small polyhedra contain different classes (cyan, green, magenta, yellow) of WO_4 tetrahedra, with tungsten at their centre. The big polyhedra contain lanthanum at their centre and oxygen of the first coordination shell at the edges. Red and blue polyhedra mark the two REI crystal sites. Additionally to the Z=4 formula units of PrLaWO per unit cell the (O) atoms necessary to complete the polyhedra, with centre-atoms (W/La) inside the unit cell, are drawn too. (The figure was created using the program Balls & Sticks and the data from Ref. [48])

the LAS z-axis by rotating the inserted cryostat assembly and using the back reflection of the laser beam, which propagated parallel to the z-axis. The parallelism of the polished crystal Z surfaces, mechanical production precision, optical spot size and measure distance limit this alignment to a precision of about $1°$. The X and Y axes were aligned by fixing the clamps/frame after carefully aligning these axes' crystal surfaces parallel to the sample holder sides and centring of the crystal by eye. Thus, the axes x/X and y/Y are supposed to be parallel. Due to the small dimensions of the sample and the lack of a solid alignment reference with respect to the sample holder sides or the field coils themselves, this alignment is expected be precise to about $5°$, with a centring precision with respect to (x, y, z) of approximately 0.5 mm).

For the RHS measurement the apparatus described in part ii was used. For the laser, the full stabilisation system (Sec. 4.1.1 and 4.1.2) except for the AOM calibration system (Sec. 4.2.1) was active. The laser was tuned to the centre of the inhomogeneously broadened $^3H_4 - ^1D_2$ zero phonon line, see figure 20. After passing through the AOM setup (Sec. 4.2) it had a collimated diameter of 1.5 mm and then was focused into the sample using a $f = 300$ mm lens. Figure 21 shows the pulse sequences used and the detailed parameters (see caption) for the recording of the RHS spectra. All optical powers quoted in the figure caption are measured in front of the cryostat entrance window, those of the RF represent values corrected for the reflected RF power in the pulsed RF experiments or the mean power dissipated in the 50 Ω load following the RF coil in the CW RF experiments. For the ground state the CW RHS technique (Sec. 3.3) and the sequence shown in Fig. 21(a) were used. The optimum temperature of the cold finger for this scheme was 4.5 K, since still lower temperatures give such slow hyperfine level relaxation rates, that it would be necessary to re-pump the hyperfine level population. Additionally, the RF sweep, besides creating the RHS coherence, shuffles the ground state hyperfine population. Both effects result in a quasi-stable signal amplitude after a few repetitions of the single
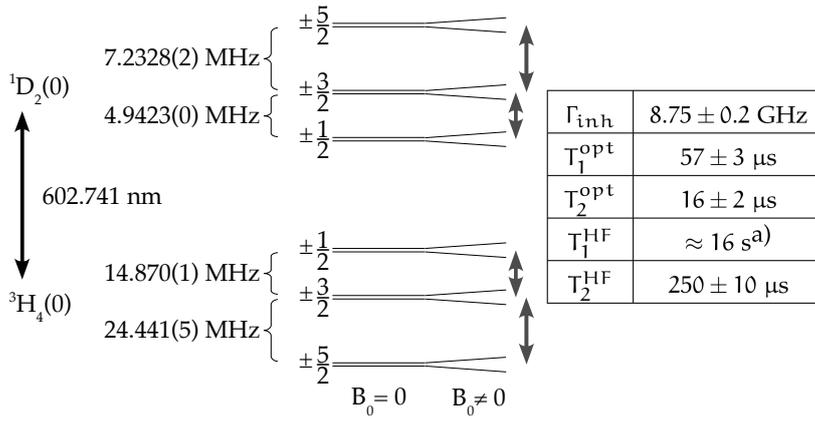
Figure 20: PrLaWO level structure of the zero phonon line levels $^3H_4(0)$ and $^1D_2(0)$, indicating their optical transition vacuum wavelength. The order of the energy levels follows from Ref. [55]. The hyperfine transition frequencies follow from this work, using (near) zero-field RHS spectra, resulting in values of higher precision (see brackets) than the previously published hole burning data. The arrows on the right indicate which Zeeman split hyperfine level manifolds have been addressed in the individual RHS experiments, as described in the text. The quantities listed in the table were measured for the 0.2 at. % sample (zero static field and $T \approx 2.5$ K) and are in good agreement with previously published data (1.4 at. % sample [54, 55]). The ground state T_1^{HF} value was taken form literature (a) [54]). Own measurements gave values in the range of 10 to 40 s.

sequence. Nevertheless, due to the complicated and not considered rate-equations incorporated with this process, the individual RHS line amplitudes lose their direct proportionality to the transition strength determined by the hyperfine Hamiltonian. Figure 20 shows which hyperfine manifolds have been accessed by the RF sweeps in separate RHS experiments. In the case of the ground state, performing two separate series of experiments was a matter of guaranteeing vertical resolution, as the RHS signal amplitude for the $|g, \pm 3/2\rangle \leftrightarrow |g, \pm 5/2\rangle$ transitions is about 10 times smaller than that of the $|g, \pm 1/2\rangle \leftrightarrow |g, \pm 3/2\rangle$ manifold (see. Fig. 29). For both series the static magnetic field vector was incremented in $N_{tot} = 101$ steps, following Eq. 7.1 and using maximum field components of $[B_x, B_y, B_z] = [7, 9, 8]$ mT. The field was generated by the room temperature coil set (Sec. 6.2), which were also used for all remaining characterisations.

To get better signal to noise ratios the excited state was investigated by the pulsed RHS technique (Sec. 3.3) using the sequence given in Fig. 21(b). Compared to the ground state the gyromagnetic factors, and thus the Zeeman line splittings, are smaller and a single RF pulse is more likely to have sufficient bandwidth to cover a full Zeeman split hyperfine transition manifold (e.g. $|e, \pm 3/2\rangle \leftrightarrow |e, \pm 5/2\rangle$). In contrast to the previously described CW RHS experiment, an optical re-pump scheme is used to avoid population trapping in the ground state. The erase beam (Fig. 21(b)) is scanned several times over a frequency range of at least twice the sum of the greatest hyperfine transition in the ground and excited state[†]. In this way, it resonates with all possible population traps being relevant for the RHS probe beam. Using high optical power, a reasonable fraction of the (trapped) ground state pop-

[†] *E.g. at zero field in PrLaWO at minimum $2 \cdot [24.44 + 14.87 + 7.23 + 4.94] = 102.97$ MHz comp. Fig. 20.*

(a) CW RHS, ground state experiments

probe P_p ν_0

RF P_{RF} ν_2
                                                                  ν_1
              τ_s τ_s

(b) Pulsed RHS, excited state experiments

erase P_e x 15 $\nu_0 + \Delta$
                                                                  $\nu_0 - \Delta$
              τ_e

probe P_p ν_0
                          τ_p τ_{dec}

RF P_{RF} ν_{RF}
                          τ_{RF}
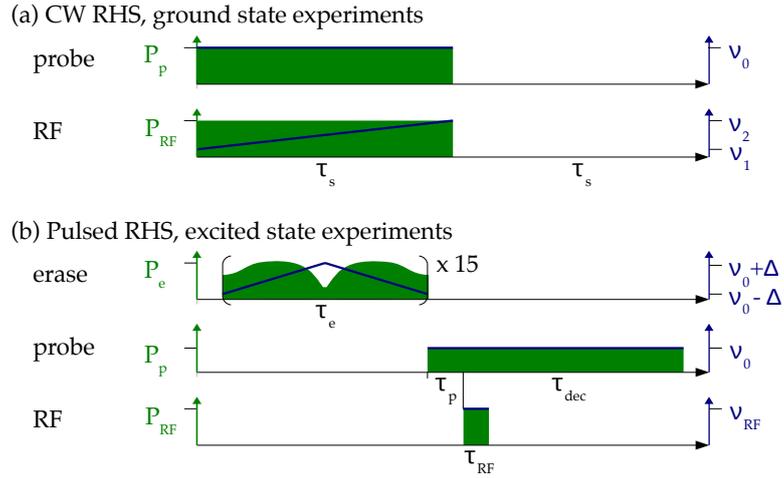
Figure 21: Used RHS pulse sequences. The blue lines indicate the frequencies and the green areas the applied optical/RF powers.
(a) A low power laser probe ($P_p = 0.3$ mW) and a scanning frequency RF ($P_{RF} \approx 1$ W, $\tau_s = 50$ ms, $\nu_1 = 7.4$ and $\nu_2 = 22.4$ MHz for $|g, \pm 1/2\rangle \leftrightarrow |g, \pm 3/2\rangle$ or respectively 17.1 and 32.1 MHz for $|g, \pm 3/2\rangle \leftrightarrow |g, \pm 5/2\rangle$) were applied to the sample for a duration τ_s and were switched off for a further τ_s to allow for relaxation. For each value of the external magnetic field the sequence was repeated 100 times to increase the SNR by accumulation.
(b) Probe and erase beam were overlapped in the sample at an angle of $0.6°$. To allow for higher repetition rate the chirped erase laser ($\Delta = 64$ MHz, $\tau_e = 10$ ms, average power $P_e \approx 20$ mW) redistributed the populations. An initial population difference between hyperfine sub levels was created by the probe beam ($P_p = 1.2$ mW, $\tau_p = 100$ μs) and was converted to coherences by an RF pulse ($\nu_{RF} = 4.94/7.23$ MHz ($|e, \pm 1/2\rangle \leftrightarrow |e, \pm 3/2\rangle$ resp. $|e, \pm 3/2\rangle \leftrightarrow |e, \pm 5/2\rangle$), $P_{RF} = 214/287$ W, $\tau_{RF} = 4$ μs). For optical heterodyne detection the same probe beam was left active for an additional time τ_{dec}. The signal was accumulated for 100 cycles of the whole sequence.

ulation is excited by each scan. Cycling the scan on a time base τ_e with $T_1^{opt} < \tau_e \ll T_1^{HF}$, the optical relaxation redistributes all ions in the ground state to some constant quasi equilibrium level in the centre of the optical scan. The optimum temperature of the cold finger, with respect to signal amplitude for this scheme, was $T = 2.4$ K. To achieve high Rabi frequencies, and thus high effective bandwidths for the RF pulses, single resonance tuned circuits (see Sec. 5.1.1) have been used. However, the limited RF pulse bandwidth of the order of 250 kHz required the measurement of the hyperfine transition manifolds in two separate experiments. For each series spectra for $N_{tot} = 251$ orientations of the static magnetic vector field have been recorded, but with maximum field amplitudes of $B_{x,y,z} = 6.5$ mT[†].

To compensate for small magnetic background fields the effect of destructive site-interference [111] for the RHS signal at real zero field was utilised. The small compensation field reduced the RHS signal amplitude to less than 10% compared to the normal situation with zero coil currents. The control software used the compensation field for the subsequent data acquisition.

† In early experiments the software limited the field components to 6.5 mT for saftey reasons.

Between the excited and ground state measurements, the crystal was remounted on the sample holder, following the same procedure as described above. This should be considered when comparing the results and crystal alignment errors.

Fitting Constrains and Best Results

The fitting procedure described in Sec. 7.3 was developed, and in later stages, tuned using the PrLaWO RHS data as a prototype. Thus, the exemplary parameter bounds given in section 7.3 already apply for PrLaWO. Explicitly for D and E the published values from hole burning [55] were used to define the centre of the search region, the latter being constrained to ± 10 % of their value. In early stages the gyromagnetic factors were unknown and the initial values were set to $g_{\alpha'} = 100$ MHz/T for the ground state and $g_{\alpha'} = 50$ MHz/T for the excited state, restricting the search extend to ± 100 % of these values. In later stages, after several fit trials starting from random parameters converged to the final values given in table 1, those final values, again generally constrained to ± 100 % , were used for refinement fits or further tuning/analysis of the general fitting procedure. The same applies for the search extents and start values for the tensor angles. In the beginning all angles were set to random values out of the full Euler angle definition range, without restricting the search region further. Later the values from table 1 were used and constrained to $\pm 50°$ for all angles. In the final stages the $(\alpha/\beta)_{C_2}$ angle were restricted further to $\pm 10°$. Using $k_{max} = 2 \cdot 10^6$ maximum iterations for the simulated annealing, the less and the more constrained initial conditions described above lead to the same global minimum, given in table 1. Nevertheless, the parameters of the more constrained searches had smaller deviations from the values in the table, before the pattern search was activated. Furthermore, the alternative least squares based objective function (f_k^{LSQ}, see Eq. 7.15) typically did not tend to converge so regularly in a local minimum[†].

As indicated above, table 1 lists the best fitting spin Hamiltonian parameters found for PrLaWO. Figure 22 shows the collected RHS data for PrLaWO and the calculated line positions following from the parameters in table 1. From the total 1221 identified (Sec. 7.3.1) ground state RHS lines $L_g = 1218$ could be unambiguously mapped (Sec. 7.3.2, 1616 theoretical lines). The best fit parameters lead to a $f_{best}^{RMS} = 32.3$ kHz deviation between calculated and measured lines. This residual deviation is 6 times smaller that the average ground state RHS line width (see Sec. 29), thus all predicted lines are within the observed line widths and close to their centre. Furthermore the RMS deviations $f^{RMS}(N)$ for the individual spectra (see Fig. 22(b)) do not show significant systematic shifts, with respect to the mean value f_{best}^{RMS} of all spectra. Both findings indicate that the residual deviation is dominated by statistical error.

A similar situation is found for the excited state. Using the best fit parameters $L_e = 2345$, experimental lines could be uniquely mapped to theoretical lines. The total number of identified lines was 2353 (4016 theoretical lines). The fit has a residual deviation of $f_{best}^{RMS} = 3.1$ kHz which, in comparison to the mean excited state RHS line width of 22.3 kHz, represents an even better overlap between calculated and observed lines than in the ground state case. Whereas the RMS deviations of the

[†]*Especially for PrLaWO there exists one particular local minimum with a deviation of $1.14 \cdot f_{best}^{RMS}$. It has similar $D/E/g_{\alpha'}$ values but incompatible angles $\alpha_{C_2} = 2.2°$ and $\beta_{C_2} = 33.0°$.*

(a) Excited state
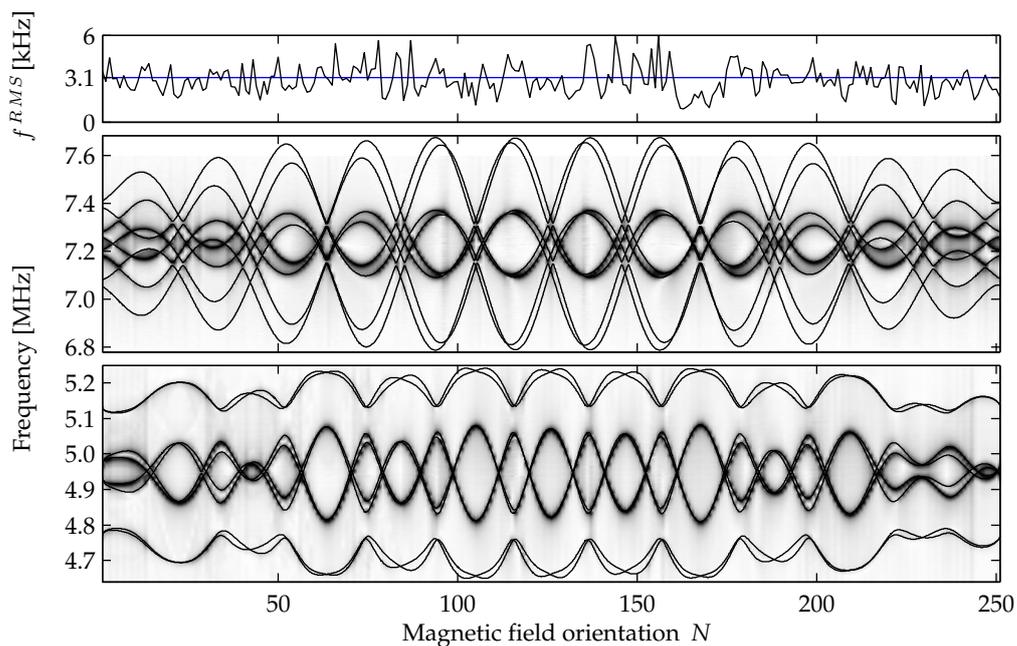
(b) Ground state
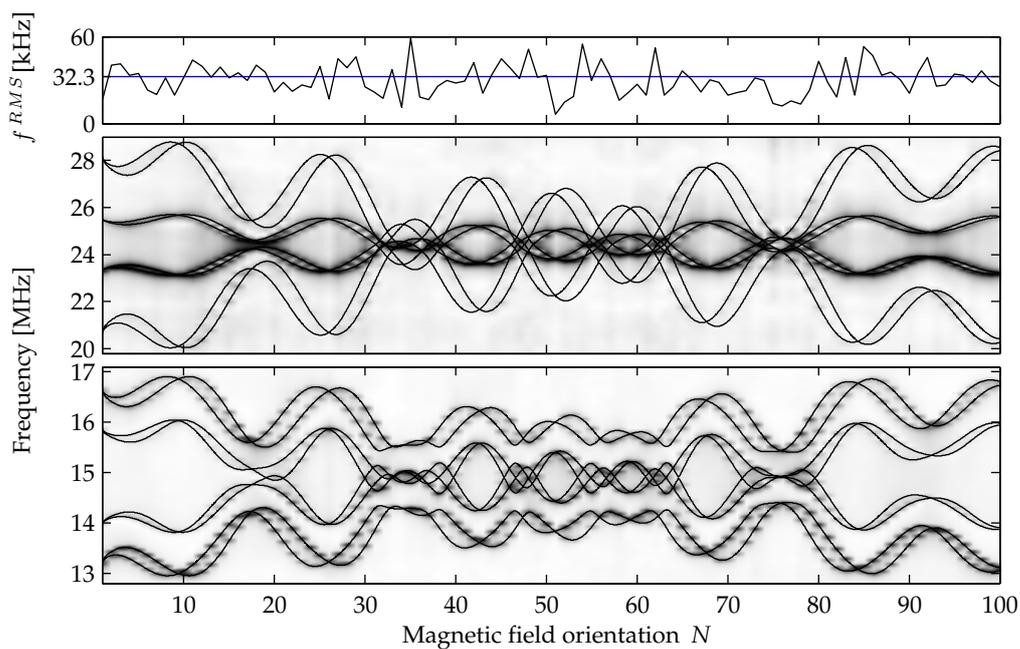
Figure 22: PrLaWO RHS data overlaid with fit. The RHS data are shown as a grayscale coded intensity plot. The maximum amplitude for each individual spectrum (indexed by N) was normalised to one, in order to obtain a uniform contrast over all orientations. The calculated line positions (using Tab. 1 and Eq. 7.2 and 7.5) are given by the overlaid black lines. For both, (a) the excited state and (b) the ground state data, additionally the RMS deviations f^{RMS} for the N individual orientations are plotted (black line in (a/b) top row plots). The blue horizontal lines indicate the mean value (see Tab. 1) of the deviations.

	ground state			excited state		
	value	$\sigma_{\nu_\sigma^{SNR}}$	$\sigma_{\nu_\sigma^{STD}}$	value	$\sigma_{\nu_\sigma^{SNR}}$	$\sigma_{\nu_\sigma^{STD}}$
D	-6.3114	0.42 ‰	0.12 ‰	1.90705	0.12 ‰	0.02 ‰
E	-0.8915	2.4 ‰	0.79 ‰	0.35665	0.40 ‰	0.09 ‰
α_Q	20.4	3.3	0.6	-18.51	0.71	0.11
β_Q	147.7	1.4	0.2	73.83	0.48	0.07
γ_Q	10.2	1.4	0.3	-84.22	0.37	0.06
g_x	-51.7	7.0 %	2.3 %	-17.22	1.5 %	0.2 %
g_y	-23.5	4.7 %	1.6 %	-14.39	0.68 %	0.13 %
g_z	-146.97	0.51 %	0.20 %	-18.37	0.75 %	0.11 %
α_M	30.1	3.8	0.8	-23.7	2.4	0.61
β_M	146.59	0.55	0.09	88.5	4.1	0.72
γ_M	13.09	0.69	0.12	80.1	1.8	0.32
α_{C_2}	88.34	0.47	0.10	88.63	0.25	0.04
β_{C_2}	92.45	0.31	0.06	92.69	0.24	0.04
f_{best}^{RMS}	32.3	2.1	0.3	3.089	0.358	0.004

Table 1: PrLaWO best fit parameters and fit errors. D and E are given in MHz, the $g_{\alpha'}$ values in MHz/T, all angles in degrees and the resulting RMS deviation f_{best}^{RMS} is given in kHz. For D, E and the $g_{\alpha'}$ the errors are given in relative units. The errors are defined by the 1σ-widths of Gaussians fitted to the histograms of the accepted parameter trials, resulting from $2 \cdot 10^6$ simulated annealing iterations with a fixed temperature level of $k_{\sigma_\iota} T_{\sigma_\iota} = \nu_\sigma^{SNR}$ for the $1\sigma_{\nu_\sigma^{SNR}}$ error and $k_{\sigma_\iota} T_{\sigma_\iota} = \nu_\sigma^{STD}$ for the $1\sigma_{\nu_\sigma^{STD}}$ error respectively. Form the ground state spectra $\nu_\sigma^{SNR} = 1.4$ kHz was found and subsequently yielded $\nu_\sigma^{STD} = 0.04$ kHz (see Sec. 7.3.4). For the excited state $\nu_\sigma^{SNR} = 136$ Hz and $\nu_\sigma^{STD} = 3$ Hz were found. For all fit parameters the source histograms showed Gaussian shape and were centred around the best fit parameter value. The errors in the f_{best}^{RMS} row correspond to the width of the RMS deviation histograms.

individual spectra are again symmetrically distributed around their mean, now in the centre of the N-range an accumulation of spectra with slightly higher deviation from the mean level (see Fig. 22(a)) seems to exist. Compared to the total spread of $f^{RMS}(N)$ values this effect seems to be barely significant, but may be an indication of a slightly higher calibration error for the x and/or y axis static magnetic field compared to the z component, which in contrast has its maximal amplitude at extremal values of N. This effect might be more visible in the excited state, since the pulsed RHS spectra are of higher quality and the RHS line widths are smaller in relation to the state's $g_{\alpha'}$ values. Furthermore, the $\hat{M}$ tensor of the excited state is almost isotropic, yielding an almost constant maximum Zeeman splitting in all spatial directions. The ground state $\hat{M}$ tensor is anisotropic, with a large projection component along the LAS z-axis, but smaller ones along y and x (in this order). Because of the latter, the ground state $f^{RMS}(N)$ graph is less sensitive to the assumed calibration error.

Referring to the estimates of the fit errors given in table 1, the uncertainty arising from the calibration error of the magnetic vector field is of similar magnitude as the statistical error for the $g_{\alpha'}$'s ($1\sigma_{\nu_\sigma^{STD}}$). In

general the ground state parameters, but especially the g-factors, show a lower sensitivity to changes in the line positions than compared to the excited state. This again can be accounted to the better quality of the excited state spectra. Nevertheless, the larger inhomogeneous broadening of ground state RHS lines and a potentially connected greater inhomogeneous distribution of the Hamiltonian parameters themselves (see. Sec. 7.4.4) may also be a reason for the larger uncertainties.

The general alignment actually reached and realignment precision seems to be approximately $3°$ and $0.5°$ respectively. This can be inferred from the comparison of the fit results for the C_2/b axis orientation of the excited and ground state, pointing out that the sample was remounted completely between those RHS measurements.

For the discussion of the tensor properties, the first thing to note is that the $\hat{Q}$ and $\hat{M}$ tensors of the ground state are more anisotropic than those of the excited state. While for the quadrupolar tensors the asymmetry parameters $\eta_g \approx 0.42$ and $\eta_e \approx 0.56$ are relatively similar, the situation for Zeeman tensors is different. The ground state Zeeman tensor has relatively similar $g_{x'}$ and $g_{y'}$ but a 400% larger $g_{z'}$ principal value. In contrast, the excited state Zeeman tensor is almost isotropic, consisting of principal values differing only by about 20 %. Due to the lack symmetry (C_1) for the Pr site in LaWO, a useful visualisation of the tensor orientations is not as straight forward as e.g. in PrYAP (see Sec. 7.4.2 on page 7.4.2). Crystal field calculations [56] approximating the PrLaWO tensor parameters by assuming a higher symmetry (C_{2v} orthorhombic) give essentially similar tensor principal values as found experimentally. At the same time these calculations in C_{2v} symmetry also predict that the $\hat{Q}$ tensors of different crystal field levels are collinear, which contradicts the experimental results for the actual symmetry of C_1 [97]. The relative tensor orientations between ground and excited state determine the nuclear overlap integrals, and thus the relative optical oscillator strengths[100]. For the latter experimental data from zero field spectral tailoring experiments exists for PrLaWO [55]. By comparing the calculated overlap integrals following from Tab. 1 with this data, a verification of at least the relative $\hat{Q}$ tensor orientations is possible. Table 2 shows the comparison of the values, using the site 1 data of Tab. 1 for both electronic states. The calculated relative oscillator strengths are in almost prefect agreement with experimental values, which greatly supports the tensor orientations by the hyperfine characterisation.

7.4.2 PrYAP

Motivation

As with many REIC in early days, the main interest in studying PrYAP was the search for efficient laser host materials. Using low doping levels, PrYAP was studied in-depth using high resolution spectroscopy techniques [101, 39, 40, 161], also revealing new non-specific properties like the Raman heterodyne interference effect [110, 111]. Due to its favourable and well studied hyperfine and coherent properties, PrYAP developed to a testbed system for the development of several high resolution magneto-optical techniques [15, 16, 18, 81, 82, 79, 80]. Besides the technological demonstration, the latter further refined the hyperfine parameters. The sign of the quadrupole parameter, $D < 0$ [16, 78], was

The actual angles between the C_2 and the LAS axes are: ground state
$C_{2x}=(88.4 \pm 0.1)°$
$C_{2y}=(3.0 \pm 0.1)°$
$C_{2z}=(87.6 \pm 0.1)°$
excited state
$C_{2x}=(88.6 \pm 0.1)°$
$C_{2y}=(3.0 \pm 0.1)°$
$C_{2z}=(87.3 \pm 0.1)°$

Actual angles between ground and excited state site 1 $\hat{Q} \setminus \hat{M}$-principal axes:
$Q_x=(50.2 \pm 0.4)°$
$Q_y=(86.1 \pm 0.5)°$
$Q_z=(74.0 \pm 0.2)°$
$M_x=(43.5 \pm 0.8)°$
$M_y=(77.4 \pm 0.6)°$
$M_z=(87.0 \pm 0.6)°$

PrLaWO	$\lvert e, \pm\frac{1}{2} \rangle$	$\lvert e, \pm\frac{3}{2} \rangle$	$\lvert e, \pm\frac{5}{2} \rangle$	
$\lvert g, \pm\frac{1}{2} \rangle$	0.09 ± 0.01	0.28 ± 0.01	0.63 ± 0.01	(exp.)
	0.084 ± 0.002	0.244 ± 0.003	0.672 ± 0.004	(calc.)
$\lvert g, \pm\frac{3}{2} \rangle$	0.33 ± 0.01	0.39 ± 0.01	0.28 ± 0.02	(exp.)
	0.311 ± 0.003	0.448 ± 0.003	0.241 ± 0.003	(calc.)
$\lvert g, \pm\frac{5}{2} \rangle$	0.55 ± 0.01	0.36 ± 0.01	0.09 ± 0.01	(exp.)
	0.605 ± 0.003	0.308 ± 0.002	0.087 ± 0.001	(calc.)

Table 2: Relative oscillator strengths for PrLaWO. The calculated values are derived from Tab. 1 (calc., site 1 for both states) and are compared to the values gained from spectral tailoring experiments (exp.) [55]. Rows correspond to transitions starting from the ground state hyperfine levels and columns correspond to transitions to different excited state hyperfine levels.

determined. Furthermore, the angle between the PAS z-axes of the excited and the ground state was corrected to $\alpha_0 \approx 42°$ [82]; different values have been published previously [161, 111, 109, 112, 17]. Nevertheless, all former studies used the approximation that the PAS of the pure quadrupole Hamiltonian coincides with that of the pseudo-quadrupolar Hamiltonian, such that the $\hat{Q}$ and $\hat{M}$ tensors are aligned. This is a good approximation for the ground state of PrYAP, nevertheless this is not the case for the excited state [161]. The more general Hamiltonian model used here (Sec. 7.2) resolves the specific orientations of the $\hat{Q}$ and $\hat{M}$ tensor PAS independently.

Crystal Structure and Sample

$YAlO_3$ has a perovskite like crystal structure of space group D_{2h}^{16} [49, 35]. Its orthorhombic unit cell, shown in figure 23, has the dimensions $a = 5.330(2)$ Å, $b = 7.375(2)$ Å and $c = 5.180(2)$ Å [35][†] and contains four Y-positions. The latter show a C_{1h} point symmetry [39] and two of the Y can be grouped to a pair subjected to the same crystal field. In figure 23 the two distinct Pr/Y-sites are given by the two upper and two lower Y-positions (blue) [78]. Both sites can be converted into each other by a translation in the bc-plane and a subsequent mirroring at the same plane. Considering the impact of this symmetry on the Raman heterodyne frequencies for each site, both sites are equivalent up to a C_2 rotation around the crystal b-axis [110]. Thus, as in the case of the PrLaWO characterisation, the orientation of the crystal b-axis with respect to the laboratory axis system will be given by the α_{C_2} and β_{C2} angles.

The Pr doping level of the sample was 0.1 at. %. The 5x5x1 mm crystal was mounted such that its thinnest dimension was aligned with the LAS z-axis. The other surfaces being aligned with the LAS x- and y-axes. For the mounting precision and procedure the same applies as in the case of PrLaWO (see page 64). Figure 24 summarises the energy level structure and the main relevant properties for PrYAP.

[†]*The dimensions are given in Pnma notation.*
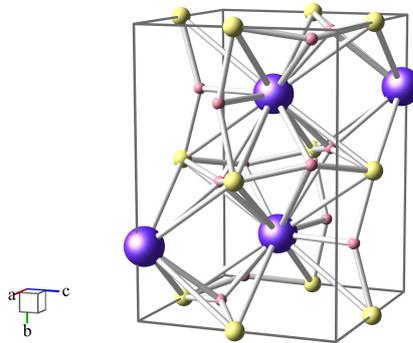
Figure 23: YAP unit cell (grey bound box). The yttrium positions are in blue colour, the aluminium ions in green and the oxygen in pink. (The figure was created using the program Balls & Sticks and the data from Ref. [49, 35])
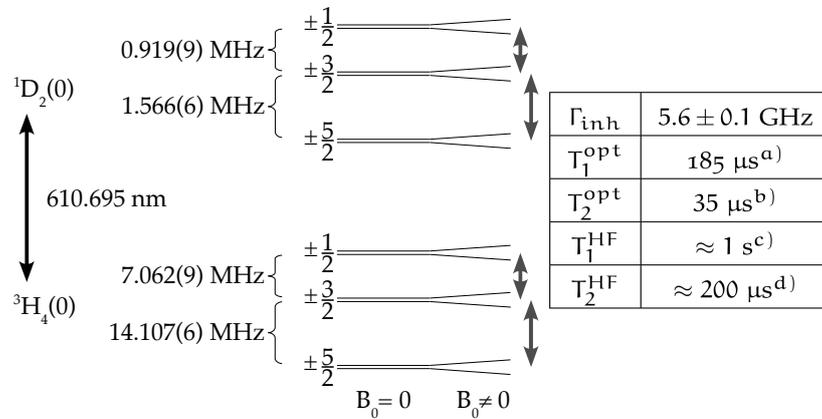

Figure 24: PrYAP level structure. The quoted zero field hyperfine transition frequencies follow from the characterisation result given in Tab. 3. The order of the $^3H_4$ state hyperfine levels follows from [16], the order for the excited state from [18, 78]. Γ_{inh} is given as a measured value for this particular sample, whereas the relaxation times ($B = 0$) are taken from literature (a) [39], b) [101], c) [113, 81], d) [41]), but fit with those measured (not shown) during this thesis. The grey arrows on the right indicate the hyperfine transition manifolds addressed during the single RHS experiments.

Hyperfine Characterisation

As in the case of PrLaWO, the PrYAP ground state hyperfine spectra were measured using the CW Raman heterodyne technique, and for the excite state, pulsed RHS spectra were acquired. To account for the different signal strengths from the different hyperfine manifolds and the limited excitation bandwidth in the pulsed case, four separate experiments for the different frequency ranges, indicated in Fig. 24, were performed. Population trapping in the ground state can be avoided by using a repetition rate lower than approximately 2 per second, since T_1^{HF} for PrYAP is sufficiently short. Thus the main differences in the pulse sequences used, compared to that used for PrLaWO (Fig. 21), were the different resonant RF frequencies and the fact that no erase beam was used. All other parameters were subjected to minor changes only [51]. For the ground state spectra $N_{tot} = 151$ field orientations with maximum magnitudes of $[B_x, B_y, B_z] = [9.5, 11, 10.5]$ mT (using Eq. 49) were measured. For the excited state $N_{tot} = 101$ and $[B_x, B_y, B_z] = [6.5, 6.5, 6.5]$ mT were used.

As mentioned before, this source data sets have recently been analysed and discussed by Glasenapp [51], but are subject of this thesis also. The best fit results shown in table 3 are the result of an unique RHS line identification (Sec. 7.3.1) and fitting. As some of the lines have to be picked manually, this causes minor changes on the parameter values compared to Ref. [51], but also checks the general robustness of the data processing procedure. Furthermore, the analysis shown here adapts to more common conventions for the Euler angles.

For the ground state, 1599 of the 1607 identified lines (2416 theoretical lines are possible) were finally considered by the line mapping. In the excited state 1153 of 1168 lines contributed (1616 theoretical lines). The best fit RMS deviations achieved for both electronic states of PrYAP, are well below the observed inhomogeneous hyperfine line widths, yielding mean-width/f_{best}^{RMS} ratios of about 7 and 10 for the ground and excited state respectively (see Fig. 30) . The calculated transitions fit decently over the whole range of measured magnetic fields, as can be seen in figure 25, showing the data and the superimposed fit.

The individual deviations for all field orientations are centred around the mean deviation and do not show a significant preference for any particular direction, indicating that the residual deviation is dominated by statistical error. Nevertheless, looking closely at some particular field indexes (e.g. $N = 76$ in Fig. 25(a)), there might be indications of small deviations. Those can be explained by overlapping lines close to the zero-field hyperfine transition frequency, some systematic effect due to not-well resolved, or not precisely picked, overlapping line positions or problems arising from an unwanted residual magnetic field. The latter effect may be expected to be more significant in the case of PrYAP, as here attempts to achieve better zero-field destructive interference by usage of a compensation field [51] were not as successful as in the PrLaWO experiments. Some decrease of RHS signal amplitude due to interference could be observed by tuning the field, but the effect was not comparable to the situation in PrLaWO. The same was observed for the PrYSO experiments, which may indicate a connection between the ease of finding a good interference/compensation-field with the inhomogeneous RHS line width, since PrYAP and especially PrYSO show much narrower RHS lines than PrLaWO (see. Sec. 7.4.4).

(a) Excited state
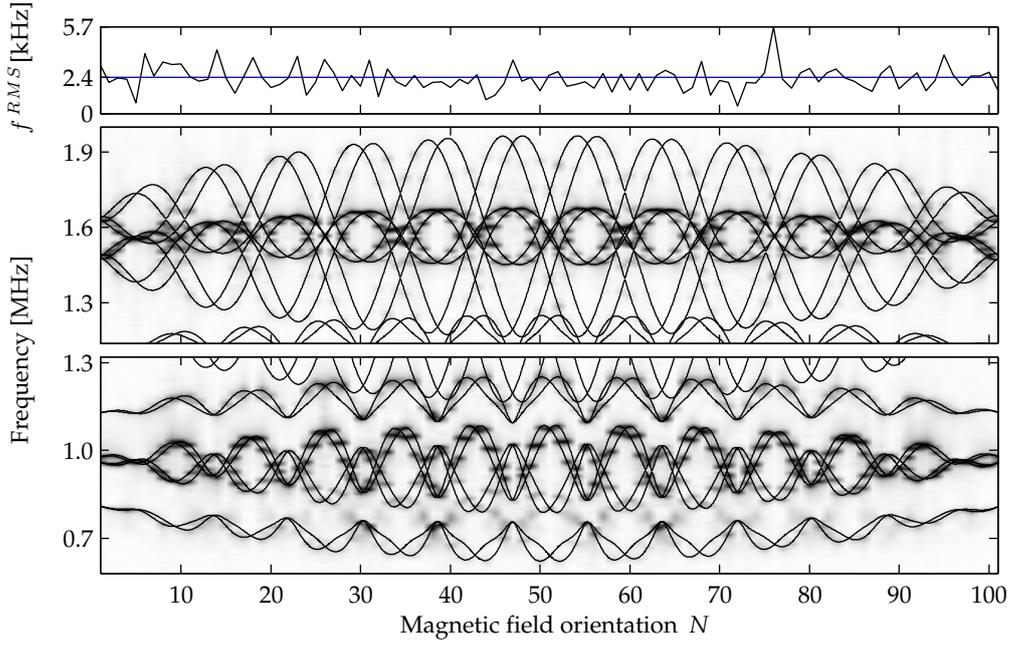
(b) Ground state
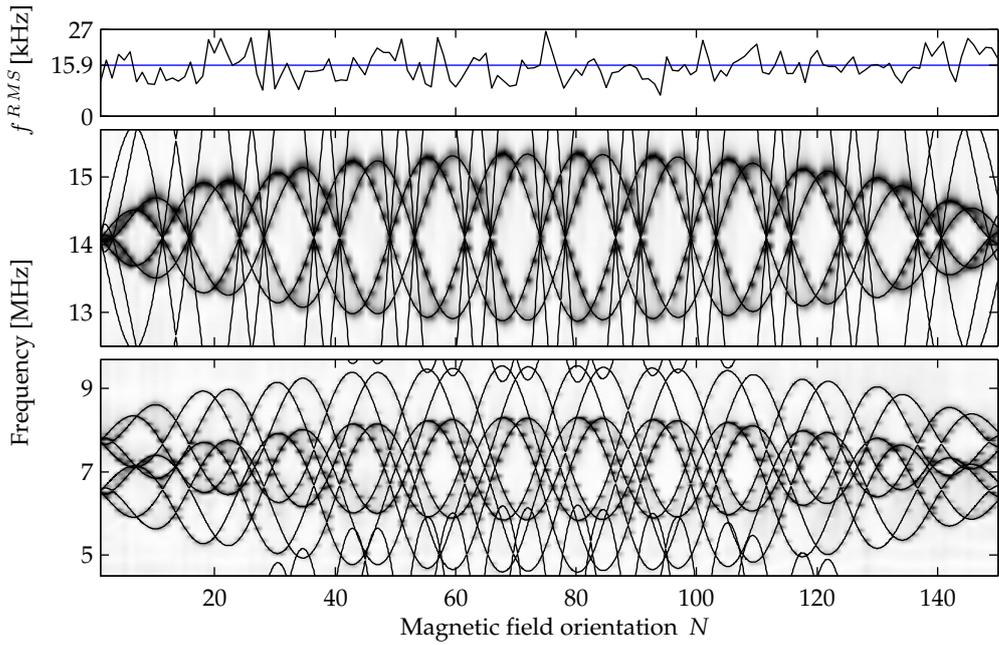
Figure 25: PrYAP RHS data overlaid with fit. The RHS data for the excited state (a) and the ground state (b), covering the range where lines have been identified, are shown as a grayscale coded intensity plot. The maximum amplitude for each individual spectrum (indexed by N) was normalised to one in order to obtain a uniform contrast over all orientations. The calculated line positions (using Tab. 3 and Eq. 7.2 and 7.5) are given by the overlaid black lines. Additionally the RMS deviations f^{RMS} for the N individual orientations are plotted (black line in (a/b) top row plots). The blue horizontal lines indicate the mean value (see Tab. 3) of the deviations.

	ground state			excited state		
	value	$\sigma_{\nu_\sigma^{SNR}}$	$\sigma_{\nu_\sigma^{STD}}$	value	$\sigma_{\nu_\sigma^{SNR}}$	$\sigma_{\nu_\sigma^{STD}}$
D	-3.5276	0.6 ‰	0.1 ‰	-0.40211	1.3 ‰	0.2 ‰
E	-0.037	54 %	6 %	-0.050463	11.2 ‰	0.4 ‰
α_Q	-88	17	3	1.6	1.0	0.2
β_Q	88.49	0.37	0.07	89.24	0.54	0.08
γ_Q	118.55	0.56	0.09	99.82	0.39	0.08
g_x	36.99	3.4 %	0.5 %	16.769	3.97 %	0.04 %
g_y	25.6	5.8 %	0.9 %	13.06	2.1 %	0.4 %
g_z	117.59	0.61 %	0.10 %	18.475	1.32 %	0.04 %
α_M	1.9	2.7	0.5	1.3238	2.5207	0.0003
β_M	88.33	0..25	0.04	86.58	5.34	0.01
γ_M	122.36	0.26	0.04	146.12	1.11	0..03
α_{C_2}	2.18	0.17	0.03	1.85	0.27	0.06
β_{C_2}	88.00	0.27	0.05	88.3	0.6	0.1
f_{best}^{RMS}	15.90	0.78	0.02	2.381	0.351	0.009

Table 3: Best fit parameters and fit errors for PrYAP. D and E are given in MHz, the $g_{\alpha'}$ values in MHz/T, all angles in degrees and the resulting RMS deviation f_{best}^{RMS} is given in kHz. For D, E and the $g_{\alpha'}$ the errors are given in relative units. The error estimation was done in the same way as for the values given in table 1. For the ground state spectra $\nu_\sigma^{SNR} = 545$ kHz was found and subsequently yielded $\nu_\sigma^{STD} = 13$ Hz. For the excited state $\nu_\sigma^{SNR} = 248$ Hz and $\nu_\sigma^{STD} = 8$ Hz were found. For all fit parameters the source histograms had Gaussian shape and were centred around the best fit parameter value. The errors in the f_{best}^{RMS} row correspond to the width of the RMS deviation histograms. Note: To describe the same physical Pr-site, (e.g.) the site 1 data of the table for the ground state and the site 2 data of the table for the excited state have to be used in conjunction (see text).

Looking at the individual parameter errors, E and α_Q for the ground state particularly stand out. Since E is very small it is difficult to determine it, which also indirectly implies that this parameter is not too critical for the deviation. The same also holds true for α_Q. In the following discussion all parameter errors will be propagated and it will become evident, that even though these two parameters have large relative errors, their contribution to the total error of the orientations is relatively small.

Comparison to Previous Studies

The relative optical transition matrix elements have implications on virtually all optical experiments in REIC systems [17]. The size of the overlap integrals between the ground and excited state nuclear wave functions, which determine the transition matrix elements, depends on the relative orientations of the ground and excited state tensor PAS systems. Due to the C_{1h} site symmetry in PrYAP, the quadrupolar and Zeeman tensors of the ground and excited state share a common quantisation axis [161], which is the crystal c-axis. This implies that the tensors' principal z-axes lie in the crystal a-b plane. In this case, knowledge of the relative angle between the $\hat{Q}$ PAS z-axes of the ground and

$$\alpha_{C2/x} = (\ 2.96 \pm 0.04)$$
$$\alpha_{C2/y} = (87.82 \pm 0.03)$$
$$\alpha_{C2/z} = (88.00 \pm 0.05)$$
$$\alpha_{gQ1} = (59.24 \pm 0.10)$$
$$\alpha_{eQ2} = (78.31 \pm 0.10)$$
$$\alpha_{gM1} = (55.43 \pm 0.05)$$
$$\alpha_{eM2} = (32.04 \pm 0.06)$$
$$\alpha_{gQM} = (\ 3.81 \pm 0.10)$$
$$\alpha_{eQM} = (46.35 \pm 0.08)$$
$$\alpha_{Q} = (42.12 \pm 0.17)$$
$$\alpha_{M} = (87.77 \pm 0.12)$$
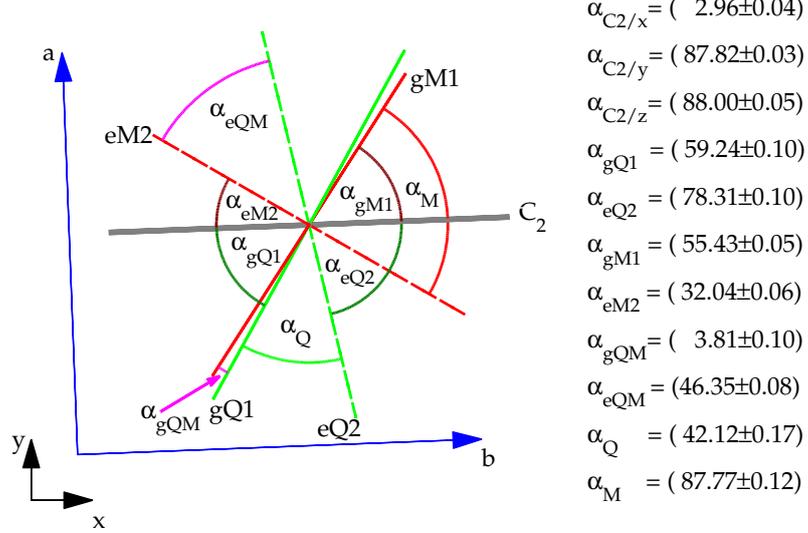
Figure 26: Orientation of the PrYAP quadrupole and Zeeman principal axes. The LAS x-y plane is given by the black and the crystal a-b plane by the blue arrows ($C_2 \parallel b$). The green lines show the z-axis of quadrupole tensors (gQ1, eQ2) and the red lines show the z-axes of the corresponding Zeeman tensors (gM1, eM2). The angles between the C_2 axis and the LAS axes (e.g., $\alpha_{C2/x}$) are only given in the figure legend, the other relevant angles are drawn in the figure: The angles between the drawn axes and the C_2 axis (α_{gQ1}, α_{eQ2}, α_{gM1}, α_{eM2}), relative angles between the $\hat{Q}$ and $\hat{M}$ z-axes within one state (α_{gQM} and α_{eQM}) and the mixing angles between the ground and excited $\hat{Q}$ and $\hat{M}$ tensor z-axes (α_Q and α_M). The angles for site 1 follow from Tab. 3 and Eq. (7.3)-(7.4) and site 2 additionally incorporates the C_2-transformation (Eq. (7.5)). Errors follow from propagation of the $\sigma_{\nu_\sigma^{STD}}$ errors.

excited state is sufficient to determine the overlap integrals [111, 100, 82]. Figure 26 shows the orientation of the principal z-axes for the quadrupole and Zeeman tensors following from the hyperfine characterisation results (Tab. 3). As discussed before the RHS signal is insensitive to the signs of the quadrupolar and the Zeeman interaction (Sec. 7.2.1), thus in the figure the directions of the axes have been omitted and the quoted angles are the smallest between them. Furthermore, the RHS scheme does not correlate a given physical Pr site from the ground state with one specific of the excited state[18]. Likewise, the fitting itself is insensitive to the assignment of the sites. The lines representing site 1 of one fit can become site 2 in a second run without affecting the resulting RMS deviation. Thus, two possible assignments for the ground to excited state sites are possible: g1/e2 or g2/e1. The relative angles between $\hat{Q}$ PAS z-axes of the ground and excited state that follow from this study are: $\alpha_Q(gQ1/eQ1) = (18.8 \pm 0.1)°$ and $\alpha_Q(gQ1/eQ2) = (42.1 \pm 0.2)°$.[†] The latest related studies, using coherent Raman beats and high resolution hole burning spectra of the excited state, showed that the most probable angle between the ground and excited state $\hat{Q}$ tensor z-axes is $\alpha_Q = (47 \pm 5)°$ [17] or, respectively, $\alpha_Q = (42 \pm 1)°$ [82]. This clearly determines the site assignment for the given fit-results (Tab. 3) to g1/e2 (and g2/e1), strongly supports the characterisation result and further

[†] *Slight deviations compared to Ref. [51] follow from the independent data analysis, the errors were being calculated with a preliminary routine and from Ref. [51] using only the angle's error for propagation.*

PrYAP	$\left|e,\pm\frac{1}{2}\right\rangle$	$\left|e,\pm\frac{3}{2}\right\rangle$	$\left|e,\pm\frac{5}{2}\right\rangle$	
$\left|g,\pm\frac{1}{2}\right\rangle$	0.244 ± 0.014	0.648 ± 0.005	0.109 ± 0.009	(calc.)
	0.239	0.647	0.114	(lit.)
$\left|g,\pm\frac{3}{2}\right\rangle$	0.541 ± 0.003	0.038 ± 0.009	0.421 ± 0.006	(calc.)
	0.549	0.003	0.417	(lit.)
$\left|g,\pm\frac{5}{2}\right\rangle$	0.215 ± 0.012	0.314 ± 0.004	0.471 ± 0.015	(calc.)
	0.212	0.319	0.469	(lit.)

Table 4: Relative oscillator strengths for PrYAP. The calculated values are derived from Tab. 3 (calc., site 1 values for the ground state and site 2 values for the excited state) and are compared to the latest published values (lit.) [82]. Rows correspond to transitions starting from the ground state hyperfine levels and columns correspond to transitions to different excited state hyperfine levels.

resolves the controversy in some of the previously published values ([161, 111] vs. [109, 112, 17, 82]). To conclude, the zero field relative oscillator strengths following from the hyperfine characterisation and the g1/e2 site assignment are compared to the published oscillator strengths by Klieber et al. [82]. Table 4 shows the results, which are in very good agreement.

All previously mentioned quantitative studies on the hyperfine Hamiltonian tensor orientation in PrYAP use a simplified model. In this the pseudo-quadrupole (x',y',z') and pure-quadrupole (x'',y'',z'') tensors PAS are considered to coincide, which approximately is the case if $D_{pQ} \gg P$. As the quadrupolar tenors are of the same form (see Sec. 2.1), they are formally merged and thus treated in a third PAS (x''',y''',z'''). Since the enhanced nuclear Zeeman interaction, respectively the $\hat{M}$ tensor PAS, is given by the pseudo-quadrupole axes (x',y',z') (Eq. 2.10) the simplified model assumes that the PAS axes of the $\hat{M}$ and $\hat{Q}$ tensors coincide. The hyperfine characterisation justifies this approximation for the ground state of PrYAP, since the observed angles between the $\hat{M}$ and $\hat{Q}$ z-axes and the b/C2 axis, $\alpha_{gM1} = (55.4 \pm 0.1)^{\circ\dagger}$ and $\alpha_{gQ1} = (59.2 \pm 0.1)^{\circ}$, correspond to those published for the simplified model $\approx 56.4^{\circ}$ [39, 40, 110, 111]. The small deviation can be attributed to the more general spin Hamiltonian model, resolving non-coincident $\hat{M}$ and $\hat{Q}$ tensor configurations. Whereas the angle between the principal axes of $\hat{M}$ and $\hat{Q}$ in the ground state $\alpha_{gQM} = (3.8 \pm 0.1)^{\circ}$ is small, and the tensors are approximately collinear in z, the situation in the excited state is different: $\alpha_{eQM} = (46.4 \pm 0.1)^{\circ\dagger\dagger}$. This measures for the first time the known violation [161] of the simplified model quantitatively. Thus, the previously published values for the angle between the excited state quadrupole tensor z-axis and the b/C_2 axis of $\approx 82^{\circ}$ [110, 111, 82] shows a greater deviation with respect to the results presented here $\alpha_{eQ2} = (78.3 \pm 0.1)^{\circ}$, since the corresponding angle for the Zeeman tensor z-axis was resolved $\alpha_{eM2} = (32.0 \pm 0.1)^{\circ\dagger\dagger\dagger}$ and differs significantly from α_{eQ2}. The fit routine *FitRotplot.m* also supports the simplified model with $\hat{Q}$ and $\hat{M}$ being forced to have the same PAS.†††† Using the $\hat{Q}$ parameters of Tab. 3 and the simplified model led to a RMS

†*Due to the site symmetry negative signs follow for the other site, e.g.* $\alpha_{gM2} \overset{C_2}{=} -\alpha_{gM1}$.

††g_z *of the excited state is only* $10 - 30\%$ *bigger than the* $g_{x/y}$ *values. The angles between* $\hat{Q}$-z *and* $\hat{M}$-x/y *axes are* $(90.6 \pm 0.1)^{\circ}$ *and* $(43.7 \pm 0.1)^{\circ}$.

†††*The corresponding* C_2 *vs.* $\hat{M}$-x/y *axes angles are* $(91.9 \pm 0.1)^{\circ}$ *and* $(58.0 \pm 0.1)^{\circ}$.

†††† *Specify the FitRotplot.m option "symQZ" instead of default "sym".*

deviation of 69 kHz for the ground state and 27 kHz for the excited state RHS data, without further fitting. A fit using the simplified model results in RMS deviations of, at best, 23 kHz for the ground state and 13 kHz for the excited state. Thus, the simplified model leads to a 145 % increase of the ground state RMS deviation and respectively an increase of 546 % for the exited state, both seen in relation to the best fit results of the model with non-constrained $\hat{Q}$ and $\hat{M}$ tensor orientation. This emphasises the importance of the new results, especially for the excited state of PrYAP in the case of experiments with high precision demands on the Hamiltonian.

The relative orientation of the ground and excited state Zeeman tensors reveals an other interesting feature, the angles between the x-axes is 2.8°, the y-axes 92.3° and the z-axes 87.8°. Thus, if the y and z axes, respectively the tensor PAS values of the excited state $\hat{M}$ tensor, are exchanged both Zeeman tensors would almost coincide: $\alpha(gM_x/eM_x) = (2.8 \pm 0.5)°$, $\alpha(gM_y/eM_z) = (3.4 \pm 0.4)°$ and $\alpha(gM_z/eM_y) = (2.6 \pm 0.1)°$. As discussed in section 7.2.2 such an exchange of axes is just a matter of convention and does not affect the general fit accuracy. Nevertheless, exchanging the y and z principal values of $\hat{M}$ without changing the corresponding Euler angles according to the conventions, lets the RMS deviation rise tenfold. Even though the Zeeman tensor is almost symmetric, the fitting is very sensitive to the small anisotropic contributions determined by the pseudo-quadrupole axes $\Lambda_{\alpha'\alpha'}$ ($\alpha' = x', y', z'$). Given that the Zeeman tensor for both electronic states are aligned, the angle between the quadrupolar tensors in both states is not influenced by the directions of the pseudo-quadrupole tensor in PrYAP. Anyway, the magnitude of the $\Lambda_{\alpha'\alpha'}$, the Landé g-factors g_J, the hyperfine coupling constants A_J and the pure-quadrupole tensor components $V_{\alpha''\alpha''}$ have an influence (see Sec. 2.1) and may change between the ground and excited state.

For the sake of readability the site assignment g1/e2 is now implicit, as discussed above.

7.4.3 *PrYSO*

Motivation

In recent years, praseodymium as a dopant in yttrium orthosilicate was the most commonly used REIC system for investigations in the field of quantum information processing. The list of achieved milestones using PrYSO is long and includes conditional phase gates [94], single qubit arbitrary rotation [132], development [122, 121] and test of efficient multimode quantum memories protocols [69, 66, 5]. The success of this compound is mainly based on the fact that it pairs strong optical transitions with very long coherence lifetimes [38]. Especially the good coherence times, attributed to the low magnetic moment density of YSO [164, 37], made the sample interesting for memory applications. For all types of experiments performed within this thesis, PrYSO gave superior signals compared to the systems PrYAP and PrLaWO.

Longdell et al. [93] were the first to use RHS spectra and simulated annealing to characterise the full hyperfine Hamiltonian of an REIC. They first characterised PrYSO [93] and then europium-doped yttrium orthosilicate and europium chloride hexahydrate [96]. Their work also serves as a basis for the development of the scheme used here, with the intention to characterise the new compound PrLaWO. The work of Longdell also was the basis for the so-called ZEFOZ (zero first order

Zeeman, see also Sec. 8.2) technique [44]. The latter minimises the residual impact of host spin fluctuations in such a way that stopped light with storage times exceeding 1 second [95] and coherence times of more than 30 seconds [46] could be demonstrated in the ground state of PrYSO. Nevertheless, it proved to be non-trivial to use the published hyperfine characterisation for PrYSO from Longdell et al. [93, 92]. Furthermore, the independent selective hole burning study from Nilsson et al. [122] revealed relative optical oscillator strengths between the ground and excited state that differ significantly from those deduced by Longdell. The characterisation shown before for PrLaWO [97] yields overlap integrals in agreement with selective hole burning data [55]. Thus a refinement of the PrYSO characterisation and a test on the observed relative oscillator strengths is the aim of this section.

Crystal Structure and Sample

Yttrium orthosilicate forms a monoclinic crystal of space group $C2/c$ (C_{2h}^6) [38], its unit cell contains eight molecules and measures $a = 14.371 \,\text{Å}$, $b = 6.71 \,\text{Å}$, $c = 10.388 \,\text{Å}$ with $\beta = 122.17°$ [29, 88]. Praseodymium can substitute two inequivalent crystallographic sites of C_1 symmetry. The ions residing in one of the particular sites have different optical transition wavelength, all experiments reported here were performed on "site 1" with $\lambda = 605.977$ nm [38]. Similarly to PrLaWO, the ions of site 1 from two magnetically inequivalent sites [93]. Those are related by a C_2 rotation, give different RHS frequencies for non-zero fields and thus will be referred to as the two distinct sites in the following.

A 10x10x10 mm sample doped with 0.05 at. % Pr was obtained from Scientific Materials Corp. [31]. For the measurements a 5x5x1 mm piece was cut out and polished. Finally the crystal was mounted with its thin dimension, the b-axis, pointing along the laser direction respectively the LAS z-axis. The D1 axis was orientated along the LAS y-axis and the D2 along the x-axis. For the mounting procedure and thus for the expected precision of the given orientations the same as in the case of PrLaWO applies (Sec. 7.4.1 on page 64).

Internal sample no. 30b.

Hyperfine Characterisation

Due to the similar coherence and population lifetimes compared to PrLaWO the same sequence (Fig. 21 on page 66) with optical and RF frequencies adopted to PrYSO (see. Fig. 27) has been used. RHS spectra were collected for $N_{tot} = 250$ field orientations with maximum magnetic field amplitudes of $[B_x, B_y, B_z] = [9.5, 11, 10.5]$ mT. The ground state data, especially the transitions of the $|\pm 1/2\rangle \leftrightarrow |\pm 3/2\rangle$ manifold, showed very good signal to noise and 3209 of 3212 identified lines (4000 theoretical lines) accounted for the fitting. The best fit for the ground state has an RMS deviation of $f_{best}^{RMS} = 7.48$ kHz, which is roughly eight times smaller than the mean RHS line width (Fig. 31) and about three times better than the value obtained by Longdell et al. [93]. Table 5 lists the characterisation results for both electronic states and figure 28 shows the spectra with the best fit. Due to the overlapping frequency ranges of the excited state hyperfine manifolds, their spectra are much more complicated due to excessive crossings and overlapping. Although the signal to noise ratio was good, a manual identification of the lines to be fit was necessary. A total of 2567 lines were identified (4000 theoret-
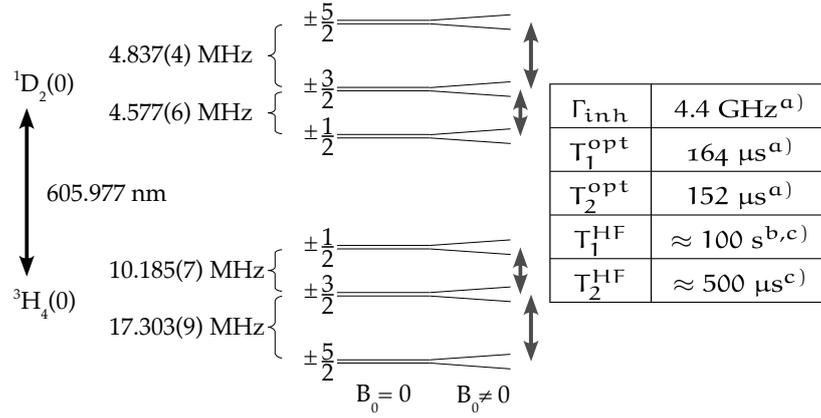
Figure 27: PrYSO level structure. The quoted zero field hyperfine transition frequencies follow from the characterisation result given in Tab. 5. The order of the hyperfine levels is taken from Ref. [71, 122], the values for Γ_{inh} (0.02 at. % Pr) and the relaxation times (B = 0) follow from a) [38], b) [130] and c) [61]. The grey arrows on the right indicate the hyperfine transition manifolds addressed during the single RHS experiments.

ical), including their line widths and amplitudes. Considering all lines restricted the best fit RMS deviation to about 13.5 kHz. It can be observed that most of the lines have only relative amplitudes of less than 30% and many of those small lines further showed a suspiciously high line width. To reduce the impact of noisy and badly shaped lines, the presented fit was carried out only on lines with an amplitude greater that 15% and with a width below 67 kHz. This reduces the number of lines to still a sufficient 1330 lines (4000 theoretical), of which 1297 finally contributed to the best fit deviation of 9.93 kHz[†]. This is slightly worse than the deviation of 7 kHz achieved by Longdell et al. [93]. A reason for this could be that Longdell used another magnetic field trajectory for the excited state experiments, keeping one component constant and just varying the other two. This results in simpler spectra with fewer line crossings and possibly fewer ill-shaped lines. In this work the helical shape for the magnetic field trajectory (Fig. 18) was always used to avoid an unwanted possible restriction of the RHS line frequency changes to a subspace.

Since the Pr site of YSO has C_1 symmetry, the tensor axes are not restricted in this case[††]. An explicit discussion of the tenor axis orientations will not be given here, but can be found to some extent in the diploma thesis of Glasenapp [51]. As mentioned already in the PrLaWO section, a check of the correctness of relative tensor orientations can be performed by comparison with spectral tailoring data. Table 6 lists relative optical oscillator strengths calculated on the basis of the new characterisation for PrYSO (Tab. 5), using the site 1 fitted parameters for both the ground and excited state. The calculated relative oscillator strengths are in perfect agreement with the zero field hole burning data of Nilsson et al. [122]. The previously published data on the PrYSO hyperfine Hamiltonian failed in this test [93, 92] and raised doubts on the reliability and applicability of RHS characterisations [122]. The throughout robust results presented in this chapter demonstrate that RHS characterisations are able to deliver correct overlap integrals.

[†]*Using the best fit parameters of the full recorded data set results in a deviation of 14 kHz.*

[††]*Actual angles between ground and excited state site 1 $\hat{Q} \setminus \hat{M}$-principal axes:*
$Q_x = (75.8 \pm 0.1)°$
$Q_y = (86.7 \pm 0.1)°$
$Q_z = (87.0 \pm 0.1)°$
$M_x = (43.9 \pm 1.1)°$
$M_y = (72.6 \pm 4.2)°$
$M_z = (73.8 \pm 0.1)°$.
Angles between the C_2 and the LAS axes: ground state
$C_{2x} = (89.5 \pm 0.1)°$
$C_{2y} = (88.5 \pm 0.1)°$
$C_{2z} = (1.6 \pm 0.1)°$
excited state
$C_{2x} = (89.7 \pm 0.1)°$
$C_{2y} = (88.6 \pm 0.1)°$
$C_{2z} = (1.7 \pm 0.1)°$

(a) Excited state
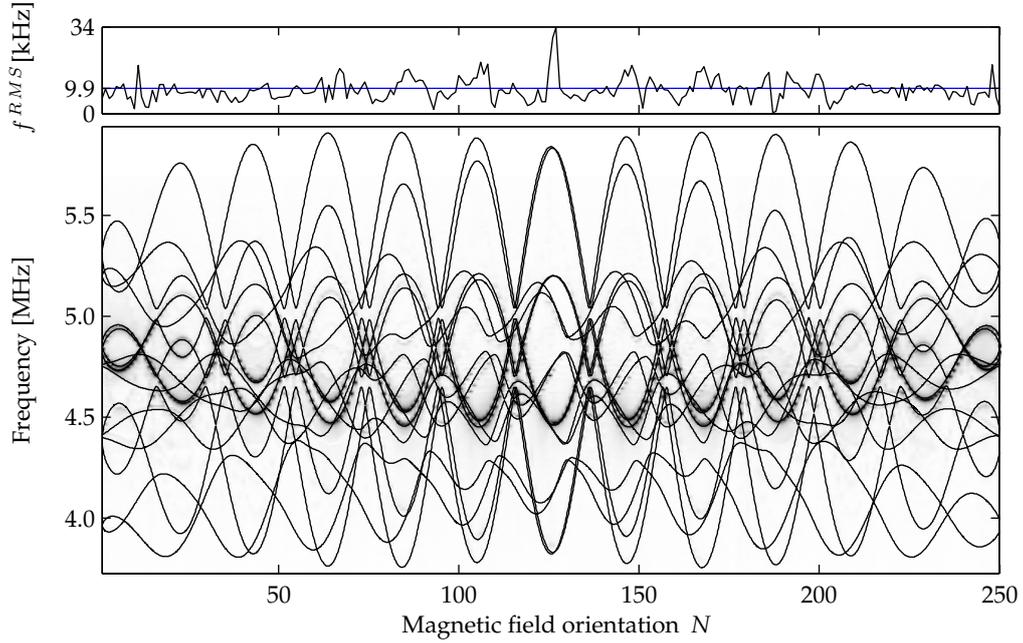
(b) Ground state
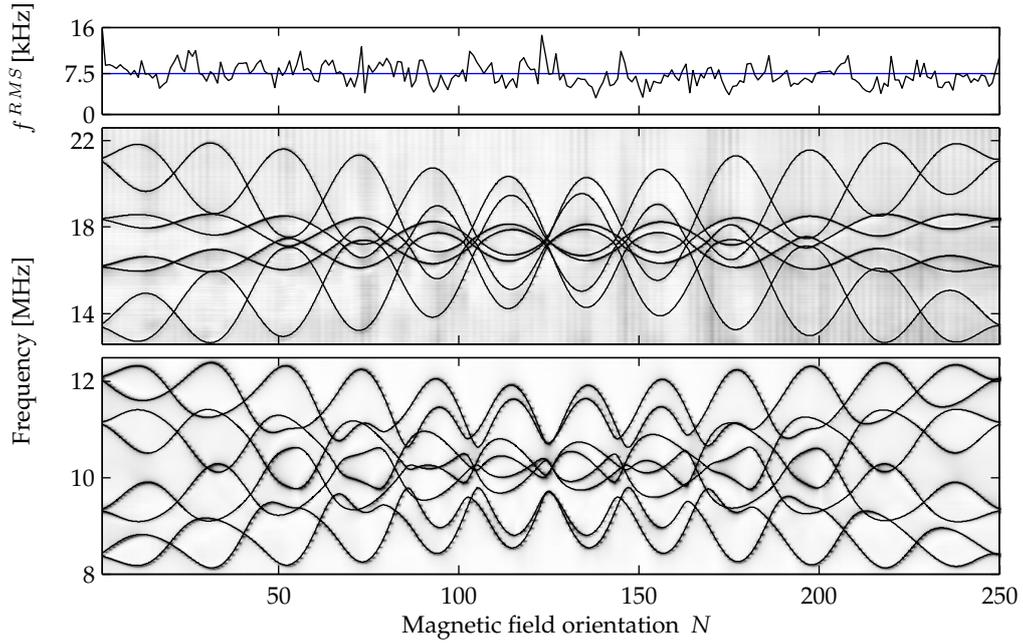
Figure 28: PrYSO RHS data overlaid with fit. The RHS data are shown as grayscale coded intensity plot. The maximum amplitude for each individual spectrum (indexed by N) was normalised to one, in order to obtain a uniform contrast over all orientations. The calculated line positions (using Tab. 5 and Eq. 7.2 and 7.5) are given by the overlaid black lines. Additionally the RMS deviations f^{RMS} for the N individual orientations are plotted (black line in (a/b) top row plots). The blue horizontal lines indicate the mean value (see Tab. 5) of the deviations.

	ground state			excited state		
	value	$\sigma_{\nu_\sigma^{SNR}}$	$\sigma_{\nu_\sigma^{STD}}$	value	$\sigma_{\nu_\sigma^{SNR}}$	$\sigma_{\nu_\sigma^{STD}}$
D	-4.4435	0.35 ‰	0.05 ‰	1.35679	0.46 ‰	0.08 ‰
E	-0.56253	2.0 ‰	0.20 ‰	0.42192	1.3 ‰	0.2 ‰
α_Q	62.1	1.0	0.1	123.51	0.60	0.09
β_Q	31.81	0.23	0.03	94.69	0.33	0.06
γ_Q	93.94	0.61	0.07	170.56	0.39	0.7
g_x	26.57	3.3 %	0.3 %	14.54	3.3 %	0.6 %
g_y	31.01	3.4 %	0.4%	14.30	2.1 %	0.3 %
g_z	113.08	0.32 %	0.05 %	33.76	1.2 %	0.2 %
α_M	112.0	4.7	0.6	44	26	6
β_M	35.68	0.14	0.02	63.91	0.38	0.07
γ_M	101.54	0.22	0.03	3.0	0.4	0.1
α_{C_2}	110.0	3.5	0.5	120	7	1
β_{C_2}	1.574	0.076	0.009	1.65	0.25	0.05
f_{best}^{RMS}	7.48	0.70	0.01	9.928	0.140	0.007

Table 5: PrYSO best fit parameters and fit errors. D and E are given in MHz, the $g_{\alpha'}$ values in MHz/T, all angles in degrees and the resulting RMS deviation f_{best}^{RMS} is given in kHz. For D, E and the $g_{\alpha'}$ the errors are given in relative units. The error estimation was done in the same way as for the values given in table 1. For the ground state spectra $\nu_\sigma^{SNR} = 535$ Hz was found and subsequently yielded $\nu_\sigma^{STD} = 9.4$ Hz. For the excited state $\nu_\sigma^{SNR} = 101$ Hz and $\nu_\sigma^{STD} = 2.9$ Hz were found. Almost all the source histograms had Gaussian shape and were centred around the best fit parameter value. The only exception was the α_M histogram for the excited state ν_{SNR}^σ error, which showed some tails compared to the Gaussian fit. The errors in the f_{best}^{RMS} row correspond to the width of the RMS deviation histograms.

The characterisation of PrLaWO, presented before, was able to predict a ZEFOZ point too (see Sec. 8.2). This test was not performed for PrYSO, but since the PrYSO characterisation was done in the same way, there is considerable prospects that this would succeed. Combined with the prediction of correct relative oscillator strengths, now a complete and non-controversial characterisation for the important compound PrYSO is present.

7.4.4 *Hyperfine Line Widths*

While identifying the line positions in RHS spectra, the line widths are fitted as well. Figure 29 shows representative RHS spectra and line width histograms for the ground and excited state of PrLaWO. For both states, $i = g$ or e, the data of the hyperfine manifolds $|i, \pm 1/2\rangle \leftrightarrow |i, \pm 3/2\rangle$ and $|i, \pm 3/2\rangle \leftrightarrow |i, \pm 5/2\rangle$ can be drawn separately, since their frequencies do not overlap. In the ground and the excited state the $|i, \pm 3/2\rangle \leftrightarrow |i, \pm 5/2\rangle$ line widths are larger. The mean line widths are $|g, \pm 1/2\rangle \leftrightarrow |g, \pm 3/2\rangle \approx 105$ kHz, $|g, \pm 3/2\rangle \leftrightarrow |, g \pm 5/2\rangle \approx 301$ kHz and approximately 196 kHz, when averaged over both manifolds. For the excited state these values are ≈ 18.3 kHz, ≈ 26.3 kHz and ≈ 22.3 kHz, given in the same sequence. Thus, as can also be seen

PrYSO	$\left|e,\pm\frac{1}{2}\right\rangle$	$\left|e,\pm\frac{3}{2}\right\rangle$	$\left|e,\pm\frac{5}{2}\right\rangle$	
$\left|g,\pm\frac{1}{2}\right\rangle$	0.55 ± 0.01	0.38 ± 0.01	0.07 ± 0.01	(exp.)
	0.560 ± 0.004	0.373 ± 0.004	0.067 ± 0.001	(calc.)
$\left|g,\pm\frac{3}{2}\right\rangle$	0.40 ± 0.01	0.60 ± 0.01	0.01 ± 0.01	(exp.)
	0.399 ± 0.004	0.594 ± 0.004	0.007 ± 0.001	(calc.)
$\left|g,\pm\frac{5}{2}\right\rangle$	0.05 ± 0.01	0.02 ± 0.01	0.93 ± 0.01	(exp.)
	0.041 ± 0.001	0.033 ± 0.001	0.936 ± 0.002	(calc.)

Table 6: Relative optical oscillator strengths for PrYSO. The calculated values are derived from Tab. 5 (calc., site 1 for both states) and are compared to the values from spectral tailoring experiments (exp.) [122]. Rows correspond to transitions starting from the ground state hyperfine levels and columns correspond to transitions to different excited state hyperfine levels.

directly in the histograms in figure 29, the transition manifolds with larger splittings also have larger line widths. For example, the ratio of the mean line widths of both manifolds in the ground state is $r_g = 301$ kHz/105 kHz ≈ 2.9 and for the excited state this quantity becomes $r_e = 26.3/18.3 \approx 1.4$ (see Fig. 29).

Single ions at different positions in the crystal see different local fields, which result in a distribution in the crystal field parameters, and thus a distribution in the single Hamiltonian parameters. The scaling of the line width as a function of the transition frequency becomes reasonable, if one focuses on the predominant part of the spin Hamiltonian (see e.g. Eq. 2.10) given by D:

$$\mathcal{H} \approx D[I_z^2 - \frac{1}{3}I(I+1)]$$
$$\hookrightarrow \Delta E(\pm^1/2 \leftrightarrow \pm^3/2) = |2D|,$$
$$\Delta E(\pm^3/2 \leftrightarrow \pm^5/2) = |4D|.$$

This factor of 2 between the splittings of the two hyperfine manifolds splittings is qualitatively in agreement with the situation shown in the histograms and the calculated ratios from above. Distributions in the $g_{\alpha'}$ values should influence the observed line widths in the same way, as they also originate from the crystal field $\hat{\Lambda}$ tensor. Furthermore, the line widths of the ground state transitions are about 9 times larger than those of the excited state, noting that the principal values of the Hamiltonian are only 3 to 4 times larger for the ground state (Tab. 1). This indicates a further proportionality between the magnitude of the Hamiltonian parameter and the width of its inhomogeneous distribution.

Qualitatively a similar effect can also be observed in PrYAP and PrYSO, whose histograms are given in the figures 30 and 31. In both cases the hyperfine manifold line width differences are not as pronounced as in PrLaWO. For PrYAP mean line widths of $|g,\pm^1/2\rangle \leftrightarrow |g,\pm^3/2\rangle \approx 104$ kHz, $|g,\pm^3/2\rangle \leftrightarrow |,g\pm^5/2\rangle \approx 134$ kHz and approximately 114 kHz, when averaged over both manifolds, have been found for the ground state. For the excited state the values are (given in the same order) ≈ 21.1 kHz, ≈ 24.7 kHz and ≈ 23.3 kHz. In the case of PrYSO
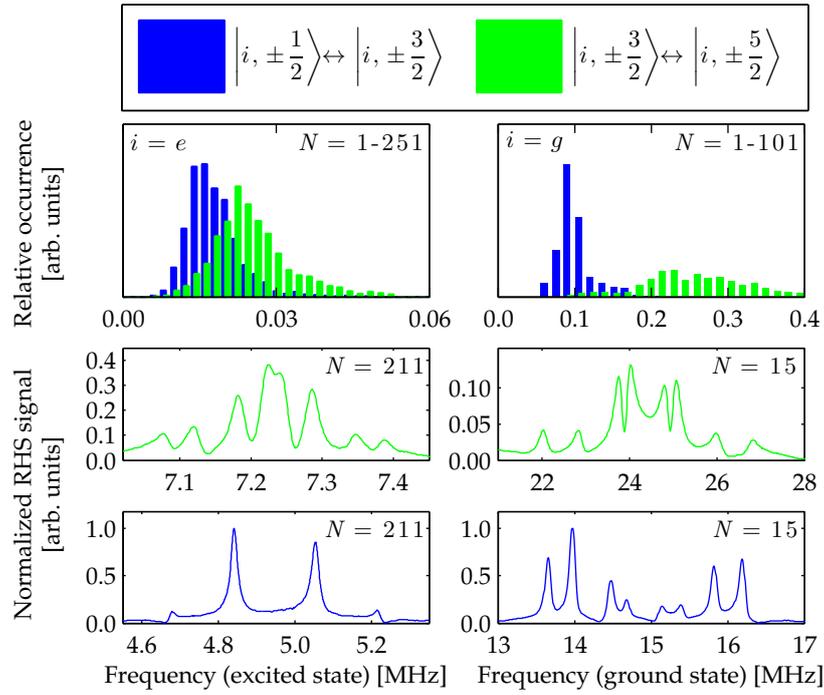
Figure 29: PrLaWO RHS line width histograms and representative ground and exited state absolute value RHS spectra.
The histograms, on the top, show the distributions of fitted full width at half maximum (FWHM) RHS line widths for all recorded data, plotted separately for the two hyperfine transitions ($|i, j\rangle \leftrightarrow |, ik\rangle$, $i = e/g$ and $j/k = \pm 1/2/ \pm 3/2$ (blue) or $\pm 3/2/ \pm 5/2$ (green)). The spectra for the ground state were recorded at $\vec{B} = (2.60, -5.27, -5.76)$ mT, those for the excited state at $\vec{B} = (4.62, 1.19, 4.42)$ mT. The spectra were normalised relative to the largest line from the shown ground or excited state spectra, respectively. The shown ground state spectra resolve all 8+8 possible RHS transitions, while in the excited state spectra not all lines are resolved.

the line widths for the ground state are $|g, \pm 1/2\rangle \leftrightarrow |g, \pm 3/2\rangle \approx 50.5$ kHz, $|g, \pm 3/2\rangle \leftrightarrow |g, \pm 5/2\rangle \approx 75.4$ kHz and approximately 61.1 kHz, when averaged over both manifolds. Since the hyperfine manifolds of the excited state were not separable only the overall line width was determined. For the restricted data set used for fitting (see. Sec. 7.4.3 and yellow histogram in Fig. 31) approximately 18.9 kHz and incorporating all lines 24.5 kHz have been found. Although the lines belonging to the two hyperfine manifolds of the excited state can not be separated in frequency, there is a bi-modal distribution in the histogram with two peaks at approximately 12 and 18 kHz.

Analogous to the discussion for PrLaWO, from the above line widths ratios of $r_g \approx 1.3$ and $r_e \approx 1.2$ for PrYAP and $r_{g,e} \approx 1.5$ for PrYSO can be calculated. Comparing the values for r_g and r_e for the different compounds supports the assumption that the inhomogeneous line widths are influenced by the magnitude of the compound's D. The indication that the line widths themselves are proportional to the magnitude of D is supported by the observed values when comparing PrLaWO and PrYAP, but not when comparing PrYAP and PrYSO. The D values for PrYSO are higher than those of PrYAP, but the line widths behave in the opposite way.
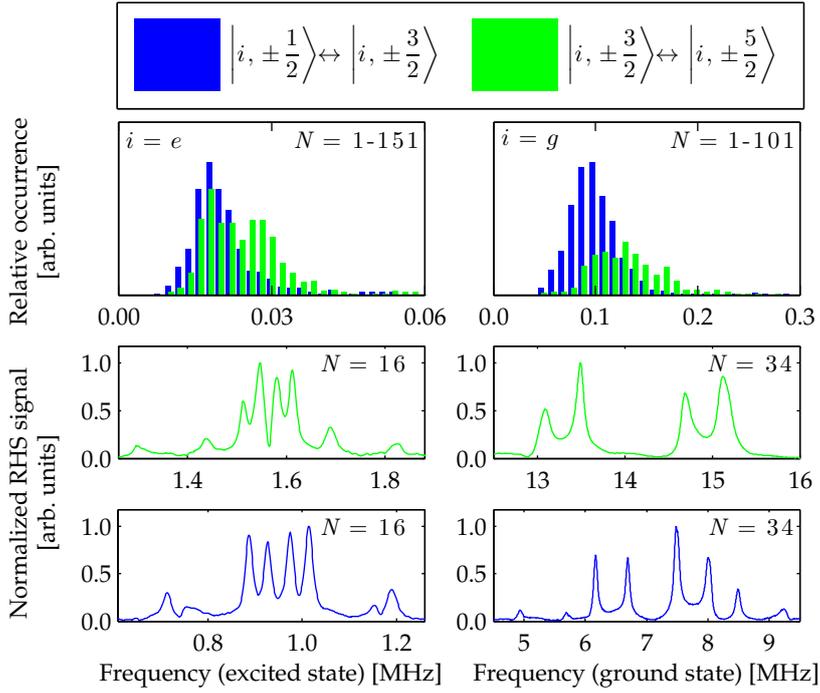
Figure 30: PrYAP RHS line width histograms and representative ground and exited state absolute value RHS spectra.

For the excited state, 47 (of 1168) lines between 1.160 and 1.252 MHz have been excluded for the histograms, since the hyperfine manifolds overlap in this region (compare Fig. 25). The ground state spectra were recorded at $\vec{B} = (-3.35, 8.25, -5.88)$ mT and for the excited state spectra $\vec{B} = (3.76, -2.73, -4.55)$ mT. The vertical scale of each single spectrum was normalised to the largest line.
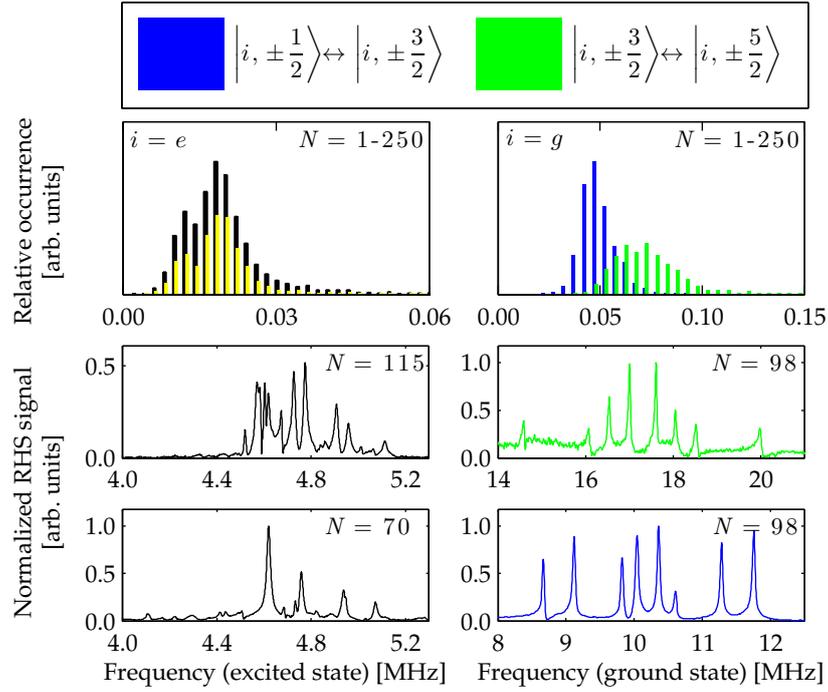
Figure 31: PrYSO RHS line width histograms and representative ground and exited state absolute value RHS spectra.

The excited state histogram shows both hyperfine manifolds binned together (black), as they overlap over the whole RHS frequency range. The yellow histogram contains only lines with a minimum amplitude of 0.15 and a maximum width of 67 kHz, which were selected for the fitting (Tab. 5). The ground state spectra were recorded at $\vec{B} = (-4.83, 9.15, -2.32)$ mT. For the excited state the spectrum with $N = 70$ a field of $\vec{B} = (-4.44, -8.40, -4.68)$ mT was used and for the spectrum with $N = 115$ $\vec{B} = (-0.18, -10.96, -0.89)$ mT was used. The vertical scale of each ground state spectrum was normalised to one on its own. Those of the excited state have been normalised to the largest line in the shown spectra.

OPTICAL TO SPIN STORAGE DECOUPLING TECHNIQUES

High speed and high density storage of classical optical data in REIC is one of the concerns for applications [119]. In REIC ratios of inhomogeneous to homogeneous optical line widths as high as $10^7 - 10^8$ [99] are present, which allows high-bandwidth frequency domain storage. Since only a diffraction limited focal spot size is needed, the data can also be distributed spatially, allowing high storage capacity. Finally, since REIC have very long optical coherence times, storing a series of pulses in the time domain can additionally increase the storage capabilities. Combing these properties may lead to very high storage density and bandwidth [84, 10, 90].

Besides density and bandwidth, the achievable storage times are also of great importance. Using an optical transition to store not only the optical power but also the phase, as required for quantum information, will limit the storage times to the optical coherence time of the system. REIC have very long optical coherence times, in particular in Er^{3+}:YSO a coherence time of up to $T_2^{opt} \approx 6.4$ ms [146, 23] was observed, which represents one of the narrowest optical lines in a solid. Even longer coherence times can be observed in the nuclear transitions of the ground state of some REI. Using special decoupling techniques hyperfine coherence times of up to 30 s were demonstrated in the ground state of PrYSO [46]. To extend the optical memory storage time, the stored optical coherence may be transferred to a nuclear spin coherence in the electronic ground state and later recalled into an optical reemission process. This will be referred to as "optical to spin" storage.

PrLaWO was suggested as new candidate material for storage and retrieval of quantum information carried by optical photons [54]. The development of quantum memories in REIC profited from decades of classical data storage and material science research in REIC. But due to the more delicate nature of quantum data compared to classical data, quantum memories require special protocols. The next sections will give a short overview of the very recent development of photon echo based memories, since their extension to longer storage times using optical to spin storage were the motivation for the experiments with PrLaWO, presented later.

Classical data storage can be carried out using populations, e.g. by a three pulse photon echo protocol [119], this allows for longer storage times.

8.1 PHOTON ECHO BASED QUANTUM MEMORIES

The classical optical data storage discussed above utilises the long optical phase memory time of REIC, but focuses mainly on the storage of the optical energy and timing of the optical pulse trains [119]. An optical quantum memory is supposed to store the full quantum information carried by photons, whether the information of the "qubits" [120] is encoded within the polarisation state of the photons, or e.g., in the relative temporal localisation or phase of the photon wave-packets, the latter being referred to as time-bin qubits [24, 33].

Figure 32: Two pulse photon echo storage scheme. Ions absorbing the input photons (grey wave-packet) are drawn as circles with grey background. The intense refocusing pulse (black) exchanges all ions (grey+black background) between ground and excited state. Ions only contributing to spontaneous emission background noise are drawn in black. The box at the end of the time scale indicates, that the system is being left with some excited and thus fluorescing REI while and after the echo emission.

Such devices are of particular importance for quantum communication. For instance quantum repeaters [25], which could be used e.g. to extend the maximum distance for secure communication based on quantum cryptography and require a quantum memory as their basic building block. Since a mapping of the optically carried quantum information to stationary absorbers is possible in atomic ensembles [85], photon echo like techniques [116, 62] in REIC [118] were proposed for quantum storage.

The most basic storage scheme is the two pulse photon echo sequence, shown in figure 32. As a first step the input pulse, carrying the information to be stored, is absorbed by the ensemble of REI (time $t = 0$). Using a small area input pulse, its information can be assumed to be mapped purely into atomic coherences, without changing the population of the system. Since the optical transition is inhomogeneously broadened the ions will start to accumulate different relative phases, which causes the excited coherence to rapidly de-phase. Irradiating an intense refocusing pulse of π area at $t = \tau$, inverts the populations and coherences of the ions in range of its ideally very high bandwidth. The inversion triggers the REI coherence to re-phase at $t = 2\tau$ and results in re-emittance of the stored pulse in form of the photon echo. The major drawback, for the use of this simple scheme as quantum memory, is the inversion of the medium by the refocusing pulse. It excites all ions within its bandwidth and causes fluorescence, which is in general still active at $t = 2\tau$. The echo therefore is overlaid by a spontaneous emission background noise [133]. The inverted population can also lead to amplification of the echo photons, since the excited ions serve as a gain medium [158]. Additionally coherent propagation effects distort the refocusing pulse, which can lead to a trailing pulse edge superimposing the reemitting echo [133, 134]. The gain effect multiplies the echo photons and the spontaneous emission noise adds photons to the echo. Remembering the quantum nature of the information to be stored and of the non-cloning theorem [139], it follows that this is detrimental

to the scheme when considering it for the storage and retrieval of single photons [133, 148, 86] in the context of a real quantum memory.

Different schemes have been proposed, which avoid e.g. the spontaneous emission noise, but still try to keep the advantageous properties of the photon echo scheme. One example is the controlled reversible inhomogeneous broadening (CRIB) protocol [117]. Here the population inversion is avoided by initiating the optical re-phasing by inversion of the inhomogeneous broadening itself, e.g. by inverting externally applied electric fields (gradients) that control the REI optical transition frequency by using their Stark-shifts [121]. With this technique very high quantum memory efficiencies of up to 69% have been demonstrated [66]. But CRIB intrinsically requires very high optical depths, since the controlled inversion of the inhomogeneous broadening only works with a small group of ions, which have to be selected in the preparation phase [122, 121]. A scheme with lower demands on the optical depth is the atomic frequency comb (AFC) protocol [4].

Here the GEM (gradient echo memory) protocol [7, 69, 70] is included, since it represents a CRIB derivate.

The AFC consists of a series of narrow, highly absorbing peaks, which are equally spaced by a fixed frequency separation Δ, with non-absorbing gaps between them. The structure is prepared in some region of the inhomogeneous REIC line by optical pumping [68, 33, 5]. A storage input pulse is absorbed by the collective of the REI provided by the highly absorptive comb peaks [4]. This is only true if the bandwidth of the input pulse is larger than the comb gaps, and can be understood on the basis of the time-energy uncertainty relation [120], broadening the atomic resonance over the short input wave-packet duration [33]. The initial ($t = 0$) in-phase collective excitation rapidly de-phases into a non-collective state, since the REI in each of the n_i comb peaks accumulates a relative phase of approximately $\phi_i = n_i \Delta \cdot t$. Since the $n_i's$ are integers, at $t = 2\pi/\Delta$ all phases will again be the same. This causes the collective state becoming reestablished and leads to the reemission of the stored information [4], without requiring an inversion pulse, which can cause spontaneous emission noise. Since the storage uses the accumulative optical depth of the comb peaks, the demands on the optical depth are strongly reduced [21]. Furthermore, the AFC bandwidth and multimode capacity is the highest of the actual quantum memory protocols [124], since the combs can be made very broad with respect to frequency [151, 22]. Until now memory efficiencies of up to 21% were demonstrated with AFCs [137], but in principle unity efficiency is possible with sufficiently high optical density [4].

CRIB and AFC both require complex state preparation and set relatively high general demands on the whole experimental setup. Compared to the simple two pulse photon echo (TPPE), the preparation steps of both schemes select only sub groups of ions. This reduces the number of total absorbers in the light-matter interfacing process, lowering the potential efficiency. Very recently a surprisingly simple scheme, called ROSE (revival of silenced echo), was proposed [32], which retains the simplicity of the two pulse photon echo but "silences" the spontaneous emission noise. A second refocusing π-pulse, which is applied at the time τ_1 after the first π-pulse of the TPPE sequence, de-excites the ions back to the ground state. When the "ROSE" echo due to all three pulses is reemitted at $t = 2\tau_1$, there are ideally no excited ions and therefore no gain or spontaneous emission. Nevertheless, to avoid a loss of quantum information due to the "TPPE" echo at $t = 2\tau$, the two π pulses have to be applied in different directions $\vec{k}_2$ and $\vec{k}_3$,
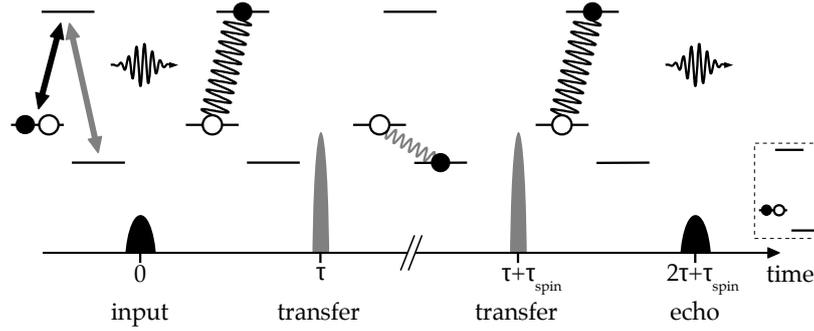
Figure 33: Basic optical to spin storage scheme. The ions, which are supposed to store the incoming wave-packet, e.g. in an AFC quantum memory, populate the upper ground state level of the Λ level scheme. The information is stored as optical coherence in the corresponding transition to the excited state (black arrow). Optical transfer pulses can efficiently [108] invert the other optical transition (grey), which is utilised for the optical to spin transfer at τ. During the spin storage (τ_{spin}) additional RF-pulses may be applied for refocusing, e.g., the hyperfine inhomogeneity. After a transfer back to optical coherences ($t = \tau + \tau_{spin}$), the optical re-phasing of e.g. the AFC protocol leads to reemission of the stored wave-packet at the enhanced storage time $t = 2\tau + \tau_{spin}$. The box at the left indicates the pure ground state population, left afterwards in case of an original quantum memory scheme.

compared to the input pulse wave vector $\vec{k}_1$. Choosing e.g. a counter propagating input with $\vec{k}_2 = \vec{k}_3 = -\vec{k}_1$ "silences" the unwanted TPPE, since $|\vec{k}_{TPPE}| = |2\vec{k}_2 - \vec{k}_1| = |-3\vec{k}_1| \neq |\vec{k}_1|$ represents a spatial phase mismatch with respect to the atomic macroscopic polarisation [32, 1]. For the quantum memory echo at $t = 2\tau_1$, $\vec{k}_{ROSE} = 2\vec{k}_3 - \vec{k}_{TPPE} = \vec{k}_1$ results in a matched phase condition, allowing the remittance of the stored input in the same direction as it was applied. A configuration with the refocussing pulses applied from the side, with angles of $(\vec{k}_1, \vec{k}_2) = (\vec{k}_2, \vec{k}_3) = \pi/3$, leads to emission of the echo in the $-\vec{k}_1$ direction and allows potential efficiencies of unity [32]. This, the high bandwidth, the experimental and systematic simplicity intrinsic to the simple TPPE scheme, on which ROSE is based on, raises some prospects that it might be very useful as a quantum memory protocol.

8.1.1 *Spin Wave Storage*

All original quantum memory schemes introduced above allow spin storage, if the selected REIC supplies a suitable Λ-system. Figure 33 shows a basic scheme using e.g. a previously prepared AFC for the optical storage and additional optical pulses for the transfer to the spin storage. This basic scheme is applicable in the same way to CRIB, ROSE or TPPE by adding the specific refocusing pulses of the protocols in an appropriate way. In all protocols at some point the optical coherences are transferred to the ground state transition of the Λ-system. Due to the much longer ground state hyperfine coherence lifetimes (see e.g. figures 20, 24 and 27), the otherwise limited pure optical storage time τ can be extended significantly adding the spin storage time τ_{spin}. Nevertheless,

See Sec. 8.3 for TPPE based examples.

since the hyperfine levels are also inhomogeneously broadened (see Sec. 7.4.4) a refocusing by e.g. RF π-pulses would be necessary to fully exploit T_2^{HF}. Further increase of the storage time is suspected if dynamical decoupling (DD) techniques or the ZEFOZ technique are used [44, 46, 148]. Using the much longer spin storage times can also be seen as enabling the memory for on-demand emittance of the stored data, since a transfer back to optical coherences can be triggered anywhere within $t = \tau$ to $\tau + \tau_{spin}$.

Most of the recent research concerning photon echo based quantum memories in REIC focuses on the development of original quantum protocols [117, 7, 4, 32], verifying their "quantum" features (e.g. entanglement preservation) [30, 138, 33], optimising the storage and retrieval efficiency [66, 137, 21, 108] or the multimode capabilities [70, 151, 22, 138]. Regarding the potential storage times many of the mentioned references point out the potential of spin storage, but just one demonstration of spin storage in such a photon echo based protocol exists [5] so far. While experiments focusing on the capabilities of the ZEFOZ technique, combined with DD pulses in PrYSO, demonstrated hyperfine coherence times of more than 30 seconds [46], stopped light experiments in the same compound showed impressive storage times of more than 1 second using these techniques [95]. Nevertheless, the storage protocol used, EIT (electromagnetically induced transparency), is supposed to have an intrinsically low bandwidth [124, 32]. Utilising the AFC protocol with a sequence corresponding to Fig. 33, Afzelius et al. [5] demonstrated a storage time of up to 20 μs incorporating a storage bandwidth of $1/450$ ns ≈ 2 MHz in PrYSO. This experiment showed a low storage time, since no hyperfine refocusing was used, but still established the record of a photon echo based implementation in an REIC.

The aim of the experiments described in the next sections was to use the capabilities of the setup described in part ii to test the spin storage in PrLaWO using photon echo based schemes, since all demonstrations so far were mostly carried out in PrYSO only.

Note, Ref. [137] quotes to not yet published storage times of up to 100 μs in PrYSO, achieved by Lars Rippe et al. in the same laboratory.

8.2 ZERO FIRST ORDER ZEEMAN TRANSITIONS

While it was known for a long time that static magnetic fields can cause an extension of the REIC optical coherence lifetimes [101, 102], Fraval et al. [44] realised that a field of specific magnitude and direction can remove the sensitivity of a REIC hyperfine transition to magnetic fluctuations. For many REI random magnetic fluctuations of nuclear moments close to the RE lattice site are an important factor for the residual dephasing [99]. Since the RE hyperfine Hamiltonian contains a magnetic field independent quadrupole term and a field dependent anisotropic Zeeman term (see Sec. 7.2) it is possible to find a magnetic field vector, where one of the hyperfine transitions shows zero frequency shift with respect to small variations around that field [44]. Such a transition or condition will be referred to as ZEFOZ (zero first order Zeeman) [96]. If the curvature of the ZEFOZ transition is small enough, the magnetic fluctuations of the host can no longer affect the ZEFOZ transition. It becomes effectively decoupled from these perturbations and in PrYSO, using this technique for the first time, a coherence time increase from 0.5 ms to 82 ms was achieved [44]. In a second approach a further increase of the coherence time for the same ZEFOZ

transition to 860 ms could be achieved due to more precise control of the magnetic field, since the technique's demands on the absolute tuning precision to the optimum ZEFOZ field are typically higher than 1/1000 [46] (see also Sec. 8.2.2). Reducing the remaining de-phasing to such a low level, enabled DD techniques [106, 154] to further increase the lifetime and to finally demonstrate a coherence time of more than 30 seconds for this ZEFOZ transition [46]. This represents the longest REIC hyperfine coherence lifetime ever reported. A few further experiments by the same research group used the ZEFOZ technique again [95, 12]. But even though they identified different ZEFOZ points, also in other compounds [96], the same PrYSO ZEFOZ transition was always used in the experiments.

The hyperfine characterisation of Sec. 7.4.1 allows to search for ZE-FOZ transitions. Therefore an experimental verification of its correctness using the ZEFOZ technique and a first test of the seemingly enormous potential of the latter technique in a compound other than PrYSO was performed.

8.2.1 *Identification of ZEFOZ Transitions*

A ZEFOZ transition is defined by its zero Zeeman shift $\vec{S}^I$ for small field deviations from the ZEFOZ field $\vec{B}_{opt}$ in any direction:

$$\vec{S}^I(\vec{B})\Big|_{\vec{B}_{opt}} \stackrel{!}{=} 0, \text{ with } \vec{S}^I(\vec{B}) = \left(\frac{\partial \nu_i(\vec{B})}{\partial B_x}, \frac{\partial \nu_i(\vec{B})}{\partial B_y}, \frac{\partial \nu_i(\vec{B})}{\partial B_z} \right). \quad (8.1)$$

Using the hyperfine characterisation results from Tab. 1 and solving for the eigenvalues of the Hamiltonian given by Eq. 7.2 and 7.5, all ground state transition frequencies ν_i can be calculated for arbitrary magnetic fields. Utilising this, a numerical search was carried out, which identified transitions fulfilling Eq. 8.1 in a range of ± 200 mT for all three field components. ZEFOZ transitions with a low curvature with respect to field variations are expected to allow longer coherence times [44, 96]. To quantify the potential quality of a ZEFOZ point the second derivatives $S_{jk}^{II}(\vec{B}_{opt})$ can be calculated:

$$S_{jk}^{II}(\vec{B}) = \frac{\partial^2 \nu_i(\vec{B})}{\partial B_j \partial B_k}\Bigg|_{\vec{B}_{opt}}. \quad (8.2)$$

Using the maximum absolute eigenvalue (s_2) of the matrix following from Eq. 8.2 as its criterium, tabular 7 lists the best ZEFOZ points found for the ground state of PrLaWO in this way. By inspection of the table it is apparent, that for each s_2 the ZEFOZ points found show similar fields and identical frequencies for site 1 and site 2. This arises from the C_2 site symmetry and the circumstance that its axis is not completely aligned with the field axis directions (see Sec. 7.4.1). These ZEFOZ points represent the same ZEFOZ conditions and are still listed for practical reasons, since the field components for the two sites expressed in the laboratory axes system deviate already significantly. Furthermore, for example, the ZEFOZ point investigated in the next section is at a field of $\vec{B}_{opt} = (57.51, 3.99, -36.14)$ mT and has, except for a sign inversion of the field, exactly the same properties as the corresponding ZEFOZ point ($\vec{B}_{opt} = (-57.51, -3.99, 36.14)$ mT) listed in table 7. This

s_2 $\frac{\text{kHz}}{(\text{mT})^2}$	$B_{\text{opt,x}}$	$B_{\text{opt,y}}$ mT	$B_{\text{opt,z}}$	site	i	ν_i MHz
5.5	20.88	2.76	38.58	1	2	3.079
	-20.78	0.65	-38.73	2		
6.0	-21.23	-2.80	-39.23	1	4	10.8604
	-21.13	0.66	-39.38	2		
7.6	62.26	-1.95	116.03	2	1	3.9115
	-62.55	-8.26	-115.59	1		
7.9	-63.21	-8.35	-116.81	1	3	9.5310
	-62.91	1.97	-117.25	2		
12.0	-57.51	-3.99	36.14	1	4	12.6025
	57.10	-10.37	-35.52	2		
15.9	-14.56	8.78	110.50	2	3	12.3059
	-14.76	1.55	110.81	1		
15.9	-96.77	-9.28	-40.73	1	3	12.3059
	-96.17	11.33	-41.61	2		
22.9	-27.47	156.93	40.07	1	4	11.1268
	-36.37	-151.08	53.26	2		
28.9	-69.56	155.87	-35.17	1	3	10.8241
	-78.51	-154.03	-21.89	2		

Table 7: List of the best 9 ZEFOZ points (site 1 and 2 listed separately) for the ground state of PrLaWO, identified within a ± 200 mT field search range. s_2 is the maximum absolute eigenvalue of the second derivate matrix Eq. 8.2 and i denotes the transition number, following from ascending transition frequencies ν_i for the given field.

is a direct consequence of the spin Hamiltonian symmetry ambiguities (Sec. 7.2.1).

8.2.2 *Experimental Verification with PrLaWO*

At the time when the hyperfine characterisation for PrLaWO was made, the superconducting coils presented in Sec. 6.2 were not available. Since the room temperature coils used for the characterisation could not reach the field magnitudes where ZEFOZ points were found, the following experiments were carried out at Lund University, with the equipment and support of Prof. Stefan Kröll's group [97]. The successful use of the characterisation result in an independent laboratory, besides being a source of additional complications, also greatly supported the quality and correctness of the characterisation data itself, including the procedure, conventions etc.

The focus of the laboratory in Lund is currently on the compound PrYSO. A sophisticated setup was built and optimised for this compound [131, 129, 74, 156]. It especially allows experiments requiring very high precision optical controls (e.g. [132, 157, 5, 137]). Measurements of the hyperfine coherence time therefore should be done by pure optical excitation of Raman echos, like it was done previously
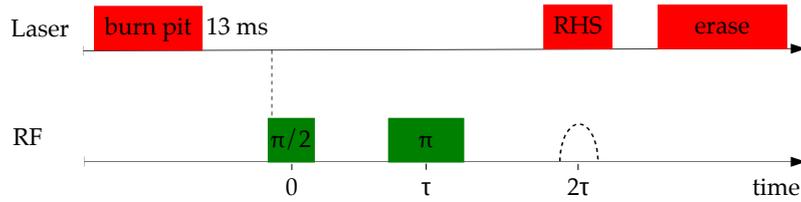
Figure 34: Sequence used to measure Raman echos at the ZEFOZ field. First the Laser was scanned repetitively to burn a transparent pit structure of 16 MHz width (burn pit) in the inhomogeneous line. After letting the fluorescence decay first an RF $\pi/2$-pulse was irradiated, exciting coherence from the ions polarised during the "burn pit" phase. After a time τ later an RF π-pulse was transmitted. Due to the limited available RF power (3 W) in Lund, only RF pulse lengths of 25 and respectively 50 µs could be achieved. Shortly before the appearance of the Raman Echo (2τ) a heterodyne probe beam (RHS) was applied, to record the Raman beating. To ensure a quasi equilibrium state of the populations for the next experiment, all ions in a ±100 MHz range were optically cycled a few times (erase). Additionally the laser was set to scan slowly (few minutes) over a range of 1 GHz.

at zero field in the same laboratory with PrLaWO [55]. In Lund the already mentioned ZEFOZ point at $\vec{B}_{opt} = (57.51,\ 3.99,\ -36.14)$ mT was chosen to be investigated. Since the existing hardware restricted the possible transition frequencies to be ideally above 12 MHz, the ZEFOZ points with even lower s_2 values had to be excluded for the measurements.

The magnetic field was created by two homebuilt superconducting coils for the x- and z-axis, where the z-axis again was also the laser direction. The y-axis field was generated by an Oxford Spectromag 7 T magnet assembly, of which also the bath-cryostat was a part of. Using a 16 bit DAC the field step resolution for the x- and z-axis was about 4 µT, the Spectromag system allowed only a step size of 100 µT in the y-axis. The x and z-axis coils were not calibrated and the sample holder also limited the alignment of the crystal to about 10° with respect to the x- and y-axis. For a first rough calibration of the actual magnetic field at the sample, CW RF Raman spectra were collected for a few current-/field settings of all coils and subsequently compared to calculated spectra using the characterisation data. After a rough match was found, the calculated ZEFOZ field was approached and fine tuned by comparing the spectra to the calculated RHS line positions at the ideal field condition. Since the ZEFOZ line shows zero slope at the correct field, RHS spectra at this point became an insensitive reference and actual measurements of the coherence time had to be utilised for further tuning of the magnetic field match. Unfortunately the pure optical bichromatic excitation of the Raman echo, which initially was planed to be used for the set up, proved to be ineffective for this transition. An RF based excitation of the Raman echo using the RHS scheme, shown in figure 34, finally led to visible echos. By maximisation of the Raman echo amplitude at elevated evolution times τ the magnetic field components were tweaked, until no further improvement could be achieved. Figure 36 shows the resultant Raman echo decay curve of the ZEFOZ transition, including some comparisons and figure 36 shows the calculated transition frequencies for all ground state hyperfine
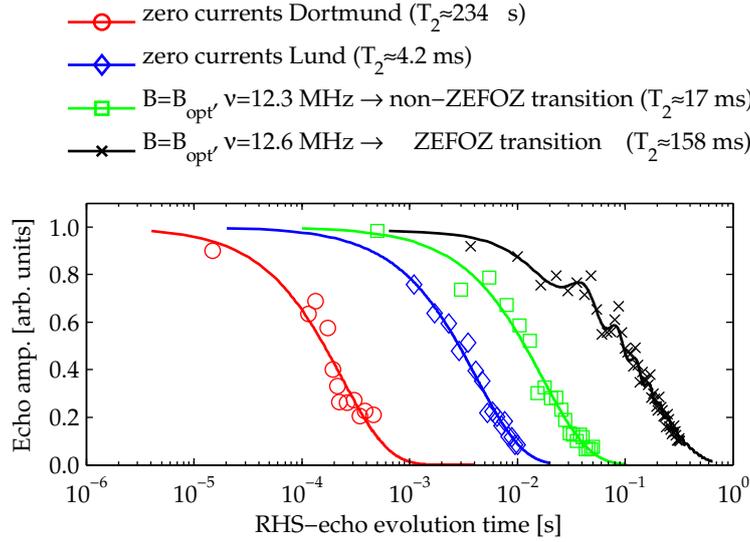
Figure 35: PrLaWO Raman echo decay curves for different magnetic fields and transitions. The red and blue data show decays of the zero-field transition (14.9 MHz), when the coil currents were set to zero. The black data represents the ZEFOZ transition decay for the best match to the ZEFOZ condition field $\vec{B}_{opt} = (57.51, 3.99, -36.14)$ mT. The green data was measured using the same field by resonating the RF pulses with an other hyperfine transition, which did not have a ZEFOZ shift at this field. All decays were fitted with a single exponential decay function. The ZEFOZ transition decay included a modulation term (see Eq. 8.3).

levels. For the ZEFOZ transition a coherence time $T_2^{HF} \approx 158$ ms could be achieved, corresponding to an increase of almost three orders of magnitude compared to the zero field value ($T_2^{HF} \approx 234 - 250$ μs, see figure 35 or [55]). Measurements on the other hyperfine transitions between 12 and 18 MHz, not showing a ZEFOZ shift at this magnetic field (see Fig. 36), gave coherence times in the range of 11 to 17 ms. This clearly demonstrates that the high increase of T_2^{HF} for the ZEFOZ transition is dominated by the ZEFOZ-effect on its own.

Nevertheless, a coherence time enhancement due to application of a weak field can also be observed, and is represented by the blue decay curve in figure 35. This curve was recorded with zero current settings for the magnet coils, but after the measurements at the high ZEFOZ field have been carried out. The long T_2^{HF} of this decay indicated that in Lund some components in the environment of the sample were magnetic, which gives a residual magnetisation when the currents were shut off. During the measurements in Lund this was not known, but the existence of a residual field of the order of $|2|$ mT could be verified afterwards by the comparison of the calculated line positions and the used currents and further by measurements in Dortmund (e.g. see the red "true" zero-field decay curve in Fig. 35, see also Sec. 8.3). In PrYSO an increase of the coherence time from the zero-field value from 0.5 ms to 6 ms by fields of $|B| > 2$ mT was reported [45], thus the effect of a small field on T_2^{HF} in PrLaWO is of similar magnitude. In PrYSO this was attributed to an effect of the Pr-Y spin interaction [45]. In this compound Pr and Y are supposed to interact via their magnetic moments. The relevant mechanism for the field influence on T_2^{HF} is the

Note: Since the ZEFOZ field was tuned by maximisation of T_2^{HF} the residual field does not affect any other argument in this paragraph.
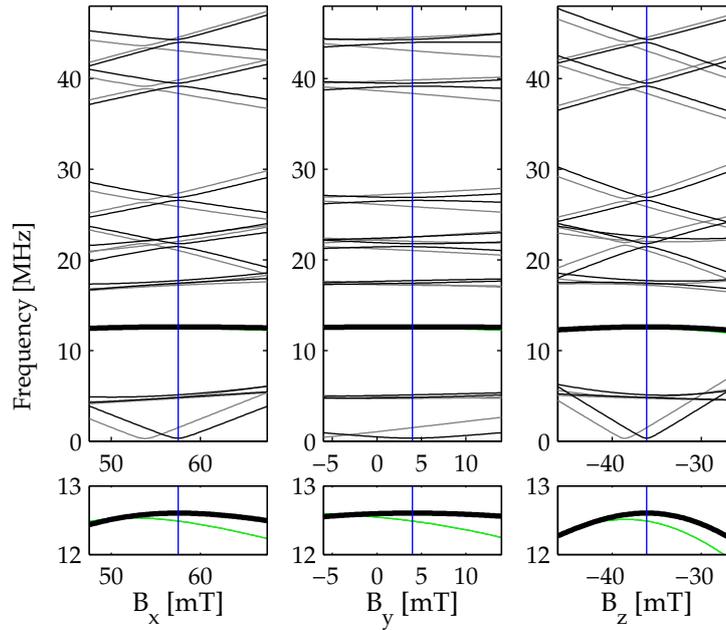
Figure 36: Calculated PrLaWO ground state hyperfine transition frequencies for the used ZEFOZ field $\vec{B}_{opt} = (57.51, 3.99, -36.14)$ mT. The field was varied by ± 10 mT around the ZEFOZ field, which is indicated by the blue vertical line. Site 1 transitions are in black, those of site 2 in grey. The ZEFOZ transition is represented by the bold black line (site 1). The green line corresponds to the transition (site 2) whose decay curve is plotted in green in figure 35. The three upper plots show the full range of ground state transitions, whereas the lower three plots show only the range closely around the ZEFOZ transition.

Pr-Y superhyperfine interaction. In many analogous REIC systems [34, 159, 104], the magnetic moment of Pr is sufficiently strong to Zeeman shift a group of the surrounding nuclear spins with respect to the remaining "bulk" of this spins in the crystal host. This group then forms a so-called "frozen-core" [34]. Since the frozen-core spins have shifted frequencies with respect to the bulk, they are partly decoupled from the bulk "noise". This causes their spins flip rates to be lower than those of the bulk spins. The reduced dynamics of the frozen-core is considered to enhance the coherence time of the Pr ion in their centre. The field of the Pr ion defines the quantisation axis for spins of the frozen-core. A change of the Pr spin state, e.g., by external excitation, mixes the spin states (e.g., Y or La) of the core and thereby causes a higher probability for their state to change subsequently. Therefore, a excitation of the Pr nuclear spin, e.g., by the RF pulses of the Raman echo sequence, leads to changes of both, the Pr and the Y spin states. This leads to many possible different quantum pathways when exciting a Pr spin echo, which can interfere during the echo decay time. The frequencies of the different pathways differ by multiples of the Y Zeeman splitting, which leads to modulations in the echo decay curves with the splitting frequency [43]. By applying a magnetic field, the role of the Pr-induced local fields for the frozen-core is degraded. For sufficiently high fields exclusively the external field defines the Y quantisation axis. At this point Pr spin flips are stopped to induce simultaneous Y spin flips by the superhyperfine coupling and the modulations in the echo decay curves
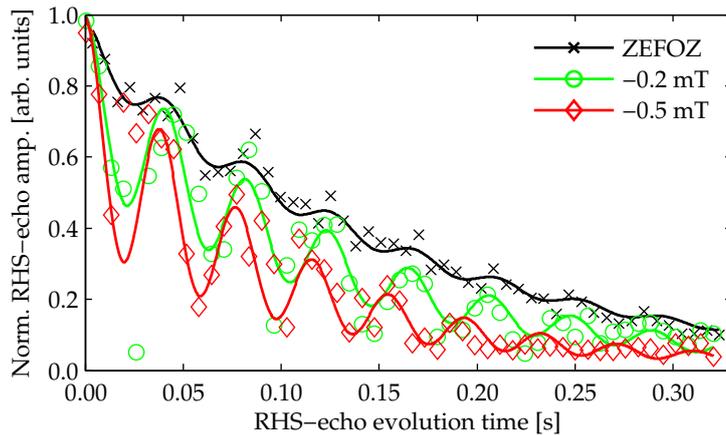
Figure 37: PrLaWO Raman echo decay curve of the ZEFOZ transition studied, recorded at the best ZEFOZ field match ($\vec{B}_{opt}$) and at -0.2 and -0.5 mT detunings in the z-direction relative to this.

disappears. In PrYSO the high field limit of the coherence time is also about 6 ms ($|B| = 100$ mT, Fraval et al. [44]), so in Ref. [45] the authors conclude the Pr-Y superhyperfine interaction effect is decoupled for fields greater than $|B| = 2$ mT. Therefore, no modulation was observed for the ZEFOZ point investigation in PrYSO at the field of about $|B| = 78$ mT [44, 46].

In contrast the ZEFOZ decay shown here for PrLaWO does show modulations. Figure 37 shows the ZEFOZ transition decay in more detail and includes measurements for the same transition but at -0.2 and -0.5 mT field detunings in the z-direction.

The modulation is strongly visible, especially in the detuned curves. Although the temporal resolution of the measurements was not fully sufficient to fit the modulation depth with high accuracy, it seems that the curve with the lower detuning (green) has a higher modulation depth than the other two (noting the outliners at $t \approx 0.025$ ms and $t \approx 0.1$ ms). The curves were fitted using

$$f(t) = [A + M\cos(2\pi\nu_M t)] \exp\left(-t/T_2^{HF}\right). \tag{8.3}$$

In all three cases the observed modulation frequency is covered by $\nu_M = 24.5 \pm 1.7$ Hz. A change of ν_M with field magnitude could not be resolved, due to the low field change. The modulation in PrLaWO may also be attributed to Pr-La spin couplings. The interaction might be more complicated to consider than in PrYSO, since lanthanum has a spin $I = 7/2$, in contrast to the $I = 1/2$ nuclear spin of yttrium. A further indication for the latter also might be the good fit of the decay envelope to a single exponential. In PrYSO an exponential decay with a quadratic time dependence was observed in the first experiments. This was interpreted to arise from a spin diffusion process due to magnetic dipole-dipole interaction with the spin system, which led to a slower reconfiguration of the spin system, compared to a magnetic dipole-dipole dephasing process [44]. A magnetic dipole-dipole dephasing in concentrated spin systems is considered to give a linear single exponential decay [44]. Thus, the possible physical origin of the 24.5 Hz modulation and its apparently very sensitive response to detunings

from the ZEFOZ field so far remains unclear and would require further investigation to be resolved.

The fitted coherence time for the ZEFOZ transition is $T_2^{HF}(\vec{B}_{opt}) = 158 \pm 7$ ms, those measured for the same transition but for the detuned fields $\vec{B}_{0.2} = \vec{B}_{opt} - (0,0,0.2)$ mT and $\vec{B}_{0.5} = \vec{B}_{opt} - (0,0,0.5)$ mT are $T_2^{HF}(\vec{B}_{0.2}) = 133 \pm 16$ ms and $T_2^{HF}(\vec{B}_{0.5}) = 97 \pm 19$ ms. These demonstrate how sensitive the hyperfine coherence time depends on a precise match of the ZEFOZ field, even though the transition has very low curvature (see. Fig. 36) with respect to field changes. Concerning the best achievable T_2^{HF} using this ZEFOZ point in PrLaWO, it should be noted that the tuning precision for this particular experiment was limited by the 1 mT step resolution of the Oxford magnet system. By iteratively approaching the ZEFOZ condition it is possible that the effective tuning precision was better than 1 mT, since the coils were not perfectly orthogonal and/or the residual magnetisation of the setup helped in that sense to achieve effective cross-talk between the low resolution y and the higher resolution x and z coils. The residual modulation in the best achieved decay curve indicates that a "perfect" match may not have been reached, but also that the residual deviation is probably not very large.

Level of Intrinsic Magnetic Fluctuations

Based on the vast increase of the coherence time, when the ZEFOZ condition removes all linear contributions of fluctuation field, a simple model of dephasing can be motivated. For PrYSO the assumption that the achieved T_2^{HF} at the ZEFOZ point was limited only by the second order Zeeman shift, led to an approximation for the intrinsic magnetic fluctuation at the Pr site of $\Delta B_{s_2} = 14$ μT. The value estimated from the Pr-Y distances in the YSO crystal and the Y magnetic dipole moment, $\Delta B_{DD} \approx 3.8$ μT [43], is only in qualitative agreement. To derive an approximate value of ΔB_{s_2} for the data presented here the hyperfine transition frequency is expanded around a field $\vec{B}$ [97]:

$$\nu_i|_{\vec{B}} = \nu_i(\vec{B}) + s_1 B_{off} + \frac{s_2}{2} B_{off}^2, \tag{8.4}$$

here B_{off} is the linearised field offset from the expansion point $\vec{B}$. For the ZEFOZ point $\vec{B} = \vec{B}_{opt}$ the first derivate vanishes, $s_1 = 0$. Due to small shifts the frequency variation then becomes

$$\Delta \nu = \frac{s_2}{2} B_{off}^2$$

and the importance of the second order shift coefficient s_2 becomes evident. Since the magnetic fluctuations at the Pr site are random, a line broadening of

$$T_2^{-1} = \frac{s_2}{2} (\Delta B_{s2})^2 \tag{8.5}$$

may be assumed. With $T_2^{HF}(\vec{B}_{opt})$ and the value for s_2 from Tab. 7 the magnitude of the fluctuations can be calculated: $\Delta B_{s2} = 32.5 \pm 1.4$ μ T. Comparing this to the value found in the same way for PrYSO gives a good match, especially when considering the zero field coherence times of 500 and 250 μs for PrYSO and PrLaWO respectively. The latter can be used as a reference, since the (enhanced) gyromagnetic ratios

(see. Tab. 5 on page 82 and Tab. 1 on page 69) are similar and thus will lead to similar s_1 values at zero field. Nevertheless using this simple model for the slightly detuned conditions shows its weakness. For a field offset $B_{off} \gg \Delta B_{s_2}$ the frequency shift becomes

$$\Delta \nu = \frac{s_2}{2} B_{off}^2 + s_2 \Delta B_{s_2} B_{off}. \tag{8.6}$$

The first term is only the static line-shift, resulting from the detuning of $\vec{B}_{opt}$ and the assumed curvature s_2 of the transition frequency curve. The second term describes the line broadening arising from the field fluctuation at this detuning. Using ΔB_{s_2} and s_2 from above then yields $T_2^{HF}(B_{off} = 0.2 \text{ mT}) \approx 13$ ms and $T_2^{HF}(B_{off} = 0.5 \text{ mT}) \approx 5$ ms, whereas both are in contradiction to the observed coherence times. This applies not only for PrLaWO, but also for the published values of PrYSO.

This result indicates that the residual dephasing might not be entirely determined by magnetic field fluctuations or that the ZEFOZ condition was not met accurately, both which can be expressed by additional terms:

$$T_2^{-1} = T_{2,0}^{-1} + s_1 \Delta B + s_2 \Delta B B_{off}. \tag{8.7}$$

The first term $T_{2,0}$ includes all contributions being independent of the random field fluctuations ΔB, e.g. phonon contributions. The second term accounts for a possible mismatch of the ZEFOZ condition. Both terms are independent of the field offsets B_{off} used and therefore can not be discriminated by the available data. Additional data recorded at different temperatures and different B_{off} might help to resolve both effects. Nevertheless, the data presented and Eq. 8.7 can be used to get a less contradictory estimate for the level of the field fluctuations.

The linear fits of $T_2^{-1}(B_{off})$ on the PrLaWO and PrYSO, shown in figure 38, yield $\Delta B(\text{PrLaWO}) = 1$ µT and $\Delta B(\text{PrYSO}) = 3$ µT. The calculated value from [43], following simulation of the magnetic dipole-dipole couplings due to the Pr-Y distances in the PrYSO crystal, was $\Delta B \approx 3.5$ µT. Thus the magnitude of the fluctuations is actually much lower than previously estimated.

Although the data consists only of three data points, the simple model set up by the equations 8.4 and 8.7 yields good explanation of the observed coherence times. This is also backed up by a superb fit of the quadratic approximation for the transition frequency (see right plot in Fig. 38) with the frequencies following from the characterisation data, especially if the z-projection ($-s_{2z} = -8.2$ kHz/mT^2) of the second derivative matrix is used for the approximation. The projected maximum ZEFOZ $T_2(B_{off} = 0)$ values for PrYSO and PrLaWO are 1.8 s and 162 ms respectively. The values reached in experiments are, with 0.86 s and 158 ms, already quite close to $T_2(B_{off} = 0)$. Ref. [96] reports measurements of a second ZEFOZ point in PrYSO, not showing any data, with $s_2 \approx 3$ kHz/mT^2 (the point discussed so far had $s_2 \approx 6$ kHz/mT^2) and a measured ZEFOZ coherence time of 1.4 seconds for it. This, together with the values for the residual dephasing indicated by the model (see left plot in Fig. 38) and its good fit to the data, justifies the assumption that the limiting term T_{20}^{-1} in PrLaWO is approximately 5 to 10 times larger than in PrYSO. The latter could arise from a more complicated Pr-La coupling, possibly including other relevant terms

Values in Ref. [43]: $T_2(0.2) = 320$ ms, $T_2(0.5) = 100$ ms, where e.g. "(0.2)" denotes a 0.2 mT detuning from the ZEFOZ with $T_2(0) = 860$ ms. Ref. [96] gives $\Delta B_{s_2} = 14$ µT. With this numbers Eq. 8.6 yields ≈ 60 ms and ≈ 24 ms for the coherence times of the two detunings.

*Using s_2 instead of s_{2z} to calculate ΔB results in a change of only ≈ 1 %.*
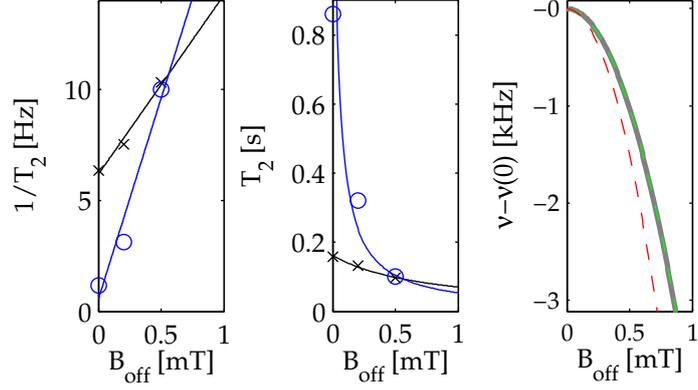
Figure 38: Estimation of ΔB based on Eq. 8.7. The coherence time dependence on a field offset B_{off} from the ZEFOZ points is shown in the plots on the left and in the middle. The PrLaWO data is given by the black crosses and the PrYSO data [43] by the blue circles. The solid lines represent the fits of Eq. 8.7 to this data, where the terms $T_{2,0}^{-1} + s_1 \Delta B$ are fitted as single offset in the T_2 axis. From this $\Delta B(\text{PrLaWO}) = 1$ μT and $\Delta B(\text{PrYSO}) = 3$ μT follow. The right plot shows the frequency of the PrLaWO ZEFOZ transition plotted against the field offset. The bold grey line corresponds to the frequency calculated using the Hamiltonian and the characterisation result from Sec. 7.4.1. The red dashed line represents the frequency that follows using the quadratic approximation of Eq. 8.4 and the second derivative $-s_2 = -12.0$ kHz/mT^2. The green dashed line (overlapping with the grey) follows using the projection of the second derivative matrix (Eq. 8.2) on the z-axis direction, $-s_{2z} = -8.2$ kHz/mT^2. s_{2z} was used to approximate $\Delta B(\text{PrLaWO})$.

since La has a nuclear spin of $I = 7/2$, in contrast to Y with $I = 1/2$. As mentioned above more data including e.g. temperature as a variable would be required to conclude this at a level with higher certainty.

Spin Diffusion at the ZEFOZ Condition

To investigate the influence of spin diffusion processes in PrLaWO, three pulse stimulated echo decay curves were also recorded. Since only a few hours of the experiment's time schedule in Lund were left at the time these measurements began, they had to be recorded at the expense of lower signal accumulation counts and no tweaking parameters. Together this resulted in poor data quality, but at least the approximate timescales and the impact of spin diffusion can be estimated from the data. Figure 39 shows the pulse sequence used (a) and the recorded stimulated echo decays (b). In the three pulse sequence the first $\pi/2$-pulse creates coherences, which evolve for a time τ_1, before a second $\pi/2$-pulse transfers the coherences (partly) into a population grating. After a time τ_2, which may be longer than τ_1, since the population life time T_1^{HF} is expected to be much longer than the coherence life time T_2^{HF}, a third $\pi/2$-pulse transfers the population grating again into coherences. The coherences will refocus a time τ_1 after the last pulse in the form of a stimulated echo. For the curves shown in Figure 39 (b) τ_1 was always kept fixed, while the decays along the varied τ_2 contain information about changes of the population grating due to e.g. spectral diffusion processes on this time scales. In
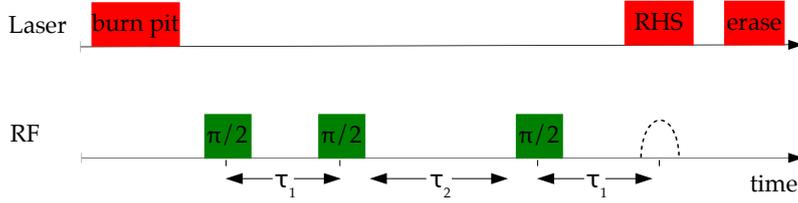
(a) Three pulse Raman echo sequence.
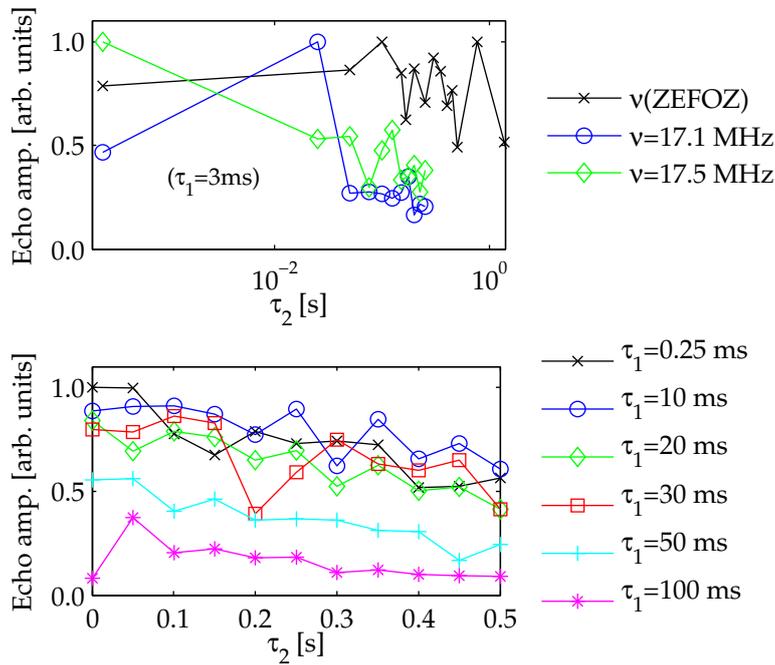
(b) Three pulse Raman echo decays.

Figure 39: Three pulse stimulated Raman echo data. (a) shows the used pulse sequence. For the optical pulse sequence the same description applies as for Fig. 34. The RF part shows the stimulated echo three pulse sequence, specifying the pulse separations τ_1 and τ_2 used in figure part (b). For the decays in the upper plot of (b) the first evolution time was fixed to $\tau_1 = 3$ ms for all three measurements. The stimulated echo decay curves of the ZEFOZ transition and two non-ZEFOZ transition, recorded at the same field, are shown. The coherence times, from two pulse echo decays, for the non-ZEFOZ transitions were $T_2^{HF}(\nu = 17.1 \text{ MHz}) \approx 11$ ms and $T_2^{HF}(\nu = 17.5 \text{ MHz}) \approx 14$ ms. The decay show in the lower plot of (b) are all recorded for the ZEFOZ transition, but with different τ_1 for each curve.

the upper plot of Fig. 39 (b) the ZEFOZ transition does not show any particular echo amplitude losses due to spectral diffusion for times τ_2 up to about 1.5 s. The non-ZEFOZ transitions, recorded with the same conditions, already show a rapid decrease for $\tau_2 \gtrless 50$ ms. The large point to point variations can mainly be attributed to the high noise level of the measurements in general and a relatively large tendency to shot-to-shot variations for the echo amplitudes. In all experiments the latter was more exaggerated for the non-ZEFOZ transitions and was partly due to small instabilities of the field currents, shifting those lines more strongly than the ZEFOZ transition. Furthermore, the Lund laser could only be run at a frequency jitter level of about 1 to 2 MHz, since it can only be further stabilised to ultra-high stability by locking it to a spectral hole of PrYSO [74, 129], which has a (far) off-resonant optical frequency with respect to the inhomogenous line of PrLaWO. In this way the only "highly" stabilised laser, besides contributing in some degree to a generally higher noise level in the RHS experiments by laser amplitude noise effects [111], also is supposed to exhibit drifts. Especially on long timescales these might have been sufficient to let the echo amplitudes vary from shot-to-shot. The lower plot of Figure 39 (b) shows the ZEFOZ transition stimulated echo decay for different τ_1. For $\tau_1 \geqslant 50$ ms a significant decrease of the echo amplitude can be observed. For lower τ_1 the curves are similar, all showing a slow almost monotonic decay with a rate of about 1 s^{-1}. The data published in [44] shows qualitatively the same attributes. The data quality shown here allows for a quantitative comparison, the decays of the ZEFOZ transition for different τ_1 values seem to be slower for PrLaWO than for PrYSO.

Summarising this section, it was demonstrated that the ZEFOZ technique can successfully be used also in other systems than PrYSO. Besides confirming the hyperfine characterisation of PrLaWO, an increase of the coherence time by 630 times could be achieved on the first attempt. Furthermore, the order of the magnetic fluctuations was approximated to be ≈ 1 µT, much lower than previously expected. The model for the dephasing in the vicinity of the ZEFOZ point indicates a more significant role of non-magnetic dephasing effects in PrLaWO. Nevertheless, the spin diffusion impact seems to be comparable to that of PrYSO and again PrLaWO demonstrated to be an interesting system for e.g. quantum memory related testbed experiments.

8.3 DYNAMIC DECOUPLING

The usage of the ZEFOZ technique in REIC already allows impressive enhancements of the ground state coherence time for the particular transition. Using a pulsed (dynamical decoupling) sequence, Fraval et al. [46] could extend the coherence times further, already coming close to the limits set by T_1^{HF} in PrYSO. In this particular experiment the ZEFOZ technique [44] increased the coherence time of the system already by about 1700 times. The resulting very low dephasing rates enabled the pulsed decoupling sequence [46], originating from NMR [106], to increase the coherence time further by an additional factor of 35. Nevertheless, the ZEFOZ technique is only effective for one specific transition at a time. Furthermore, the relatively high magnetic field incorporated, also generates complicated hyperfine spectra. The

latter may lead to problems when, for example, spectral tailoring of the optical absorption is indispensable for the planned experiments.

The idea to investigate the dynamical decoupling potential in PrLaWO was motivated by the observation of millisecond-range ground state coherence times at low magnetic fields, while investigating the ZEFOZ transition (see Fig. 35). Since RF Rabi frequencies in the range of a few hundred kHz are readily achievable with the present spectrometer hardware (Sec. 5), application of dynamical decoupling pulse sequences was assumed to considerably enhance the coherence times in PrLaWO.

The basic idea of dynamical decoupling (DD) is to decouple the quantum system of interest $\mathcal{H}_S$ from the effect of a perturbing environment $\mathcal{H}_E$ by application of strong control operations acting exclusively on the system $\mathcal{H}_S$'s degrees of freedom [154, 155].

$$\mathcal{H} = \mathcal{H}_S + \mathcal{H}_{SE} + \mathcal{H}_E$$

The system interacts with the environment due to the system-environment interaction $\mathcal{H}_{SE}$, which may change on time scales of the environment correlation time τ_E. The control operations are applied to the system in a stroboscopic manner and will change its state periodically. During this time the system can be considered to evolve under the action of an effective Hamiltonian $\mathcal{H}_{eff}$, which may be expressed by a series expansion [58]:

$$\mathcal{H}_{eff} = \mathcal{H}^{(0)} + \mathcal{H}^{(1)} + \mathcal{H}^{(2)} + ...$$

An ideal DD control sequence inverts the system-state on time scales $\tau_c \ll \tau_E$, significantly faster than the environment changes. In the case of non-interacting spins $(\mathcal{H}_S + \mathcal{H}_{SE})$ averages over the time and the effective Hamiltonian becomes $\mathcal{H}_{eff} = \mathcal{H}_E$ [8]. Thus the evolution is independent of $\mathcal{H}_S$ and $\mathcal{H}_{SE}$, and the system was effectively decoupled from the environment during this time. For real physical systems and sequences this averaging will not work perfectly. When the environment is weakly coupled to the system [103, 76], the system evolution can be described by

$$U_{eff}(t) = e^{-i\mathcal{H}_{eff}t} \approx exp\left\{-i\mathcal{H}_E t + \mathcal{O}\left([\tau_c/\tau_E]^{n+1}\right)\right\}, \qquad (8.8)$$

with the decoupling being effective up to an order n [163, 8]. For non-ideal conditions, e.g. $\tau_c \sim \tau_E$, higher order terms will contribute and will lead to residual dephasing.

8.3.1 *Decoupling Sequence Performance using Raman Heterodyne Scattering*

Dynamic decoupling has it roots in experiments as early as those done by Hahn [59], using "intense radiofrequency power in the form of pulses" to refocus the inhomogenous dephasing and thereby remove its effect by the formation of spin-echos (see, e.g. RF-part of Fig. 34). Applying a periodic sequence of identical inverting RF pulses can lead to an increase of the coherence time compared to that measured with a Hahn echo, as already indicated by Carr and Purcell when publishing their famous CP-sequence [28]. Repeating the pulses rapidly, allows fulfilment of $\tau_c \ll \tau_E$ in Eq. 8.8 for longer total evolution

times $\tau_{tot} = N \cdot \tau_c$ of the system compared to the Hahn echo, where $\tau_{tot} = \tau_c = 2\tau$.

But not only the rate of the pulses is of importance. Errors in, e.g. the flip-angle of the pulses will lead to non-perfect refocusing. Given that each applied pulse rotates the spins a bit too far, this will accumulate over the whole sequence and lead to a quick loss of the coherence. This effect can also be used to very precisely adjust the pulse length [26]. Nevertheless, pulse sequences intended for decoupling are made such that these unavoidable experimental errors, like length, phase, homogeneity or off-resonance, are compensated for by their design[50]. As an example, a simple modification of the CP sequence, by matching the axis of the refocusing pulses with the initial spin orientation will lead to an effective compensation of the pulse length error [106, 163]. This latter sequence is called CPMG sequence and is still one of the most effective decoupling sequences for special conditions [8, 6]. Figure 40 shows a short-hand notation for this and other used sequences, including a visualisation of their robustness with respect to flip-angle and off-resonance to the spin transition pulse-errors.

Changing the phase of the initial spin coherence phase by 90° transforms the effective CPMG sequence back to the less effective CP sequence. Thus, CPMG can be considered as sensitive to the "input phase". Especially in the context of quantum information processing it is important that the DD sequence decouples the system effectively from the environment independently of the initial system state or the type of the system-environment interaction. A sequence, originating from NMR [105], called PDD (periodic dynamical decoupling) was realised to fulfil these criterions in the context of DD [76]. It consists of a basic building block of four inversion pulses (see Fig. 40b) with perpendicular rotation axes, which makes the sequence less sensitive to the actual initial system state. The reason to use 4 pulses instead of only 2 pulses to define the PDD sequence, is that each cycle of a DD sequence is supposed to leave the system (ideally) in the same state as before the DD. Applying 2 π-rotations around one axis fulfils that trivially, but incorporating more axes also requires more pulses, e.g. 4 in the case of PDD.

By comparison of Fig. 40a and 40b it becomes apparent that the additional pulses and rotation axes improve the robustness[†] of the DD sequence, not just with respect to pulse length errors, but also with respect to other errors, in this case frequency offset errors. The so-called KDD sequence, which is shown in Fig. 40c, compensates such errors even better [143]. This new sequence is of a special kind. It has its roots in a so-called composite-pulse. In NMR composite pulses were developed to compensate the pulse-error effects within a single pulse. This is done by subdivision of the complete intended pulse rotation into small parts, each rotating around different axes [89]. Such a pulse was recently found to be very robust and effective for decoupling experiments with nitrogen-vacancies in diamond [135]. This specific composite pulse represents five π-rotations around different axes, resulting in an effective rotation of 60° around the (spin) Z-axis followed by a π-rotation around the X-axis (same phase notation as in Fig. 40). Souza et al. [143] have put delays in-between the single π-rotation segments (see Fig. 40c) and by doing this created a DD sequence - KDD - out of a composite pulse. For a higher total compensation of the pulse errors, the KDD sequence consists of four primitive KDD_ϕ-blocks

[†]*Here compared by using a fidelity:*
$F = \frac{|TrAB^\dagger|}{\sqrt{TrAA^\dagger TrBB^\dagger}}$,
$A = \hat{1} = "ideal"$,
$B = U_{eff}(\tau_{tot})$.

$$\left(\frac{X}{2}\right) - \left[\frac{\tau}{2} - Y - \tau - Y - \frac{\tau}{2}\right]^N$$

(a) CPMG sequence, with $n_{DD} = 2$ pulses.

$$\left(\frac{X}{2}\right) - \left[\frac{\tau}{2} - X - \tau - Y - \tau - X - \tau - Y - \frac{\tau}{2}\right]^N$$

(b) PDD sequence, with $n_{DD} = 4$ pulses.

$$\left(\frac{X}{2}\right) - \left[KDD_0 - KDD_{\pi/2} - KDD_0 - KDD_{\pi/2}\right]^N,$$

$$\text{with } KDD_\phi = \left[\frac{\tau}{2} - X_{\frac{\pi}{6}+\phi} - \tau - X_\phi - ...\right.$$

$$\left....\tau - X_{\frac{\pi}{2}+\phi} - \tau - X_\phi - \tau - X_{\frac{\pi}{6}+\phi} - \frac{\tau}{2}\right]$$

(c) KDD sequence, with $n_{DD} = 4 \cdot 5$ pulses.
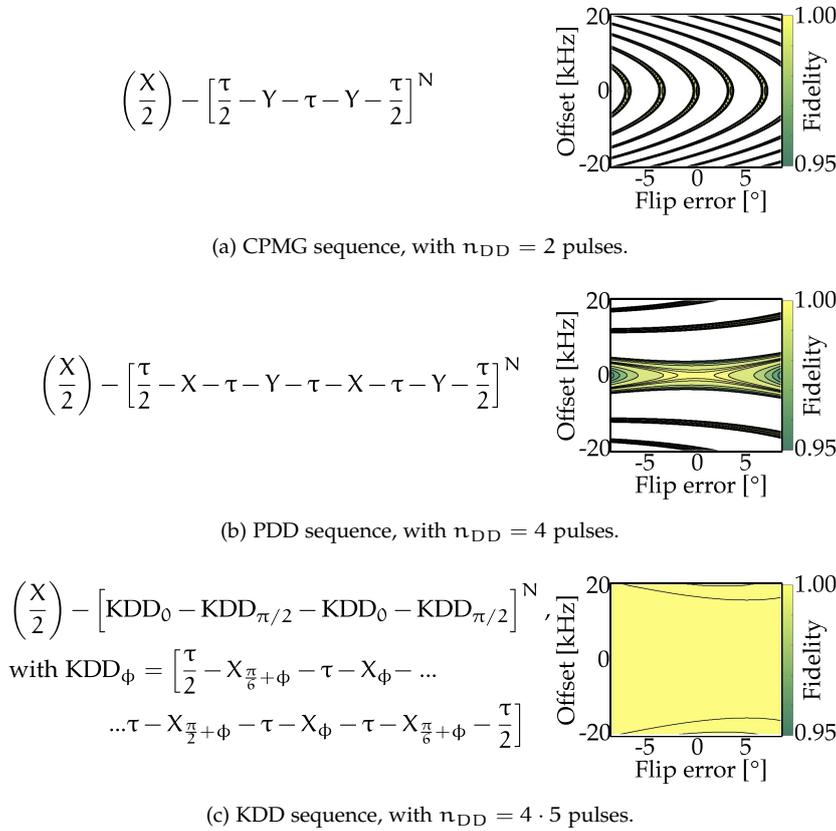
Figure 40: The dynamical decoupling sequences used are given in short-hand notation within the rectangular brackets $[...]^N$. τ is a delay and X, Y denote pulses of π-area, with $0°$, respectively $90°$ relative RF phase. For the KDD-sequence, e.g. X_ϕ denotes a π-pulse with a relative phase of $0° + \phi$. For each sequence the first bracket defines the standard initial phase, since it is assumed that the initial coherence is created starting from an equilibrium state ("Z"). All sequences are symmetric with respect to their basic building block $[...]^N$, which are repeated N times. The duration of each block is τ_c and the π-pulses have a duration of τ_p. The plots on the right, reproduced from Ref. [143], show the fidelity (see margin note ($\dagger$) on page 104) of the sequences with respect to flip angle and off-resonance pulse-errors. The fidelities were calculated for typical (NMR) pulse-error parameters and a total of 100 applied pulses [143].
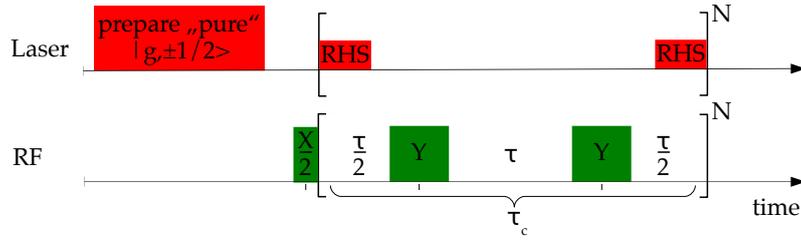
Figure 41: RHS-DD sequence. Each experiment started with a optical spectral tailoring sequence, which empties the $\left|g, \pm\frac{3}{2}\right\rangle$ levels and populates the active REIC $\left|g, \pm\frac{1}{2}\right\rangle$ levels (see Fig. 49b). From this a $\pi/2$-area RF pulse creates hyperfine coherence. Then the DD sequence, e.g. CPMG, is repeated N times. Synchronised with this, a weak RHS probe laser beam is switched on shortly at the beginning and at the end of the RF-DD sequence. Within this time-windows the current coherence is probed and recorded by a sample and hold amplifier or the gated demodulator (see Sec. 5.1). The RHS probe had about 15 kHz Rabi-frequency, resonates with the $\left|g, \pm\frac{3}{2}\right\rangle \leftrightarrow |e\rangle$ transition and had a total on-time for one DD cycle of less than 200 ns.

(see Fig. 40c) shifted in phase analogous to the single pulses in the PDD sequence .

The efficiency of such DD sequences in real experiments is a function of many experimental control variables, including τ_c, τ_p , symmetric and asymmetric transient errors of the pulse phase [58, 26]. Furthermore each physical system has its own specific properties. An REIC system, besides having many close hyperfine transitions at low magnetic field, also requires special detection techniques for the coherence subjected to the DD sequence. Whereas the DD sequence is applied to the system by RF pulses, the detection cannot be done by magnetic induction as in NMR, since typical REI doping levels are only about 0.1 %. To probe the potential of the shown DD sequences in PrLaWO hyperfine transitions, a RHS-DD scheme was used, since it is the most basic sufficiently

For photon echos and DD see Sec. 8.3.2.

sensitive technique. Figure 41 shows the basic pulse sequence used for all RHS based DD measurements presented in this section. The optical preparation creates an approximately 1.5 MHz broad absorptive peak, within an ≈ 16 MHz broad non-absorptive region of the inhomogenous optical line. Due to the frequencies used for the optical pumping, the peak represents REI having only their $\left|g, \pm\frac{1}{2}\right\rangle$ and $\left|g, \pm\frac{5}{2}\right\rangle$ levels populated (see Fig. 49b on page 116). The DD-RF is only resonant with the $\left|g, \pm\frac{1}{2}\right\rangle \leftrightarrow \left|g, \pm\frac{3}{2}\right\rangle$ transition. To detect the coherence after a time $N \cdot \tau_c$ a RHS probe beam resonant with $\left|g, \pm\frac{3}{2}\right\rangle \leftrightarrow |e\rangle$ transition, with respect to the centre of the absorptive peak, is applied. Since working in an REI ensemble it was possible to monitor the coherence while the DD sequence was still active. Figure 41 shows the windows within the coherence was Raman scattered for detection of its current amplitude. Since the RHS probe beam will also optically pump the ions, a loss of coherence is incorporated with the monitoring [41]. To avoid a significant RHS beam pump-effect a very low power probe beam, which was switched on only for very short times, was used. For each series of measurements the effect of the RHS probe on the DD-decay was checked by activating the RHS probe only for each nth DD-cycle ($n = 2, 3, 4, ..., N$). n was increased until the DD-decay did not change

(a) $B = 0$

(b) $\vec{B} = \vec{B}_a = -(1.8, 8.0, 0.0)$ mT

Figure 42: Transition frequencies for the $\left|g, \pm\frac{1}{2}\right\rangle \leftrightarrow \left|g, \pm\frac{3}{2}\right\rangle$ transitions of PrLaWO for two different magnetic fields. The vertical blue line indicates the field around which the transition frequencies are calculated within a window of ± 0.5 mT. Note that the vertical and horizontal scales are the same and thus allow to directly compare the transition slope.

anymore due to pumping effects and this configuration was then used to record the decay. The validity of this procedure was also verified by comparing the RHS-echo amplitude after many $N \cdot \tau_c$ cycles to the RHS-echo amplitude resultant when the probe was inactive except for the very last detection window of the same number of cycles.

Magnetic Field Influence

As mentioned in real systems all DD sequences will show different "performance", which will be measured here by the remaining coherence/echo amplitude after $\tau_{tot} = N \cdot \tau_c$. The performance for different systems will differ, since each has unique system-environment couplings and the incorporated time scales (e.g., τ_E) will be different. In REIC systems the timescales for one particular compound can already change when the static magnetic field is changed. This has been shown for the ZEFOZ technique in Sec. 8.2, but also happens for small fields with non-specific orientations. One effect is the (partial) change of the quantisation axis for the local host spin environment of the REI (see "frozen-core" discussion in Sec. 8.2.2 on page 96). Furthermore, the slope of the transition frequency also changes. This varies the impact of small magnetic fluctuations of the host's spins on the coherence time. The latter also differs for different hyperfine transitions at the same magnetic field. This can be seen in figure 42, showing the transitions for fields used in the following. Figure 43 shows the coherence lifetimes recorded using Hahn echos (circles) and the CPMG sequence (squares), for magnetic fields of zero (blue) and at about 8 mT (green, $\vec{B}_a$ see caption). Additionally, a FID (black) for the 8 mT field is shown.
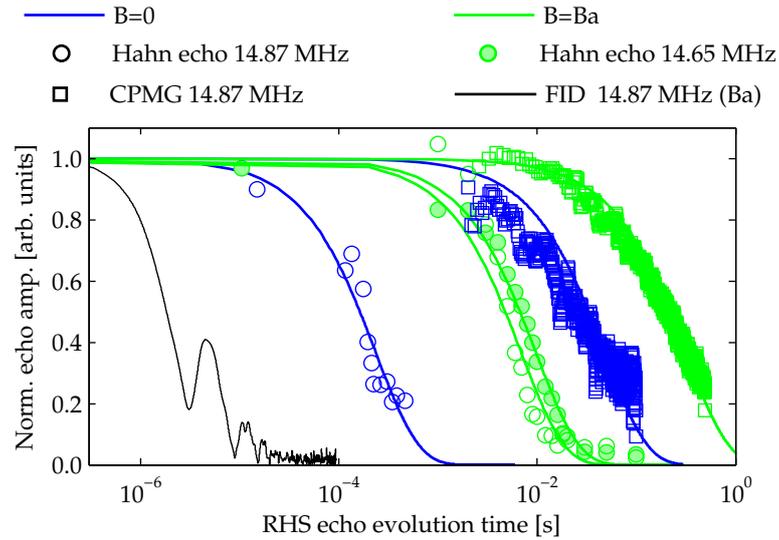
Figure 43: Comparison of the coherence lifetimes for different magnetic fields and DD sequences, using the $\left|g, \pm\frac{1}{2}\right\rangle \leftrightarrow \left|g, \pm\frac{3}{2}\right\rangle$ transitions of PrLaWO. For the blue data the field was approximately 0, whereas for the black and green data the field was $\vec{B}_a = -(1.8, 8.0, 0.0)$ mT. The black curve shows a FID decay ($\vec{B}_a$). The data represented by circles shows Hahn echo decay data for the corresponding field. The data represented by squares show examples of CPMG decay curves at those fields. For $B \approx 0$ the (nearly) degenerated $\pm 1/2 - \pm 3/2$ transition at 14.87 MHz was excited resonantly. The Hahn echo curves for the field $\vec{B}_a$ measure the T_2 of the 14.65 MHz transition (filled circles) and of the 14.87 MHz transition (empty circles, see Fig. 42b) . The pulses for the shown CPMG curves were resonant with the 14.87 MHz transition at the two fields (comp. Fig. 42a and 42b).

Note: Measured T_2 values, for fields of ≈ 5, 9 and 14 mT magnitude, at corresp. transitions at 14.8, 14.8 and 14.3 MHz, are 4.5, 5.1 and 4.7 ms. Which may be indicated as limiting order for $T_2(|\vec{B}|) \gtrapprox 5$ mT.

The effect of the static magnetic field can be seen by comparison of the Hahn echo curves (circles). Since the slopes of the 14.87 MHz transition at $B = 0$ and $\vec{B}_a$ are similar, the corresponding Hahn echo decay curves (blue circles, and empty green circles in Fig. 43) yielding coherence lifetimes of 234 μs and 6.9 ms respectively, indicate the effect of a changing quantisation axis for the local host-spin environment. The effect of the transition frequency slope with respect to field changes is demonstrated by the longer coherence lifetime of 9.7 ms measured for the 14.65 MHz transition (filled circles in Fig. 43), since this has a much smaller slope in comparison to the 14.87 MHz transition at the same field $\vec{B}_a$ (see Fig. 42b).

The CPMG DD data sets were both recorded for the 14.87 MHz transition, but at different fields. For the field $\vec{B}_a$ the CPMG (green squares, pulse delay $\tau = 80$ μs) coherence time of about 313 ms exceeds that of the Hahn echo (6.9 ms) by a factor of 45. For zero field data the factor is 205, representing an increase from 234 μs (Hahn echo) to 48 ms (CPMG, blue squares, $\tau = 40$ μs). Although the fractional increase of the coherence time at zero field was higher, the coherence time achieved for the small field of about 8 mT magnitude is significantly higher. The latter is attributed to the reduced dynamics of the dephasing environment at this field, which also allows for higher DD τ_c's to be used [8, 143].

Figure 44: PrLaWO ground state T_2 as function of the DD pulse separation τ. T_2 decay times resulting from different CPMG (green), KDD (blue) and PDD (red) data is plotted. Data for zero field are connected by solid lines, those for $\vec{B}_\alpha$ are connected by dashed lines. The data markers refer to different RF pulse lengths and frequency (see legend). The bold, grey lines indicate coherence lifetimes (values adjacent to lines) measured with Hahn echos for the two different transition frequencies ($\nu_{1,2}$) and magnetic fields. The RF pulse power levels were adjusted to obtain optimum signals for the used pulse lengths of $\tau_{p1} = 1.5$ μs and $\tau_{p2} = 4.0$ μs, and other parameters.

Influence of the Pulse Separation - T_2

The range of parameters defining the DD sequence, together with the REIC specific choice of the magnetic field and the hyperfine transition, results in a diverse parameter space for the DD characterisation. A systematic variation in all parameters was not in the scope of this work, but a selection of tested parameters suitable for the quantum memory experiments (see Sec. 8.3.2) is shown in Figure 44. The figure shows the T_2 values resulting from single exponential fits to the RHS echo decays of different DD sequences for two magnetic fields: $B = 0$ and $\vec{B}_\alpha$ (see previous paragraph). Here T_2 is plotted as a function of the pulse separation τ. This compares the efficiency of the DD sequences based on the same number of pulses per time, rather than cycles ($M \cdot \tau_c$). Since a KDD cycle consists of 20 pulses and the CPMG cycle only of two, plotting $T_2(\tau)$ is more reasonable than $T_2(\tau_c)$. Nevertheless, since the sequences are constructed to obey $\tau_c = n_{DD}\tau$ both representations are equivalent.

As introduced before the cycle time τ_c of the sequence should be as short as possible. One reason is that more rapidly following DD

Recent related NMR studies are, e.g., Ref. [8, 143].

control pulses can decouple faster dynamics of the system-environment interaction, and thus lead to more effective decoupling in real systems. The other benefit is to avoid higher order terms in Eq. 8.8 to become significant. On the other hand, by making τ_c shorter the total number of pulses $(N \cdot n_{DD})$ and the impact of their cumulative errors will increase for the same observation time $\tau_{tot} = N \cdot \tau_c = N \cdot n_{DD}\tau$. Each DD sequence compensates such errors in a different way, therefore the efficiency of some DD sequences will be less sensitive to higher error contributions for short τ. Further effects arise from the finite pulse lengths and characteristics of the RF-circuits, causing phase transient errors to be a function of the pulse length. This is evident in figure 44 for the PDD and CPMG data using pulse lengths of $\tau_{p1} = 1.5$ μs and recorded at $\vec{B}_a$ (red/green circles, dashed line). First, starting from high τ values, the $T_2(\tau)$ becomes larger towards smaller pulse separations, because the rate of control operation becomes higher. $T_2(\tau)$ will increase up to the point were the effect of the pulse errors starts to dominate, which is roughly at the maximum of the curve. The KDD data (blue circles, dashed line) is almost independent of τ attributed to its higher error compensation (see Fig. 40). On the other hand the KDD coherence times of ≈ 20 ms are much lower than those of the CPMG and PDD data, which reach almost 400 ms using the same parameters.

Comparing the data of CPMG, KDD and PDD for τ_{p1} at zero field (green, blue and red circles, solid line) it is apparent that now only CPMG shows very long decay times (up to 77 ms). KDD achieves at maximum 7.4 ms, whereas PDD reaches 3.6 ms for zero field, although PDD was very efficient for the $\vec{B}_a$ field. Nevertheless, using a different RF pulse length of $\tau_{p2} = 4$ μs the coherence life time with PDD became as large as 19 ms, showing the typical maximum for a specific τ. PDD with the pulse lengths set to τ_{p2} was also tested for the field $\vec{B}_a$. The red diamonds connected by a dashed line show the PDD data. For this measurement the RF pulses were in resonance with the low-slope transition at $\nu_2 = 14.65$ MHz (compare Fig. 42b). This PDD decay shows relatively high T_2 of up to 58 ms and as suspected the $T_2(\tau)$ maximum, although not in the range of the probed τs, seems to be at a higher pulse separation than for the higher slope transition at $\nu_1 = 14.87$ MHz. This is in contrast to the zero field situation, where the PDD decay for τ_{p1} shows much higher T_2 values, even if it was measured at the low-slope transition ν_2.

Absolute Echo Amplitude

A property that also has to be considered is the total signal after a given evolution time. In Fig. 44 the echo decay times were obtained from fits to the corresponding decay curves, assuming their decays are single exponential. This is a good approximation for the majority of the data points in a single decay curve. In some decay curves the signal amplitude oscillates during the very first DD cycles, but after only a few cycles the decays become smooth and well approximated by a single decay rate. Nevertheless, some of the decays showing long coherence lifetimes have smaller maximum signal amplitude than decays with short coherence lifetimes. Figure 45 shows the non-scaled echo decay signal amplitudes for two of the data points in Fig. 44. At zero field, using a pulse separation of $\tau = 10$ μs, the echo signal for the CPMG sequence ($T_2 \approx 73$ ms) decays much slower than for KDD ($T_2 \approx 2$ ms). Nevertheless, up to an evolution time of about 2 ms KDD preserves the
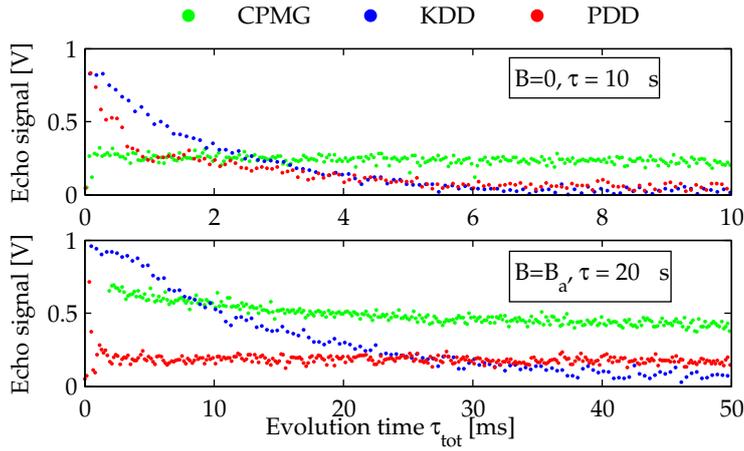
Figure 45: Non-scaled RHS echo signal amplitude at $B = 0$ and $\vec{B}_a$ for CPMG (green), KDD (blue) and PDD (red) with $\tau = 10$ μs and $\tau = 20$μs. The pulse power was adjusted to achieve a pulse length of $\tau_{p1} = 1.5$ μs and the RF frequency was $\nu_1 = 14.87$ MHz.

echo amplitude better than CPMG (see upper plot in Fig. 45). For the magnetic field set to $\vec{B}_a$ and using $\tau = 20$ μs a similar behaviour can be observed. In comparison to CPMG ($T_2 \approx 220$ ms) the KDD sequence ($T_2 \approx 21$ ms) can preserve the coherences better, up to a time of about 7 ms (see lower plot in Fig. 45). For PDD this time extends to about 25 ms. As can be seen in the figure PDD already loses most of the coherences after a few basic cycles, but then tends to preserve the residual echo amplitude for very long times with $T_2 \approx 222$ ms.

Input Phase Sensitivity

In the most general case the state of the system prior to the application of the DD sequence is supposed to be unknown. For a quantum memory the information will be coded into coherences, in general with an arbitrary phase. Thus it is important, that the DD sequences preserve the coherence independently of the "input phase". As introduced before, the performance of CPMG is known to be very sensitive to the input phase. Attributed to their design, KDD and PDD are supposed to be less sensitive to the initial state phase [105, 8, 143]. To test the input phase sensitivity of the DD sequences in PrLaWO, the RF phase for the π/2-pulse, that creates the coherences (see Fig. 41), was varied relative to the constant phase of the DD-sequence pulses. Figure 46 shows data that demonstrate the sensitivity of CPMG (green). The decays measured with the ideal CPMG input phase 0° result in about 28 times higher coherence lifetimes compared those with the worst-case input phase. With a corresponding ratio of 5, PDD (red) is less sensitive than CPMG. Nevertheless, recent NMR studies [8] showed a much lower sensitivity of PDD on the input coherence phase in adamantane. The reason for the relatively large phase sensitivity of PDD found here is not known. The KDD sequence (blue) shows effectively no sensitivity of the input coherence phase and outperforms PDD and CPMG with respect to this criterion.

Summarising the above results for the three tested sequences, KDD should be ideal with respect to the survival probability of an unknown coherence. This still holds, when only considering "storage times" up
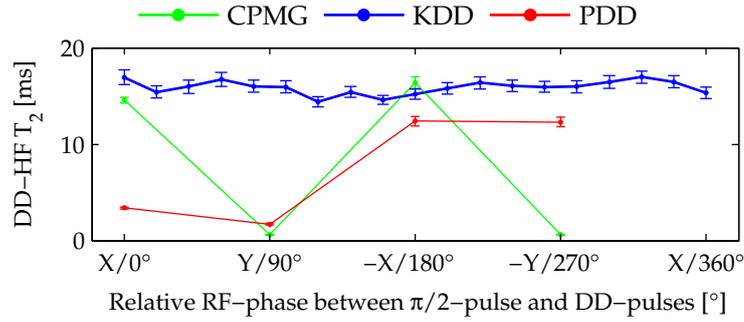
Figure 46: DD coherence lifetime as function of the input coherence phase. The abscissa is given as relative phase between the initial $\frac{\pi}{2}$-pulse and the following π-pulses of the DD sequences, with X/0° representing the default phase of the $\frac{\pi}{2}$-pulse, as defined in Fig. 41. The CPMG (green) and PDD (red) data were obtained for zero field, with $\nu_1 = 14.87$ MHz, $\tau_{p1} = 4$ µs and $\tau = 25$ µs. The KDD (blue) data was measured in an other series of experiments. There the field was set to $\vec{B}_\alpha$ and the pulse sequences parameters were ν_1, $\tau_{p2} = 1.5$ µs and $\tau = 40$ µs.

to the KDD-decay constant. There the absolute echo amplitudes, associated to the residual coherence, are almost always higher than those of PDD and CPMG (see Fig. 45). Although showing long decay times for optimum input states (see Fig. 44), CPMG is not suited for general quantum memories.

8.3.2 *Quantum Memory Testbed*

In the previous section the initial coherence was created by an RF pulse, directly within the ground state hyperfine levels. It was demonstrated that DD techniques can effectively increase the coherence lifetime for such a situation. In a quantum memory the absorption of an optical input pulse creates a pure optical initial coherence, which in a subsequent optical to spin storage (OTSS) step, has to be transferred into a ground state hyperfine coherence (see Fig. 33).

For REIC only for two EIT based experiments [95, 67] RF spin echo and DD sequences have been demonstrated to enhance the spin storage time of an optically created input coherence. Although in Ref. [95] an impressive OTSS time of more than one second was reached, both demonstrations only used a very low bandwidth input pulse of 20 µs duration. The narrow optical feature, intrinsic for the EIT scheme of these experiments with PrYSO, limited the absorbable optical bandwidth to about 50 kHz. In comparison to the MHz bandwidths of typical photon echo based storage schemes, this is already close to the homogeneous optical line width of $1/\pi T_2^{opt} \approx 2$ kHz for this compound.

Although it is generally expected that RF decoupling techniques will also improve the storage time in a photon echo based quantum memory [4, 66, 32], no demonstration of spin echo or DD enhanced OTSS times for those exist up to now. This section provides a study of the effect of RF DD techniques on the achievable total storage times in optical to spin storage experiments with PrLaWO.
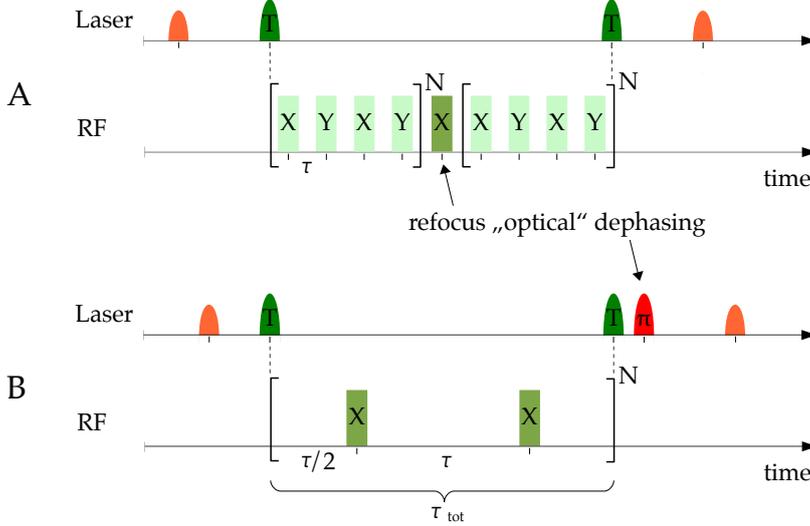
Figure 47: Basic OTSS schemes including RF hyperfine rephasing. The laser sequences show the optical input pulses (orange), the optical transfer pulses (green, T) and for the standard TPPE scheme B also the additional optical π-pulse (red, π). For the RF sequence of scheme A, besides the timing for optional DD sequences (e.g. for PDD pulses (light-green)) the position of the necessary RF π-pulse (green) is shown. In both schemes the separation between the optical transfer pulses and the adjacent RF pulses is equal to $\tau/2$, with τ representing the separation in between the RF pulses. For scheme B only the (optional) minimum RF rephasing pulses are shown.

Optical to Spin Storage Schemes

Due to its intrinsic photon noise and gain issues (see Sec. 8.1), the TPPE is a bad quantum memory scheme. Besides this, the optical to spin storage process itself, the way how optical coherences are excited and evolve in TPPE are very similar compared to the more complex photon echo based original quantum memory schemes, e.g. CRIB, AFC or ROSE. In order to reduce the experimental demands and focus more on the RF decoupling performance, the experiments presented in the following used simple TPPE based schemes as testbed for the optical to spin storage in quantum memories.

Figure 47 shows two basic prototype schemes. In both schemes, after absorption of the input pulse (orange), the initially in-phase coherences dephase due to the optical inhomogenous broadening. In the standard TPPE-OTSS scheme, represented by sequence "B" (see Fig. 47), this dephasing is refocused by an optical π-pulse. In scheme "A" the refocusing is accomplished by inversion of the ground state hyperfine levels, by a π-RF pulse in the centre of the spin storage time. For scheme B the optical refocusing pulse can be irradiated before or after (see, e.g. 56a) the optical to spin transfer pulses (green). To retrieve the stored pulse in the forward direction of the input pulse [95], for scheme B the RF pulses applied during the spin storage time τ_{tot} must in total represent a $2n \cdot \pi$-rotation, with $n = 0, 1, 2....$. To achieve the same for scheme A, the total effect of the RF pulses must represent a $(2n + 1) \cdot \pi$-rotation. For the use of DD sequences with OTSS scheme A this implies that one additional π-RF pulse has to be placed symmetrically in the centre of the τ_{tot} spin storage window, since the DD sequences typically repres-
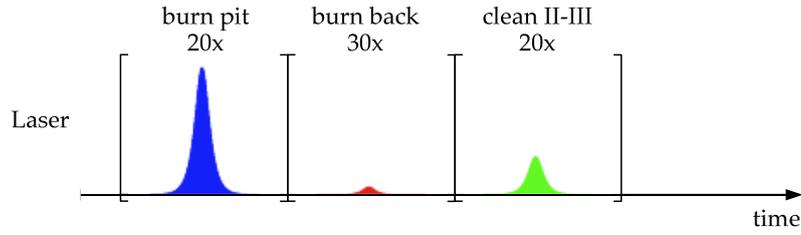
Figure 48: Spectral tailoring sequence used as preparation for each experiment. Typical hyperbolic secants pulse parameters for the pit burn pulses (blue) were: non-zero amplitude pulse length (FWHM) $\tau_{p,pit} = 0.1$ ms, total segment (cutoff) length $\tau_{co,pit} = 1$ ms, frequency range $\Delta\nu_{pit} = 25$ MHz, centre frequency relative to the $|g, \pm 1/2\rangle \leftrightarrow |e, \pm 1/2\rangle$ transition $\nu_{0,pit} = 19.69$ MHz and maximum instantaneous Rabi frequency for the $|g, \pm 1/2\rangle \leftrightarrow |e, \pm 5/2\rangle$ transition $r_{max,pit} = 1$ MHz. For the burn back pulse (red) these parameters were $\tau_{p,bb} = 0.08$ ms, $\tau_{co,bb} = 1$ ms, $\Delta\nu_{bb} = 1$ MHz, $\nu_{0,bb} = 51.48$ MHz, $r_{max,bb} = 0.1$ MHz and for the clean wrong classes pulses (green) $\tau_{p,cwc} = 0.1$ ms, $\tau_{co,cwc} = 1$ ms, $\Delta\nu_{cwc} = 12.3$ MHz, $\nu_{0,cwc} = 23.14$ MHz, $r_{max,cwc} = 0.5$ MHz. The number of pulse repetitions is quoted above the pulses.

ent effective rotations by multiples of 2π. In the standard TPPE scheme B, the π-RF pulses shown in figure 47 can directly be replaced by, e.g. PDD. Both OTSS schemes have shown almost the same DD coherence lifetimes for the same pulse parameters. In the following each time one will be chosen on the basis of the current timing or variation needs.

Pure State Preparation

For a temperature of 2 K, in thermal equilibrium all ground state hyperfine levels of PrLaWO are equally populated. The optical inhomogeneous broadening is much larger than the hyperfine splittings. Therefore, if starting from thermal equilibrium, any optical absorption would incorporate different ion classes, for which different hyperfine levels of the ground and excited state would be resonant with the optical input (see figure 49a). Since the relative oscillator strengths for optical transitions between different ground and excited state hyperfine levels differ (see Tab. 2 on page 71) , the implementation of an efficient and selective optical to spin transfer pulse is typically not possible for this situation. Furthermore, as discussed in Sec. 8.2 and 8.3.1, each hyperfine level will show different coherence lifetimes during the spin storage time. Thus, starting each experiment with only one specific ground state level being populated greatly reduces the complexity of the system and reduces the experimental demands.

To simplify the following discussion, the hyperfine transition frequencies and levels will be denoted in a short form. For example, the notation "δ_{g2}" will be used for the transition frequency between $|g, \pm 1/2\rangle$ and $|g, \pm 3/2\rangle$, and the latter energy levels will be denoted by "g1" and "g3" respectively. Optical transition frequencies will be given relative to the g1 $\leftrightarrow$e1 transition, the latter conventionally selected to be zero.

A pure and specific ground state population in PrLaWO was created by the optical spectral tailoring sequence, shown in figure 48. This preparation sequence consisted of three steps. In the first, a wide spectral window of the inhomogenous optical line was completely

emptied from absorbers by optical hole-burning. This "pit" was burned by a series of 20 identical hyperbolic secant pulses [130, 140] . Each pulse effectively excited all ions in a window of $\Delta\nu_{pit} = 25$ MHz. The total length of a single pulse segment was 1 ms, while the optically active pulse width was set to 100 µs (FWHM) (see Fig. 48). This allowed efficient population redistribution of the ground state levels, since in PrLaWO the excited state lifetime $T_1^{opt} \approx 60$ µs is much shorter than the ground state hyperfine population lifetime $T_1^{HF} \approx 16$ s. The structure burned into the inhomogenous optical line is shown in figure 49b(i).

In the second step of the preparation a "burn back" pulse excited transitions outside the transparent pit and thereby transferred some population back into the pit. By setting the relative frequencies of the pit burn and the burn back pulse, the absorption of different classes of ions can be transferred into the pit [122]. Setting the burn back frequency to $\nu_{0,bb} = \delta_{g1} + \delta_{g2} + \delta_{e1} + \delta_{e2}$ and the pit window to $\nu_{0,pit} \approx \delta_{g2}/2 + \delta_{e1} + \delta_{e2}$ with a width of $\Delta\nu_{pit} \gtrsim \delta_{g2}$, produced the situation shown in figure 49a, which is similar to the scheme described in [55]. Due to the combination of different burn and probe frequencies, only the ions of classes I to III were brought back into the pit by the burn back pulse. As shown in figure 49b(ii), the non-zero absorption within the pit window was only due to transitions starting with g1 or g3 to one other excited state level, after the burn back pulses have been applied.

In the third step of the sequence, pulses were applied, which were intended to "clean" the pit from unwanted wrong class ions. The frequencies for these pulses were set from just above the class I g1 → e5 transition to just below the pit window edge (see green bar in figure 49b (iii)). This pumped all g1 and g3 populations of the classes II and III to g5, since for both, transitions to the excited state were possible. For class I the g3 transitions to the excited state were also in resonance and thus g3 was also emptied by the clean wrong class pulses.

Finally, only the class I g1 → e5 transition was left in the apart from that transparent pit window. The optical input pulses for the OTSS experiments of the next paragraphs were in resonance with this absorption line. Therefore, only the relative optical transition strengths (see Tab. 2) for the g1 ↔ e5 (optical refocussing pulse) and the g3 ↔ e5 transition (transfer pulses) had to be considered. The maximum absorbable input pulse bandwidth is given by the width of the prepared g1 ↔ e5 absorption peak. Here this was limited to about 1.5 MHz by the chosen burn back frequency range of $\Delta\nu_{bb} = 1$ MHz. The principal upper limit for this scheme is given by the hyperfine separation $\delta_{e1} = 4.94$ MHz. Input pulses with bandwidths higher than $\approx 2\delta_{e1}$ would always excite wrong class ions in the near edge of the pit. The information of input pulses with bandwidths below $2\delta_{e1}$ will be "band-pass filtered" by the overlap with the g1 ↔ e5 absorption peak (e.g. as can be seen in figure 50).

The magnetic field $\vec{B}_a = -(1.8, 8, 0)$ mT, used throughout the whole Sec. 8.3, was chosen since this field did not change the inhomogenous absorption profiles significantly from those prepared at zero field (Fig. 49b(i) to (iii)). Although $\vec{B}_a$ lifted the degeneracy of the hyperfine levels, their Zeeman splittings were sufficiently low (see Fig. 42b), so that the finally prepared peak in the pit still represented only g1 ↔ e5 transitions.

$\delta_{e2} = e5 - e3 = 7.23$ MHz
$\delta_{e1} = e3 - e1 = 4.94$ MHz

$\delta_{g2} = g1 - g3 = 14.87$ MHz
$\delta_{g1} = g3 - g5 = 24.44$ MHz

——— burn pit ——— burn back ——— clean II–III ——— probe
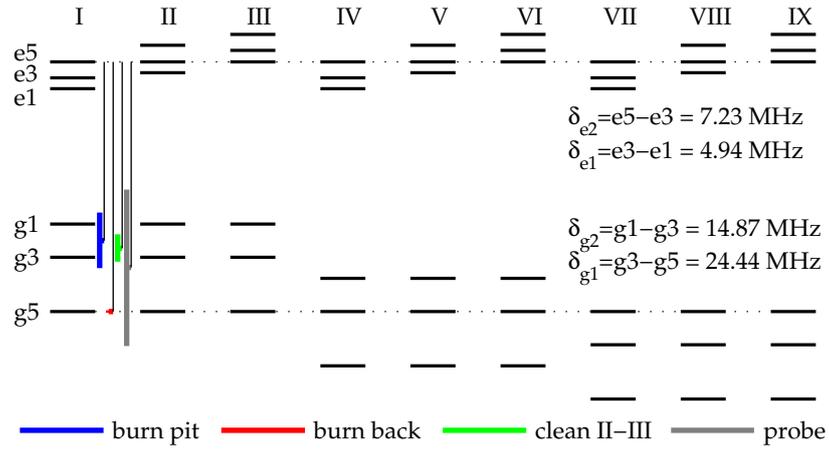
(a) Different ion classes hyperfine level schemes, relevant for the preparation spectral tailoring scheme. The dotted horizontal lines (burn back frequency) are used to discriminate between the classes.
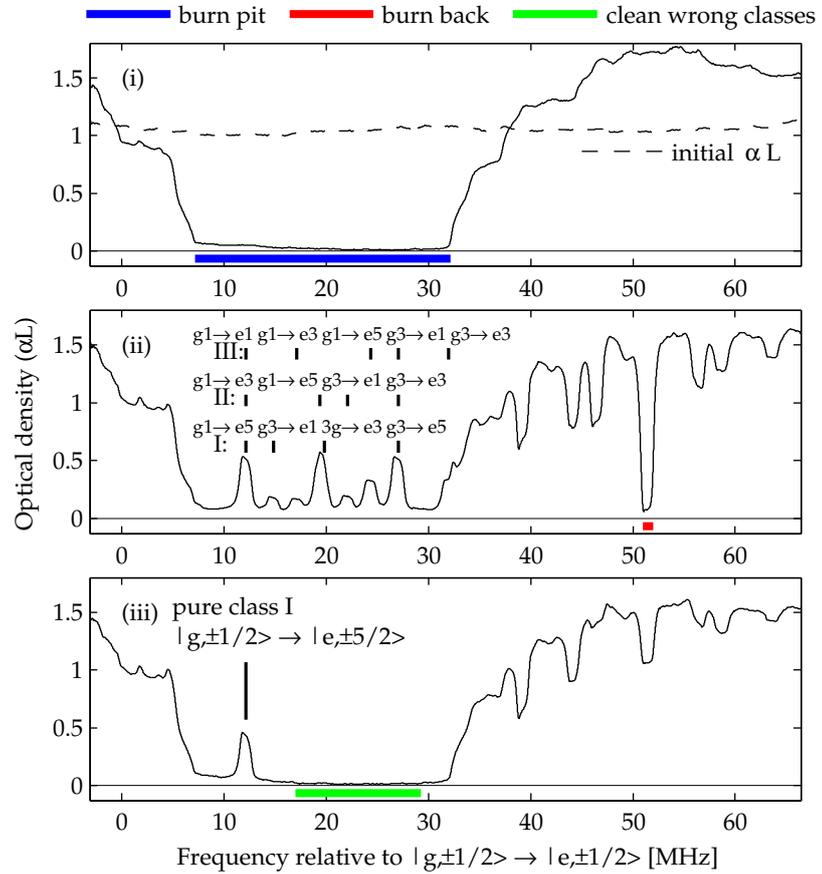
(b) Tailored inhomogenous absorption line. The absorption shown in (i) was probed after the pit burn pulses have been applied only. The dashed line shows the absorption for (approximate) thermal equilibrium population. (ii) and (iii) show the situation after pit burn and burn back pulses, and after all three preparation steps respectively. The vertical sticks indicate the optical transition frequencies for the different ion classes (see Fig. 49a). The probe beam was chirped within 1 ms over the full 70 MHz range shown. It had a Rabi frequency of 20 kHz for the g1 ↔ e5 transition.

Figure 49: Pure state preparation using the spectral tailoring sequence from Fig. 48. The hyperfine level scheme (a) and the probe absorption (b) are given for zero magnetic field. The vertical (a) and horizontal (b) bars (coloured) indicate the resonant range of the pit, burn back, clean wrong classes and (a) probe pulses. The different hyperfine levels are given in simplified notation, e.g. "e5" stands for $|e, \pm 5/2\rangle$.
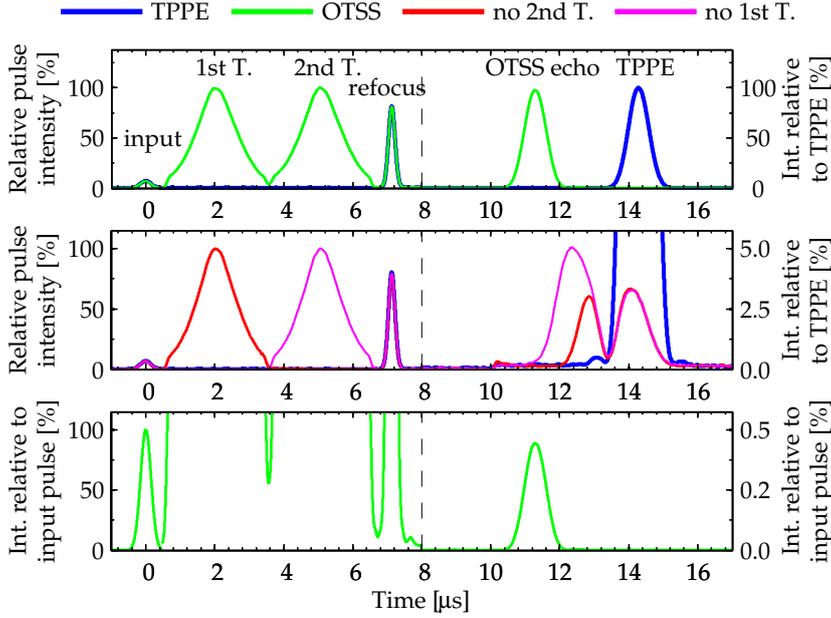
Figure 50: Optical to spin storage and retrieval efficiency. The upper two traces show comparisons of a TPPE experiment (blue thick lines) to a full OTSS sequence (upper trace, green) and two OTSS experiments with only one of the transfers being active (middle, red and magenta). The bottom trace compares the input pulse intensity to the OTSS echo intensity. In all plots the total evolution times, $\tau_{TPPE} = \tau_{opt} = 7$ µs and $\tau_{OTSS} = \tau_{spin} + \tau_{opt}$ with a spin storage time $\tau_{spin} = 3$ µs and $\tau_{opt} = 4$ µs, were the same. The data on the left and right side of the vertical dashed line refer to the corresponding side's scales. The input Gaussians had $\tau_{p,in} = 0.5$ µs pulse width, $\tau_{co,in} = 1$ µs cutoff length and $r_{max,in} = 0.5$ MHz maximum instantaneous Rabi frequency. The transfer pulse parameters were $\tau_{p,T} = 1.5$ µs, $\tau_{co,T} = 3$ µs, $\Delta\nu_T = 2$ MHz frequency width, $\nu_{0,T} = 27.1$ MHz centre frequency relative to g1 →e1, $r_{max,T} = 1.1$ MHz and those of the optical refocusing Gaussians were $\tau_{p,\pi} = 0.294$ µs, $\tau_{co,\pi} = 1$ µs and $r_{max,\pi} = 1.7$ MHz. The Rabi frequencies are given for the resonant transitions.

Optical to Spin Storage Efficiency

Besides a bandwidth mismatch, the finite optical depth of the peak and the efficiencies of the transfer and refocus pulses limit the total efficiency of the memory. Figure 50 shows the optical transients of the input, transfers and refocus pulses and relates their amplitudes to the output two pulse photon echo and the optical to spin storage echo. The optical input and the π-pulse of the shown TPPE and OTSS sequences had the same timings. Having both transfers active in the OTSS sequence (green, upper plot) no echo was visible at the TPPE time (blue transient). Since the resulting OTSS echo had 97.5 % intensity compared to the TPPE echo (upper plot), the conversions of the optical input coherence into a spin coherence and back again to the optical transition were rather effective.

The plots in the centre of figure 50 show the effect of having only one transfer active in the OTSS scheme. Already one transfer pulse reduced the TPPE echo to about 3 % of its original intensity, which directly

demonstrates the good hyperbolic secants transfer pulse efficiency [130, 140].

In the bottom plot of Fig. 50 the absolute intensity of the input pulse is compared to the OTSS echo. The retrieved echo (intensity of TPPE≈OTSS) had only about 0.45 % of the input pulse intensity. The low absolute efficiency can mainly be attributed to the low optical density of the sample and the generally low efficiency of the photon echo in this case [148]. Furthermore, a fraction of the input pulse was not absorbed due to a bandwidth mismatch, since the input pulse bandwidth was ($1/\tau_{p,in} \approx 2$ MHz) larger than the g1 ↔ e5 absorption peak line width. The duration of the TPPE and the OTSS echo, which are longer than the input pulse duration (see e.g. bottom trace of Fig. 50), show the effect of the bandwidth mismatch. In order to use the full available absorption of the prepared peak, the bandwidth of the input pulse was usually chosen higher than the peak width.

Although the low absolute memory efficiency yielded only low SNR for the OTSS echo, this testbed scheme still allowed studying of the effect of DD sequences on the stored coherences. For most of the following experiments similar optical pulses have been used. The hyperbolic secants pulses showed the best transfer efficiency, but in cases when the pulse duration was critical, they were replaced by shorter Gaussian pulses of π-area as in the following interference experiments.

Preservation of the Optical Phase Information During the Spin Storage

Besides storing the energy of the input pulse, which in principle was verified in the last paragraph, accurate storage of the input pulse phase is a crucial requirement for a quantum memory [148]. This property was demonstrated to be fulfilled by photon echo based protocols in several experiments, e.g. [145, 144, 151, 30]. The preservation of the optical phase information after enhancing the spin storage time by RF DD techniques in a related protocol, is demonstrated for the first time by the results presented in the following.

To see an effect of the input pulse phase, two input pulse modes with different phases were stored in the memory, using the sequence shown in Fig. 51a. Both input pulses (1 and 2) were temporally separated by 1 μs, before being absorbed by the REIC. Since the memory efficiency was low, both input pulses were only partly absorbed, and thereby each excited about the same number of absorbers. The coherences created by both pulses were transferred to the ground state hyperfine levels by two separated transfer pulses (a and b), following the inputs with the same separations (1 μs). Both, transfer and input pulses, were realised by Gaussian pulses. Due to their finite efficiency, each of the transfer pulses a and b transferred only a fraction of the input coherences 1 and 2 to the ground state hyperfine levels. The later rephasing of the optical coherences was accomplished by the usage of the scheme A storage protocol (see Fig. 47). To retrieve the OTSS echos, after application of the RF DD pulses, a single transfer pulse bought the information of both input pulses back to the optical domain. Since each of the inputs 1 and 2 have been partly transferred by the pulses a and b, after the last transfer pulse, three two-pulse-echos will be observed at timings separated by 1 μs and denoted by 2a, 1a+2b and 1b. Figure 51b shows the intensity of the OTSS echo at the timing 1a+2b. There the two-pulse-echos from input 1 and transfer a, and that due to input 2 and transfer b coincide, which leads to interference if the phase was preserved.

As noted before, here Gaussian pulses were used, since they allowed for better pulse and echo separations compared to (usually longer) hyperbolic secants pulses.
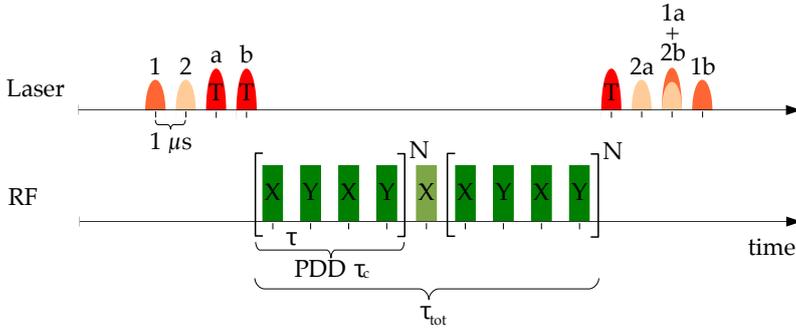
(a) Sequence for the input pulse interference experiment . All optical pulses are Gaussians with cutoff durations of $\tau_{co} = 1$ µs. The sub-$\pi/2$-area input pulses (1 and 2, orange) had $\tau_{p,in} = 0.2$ µs and the π-area transfer pulses had $\tau_{p,T} = 0.35$ µs.
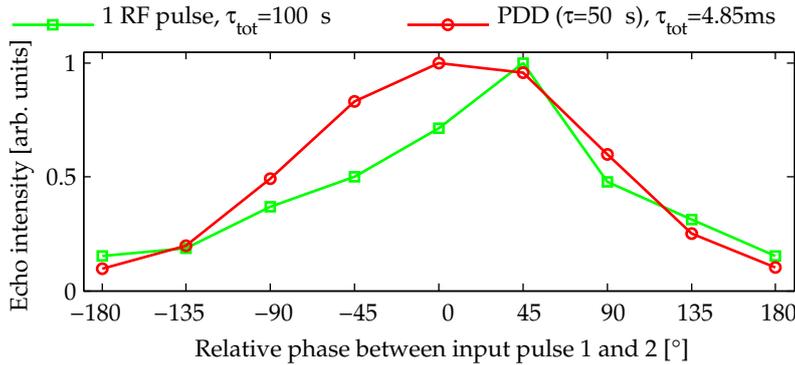
(b) Intensity of the OTSS echo at the interference position (1a+2b, see Fig. 51a), plotted as a function of the relative phase between the optical input pulses. The data plotted in green, was recorded for a low magnetic field of $\vec{B}_b = -(0.13, 0.52, 0)$ mT, using just one RF π-pulse in the centre of the spin storage time $\tau_{tot} = 0.1$ ms. For the other data (red) the field $\vec{B}_a = -(1.8, 8, 0)$ mT was used and the interference was observed after a storage time of $\tau_{tot} = 4.85$ ms, enabled for by a total of $N = 2 \cdot 12$ PDD cycles using $\tau_p = 4$ us and $\tau = 50$ µs. Each point represents an average of 100 echos.

Figure 51: Test of the preservation of the optical phase information after applying a RF rephasing pulse or additionally DD sequences in the spin storage phase.

Using PDD during the spin storage allowed recording of the echo interference at a storage time of $\tau_{tot} = 4.85$ ms, which is about 60 times higher than the longest reported storage time for a photon echo based quantum memory experiment up to now [32][†], and about 1200 times longer than for any published REIC photon echo based memory interference experiment [66, 137].

In the case of destructive interference the echo diminished to about 10 % of the constructive interference echo intensity, representing an interference fringe visibility of $V \approx 82$ %.[††] This demonstrates that RF-PDD spin decoupling is able to preserve the relative phase information of the optical input pulses for long periods of time.

Using a low field of $\vec{B}_b = -(0.13, 0.52, 0)$ mT, the interference was also recorded using only the required π-RF pulse for storage scheme A (Fig. 47). With this field and a single RF-pulse, a storage time of $\tau_{tot} = 100$ µs yielded about the same intensity for the OTSS echo as in the case of using the PDD sequence. Although the visibility of the interference $V \approx 73$ % is comparable to the PDD experiment, the shape of the interference echo intensity, with respect to the relative input

[†] Note, Damon et al. [32] used Er^{3+}:YSO at a field of 2.2 T, which offered very long decay times: $T_1^{opt} \approx 10$ ms, $T_2^{opt} \approx 230$ µs.

[††] $V = \frac{I_{max} - I_{min}}{I_{max} + I_{min}}$
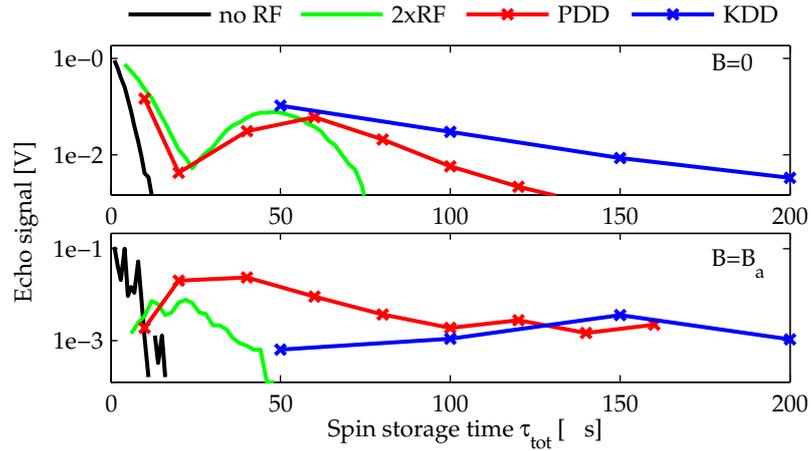
Figure 52: Best OTSS decays for using a RF π-pulse length of $\tau_p = 1.5$ μs (zero field) or $\tau_p = 2.0$ μs ($\vec{B}_a$). All data was recorded using the OTSS scheme B (Fig. 47). The pulse separation for the PDD and KDD sequences was $\tau = 5$ μs. Due to the fast decay of the echo, for KDD the echo intensity was recorded after each 5th RF pulse (starting after the first 10 pulses), instead of only recording after a full cycle consisting of 20 pulses.

phase, became asymmetric. This may be attributed to a worse relative phase preservation, due to the usage of only one rephasing RF pulse in comparison to a PDD.

Although the interference visibilities are satisfying, they may already be limited by the SNR of the echo signal. For the storage times used, in both cases, the echo signal was only about 1 to 5 % of the extrapolated echo signal at $\tau_{tot} = 0$. This is attributed to the much lower coherence lifetimes observed in OTSS scheme compared to the those measured with the DD-RHS technique (Sec. 8.3.1).

Effect of the RF Pulse Width on the OTSS Coherence Lifetimes

The decay times of OTSS echos can be enhanced by the use of DD techniques, but unfortunately the best achieved OTSS coherence lifetimes are (at best) about 10 times smaller than those achieved in the RHS based DD experiments obtained under the same conditions.

One initial assumption attributed this to potentially too low excitation bandwidths of the RF pulses. By improvement of the tuned RF circuits, the pulse length for a RF pulse of π-area could be reduced from the initial value of $\tau_p = 4$ μs to $\tau_p = 1.5$ μs, which increased the bandwidth by about 2.5 times. As discussed in Sec. 8.3.1 the higher bandwidth RF pulses resulted in very long coherence times up to 0.4 s for the field $\vec{B}_a$. In contrast at zero field, the RHS coherence times using $\tau_p = 1.5$ μs for KDD and PDD became worse compared to the $\tau_p = 4$ μs results (see Fig. 44). As shown in figure 52 for the OTSS scheme this became even more pronounced.

The decays shown in figure 52 represent the best obtained using RF pulse lengths of $\tau_p = 1.5$ μs for zero field and $\tau_p = 2.0$ μs for $\vec{B}_a$. In order to see at least any reasonable OTSS echo intensity the pulse separation for PDD and KDD had to be reduced to $\tau = 5$ μs. Without any RF rephasing (black), the OTSS echo decayed on a time scale of $5 - 10$ μs. PDD (red) and KDD (blue) extended the coherence lifetime
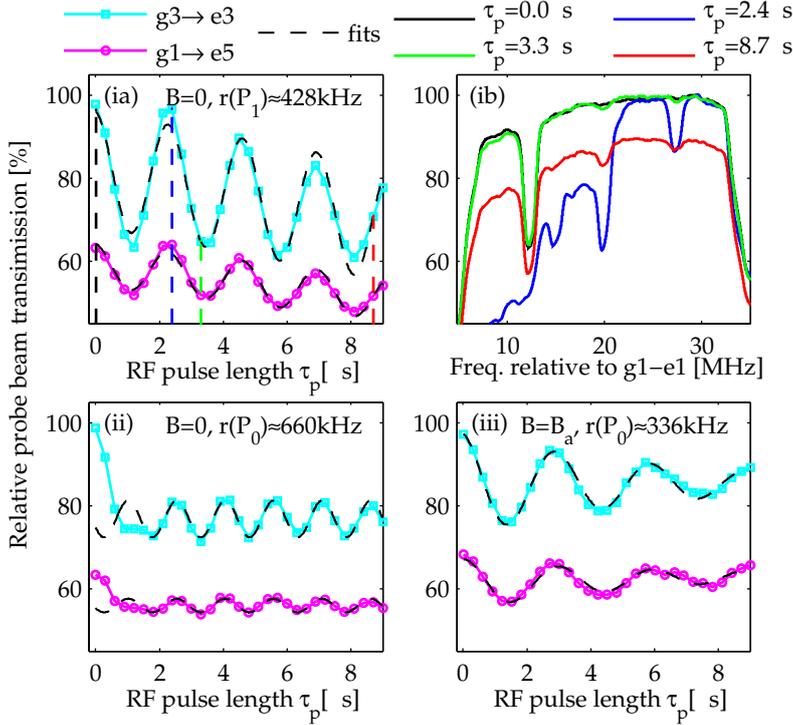
Figure 53: The effect of a preceding RF pulse on the pit structure. A single RF pulse was applied 1 ms before the probe chirp started. The cyan and magenta lines in (ia), (ii) and (iii) represent the probe absorption at the $g3 \rightarrow e3$ (≈ 19.8 MHz) and the $g1 \rightarrow e5$ (peak, ≈ 12.3 MHz) positions of the pit, recorded as a function of the RF pulse length. The plot in (ib) represents some of the source data for plot (ia), showing the pit structure after an RF pulse of the length indicated by the colour (see legend) was applied. In (ia) the corresponding pulse lengths of (ib) are indicated the by the vertical dashed lines of the same colour. $r(P)$ denotes the fitted Rabi frequency of the observed oscillations. For (ii) (zero field) and (iii) ($\vec{B}_a$) the RF powers were the same (P_0). For (ia) an attenuator was placed between amplifier and RF resonance-circuit.

to higher values than the pure rephasing RF pulses (green) did, but the echo intensity dropped down to unusable levels after a few RF pulses have been applied.

Although the reduction of the coherence lifetime due to too high pulse bandwidths is not yet fully understood, there is some indication the greater impact for the OTSS scheme may be attributed to a significant admixture of wrong class ions at the position of the prepared spectral feature. Figure 53 shows the absorption of the pit-structure recorded directly after application of an RF pulse. The pulse was resonant with the $g1 \rightarrow g3$ transition, as in the DD sequences.

As can be seen in part (ib) of the figure, the RF pulse pushed different ion classes from the lower frequency edge of the pit into the transparent window. Whereas for pulses with reduced Rabi frequency (see (ia), $r(P_1) \approx 428$ kHz $\rightarrow \tau_p \approx 2.3$ µs) the reversibility of this, for pulse lengths corresponding to $n \cdot 2\pi$-area, was relatively good, it was worse for higher power pulses (see (ib), $r(P_1) \approx 660$ kHz $\rightarrow \tau_p \approx 1.5$ µs). Nevertheless, the initial conditions were never reached again for longer pulse durations.

Ideally the transmission on the g3 →e3 transition should approach the initial value of about 100 % for pulse areas of $n \cdot 2\pi$, but in fact for the high power pulse (Fig. 53(ii)) its transmission approached about 75 % after 1.5 μs ($\approx \pi$) and then stayed below at maximum 81 %. The reason for the lower amplitude of the population changes for pulses longer than $\tau_p \approx 1.5$ μs at this RF power level was not yet identified.

For the data recorded at $\vec{B}_a$ (Fig. 53(iii)) a significant decay of the RF driven population changes was observed. This is reasonable, since the field lifted the hyperfine level degeneracy and the transitions between the different levels have different Rabi frequencies for the same RF pulse power. The slower decay of the RF driven population changes in Fig. 53(ia) is mainly attributed to the inhomogenous line width of the g1 →g3 (≈ 105 kHz) hyperfine transitions. Using a 1.5 times higher Rabi frequency (Fig. 53(ii)) almost no decay was observed.

In conclusion, potentially the longest OTSS echo decays could be observed in the series of experiments using $\tau_p = 4$ μs, since here the admixture of wrong class ions into the pit window is minimal. Wrong class ions, which are shifted into the pit by the RF pulses during the spin storage time, may be excited by the subsequent (last) optical transfer and refocusing pulse. From REIC related literature it is known, that optical excitations of neighbouring REI can cause abrupt and random shifts of the target-REI optical transition frequency over various mechanisms [37]. Since these laser pulse-induced "instantaneous spectral diffusion" frequency shifts were not present from the beginning of the optical input coherence dephasing, the rephasing of the retrieved echo would become incomplete [38]. Thus, for the OTSS scheme in conjunction with RF-DD pulses, this effect may lead to reduced OTSS coherence lifetimes compared to the DD-RHS ground state coherence lifetimes.

DD Enhanced OTSS Coherence Times

Figure 54 shows examples for the best achieved OTSS decays (a) and the OTSS coherence lifetime as function of the DD pulse separation (b). The longest achieved OTSS coherence lifetimes were between $T_2 \approx 1-2$ ms, which is one order of magnitude shorter that for the RHS-DD experiments, using the same parameters (see Fig. 54b). This applied for all tested magnetic fields. At zero field PDD increased the OTSS coherence time to about 1.4 ms, which is about 40 times the decay time measured with a single RF. For $\vec{B}_a$ PDD did not increase the decay time above 1.9 ms[†], which is about the same as a single refocusing RF pulse could yield.

The data collected for different PDD pulse separations τ (red), show a plateau of $T_2(\tau)$ for $\tau \gtrsim 60$ μs. In comparison, the RHS-DD data clearly shows a reduction of $T_2(\tau)$ due to too slow control operations for longer τ, noting a small positive curvature for the highest τ values. This, and the OTSS plateau, indicate that for the OTSS scheme the coherence time is limited due to other mechanisms than in the RHS experiments.

Limiting Mechanisms for the OTSS Coherence Lifetime

A first suspicion for the generally lower OTSS coherence lifetimes was a temperature increase due to the RF pulses. In comparison to the hyperfine T_2^{HF}, the optical T_2^{opt} is very sensitive to small changes of the sample temperature. For the particular experimental conditions, a

[†]*One recorded OTSS decay at $\vec{B}_a$ had a decay constant of $T_2 = (3.8 \pm 0.3)$ ms, but repeating the experiment with the same parameters at later times yielded only values of $T_2 \approx 1.9$ ms.*
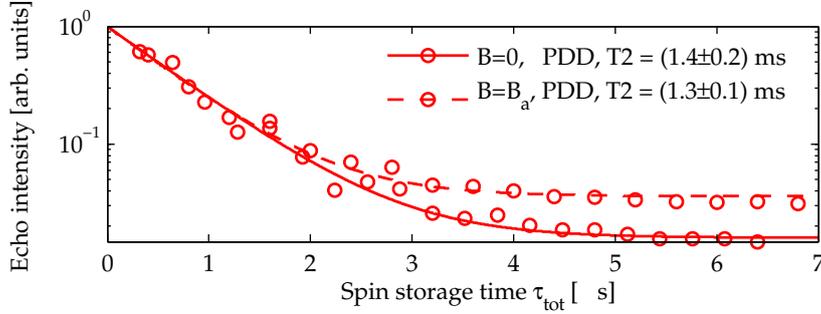
(a) Normalised echo intensity as function of the spin storage time τ_{tot}. The data measured at zero field used a pulse separation on $\tau = 80$ µs for the PDD sequence, that recorded at $\vec{B}_a$ used $\tau = 100$ µs. The lines represent single exponential decay rate fits of the data, which include an offset term. The different offsets result from similar noise but about two times smaller absolute echo signals for the $\vec{B}_a$ data.
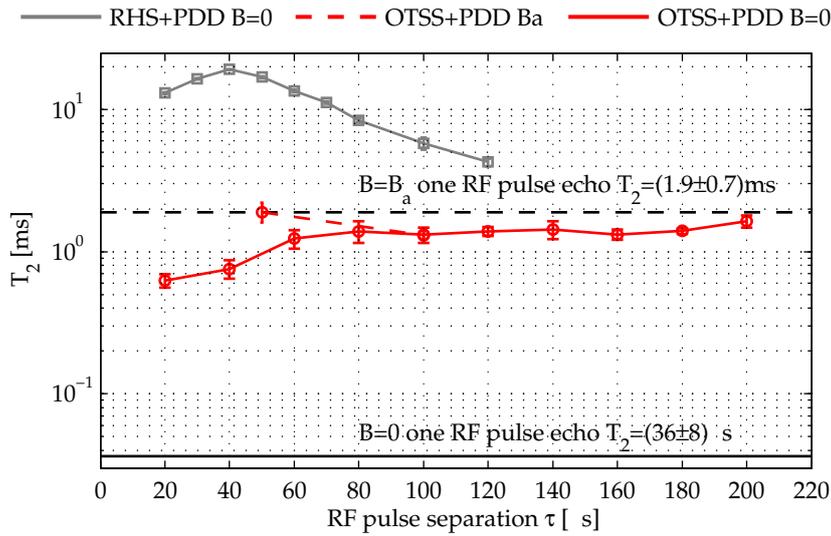
(b) Coherence lifetimes as function of the PDD pulse separation τ. The T_2 times follow from single exponential fits to OTSS (red) and RHS based (grey, reproduced from Fig. 44) data. Solid lines indicate data recorded for zero field, the dashed line indicates $\vec{B}_a$. The black horizontal lines indicate the coherence times resulting from a OTSS scheme A (Fig. 47) decay without the usage of DD pulses, but with a single RF pulse refocusing the hyperfine inhomogeneous dephasing.

Figure 54: Best achieved OTSS coherence lifetimes times. All shown data was recorded using the OTSS scheme B (Fig. 47), with RF pulse lengths of $\tau_p = 4$ µs.
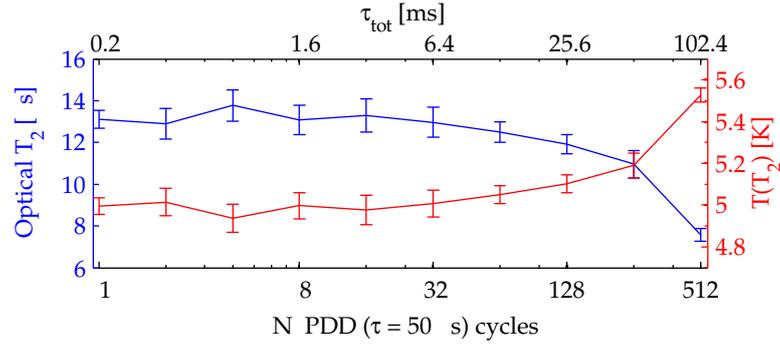
Figure 55: Optical coherence time T_2^{opt} and sample temperature deduced from TPPE decay measurements after N PDD cycles have been applied. ($\tau_p = 4$ μs, $\tau = 50$ μs).

temperature increase by about 2 K would reduce T_2^{opt} from ≈ 16 μs to about 1 μs. In the OTSS scheme it is not avoidable that the stored coherence will evolve as an optical coherence after the last transfer pulse. In the experiments presented here the minimum optical evolution time after the last transfer was about 1 μs, which in conjunction with $T_2^{opt} \approx 1$ μs would reduce the apparent OTSS coherence lifetime considerably.

Since the sample was mounted on a coldfinger, the values derived from the temperature sensors are not necessarily conclusive for the real sample temperature. Furthermore, a transport of the RF deposited heat might happen faster than the sensors are readout. In order to measure a potential temperature increase due to the RF pulses, the optical TPPE coherence time was measured directly after applying a number of RF PDD cycles. A $T_2^{opt}(T)$ calibration curve for PrLaWO[†], from experiments using a bath cryostat, was obtained from Philippe Goldner's laboratory at LCMCP and used to calibrate the sample temperature in Dortmund based on the measured T_2^{opt} values. Figure 55 presents the results. Although a heating due to the RF pulses was observable, for the storage times of $\tau_{tot} \lesssim 10$ ms surveyed above, the increase of the sample temperature was well below 0.5 K and could not explain the low OTSS coherence lifetimes.

A major difference between the RHS-DD experiments and the OTSS scheme is that the input coherence in the latter is created by pure optical means. This implies that the relative phase of the optical input pulse and the RF pulses will typically change for each execution of the pulse sequence. Here the repetition rate for the pulse sequences was between $5 - 10$ Hz. In between two executions the laser will change its phase with very high probability (see Sec. 4.1.2). This represents one reason to use input coherence phase insensitive sequences like PDD or KDD. Another effect due to the optically created input coherence is that the "nuclear spin" memory has to store a distribution of optical coherences. Beginning from the moment of absorption, the optical coherences start to dephase, resulting in a quasi isotropic transverse phase distribution after only a few $\tau_{p,in}$[††]. Although the high transfer pulse efficiency demonstrated an effective transfer of the full optical phase distribution to the hyperfine levels (Fig. 50), for the pure nuclear ground state levels this phase is just random. Any change to the (optical) distribution will result in a lower echo intensity after the last transfer

[†] $T_2^{opt}(T[K]) \approx (9.7 \cdot e^{(\frac{T}{0.6})} + 37100)^{-1}s$

[††] Or a few times [1/(absorption peak width)].
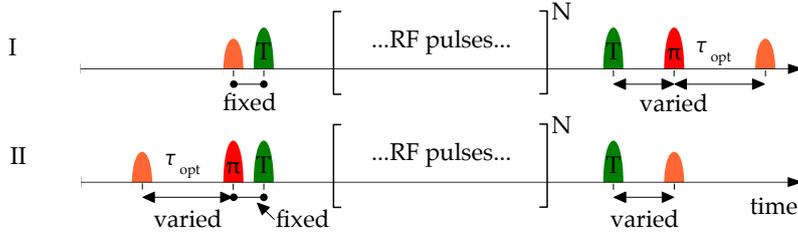
(a) Optical pulse sequences to test the effect of a fixed (I) or variable (II) optical input phase distribution in the OTSS scheme utilising DD techniques. In both cases the optical T_2 is measured by variation of the effective separation τ_{opt} of the input (orange) and refocus pulse (red). During the spin storage, between the transfer pulses (green), DD sequences on the RF channel (not shown) are applied.
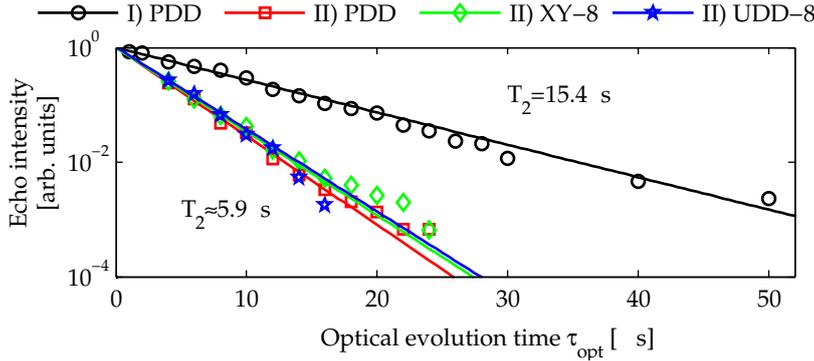
(b) Comparison of $T_2(\tau_{opt})$ decays for sequence I (black), using PDD, and sequence II, using ether PDD (red), the XY-8 (green,) or the UDD-8 (blue) RF-DD sequence. The solid lines represent single exponential fit (no offset term) to the data.

Figure 56: Probing the effect of a varying optical input phase distribution.

of the OTSS sequence. Since the temporal separation between input pulse and first transfer determines the "width" of the optical phase distribution, the effect of a varying input phase distribution can be probed independently of the potential effect of instantaneous spectral diffusion due to excited wrong class ions (Fig. 53). Figure 56a illustrates two suitable pulse sequences.

In sequence I the separation τ_{opt} between the second transfer (green, T) and the optical π-refocusing pulse (red) is varied and the intensity of the OTSS echo is recorded as a function of τ_{opt}. During the spin storage (between both transfers) a fixed number of RF-DD cycles is applied to the ground state hyperfine transition. Since the separation between input and first transfer pulse is fixed for all experiments, the DD sequence is always subjected with the same optical input phase distribution. The OTSS echo intensity should scale with the usual $T_2^{opt} = T_2(\tau_{opt})$ time, if other effects, e.g. instantaneous spectral diffusion, are of minor importance.

Sequence II differs in that the pulse timing τ_{opt} is varied before the spin storage phase. To do that, the optical refocus pulse was moved between input and first transfer pulse. Variation of τ_{opt} now will change the optical phase distribution, because the distance between the optical input and the first transfer pulse changes as a function of τ_{opt}. If the DD sequence can not preserve arbitrary optical phase distributions equally well, the refocusing after the second transfer will be corrupted, resulting in $T_2(\tau_{opt}) < T_2^{opt}$. Figure 56b demonstrates that the latter is

the case. Furthermore, the effect seems to be independent of the DD sequence used. Here PDD (red) was compared to XY-8, which is built by a concatenation of PDD and has a higher order pulse error correction [57, 136], and to UDD-8, which uses non-equidistant pulses [150] and showed a higher decoupling efficiency in systems with high frequency or strong cutoff environment noise [14, 126, 135]. All three decays showed almost the same decay constant. The experiment demonstrates the inability of all three DD sequences to preserve an arbitrary optical phase distribution perfectly. Since all have the same decay constants, this further indicates a more general underlying mechanism.

Other possible mechanisms, which randomise the optical phase distribution during the spin storage time, might be potential spectral diffusion processes. Those could arise from an intrinsic physical mechanism in PrLaWO or might be triggered by some effect of the DD-RF pulses. Experiments to probe for such spectral diffusion processes are in preparation.

SUMMARY

Precisely characterised rare earth ion crystal Hamiltonian parameters allow to exploit the full potential of these optical compounds. One specific application is the storage of the quantum information carried by optical photons into a rare earth ion doped crystal. The quantum storage protocols require precise optical controls for efficient quantum state preparation and manipulation. Furthermore, long storage times of the quantum information in the nuclear spin levels of the system is highly desired and can be offered by the use of static magnetic field- and RF-decoupling techniques. The developed magneto-optical setup allows to control the systems with optical, RF and static magnetic fields at the same time. It offers high precision, stability and reproducibility in all components and allows combined use of various magneto-optical techniques without the need of further adaptation.

Using this setup the full characterisation of the spin Hamiltonians of three rare earth ion compounds is demonstrated. The principal axis values and tensor orientations of the effective quadrupole and Zeeman tensors are determined with high accuracy using precisely controlled magnetic fields to record high resolution RHS spectra for about $250 - 500$ field orientations for each sample. The large number of 13 Hamiltonian parameters and their complicated interdependency requires more suited fitting methods than ordinary least squares regression. A method based on simulated annealing is implemented, which compares the measured RHS line positions to calculated line position based on trial Hamiltonian parameter sets. The implementation robustly yields Hamiltonian parameters representing a global minimum solution of the optimisation for each of the three investigated samples. The full analysis procedure, the Hamiltonian model and the used conventions are described in detail. This allows other research groups to use the presented results.

The new characterisation of the PrYSO, presented in this work, has a three times smaller residual deviation between ground state data and fitted model than the former characterisation by Longdell et al. [93]. Furthermore the relative optical transition strengths form purely optical measurements fit almost perfectly to the calculated values using the new PrYSO characterisation. Since the underlying nuclear wave function overlap is very sensitive to the relative tensor orientations in the ground and excited state, this verifies the results. This emphasises the justification for the new PrYSO characterisation, since the former characterisation by Longdell et al. did not match with the experimental relative optical transition strengths. The importance of the new characterisation becomes evident, since PrYSO is so far the most frequently used compound for quantum memory prototype implementations. Quantum storage experiments with a high level of complexity or experiments that incorporate optimal control techniques, may greatly profit from the fully characterised Hamiltonians, since they allow accurate simulation during the planning.

In the case of PrYAP the first full characterisation using independent effective quadrupole and Zeeman tensor orientations is presented. The literature investigating PrYAP uses an approximation, which assumes collinear principal axis systems for the effective quadrupole and Zeeman tensor. For the ground state a good agreement of this approximation is confirmed by the presented characterisation. The approximation is shown to be invalid for the excited state, since the principal z-axes of the effective quadrupole and Zeeman tensor share an angle of $\approx 46°$. The relative optical transition strengths, following from fitting of zero field hole burning data and those calculated from the presented characterisation, are in almost perfect agreement, which verifies the accuracy of the tensor orientations. For non-zero magnetic fields the new model predicts the hyperfine transition frequencies with a much higher accuracy than the approximation used in the literature. This is especially evident for the excited state, where the residual deviation between observed and calculated transition frequencies is more than five times smaller when the new model is used.

The presented spin Hamiltonian characterisation of the relatively new compound PrLaWO determines the first time the gyromagnetic factors of the Zeeman tensor and the relative orientations of the effective quadrupole and Zeeman tensors of the ground and the excited state. Again the calculated relative optical transition strengths are in almost perfect agreement with those from pure optical measurements. Nevertheless, the almost perfect match of predicted and measured relative optical transition strengths for all three investigated samples should not be understood as a matter of course. The long standing contradiction in this point for the former spin Hamiltonian characterisation of PrYSO demonstrates this. In conclusion the characterisation procedure proves to be very reliable in the specific way it is implemented in this work.

The RHS spectra recorded for all three compounds are analysed for their inhomogeneous line widths. The $|\pm 1/2\rangle \leftrightarrow |\pm 3/2\rangle$ and $|\pm 3/2\rangle \leftrightarrow |\pm 5/2\rangle$ hyperfine manifolds show different inhomogeneous broadening, which is attributed to the larger relative impact of the inhomogeneously broadened effective quadrupole constants in the matrix elements of the Hamiltonian for the $|\pm 3/2\rangle \leftrightarrow |\pm 5/2\rangle$ manifold. A further scaling with the magnitude of the Hamiltonian principal values is discussed by comparison of the ground and excited state data of each sample, and by comparison of the samples to each other.

Utilising the characterisation data for PrLaWO ground state zero first order Zeeman transitions are numerically identified and one ZEFOZ transition is experimentally verified in an independent laboratory. Compared to zero field, an increase from ≈ 0.25 ms to 158 ms for the hyperfine coherence time is demonstrated by using the ZEFOZ-field and -transition. The increase by a factor of 630 is an important result under two distinct aspects: Firstly it is the first demonstration of the ZEFOZ technique in a compound other than PrYSO. Secondly it shows that also rare earth ion compounds with a high magnetic noise contribution from the host crystal can yield long coherence times. Therefore, such compounds should also be considered for implementation. Some compounds, previously excluded due to their high intrinsic noise, may offer other advantageous properties like a higher optical depth.

An analysis of spin echo decays of the ZEFOZ transition with optimum ZEFOZ magnetic field and slightly detuned fields indicates that

the magnetic fluctuations from the host spins at the praseodymium site in PrLaWO are only of the order of ≈ 1 µT. The same analysis with PrYSO data from the literature yields ≈ 3 µT. This value is in contradiction to a previous ZEFOZ-based estimation (≈ 14 µT) in the literature, but in very good agreement with a microscopic approximation (≈ 4 µT) form the same research group.

The PrLaWO spin echo decays close to the ZEFOZ field show a modulation with ≈ 25 Hz. The modulation is similar to effects one would expect for a Pr-host spin superhyperfine interaction, but the mechanism for PrLaWO remains unclear. In PrYSO such effects disappear for fields $\gtrsim 2$ mT, which is attributed to a frozen-core, whose quantisation axis at this field stops being dominated by the magnetic moment of its local Pr spin centre. Nevertheless, the coherence time in PrYSO is increased when a small magnetic field is applied and the same effect is also observed in PrLaWO. The presented spin echo decays for different magnetic field strengths indicate an effect of a local Pr-host spin decoupling, similar to a frozen-core behaviour. Analogous measurements for hyperfine transitions having different slopes with respect to magnetic field variations show the impact of pure Zeeman-shifts on the coherence time for similar field strengths. The analysis for detuned ZEFOZ conditions further indicates that the ZEFOZ coherence times in PrLaWO are more limited than in PrYSO. This is possibly attributed to a more complicated Pr-La coupling, since La has a spin of $I = 7/2$ in comparison to Y with $I = 1/2$. Further measurements with different fields and other varied parameters (time scales and temperatures) may help to reveal the relevant dynamics.

The use of ZEFOZ transitions is one possible way to extent the nuclear storage time in optical quantum memories. Another are dynamical decoupling techniques, which are applied to the ground state hyperfine transitions. Using Raman heterodyne scattering the hyperfine coherence time increase by different RF decoupling multi-pulse sequences is studied. A single RF pulse creates a hyperfine coherence, then decoupling pulses are applied in order to increase it's lifetime. For zero magnetic field the coherence time of the $|\pm 1/2\rangle \leftrightarrow |\pm 3/2\rangle$ transition in PrLaWO is extended from 0.25 ms up to 77 ms. For a weak field of $\approx |8|$ mT the pulse sequences extend the coherence times in the same transition (14.87 MHz) to about 400 ms at maximum. This promises a large increase of the storage times in optical to spin storage quantum memories by these techniques. Furthermore, in particular the KDD sequence provides a decoupling efficiency independent of the input coherence phase, which is important for quantum memories in general.

In optical to spin storage experiments an optical input pulse is absorbed and then transferred to nuclear spin coherences. After some spin storage time, it is transferred back to the optical transition and reemitted as output pulse. Longdell et al. demonstrated that the ZEFOZ technique together with dynamical decoupling RF pulses can increase the spin storage time to seconds. Their demonstration used PrYSO and electromagnetically induced transparency (EIT). Despite this potentially long spin storage time, EIT is a low optical bandwidth technique compared to the more recently developed photon echo based quantum memory schemes. Up to date only one photon echo based quantum memory related optical to spin storage demonstration is present. In this particular atomic frequency comb experiment nevertheless no RF

pulses have been used to increase the spin storage time [5]. In this work a photon echo based optical to spin scheme is used to study the potential of dynamical decoupling pulses for enhancements of the spin storage time.

Total storage times of ≈ 10 ms for an optical input pulse are achieved. Accurate storage of the relative phase of optical input pulses is demonstrated for a storage time of about 5 ms, which is about 1200 times longer than for any published REIC photon echo based memory interference experiment.

Nevertheless the achievable spin storage times are much smaller in the optical to spin storage scheme, than would have been expected from the dynamical decoupling coherence times measured with RHS. The longest observed coherence times in the optical to spin storage experiments are about one order of magnitude smaller than those of the RHS based experiments using the same conditions for the dynamical decoupling. The storage scheme uses a previously prepared narrow absorption peak, which contains only one particular (hole burning) class of ions. The data shows that the RF pulses shift other wrong class ions to the optical frequency position of the prepared absorption peak. The optical pulse, used to transfer the spin coherence to the optical transition, excites these wrong class ions too. This may lead to instantaneous spectral diffusion, which can impair the optical refocusing after the storage time and thus the output signal intensity.

The ability of the RF dynamical decoupling pulse sequences to preserve an input state of arbitrary phase is of major relevance for the optical to spin storage scheme. For the optical to spin storage scheme this property is investigated by subjecting the decoupling sequences with variable optical input phase distributions. The experiment demonstrates the inability of all tested sequences to preserve an arbitrary optical phase distribution perfectly. The fact that all sequences show the same performance indicates a more general underlying mechanism. Experiments probing if potential spectral diffusion processes are intrinsic to the compound PrLaWO or might be triggered by some effect of the RF pulses are in preparation.

The optical to spin storage experiments in this thesis demonstrate that nuclear spin decoupling may significantly enlarge photon echo based quantum memory storage times. At the same time this study shows that the efficiency of nuclear spin decoupling techniques observed in other experimental schemes in general does not have to be completely transferable to quantum memories.

[1] I. D. Abella, N. A. Kurnit, and S. R. Hartmann. Photon echoes. *Phys. Rev.*, 141(1):391, 1966. (Cited on pages 15 and 90.)

[2] A. Abragam. *The Principles of Nuclear Magnetism*. Oxford University Press, London, 1994. (Cited on page 52.)

[3] A. Abragam and B. Bleaney. Enhanced nuclear magnetism: Some novel features and prospective experiments. *Proc. R. Soc. Lond. A*, 387:221–256, 1983. (Cited on page 10.)

[4] M. Afzelius, C. Simon, H. de Riedmatten, and N. Gisin. Multimode quantum memory based on atomic frequency combs. *Phys. Rev. A*, 79:52329, 2009. (Cited on pages 2, 62, 89, 91, and 112.)

[5] M. Afzelius, I. Usmani, A. Amari, B. Lauritzen, A. Walther, C. Simon, N. Sangouard, J. Minář, H. de Riedmatten, N. Gisin, and S. Kröll. Demonstration of atomic frequency comb memory for light with spin-wave storage. *Phys. Rev. Lett.*, 104(4):040503, 2010. (Cited on pages 2, 62, 78, 89, 91, 93, and 130.)

[6] A. Ajoy, G. A. Álvarez, and D. Suter. Optimal pulse spacing for dynamical decoupling in the presence of a purely dephasing spin bath. *Phys. Rev. A*, 83:32303, 2011. (Cited on page 104.)

[7] A. L. Alexander, J. J. Longdell, M. J. Sellars, and N. B. Manson. Photon echoes produced by switching electric fields. *Phys. Rev. Lett.*, 96:043602, 2006. (Cited on pages 89 and 91.)

[8] G. A. Álvarez, A. A., X. Peng, and D. Suter. Performance comparison of dynamical decoupling sequences for a qubit in a rapidly fluctuating spin bath. *Phys. Rev. A*, 82:42306, 2010. (Cited on pages 103, 104, 108, 109, and 111.)

[9] C. Audet and J. E. Dennis. Analysis of generalized pattern searches. *Siam J. Optim.*, 13(3):889–903, 2003. (Cited on page 55.)

[10] W. R. Babbitt and T. W. Mossberg. Quasi-two-dimensional time-domain color memories: process limitations and potentials. *J. Opt. Soc. Am. B*, 11:1948, 1994. (Cited on pages 1 and 87.)

[11] J. M. Baker and B. Bleaney. Paramagnetic resonance in some lanthanon ethyl sulphates. *Proc. R. Soc. Lond. A*, 245:156, 1958. (Cited on pages 8 and 10.)

[12] S. E. Beavan, E. Fraval, M. J. Sellars, and J. J. Longdell. Demonstration of the reduction of decoherent errors in a solid-state qubit using dynamic decoupling techniques. *Phys. Rev. A*, 80(3):032308, 2009. (Cited on page 92.)

[13] H. Bethe. Termaufspaltung in Kristallen. *Ann. Phys.*, 395:133, 1929. (Cited on page 8.)

[14] M. J. Biercuk, H. Uys, A. P. Vandevender, N. Shiga, W. M. Itano, and J. J. Bollinger. Optimized dynamical decoupling in a model quantum memory. *Nature*, 458(7241):996, 2009. (Cited on page 126.)

[15] T. Blasberg and D. Suter. Nuclear-spin relaxation of Pr^{3+} in YALO$_3$ - a temperature-dependent optical-rf double-resonance study. *Chem. Phys. Lett.*, 215(6):668–673, 1993. (Cited on pages 62 and 70.)

[16] T. Blasberg and D. Suter. Determination of the absolute sign of nuclear quadrupole interactions by laser radio-frequency double-resonance experiments. *Phys. Rev. B*, 48:9524, 1993. (Cited on pages 14, 48, 52, 70, and 72.)

[17] T. Blasberg and D. Suter. Determination of relative oscillator-strengths by coherent raman beats. *Opt. Commun.*, 120(1-2):55–62, 1995. (Cited on pages 71, 75, 76, and 77.)

[18] T. Blasberg and D. Suter. Determination of oscilator-strengths in Pr^{3+}:YAlO$_3$ by raman heterodyn and hole-burning spectroscopy. *J. Lumin.*, 65(4):199–209, 1995. (Cited on pages 49, 62, 70, 72, and 76.)

[19] T. Blasberg and D. Suter. Interference of scattering pathways in raman heterodyne spectroscopy of multilevel atoms. *Phys. Rev. B*, 51:12439, 1995. (Cited on page 18.)

[20] B. Bleaney. Enhanced nuclear magnetism. *Physica*, 69:317, 1973. (Cited on page 10.)

[21] M. Bonarota, J. Ruggiero, J.-L. Le Gouët, and T. Chanelière. Efficiency optimization for atomic frequency comb storage. *Phys. Rev. A*, 81(3):033803, 2010. (Cited on pages 89 and 91.)

[22] M. Bonarota, J. L. Le Gouët, and T. Chanelière. Highly multimode storage in a crystal. *New J. Phys.*, 13:3013, 2011. (Cited on pages 2, 89, and 91.)

[23] T. Böttger, C. W. Thiel, R. L. Cone, and Y. Sun. Effects of magnetic field orientation on optical decoherence in Er^{3+}:Y$_2$SiO$_5$. *Phys. Rev. B*, 79:115104, 2009. (Cited on page 87.)

[24] J. Brendel, N. Gisin, W. Tittel, and H. Zbinden. Pulsed energy-time enangled twin-photon source for quantum communication. *Phys. Rev. Lett.*, 82(12):2594–2597, 1999. (Cited on page 87.)

[25] H. J. Briegel, W. Dur, J. I. Cirac, and P. Zoller. Quantum repeaters: The role of imperfect local operations in quantum communication. *Phys. Rev. Lett.*, 81(26):5932–5935, 1998. (Cited on pages 2 and 88.)

[26] D. P. Burum, M. Linder, and R. R. Ernst. A new tune-up NMR pulse cycle for minimizing and characterizing phase transients. *J. Magn. Reson.*, 43(3):463–471, 1981. (Cited on pages 104 and 106.)

[27] A. Caprez, P. Meyer, P. Mikhail, and J. Hulliger. New host-lattices for hyperfine optical hole burning: Materials of low nuclear spin moment. *Mater. Res. Bull.*, 32(8):1045–1054, 1997. (Cited on page 63.)

[28] H. Y. Carr and E. M. Purcell. Effects of diffusion on free precession in nuclear magnetic resonance experiments. *Phys. Rev.*, 94:630, 1954. (Cited on page 103.)

[29] W. Y. Ching, Lizhi Ouyang, and Yong-Nian Xu. Electronic and optical properties of Y_2SiO_5 and $Y_2Si_2O_7$ with comparisons to α-SiO_2 and Y_2O_3. *Phys. Rev. B*, 67:245108, 2003. (Cited on page 79.)

[30] C. Clausen, I. Usmani, F. Bussières, N. Sangouard, M. Afzelius, H. de Riedmatten, and N. Gisin. Quantum storage of photonic entanglement in a crystal. *Nature*, 469(7331):508–511, 2011. (Cited on pages 2, 91, and 118.)

[31] Scientific Material Corporation. Laser materials Y_2SiO_5, 2010. URL `http://www.scientificmaterials.com/downloads/YSO.pdf`. (Cited on page 79.)

[32] V. Damon, M. Bonarota, A. Louchet-Chauvet, T. Chanelière, and J.-L. Le Gouët. Revival of silenced echo and quantum memory for light. *New J. Phys.*, 13:3031, 2011. (Cited on pages 2, 62, 89, 90, 91, 112, and 119.)

[33] H. de Riedmatten, M. Afzelius, M. U. Staudt, C. Simon, and N. Gisin. A solid-state light–matter interface at the single-photon level. *Nature*, 456(7223):773–777, 2008. (Cited on pages 62, 87, 89, and 91.)

[34] R. G. Devoe, A. Wokaun, S. C. Rand, and R. G. Brewer. Monte carlo theory of optical dephasing in LaF_3:Pr^{3+}. *Phys. Rev. B*, 23:3125, 1981. (Cited on page 96.)

[35] R. Diehl and G. Brandt. Crystal structure refinement of $YAlO_3$, a promising laser material. *Mat. Res. Bull.*, 10:85–90, 1975. (Cited on pages 71 and 72.)

[36] R. W. P. Drever, J. L. Hall, F. V. Kowalski, J. Hough, G. M. Ford, A. J. Munley, and H. Ward. Laser phase and frequency stabilization using an optical resonator. *Appl. Phys. B*, 31:97, 1983. (Cited on page 25.)

[37] R. W. Equall, Y. Sun, R. L. Cone, and R. M. Macfarlane. Ultraslow optical dephasing in Eu^{3+}:Y_2SiO_5. *Phys. Rev. Lett.*, 72:2179, 1994. (Cited on pages 1, 78, and 122.)

[38] R. W. Equall, R. L. Cone, and R. M. Macfarlane. Homogeneous broadening and hyperfine structure of optical transitions in Pr^{3+}:Y_2SiO_5. *Phys. Rev. B*, 52:3963, 1995. (Cited on pages 2, 62, 63, 78, 79, 80, and 122.)

[39] L. E. Erickson. Hyperfine interaction in the lowest levels of the $^3H_4$ and $^1D_2$ states of trivalent praseodymium in yttrium aluminum perovskite ($YAlO_3$). *Phys. Rev. B*, 19:4412, 1979. (Cited on pages 49, 50, 62, 70, 71, 72, and 77.)

[40] L. E. Erickson. Addendum to "hyperfine interaction in the lowest levels of the $^3H_4$ and $^1D_2$ states of trivalent praseodymium in yttrium aluminum perovskite ($YAlO_3$)". *Phys. Rev. B*, 24:5388, 1981. (Cited on pages 62, 70, and 77.)

[41] L. E. Erickson. Optical-pumping effects on raman-heterodyne-detected multipulse rf nuclear-spin-echo decay. *Phys. Rev. B*, 42:3789, 1990. (Cited on pages 72 and 106.)

[42] R. R. Ernst, G. Bodenhausen, and A. Wokaun. *Principles of Nuclear Magnetic Resonance in One and Two Dimensions*. Oxford University Press, Oxford, 1997. (Cited on page 15.)

[43] E. Fraval. *Minimising the decoherence of rare earth ion solid state spin qubits*. PhD thesis, Australian National University, 2005. (Cited on pages 1, 96, 98, 99, and 100.)

[44] E. Fraval, M. J. Sellars, and J. J. Longdell. Method of extending hyperfine coherence times in $Pr^{3+}:Y_2SiO_5$. *Phys. Rev. Lett.*, 92(7): 077601, 2004. (Cited on pages 2, 47, 79, 91, 92, 97, and 102.)

[45] E. Fraval, M. J. Sellars, A. Morrison, and A. Ferris. Pr-Y interaction in $Pr^{3+}:Y_2SiO_5$. *J. Lumin.*, 107:347–350, 2004. (Cited on pages 95 and 97.)

[46] E. Fraval, M. J. Sellars, and J. J. Longdell. Dynamic decoherence control of a solid-state nuclear-quadrupole qubit. *Phys. Rev. Lett.*, 95(3):030506, 2005. (Cited on pages 2, 79, 87, 91, 92, 97, and 102.)

[47] A. J. Freeman and R. E. Watson. Theoretical investigation of some magnetic and spectroscopic properties of rare-earth ions. *Phys. Rev.*, 127:2058, 1962. (Cited on page 7.)

[48] M. Gärtner, D. Abeln, A. Pring, M. Wilde, and A. Reller. Synthesis, structure, and reactivity of novel lanthanum tungstates. *J. Solid State Chem.*, 111:128, 1994. (Cited on pages 63 and 64.)

[49] S. Geller and E. A. Wood. Crystallographic studies of perovskite-like compounds .1. rare earth orthoferrites and $YFeO_3$, $YCrO_3$, $YAlO_3$. *Acta Crystallogr.*, 9(6):563–568, 1956. (Cited on pages 71 and 72.)

[50] B. C. Gerstein and C. R. Dybowski. *Transient Techniques in NMR of Solids: an Introduction to Theory and Practice*. Academic Press, New York, 1985. (Cited on page 104.)

[51] P. Glasenapp. Charakterisierung der Hyperfein- und Zeeman-Wechselwirkung in Seltenerd-Ion dotierten Kristallen. Diploma thesis, Technische Universität Dortmund, 2011. (Cited on pages 42, 53, 58, 62, 73, 76, and 80.)

[52] P. Goldner, O. Guillot-Noël, F. Beaudoux, Y. Le Du, J. Lejay, T. Chanelière, J.-L. Le Gouët, L. Rippe, A. Amari, A. Walther, and S. Kröll. Long coherence lifetime and electromagnetically induced transparency in a highly-spin-concentrated solid. *Phys. Rev. A*, 79:33809, 2009. (Cited on pages 62 and 63.)

[53] H. Goldstein, C. P. Poole, and J. L. Safko. *Classical Mechanics*. Addison Wesley, San Francisco, 2002. (Cited on page 50.)

[54] O. Guillot-Noël, P. Goldner, Y. Le Du, P. Loiseau, B. Julsgaard, , L. Rippe, and S. Kröll. Hyperfine structure, optical dephasing, and spectral-hole lifetime of single-crystalline $Pr^{3+}:La_2(WO_4)_3$. *Phys. Rev. B*, 75:205110, 2007. (Cited on pages 2, 49, 62, 63, 65, and 87.)

[55] O. Guillot-Noël, P. Goldner, F. Beaudoux, Y. Le Du, J. Lejay, A. Amari, A. Walther, L. Rippe, and S. Kröll. Hyperfine structure and hyperfine coherent properties of praseodymium in single-crystalline $La_2(WO_4)_3$ by hole-burning and photon-echo techniques. *Phys. Rev. B*, 79:155119, 2009. (Cited on pages 48, 52, 62, 65, 67, 70, 71, 79, 94, 95, and 115.)

[56] O. Guillot-Noël, Y. Le Du, F. Beaudoux, E. Antic-Fidancev, M. F. Reid, R. Marino, J. Lejay, A. Ferrier, and P. Goldner. Calculation and analysis of hyperfine and quadrupole interactions in praseodymium-doped $La_2(WO_4)_3$. *J. Lumin.*, 130:1557, 2010. (Cited on page 70.)

[57] T. Gullion, D. B. Baker, and M. S. Conradi. New, compensated carr-purcell sequences. *J. Magn. Reson.*, 89(3):479–484, 1990. (Cited on page 126.)

[58] U. Haeberlen. *High Resolution NMR in Solids: Selective Averaging*. Academic Press, New York, 1976. (Cited on pages 103 and 106.)

[59] E. L. Hahn. Spin echoes. *Phys. Rev.*, 80:580, 1950. (Cited on pages 15 and 103.)

[60] B. S. Ham, M. S. Shahriar, M. K. Kim, and P. R. Hemmer. Frequency-selective time-domain optical data storage by electromagnetically induced transparency in a rare-earth-doped solid. *Opt. Lett.*, 22:1849, 1997. (Cited on page 63.)

[61] B. S. Ham, M. S. Shahriar, M. K. Kim, and P. R. Hemmer. Spin coherence excitation and rephasing with optically shelved atoms. *Phys. Rev. B*, 58(18):R11825–R11828, 1998. (Cited on page 80.)

[62] K. Hammerer, A. S. Sørensen, and E. S. Polzik. Quantum interface between light and atomic ensembles. *Rev. Mod. Phys.*, 82:1041, 2010. (Cited on page 88.)

[63] S. E. Harris. Electromagnetically induced transparency. *Phys. Today*, 50(7):36–42, 1997. (Cited on page 2.)

[64] T. L. Harris, K. D. Merkel, R. K. Mohan, T. Chang, Z. Cole, A. Olson, and Wm. R.Babbitt. Multigigahertz range-doppler correlative signal processing in optical memory crystals. *Appl. Opt.*, 45:343, 2006. (Cited on page 1.)

[65] W. K. Hastings. Monte-carlo sampling methods using markov chains and their applications. *Biometrika*, 57(1):97–109, 1970. (Cited on page 55.)

[66] M. P. Hedges, J. J. Longdell, Y. Li, and M. J. Sellars. Efficient quantum memory for light. *Nature*, 465(7301):1052–1056, 2010. (Cited on pages 2, 62, 78, 89, 91, 112, and 119.)

[67] G. Heinze, A. Rudolf, F. Beil, and T. Halfmann. Storage of images in atomic coherences in a rare-earth-ion-doped solid. *Phys. Rev. A*, 81:11401, 2010. (Cited on page 112.)

[68] W. H. Hesselink and D. A. Wiersma. Picosecond photon echoes stimulated from an accumulated grating. *Phys. Rev. Lett.*, 43:1991, 1979. (Cited on page 89.)

[69] G. Hétet, J. J. Longdell, A. L. Alexander, P. K. Lam, and M. J. Sellars. Electro-optic quantum memory for light using two-level atoms. *Phys. Rev. Lett.*, 100:23601, 2008. (Cited on pages 2, 78, and 89.)

[70] G. Hétet, J. J. Longdell, M. J. Sellars, P. K. Lam, and B. C. Buchler. Multimodal properties and dynamics of gradient echo quantum memory. *Phys. Rev. Lett.*, 101:203601, 2008. (Cited on pages 89 and 91.)

[71] K. Holliday, M. Croci, E. Vauthey, and U. P. Wild. Spectral hole burning and holography in an Y_2SiO_5:Pr^{3+} crystal. *Phys. Rev. B*, 47:83777, 1993. (Cited on pages 49, 62, 63, and 80.)

[72] S. Hüfner. *Optical Spectra of Transparent Rare Earth Compounds*. Academic Press, New York, 1978. (Cited on page 8.)

[73] K. Ichimura. A simple frequency-domain quantum computer with ions in a crystal coupled to a cavity mode. *Opt. Commun.*, 196:119, 2001. (Cited on page 1.)

[74] B. Julsgaard, A. Walther, S. Kröll, and L. Rippe. Understanding laser stabilization using spectral hole burning. *Optics Express*, 15: 11444, 2007. (Cited on pages 28, 29, 93, and 102.)

[75] N. Khaneja, T. Reiss, C. Kehlet, T. Schulte-Herbrüggen, and S. J. Glaser. Optimal control of coupled spin dynamics: design of NMR pulse sequences by gradient ascent algorithms. *J. Magn. Reson.*, 172:296, 2005. (Cited on page 47.)

[76] K. Khodjasteh and D. A. Lidar. Performance of deterministic dynamical decoupling schemes: Concatenated and periodic pulse sequences. *Phys. Rev. A*, 75(6):062310, 2007. (Cited on pages 103 and 104.)

[77] S. Kirkpatrick, C. D. Gelatt, and M. P. Vecchi. Optimization by simulated annealing. *Science*, 220:671, 1983. (Cited on pages 54 and 55.)

[78] R. Klieber. *Optisch-detektierte Kernspinresonanz an Pr^{3+}:$YAlO_3$*. PhD thesis, Universität Dortmund, 2006. (Cited on pages 48, 49, 52, 70, 71, and 72.)

[79] R. Klieber and D. Suter. Correlating NQR transitions of ground and excited electronical states. *Phys. Rev. B*, 71:224418, 2005. (Cited on pages 49, 62, and 70.)

[80] R. Klieber and D. Suter. Time-resolved coherent double raman detection of nuclear spin transitions. *Phys. Rev. B*, 73:94408, 2006. (Cited on pages 62 and 70.)

[81] R. Klieber, A. Michalowski, R. Neuhaus, and D. Suter. All-optical measurement of nuclear-spin relaxation. *Phys. Rev. B*, 68:54426, 2003. (Cited on pages 62, 70, and 72.)

[82] R. Klieber, A. Michalowski, R. Neuhaus, and D. Suter. Nuclear quadrupole resonance of an electronically excited state from high-resolution hole-burning spectroscopy. *Phys. Rev. B*, 67:184103, 2003. (Cited on pages 14, 62, 70, 71, 76, and 77.)

[83] F. Könz, Y. Sun, C. W. Thiel, R. L. Cone, R. W. Equall, R. L. Hutcheson, and R. M. Macfarlane. Temperature and concentration dependence of optical dephasing, spectral-hole lifetime, and anisotropic absorption in $Eu^{3+}:Y_2SiO_5$. *Phys. Rev. B*, 68:85109, 2003. (Cited on page 62.)

[84] S. Kröll and P. Tidlund. Recording density limit of photon-echo optical storage with high-speed writing and reading. *Appl. Opt.*, 32:7233, 1993. (Cited on pages 1 and 87.)

[85] A. Kuzmich, K. Mølmer, and E. S. Polzik. Spin squeezing in an ensemble of atoms illuminated with squeezed light. *Phys. Rev. Lett.*, 79:4782, 1997. (Cited on page 88.)

[86] P. M. Ledingham, W. R. Naylor, J. J. Longdell, S. E. Beavan, and M. J. Sellars. Nonclassical photon streams using rephased amplified spontaneous emission. *Phys. Rev. A*, 81:12301, 2010. (Cited on page 89.)

[87] J. Lekavich. Basics of acousto-optic devices. *Lasers & Applications*, pages 59–64, 1986. (Cited on page 32.)

[88] N. Leonyuk. High-temperature crystallization and x-ray characterization of Y_2SiO_5, $Y_2Si_2O_7$ and $LaBSiO_5$. *J. Cryst. Growth*, 205: 361, 1999. (Cited on page 79.)

[89] M. Levitt. Composite pulses. *Prog. Nucl. Magn. Reson. Spectrosc.*, 1986. (Cited on page 104.)

[90] H. Lin, T. Wang, and T. W. Mossberg. Demonstration of 8-Gbit/in.2 areal storage density based on swept-carrier frequency-selective optical memory. *Opt. Lett.*, 20:1658, 1995. (Cited on pages 1 and 87.)

[91] X. Lin, Y. Chen, J. Liao, Z. Luo, and Y. Huang. Czochralski growth and spectral properties of $Er^{3+}:La_2(WO_4)_3$ crystals. *J. Cryst. Growth*, 266(4):487–491, 2004. (Cited on page 63.)

[92] J. J. Longdell. *Quantum information processing in rare earth ion doped insulators*. PhD thesis, Australian National University, 2003. (Cited on pages 52, 59, 60, 79, and 80.)

[93] J. J. Longdell, M. J. Sellars, and N. B. Manson. Hyperfine interaction in ground and excited states of praseodymium-doped yttrium orthosilicate. *Phys. Rev. B*, 66:35101, 2002. (Cited on pages 2, 48, 54, 59, 62, 78, 79, 80, and 127.)

[94] J. J. Longdell, M. J. Sellars, and N. B. Manson. Demonstration of conditional quantum phase shift between ions in a solid. *Phys. Rev. Lett.*, 93(13):130503, 2004. (Cited on pages 1 and 78.)

[95] J. J. Longdell, E. Fraval, M. J. Sellars, and N. B. Manson. Stopped light with storage times greater than one second using electromagnetically induced transparency in a solid. *Phys. Rev. Lett.*, 95 (6):063601, 2005. (Cited on pages 2, 79, 91, 92, 112, and 113.)

[96] J. J. Longdell, A. L. Alexander, and M. J. Sellars. Characterization of the hyperfine interaction in europium-doped yttrium orthosilicate and europium chloride hexahydrate. *Phys. Rev. B*, 74:195101, 2006. (Cited on pages 78, 91, 92, and 99.)

[97] M. Lovrić, P. Glasenapp, D. Suter, B. Tumino, A. Ferrier, P. Goldner, M. Sabooni, L. Rippe, and S. Kröll. Hyperfine characterization and spin coherence lifetime extension in $Pr^{3+}:La_2(WO_4)_3$. *Phys. Rev. B*, 84:104417, 2011. (Cited on pages 63, 70, 79, 93, and 98.)

[98] M. D. Lukin and P. R. Hemmer. Quantum entanglement via optical control of atom-atom interactions. *Phys. Rev. Lett.*, 84(13): 2818–2821, 2000. (Cited on page 1.)

[99] R. Macfarlane. High-resolution laser spectroscopy of rare-earth doped insulators: a personal perspective. *J. Lumin.*, 100:1–20, 2002. (Cited on pages 1, 11, 15, 62, 87, and 91.)

[100] R. M. Macfarlane and R. M. Shelby. Spectroscopy of solids containing rare earth ions. In A. A. Kaplyanskii and R. M. Macfarlane, editors, *Modern Problems in Condensed Matter Sciences*, volume 21, pages 51–184. North Holland, Amsterdam, 1987. (Cited on pages 1, 8, 9, 11, 13, 15, 16, 47, 62, 70, and 76.)

[101] R. M. Macfarlane, R. M. Shelby, and R. L. Shoemaker. Ultrahigh-resolution spectroscopy: Photon echoes in $YAlO_3:Pr^{3+}$ and $LaF_3:Pr^{3+}$. *Phys. Rev. Lett.*, 43:1726, 1979. (Cited on pages 62, 70, 72, and 91.)

[102] R. M. Macfarlane, C. S. Yannoni, and R. M. Shelby. Optical line narrowing by nuclear spin decoupling in $Pr^{3+}:LaF_3$. *Opt. Commun.*, 32:101, 1980. (Cited on page 91.)

[103] W. Magnus. On the exponential solution of differential equations for a linear operator. *Comm. Pure Appl. Math.*, 7(4):649–673, 1954. (Cited on page 103.)

[104] N. B. Manson, M. J. Sellars, P. T. H. Fisk, and R. S. Meltzer. Hole-burning of rare-earth ions with kHz resolution. *J. Lumin.*, 64(1-6): 19–23, 1995. (Cited on page 96.)

[105] A. A. Maudsley. Modified carr purcell meiboom gill sequence for NMR fourier-imaging applications. *J. Magn. Reson.*, 69(3):488–491, 1986. (Cited on pages 104 and 111.)

[106] S. Meiboom and D. Gill. Modified spin-echo method for measuring nuclear relaxation times. *Rev. Sci. Instrum.*, 29:688, 1958. (Cited on pages 92, 102, and 104.)

[107] N. Metropolis, A. W. Rosenbluth, M. N. Rosenbluth, A. H. Teller, and E. Teller. Equation of state calculations by fast computing machines. *J. Chem. Phys.*, 21(6):1087–1092, 1953. (Cited on page 55.)

[108] J. Minář, N. Sangouard, M. Afzelius, H. de Riedmatten, and N. Gisin. Spin-wave storage using chirped control fields in atomic frequency comb-based quantum memory. *Phy.s Rev. A*, 82:42309, 2010. (Cited on pages 90 and 91.)

[109] M. Mitsunaga. cw photon echo: Theory and observations. *Phys. Rev. A*, 42:1617, 1990. (Cited on pages 71 and 77.)

[110] M. Mitsunaga, E. S. Kintzer, and R. G. Brewer. Raman heterodyne interference of inequivalent nuclear sites. *Phys. Rev. Lett.*, 52:1484, 1984. (Cited on pages 18, 49, 62, 63, 70, 71, and 77.)

[111] M. Mitsunaga, E. S. Kintzer, and R. G. Brewer. Raman heterodyne interference: Observations and analytic theory. *Phys. Rev. B*, 31: 6947, 1985. (Cited on pages 11, 18, 49, 62, 63, 66, 70, 71, 76, 77, and 102.)

[112] M. Mitsunaga, R. Yano, and N. Uesugi. Stimulated-photon-echo spectroscopy. II. echo modulation in Pr^{3+}:YAlO$_3$. *Phys. Rev. B*, 45 (22):12760–12768, 1992. (Cited on pages 71 and 77.)

[113] M. Mitsunaga, N. Uesugi, and K. Sugiyama. Kilohertz-resolution pump-probe spectroscopy in Pr^{3+}:YAlO$_3$. *Opt. Lett.*, 18(15):1256–1258, 1993. (Cited on page 72.)

[114] J. Mlynek, N. C. Wong, R. G. DeVoe, E. S. Kintzer, and R. G. Brewer. Raman heterodyne detection of nuclear magnetic resonance. *Phys. Rev. Lett.*, 50:993, 1983. (Cited on page 16.)

[115] R. K. Mohan, T. Chang, M. Tian, S. Bekker, A. Olson, C. Ostrander, A. Khallaayoun, C. Dollinger, W. R. Babbitt, Z. Cole, R. R. Reibel, K. D. Merkel, Y. Sun, R. Cone, F. Schlottau, and K. H. Wagner. Ultra-wideband spectral analysis using S2 technology. *J. Lumin.*, 127(1):116–128, 2007. (Cited on page 1.)

[116] S. A. Moiseev. Quantum memory on the basis of photon echo in three-level optically dense gaseous media with the Ξ-configuration of atomic transitions. *Optics and Spectroscopy*, 94: 788, 2003. (Cited on page 88.)

[117] S. A. Moiseev and S. Kröll. Complete reconstruction of the quantum state of a single-photon wave packet absorbed by a Doppler-broadened transition. *Phys. Rev. Lett.*, 87(17):173601, 2001. (Cited on pages 2, 89, and 91.)

[118] S. A. Moiseev, V. F. Tarasov, and B. S. Ham. Quantum memory photon echo-like techniques in solids. *J. Opt. B: Quantum Semiclass. Opt.*, 5:497, 2003. (Cited on page 88.)

[119] T. W. Mossberg. Time-domain frequency-selective optical data storage. *Opt. Lett.*, 7:77, 1982. (Cited on pages 1 and 87.)

[120] M. A. Nielsen and I. L. Chuang. *Quantum Computation and Quantum Information*. Cambridge University Press, Cambridge, 2005. (Cited on pages 1, 87, and 89.)

[121] M. Nilsson and S. Kröll. Solid state quantum memory using complete absorption and re-emission of photons by tailored and externally controlled inhomogeneous absorption profiles. *Opt. Commun.*, 247(4-6):393–403, 2005. (Cited on pages 78 and 89.)

[122] M. Nilsson, L. Rippe, S. Kröll, R. Klieber, and D. Suter. Hole-burning techniques for isolation and study of individual hyperfine transitions in inhomogeneously broadened solids demonstrated in Pr^{3+}:Y$_2$SiO$_5$. *Phys. Rev. B*, 70(21):214116, 2004. (Cited on pages 3, 14, 47, 48, 52, 62, 78, 79, 80, 83, 89, and 115.)

[123] M. Nilsson, L. Rippe, S. Kröll, R. Klieber, and D. Suter. Erratum: Hole-burning techniques for isolation and study of individual hyperfine transitions in inhomogeneously broadened solids demonstrated in Pr^{3+}:Y$_2$SiO$_5$ [Phys. Rev B 70, 214116 (2004)]. *Phys. Rev. B*, 71:149902, 2005. (Cited on page 62.)

[124] J. Nunn, K. Reim, K. C. Lee, V. O. Lorenz, B. J. Sussman, I. A. Walmsley, and D. Jaksch. Multimode memories in atomic ensembles. *Phys. Rev. Lett.*, 101(26):260502, 2008. (Cited on pages 89 and 91.)

[125] T. Paschen. Untersuchung der Nichtlinearitäten eines optischen Retroreflexaufbaus zur Erzeugung von korrigierten arbiträren optischen Pulsformen. Bachelor's thesis, Technische Universität Dortmund, 2010. (Cited on page 33.)

[126] S. Pasini and G. S. Uhrig. Optimized dynamical decoupling for power-law noise spectra. *Phys. Rev. A*, 81:12309, Jan 2010. (Cited on page 126.)

[127] W. H. Press. *Numerical Recipes: The Art of Scientific Computing*. Cambridge University Press, Cambridge, 2007. (Cited on page 59.)

[128] P. Raghavan. Table of nuclear moments. *At. Data Nucl. Data Tables*, 42:189, 1989. (Cited on page 63.)

[129] L. Rippe. *Quantum computing with naturally trapped subnanometre-spaced ions*. PhD thesis, Lund University, 2007. (Cited on pages 93 and 102.)

[130] L. Rippe, M. Nilsson, S. Kröll, R. Klieber, and D. Suter. Experimental demonstration of efficient and selective population transfer and qubit distillation in a rare-earth-metal-ion-doped crystal. *Phys. Rev. A*, 71:62328, 2005. (Cited on pages 33, 80, 115, and 118.)

[131] L. Rippe, B. Julsgaard, A. Walther, and S. Kröll. Laser stabilization using spectral hole burning. *arXiv*, quant-ph:0611056v1, 2006. (Cited on pages 29 and 93.)

[132] L. Rippe, B. Julsgaard, A. Walther, Y. Ying, and S. Kröll. Experimental quantum-state tomography of a solid-state qubit. *Phys. Rev. A*, 77(2):022307, 2008. (Cited on pages 1, 78, and 93.)

[133] J. Ruggiero, J. L. Le Gouët, C. Simon, and T. Chanelière. Why the two-pulse photon echo is not a good quantum memory protocol. *Phys. Rev. A*, 79:53851, 2009. (Cited on pages 1, 88, and 89.)

[134] J. Ruggiero, T. Chanelière, and J.-L. Le Gouët. Coherent response to optical excitation in a strongly absorbing rare-earth ion-doped crystal. *J. Opt. Soc. Am. B*, 27(1):32–37, 2010. (Cited on pages 2 and 88.)

[135] C. A. Ryan, J. S. Hodges, and D. G. Cory. Robust decoupling techniques to extend quantum coherence in diamond. *Phys. Rev. Lett.*, 105(20):200402, 2010. (Cited on pages 104 and 126.)

[136] A. M. S., G. A. Álvarez, and D. Suter. Effects of time reversal symmetry in dynamical decoupling. *arXiv*, quant-ph:1110.1011v1, 2011. (Cited on page 126.)

[137] M. Sabooni, F. Beaudoin, A. Walther, N. Lin, A. Amari, M. Huang, and S. Kröll. Storage and recall of weak coherent optical pulses with an efficiency of 25%. *Phys. Rev. Lett.*, 105:60501, 2010. (Cited on pages 89, 91, 93, and 119.)

[138] E. Saglamyurek, N. Sinclair, J. Jin, J. A. Slater, D. Oblak, F. Bussières, M. George, R. Ricken, W. Sohler, and W. Tittel. Broadband waveguide quantum memory for entangled photons. *Nature*, 469 (7331):512–515, 2011. (Cited on pages 2 and 91.)

[139] V. Scarani, S. Iblisdir, N. Gisin, and A. Acín. Quantum cloning. *Rev. Mod. Phys.*, 77:1225, 2005. (Cited on page 88.)

[140] F. De Seze, F. Dahes, V. Crozatier, I. Lorgere, F. Bretenaker, and J. L. Le Gouët. Coherent driving of Tm^{3+}:YAG ions using a complex hyperbolic secant optical field. *Eur. Phys. J. D.*, 33(3): 343–355, 2005. (Cited on pages 115 and 118.)

[141] R. D. Shannon and C. T. Prewitt. Effective ionic radii in oxides and fluorides. *Acta Crystallogr. Sect. B*, 25(5):925–946, 1969. (Cited on pages 62 and 63.)

[142] C. P. Slichter. *Principles of Magnetic Resonance*. Harper & Row, New York, 1963. (Cited on page 8.)

[143] A. M. Souza, G. A. Álvarez, and D. Suter. Robust dynamical decoupling for quantum computing and quantum memory. *Phys. Rev. Lett.*, 106:240501, 2011. (Cited on pages 104, 105, 108, 109, and 111.)

[144] M. U. Staudt, M. Afzelius, H. de Riedmatten, S. R. Hastings-Simon, C. Simon, R. Ricken, H. Suche, W. Sohler, and N. Gisin. Interference of multimode photon echoes generated in spatially separated solid-state atomic ensembles. *Phys. Rev. Lett.*, 99:173602, 2007. (Cited on page 118.)

[145] M. U. Staudt, S. R. Hastings-Simon, M. Nilsson, M. Afzelius, V. Scarani, R. Ricken, H. Suche, W. Sohler, W. Tittel, and N. Gisin. Fidelity of an optical memory based on stimulated photon echoes. *Phys. Rev. Lett.*, 98:113601, 2007. (Cited on page 118.)

[146] Y. Sun, C. W. Thiel, R. L. Cone, R. W. Equall, and R. L. Hutcheson. Recent progress in developing new rare earth materials for hole burning and coherent transient applications. *J. Lumin.*, 98(1-4): 281–287, 2002. (Cited on pages 1 and 87.)

[147] M. A. Teplov. Magnetic resonance on Pr^{141} nuclei in a $Pr_2(SO_4)_3 \cdot 8H_2O$ single crystal. *Sov. Phys. JETP*, 26:872, 1968. (Cited on page 9.)

[148] W. Tittel, M. Afzelius, T. Chaneliére, R. L. Cone, S. Kröll, S. A. Moiseev, and M. J. Sellars. Photon-echo quantum memory in solid state systems. *Laser & Photon. Rev.*, 4(2):244–267, 2010. (Cited on pages 1, 2, 62, 89, 91, and 118.)

[149] V. Torczon. On the convergence of pattern search algorithms. *Siam J. Optim.*, 7(1):1–25, 1997. (Cited on page 55.)

[150] G. S. Uhrig. Keeping a quantum bit alive by optimized π-pulse sequences. *Phys. Rev. Lett.*, 98:100504, 2007. (Cited on page 126.)

[151] I. Usmani, M. Afzelius, H. de Riedmatten, and N. Gisin. Mapping multiple photonic qubits into and out of one solid-state atomic ensemble. *Nature Commun.*, 1(1):1–7, 2010. (Cited on pages 2, 89, 91, and 118.)

[152] J. H. van Vleck. The theory of electric and magnetic susceptibilities. In R. H. Fowler and P. Kapitza, editors, *The International Series of Monographs on Physics*, page 384. Oxford University Press, London, 1932. (Cited on page 8.)

[153] J. H. van Vleck. The puzzel of rare-earth spectra in solids. *J. Phys. Chem.*, 41:67–80, 1937. (Cited on pages 1 and 8.)

[154] L. Viola and S. Lloyd. Dynamical suppression of decoherence in two-state quantum systems. *Phys. Rev. A*, 58(4):2733–2744, 1998. (Cited on pages 92 and 103.)

[155] L. Viola, E. Knill, and S. Lloyd. Dynamical decoupling of open quantum systems. *Phys. Rev. Lett.*, 82(12):2417–2421, 1999. (Cited on page 103.)

[156] A. Walther. *Coherent Processes in Rare-Earth-Ion-Doped Solids*. PhD thesis, Lund University, 2009. (Cited on page 93.)

[157] A. Walther, B. Julsgaard, L. Rippe, Y. Ying, S. Kröll, R. Fisher, and S. Glaser. Extracting high fidelity quantum computer hardware from random systems. *Phys. Scripta*, 137:4009, 2009. (Cited on pages 47 and 93.)

[158] T. Wang, C. Greiner, J. Bochinski, and T. Mossberg. Experimental study of photon-echo size in optically thick media. *Phys. Rev. A*, 1999. (Cited on page 88.)

[159] R. Wannemacher. Nuclear spin-flip sidebands in optical spectral holeburning and fluorescence line narrowing of the Er^{3+} ion. *J. Lumin.*, 48:309, 1991. (Cited on page 96.)

[160] P. Wirth. Inbetriebnahme eines supraleitenden Vektormagneten für opto-magnetische Experimente. Bachelor's thesis, Technische Universität Dortmund, 2011. (Cited on page 42.)

[161] A. Wokaun, S. C. Rand, R. G. Devoe, and R. G. Brewer. Anticrossings in solid-state laser spectroscopy. *Phys. Rev. B*, 23:5733, 1981. (Cited on pages 49, 62, 70, 71, 75, and 77.)

[162] N. C. Wong, E. S. Kintzer, J. Mlynek, R. G. DeVoe, and R. G. Brewer. Raman heterodyne detection of nuclear magnetic resonance. *Phys. Rev. B*, 28:4993, 1983. (Cited on pages 16, 17, and 48.)

[163] W. Yang, Z. Y. Wang, and R. B. Liu. Preserving qubit coherence by dynamical decoupling. *Front. Phys.*, 6(1):2–14, 2010. (Cited on pages 103 and 104.)

[164] R. Yano, M. Mitsunaga, and N. Uesugi. Ultralong optical dephasing time in Eu^{3+}:Y_2SiO_5. *Opt. Lett.*, 16:1884, 1991. (Cited on page 78.)

ACKNOWLEDGMENTS